Computational Study of Particle Clustering and Dispersion in Turbulence

George Harry Downing
Civil Engineering, Imperial College London
PhD

October 2024

Abstract

This thesis presents a comprehensive investigation into aerosol dispersion and the preferential concentration of particles in turbulent flows, with a focus on computational modelling. It introduces an Eulerian computational method based on the Roe-flux scheme, enhancing the efficiency of particle-laden flow simulations by incorporating second-order velocity moments. This method, compared to traditional Lagrangian particle tracking, is applied to Direct Numerical Simulations (DNS) of both the turbulent flow and particle phase, offering new insights into particle velocity and concentration fluctuations.

The research explores the effects of the Stokes ($0 < Stk < 10$), Reynolds ($50 < Re_\lambda < 120$), and Froude ($0 < Fr_l < 5$) numbers on particle clustering. Particles with Stokes numbers near unity exhibit the strongest clustering, while higher Stokes numbers reveal that increasing Reynolds and Froude numbers influence clustering patterns at different scales. A novel empirical model is developed to predict the spectra of particle concentration fluctuations under varying conditions, providing a practical tool for analysing aerosol behaviour in environments where detailed computations may be infeasible.

A significant contribution of this thesis is the investigation into the role of Lagrangian Coherent Structures (LCS) in generating preferential concentration. By using the Lagrangian-averaged vorticity deviation (LAVD), the research shows that rotational coherence in turbulent flows plays a critical role in particle clustering, improving upon previous approaches like the Q criterion. Additionally, it demonstrates that incorporating time delays between fluid structures and particle positions significantly enhances the correlation between particle clusters and turbulent features.

These findings contribute to a deeper understanding of particle-turbulence interactions and have important applications in atmospheric aerosol dispersion, pollution control, and industrial processes, offering predictive models that can help manage aerosol behaviour in complex, large-scale environments.

Statement of Originality

I, George Downing, declare that this thesis and the work presented in it are my own and have been generated by me as the result of my own original research. Where I have drawn on the work of others, this has been fully acknowledged in accordance with academic standards and ethical guidelines. This thesis has not been submitted, either in whole or in part, for a degree or diploma at any other institution.

Copyright Declaration

The copyright of this thesis rests with the author. Unless otherwise indicated, its contents are licensed under a Creative Commons Attribution-Non Commercial 4.0 International Licence (CC BY-NC).

Under this licence, you may copy and redistribute the material in any medium or format. You may also create and distribute modified versions of the work. This is on the condition that: you credit the author and do not use it, or any derivative works, for a commercial purpose.

When reusing or sharing this work, ensure you make the licence terms clear to others by naming the licence and linking to the licence text. Where a work has been adapted, you should indicate that the work has been changed and describe those changes.

Please seek permission from the copyright holder for uses of this work that are not included in this licence or permitted under UK Copyright Law.

Acknowledgments

I would like to express my deepest gratitude to my supervisor, Prof. Yannis Hardalupas, for his invaluable guidance, support, and encouragement throughout the course of my research. His expertise and insights were essential to the successful completion of this work.

I am also deeply grateful for the financial support provided by the Centre for Doctoral Training in Aerosol Science (EP/S023593/1), without which this research would not have been possible. I would like to extend my thanks to the CDT Centre Director, Prof. Jonathan Reid, and CDT Course Manager, Dr. Rachael Miles, for their assistance and commitment in facilitating my studies.

I would like to acknowledge the Engineering and Physical Sciences Research Council (EP/V050516/1) and the UK Collaboratorium for Research in Infrastructure & Cities: Urban Observatories (Strand B) (EP/P016782/1), whose funding supported specific aspects of my research.

Furthermore, I wish to thank DSTL (Defence Science and Technology Laboratory) for providing the opportunity to undertake an industrial placement, and I am particularly grateful to Timothy Foat and Joseph Drodge for their mentorship and collaboration during my time with DSTL.

Lastly, I extend my heartfelt thanks to my family, friends, and colleagues for their unwavering support and encouragement throughout my PhD journey.

Contents

Statement of Originality **3**

Copyright Declaration **4**

Acknowledgments **5**

1 Introduction **19**

1.1 The Problem Considered 19
1.2 Turbulence 23
1.2.1 Fundamentals of Turbulence 23
1.2.2 Energy Cascade of Turbulence 26
1.2.3 Statistical Description of Turbulence 27
1.2.4 Homogeneous Isotropic Turbulence 29
1.3 Particle Dynamics 30
1.3.1 Equation of Motion 30
1.3.2 Preferential Concentration 33
1.3.3 Two-Way Coupling 39
1.3.4 Gravitational Settling 41
1.3.5 Interactions Between Particles 42
1.4 Numerical Simulation of Turbulent Flows 43
1.4.1 Direct Numerical Simulation With Pseudo-Spectral Simulation 44
1.4.2 Fast Fourier Transform 46
1.4.3 Gibbs oscillations 47
1.4.4 Time Stepping 47
1.5 Numerical Simulation of Particle Flows 49
1.5.1 Lagrangian Point-Particle Method 50
1.5.2 Eulerian Methods 52
1.5.3 Numerical Simulation of Preferential Concentration 54
1.6 Summary 55
1.7 Current Contribution 58

2 Computational and Experimental Study of Aerosol Dispersion in a Ventilated Room 61
2.1 Abstract . . . 61
2.2 Introduction . . . 62
2.3 Methodology . . . 64
2.3.1 Experimental Methods . . . 64
2.3.2 Computational Methods . . . 67
2.4 Results . . . 72
2.4.1 Evaluation of Fluid flow Computation . . . 72
2.4.2 Aerosol Characteristics . . . 73
2.4.3 Discussion . . . 78
2.5 Conclusion . . . 82

3 Spectral Characteristics of Particle Preferential Concentration in Turbulence Computed by Eulerian and Lagrangian Methods 83
3.1 Abstract . . . 83
3.2 Introduction . . . 84
3.3 Numerical Method . . . 87
3.3.1 Carrier Fluid Simulations . . . 87
3.3.2 Particle Simulations . . . 88
3.4 Results . . . 93
3.4.1 Instantaneous Particle Concentration Spatial Distributions . 95
3.4.2 Effect of Grid Resolution . . . 99
3.4.3 Particle Concentration Spectra . . . 100
3.4.4 Particle Momentum Spectra . . . 104
3.4.5 Particle Velocity Spectra . . . 106
3.4.6 Particle Energy Spectra . . . 108
3.5 Conclusions . . . 110

4 Spectral Analysis of Preferential Concentration in Turbulent Flows: Parametric Dependence on Reynolds, Stokes, and Froude Numbers 113
4.1 Abstract . . . 113
4.2 Introduction . . . 114
4.3 Numerical Method . . . 120
4.3.1 Carrier Fluid Simulations . . . 120
4.3.2 Inertial Particle Simulations . . . 121
4.3.3 Simulation Conditions . . . 122
4.3.4 Spectra Analysis Methods . . . 123

4.4 Results . . . 124
4.4.1 Instantaneous spatial distributions of particle concentration 124
4.4.2 Spectra of particle number density fluctuations for different Stokes numbers . . . 126
4.4.3 Spectra of particle number density fluctuations for different Reynolds numbers . . . 127
4.4.4 Spectra of particle number density fluctuations for different Froude numbers . . . 130
4.4.5 Empirical Relations . . . 132
4.5 Conclusions . . . 144

5 Investigating Preferential Concentration of Inertial Particles through Lagrangian Coherent Structures in Turbulent Flows 146
5.1 Abstract . . . 146
5.2 Introduction . . . 147
5.3 Numerical Method . . . 149
5.3.1 Carrier Fluid Simulations . . . 149
5.3.2 Inertial Particle Simulations . . . 150
5.3.3 Simulation Conditions . . . 151
5.3.4 Lagrangian Coherent Structures . . . 151
5.3.5 Finite-Time Lyapunov Exponent . . . 152
5.3.6 Lagrangian-Averaged Vorticity Deviation . . . 153
5.4 Results . . . 155
5.4.1 Influence of Q-Criterion . . . 155
5.4.2 Influence of Enstrophy . . . 162
5.4.3 Time delay of Q-Criterion . . . 164
5.4.4 Finite-Time Lyapunov Exponent (FTLE) . . . 170
5.4.5 Lagrangian-Averaged Vorticity Deviation (LAVD) . . . 175
5.5 Conclusions . . . 180

6 Conclusions 183
6.1 Summary . . . 183
6.2 Future Work . . . 185

References 186

A Roe Decomposition 203

List of Figures

2.1 Top-down view of the false ceiling with ducting placement. Outside air flows into the false ceiling via the heat exchanger (green line) where is mixes with air being brought up from WS401 from the square grill. This mixed air is then drawn into the heat pump inlet where it enters WS401 via the swirl diffusers. The experimental room was WS401 in this diagram. 65

2.2 Droplet size distribution (measured by an APS) from the 500 mL humidifier, as measured close to the humidifier exit, so that the droplets had not evaporated. 66

2.3 Top-down view of the room and sensor placements within the test room. All nodes are at a height of 1.6 m apart from Nodes 1, 3, 6, 10 & 12, which are at a height of 1.2 m. Diagram to scale. 67

2.4 Top-down view of the velocity field at a height of 1.6 m. Grid size is 10 cm as seen in the figure and the velocity magnitude is according to the colour scale. (Figure 2.3 shows the room features for comparison.) 69

2.5 Time dependent aerosol particle number concentration computed at node 1 of a 5 cm grid (blue) and a 10 cm grid (red). 72

2.6 Aerosol injection pulses used in the experiment. 0 indicates the aerosol generator was switched off; 1 indicates the aerosol generator was switched on. The temporal sequence of the pulse included five 1-minute pulses followed by three 15-second pulses and finally two 30-second pulses. 73

2.7 Model (dashed) and experimental (solid) temporal concentrations for 2.0 µm particles for Node 12 (placed near the aerosol generator, blue) and Node 1 (placed far from the aerosol generator, red). This model assumes no aerosol recirculation by the ventilation system. Model particle concentration rates were scaled by matching the mean of the model and experiment. (a) Shows the full response (b) Shows the response after 50 minutes on a logarithmic scale. . . 74

2.8 Experimental decay rates (blue) along with theoretical decay rates assuming 0% recycled particles (red, solid) and 100% recycled particles (green, solid) for different particle sizes. The error bar of the experimental data represents the standard error of the exponential fit. The error in the theoretical decay rates (distance between the two dashed lines) represents the width of the bin size of the low-cost sensors. 76
2.9 Calculated recycling ratios (blue) as a function of particle size based on results of Figure 2.8, and best fit line (red) used in the computations with the Experimentally Informed CFD Model. Arrow heads represent the uncertainty. For the linear portion $r^2 = 0.97$. 77
2.10 Model (dashed) and experimental (solid) temporal responses for the concentration of the 2.0 µm particles for Node 12 (blue) and Node 1 (red). This model uses the recycling ratios defined in Figure 2.8. Model and experimental values were scaled together by matching their median values. (a) Shows the full response (b) Shows the response after 50 minutes on a logarithmic scale. 78
2.11 Time-dependent experimental measurements (solid) and model predictions (dashed) of aerosol number concentration at Node 12 (blue) and Node 1 (red) for (a) 1.5 µm and (b) 7.25 µm particles. 79
2.12 Showing PM_{10} for all nodes (except Node 12). Nodes are ordered based on distance from the aerosol generator. Blue (E) lines are the experimental values, orange (M) lines are the CFD model with recycling. All graphs have the same axis scales. 80

3.1 An example instantaneous kinetic energy distribution in a 2D slice of a 3D Direct Numerical Simulation (DNS) fluid simulation at $Re_\varepsilon = 1500$. 89
3.2 Spectral energy of the particle number concentration against the wavenumber for $Stk = 1.0$ and $Re_\varepsilon = 1500$ estimated from the particle distribution calculated with 4 different methods, the direct spectrum from the Lagrangian method (solid red), the box-averaged Lagrangian method (solid blue), the Eulerian method with energy contributions (dashed), and the Eulerian method without energy contributions (dashed-dotted). 96

3.3 Instantaneous particle concentration spatial distribution on a 2D slice for $Stk = 0.0$ (Fluid particle) and $Re_\varepsilon = 1500$ calculated with 3 different methods. Left is the Eulerian method without energy contributions, middle is the Eulerian method with energy, right is the Lagrangian approach. 97
3.4 Instantaneous particle concentration spatial distribution on a 2D slice for $Stk = 0.5$ and $Re_\varepsilon = 1500$ calculated with 3 different methods. Left is the Eulerian method without energy contributions (error metric $\delta = 2.13$), middle is the Eulerian method with energy ($\delta = 2.13$), right is the Lagrangian approach ($\delta = 0.96$). 98
3.5 Instantaneous particle concentration spatial distribution of a 2D slice for $Stk = 1.0$ and $Re_\varepsilon = 1500$ calculated with 3 different methods. Left is the Eulerian method without energy contributions ($\delta = 2.60$), middle is the Eulerian method with energy ($\delta = 2.45$), right is the Lagrangian approach ($\delta = 1.03$). 99
3.6 Instantaneous particle concentration spatial distribution of a 2D slice for $Stk = 2.0$ and $Re_\varepsilon = 1500$ calculated with 3 different methods. Left is the Eulerian method without energy contributions ($\delta = 2.59$), middle is the Eulerian method with energy ($\delta = 1.71$), right is the Lagrangian approach ($\delta = 0.97$). 100
3.7 Instantaneous particle concentration spatial distribution of a 2D slice for $Stk = 5.0$ and $Re_\varepsilon = 1500$ calculated with 3 different methods. Left is the Eulerian method without energy contributions ($\delta = 2.96$), middle is the Eulerian with energy ($\delta = 1.06$), right is the Lagrangian approach ($\delta = 0.89$). 101
3.8 Spectral energy of the particle number concentration against the wavenumber for $Stk = 2.0$ and $Re_\varepsilon = 1500$ estimated from the particle distribution calculated with 3 different methods, namely the Lagrangian method (solid), the Eulerian method with energy contributions (dashed), and the Eulerian method without energy contributions (dashed-dotted). The four plots each have differing grid sizes $N = 64$ (top left), 128 (top right), 256 (bottom left) and 512 (bottom right). 102

3.9 Spectral energy of the particle number concentration against the wavenumber for $Stk = 0.5$ (top left), 1.0 (top right), 2.0 (bottom left) and 5.0 (bottom right) and $Re_\varepsilon = 1500$ estimated from the particle distributions calculated with 3 different methods with grid resolution of $N = 256$, the Lagrangian method (solid blue), the Eulerian method with energy contributions (dashed orange), and the Eulerian method without energy contributions (dashed-dotted green). The black line indicates the -5/3 slope of the carrier phase velocity spectra. 103
3.10 Spectral energy of the total particle momentum (flux) against the wavenumber for $Stk = 0.5$ (top left), 1.0 (top right), 2.0 (bottom left) and 5.0 (bottom right) and $Re_\varepsilon = 1500$ estimated from the particle distributions calculated with 3 different methods with grid resolution of $N = 256$, the Lagrangian method (solid blue), the Eulerian method with energy contributions (dashed orange), and the Eulerian method without energy contributions (dashed-dotted green). The black line indicates the best power law fit. 105
3.11 Spectral energy of the conditionally averaged particle velocity against the wavenumber for $Stk = 0.5$ (top left), 1.0 (top right), 2.0 (bottom left) and 5.0 (bottom right) and $Re_\varepsilon = 1500$ estimated from the particle distributions calculated with 2 different methods with grid resolution of $N = 256$, the Eulerian method with energy contributions (dashed orange), and the Eulerian method without energy contributions (dashed-dotted green). The background carrier fluid velocity spectrum (solid blue) is also plotted for comparison. The black line indicates the -5/3 slope of the carrier phase velocity spectra. 107
3.12 Spectral energy of the total particle energy (momentum flux) against the wavenumber for $Stk = 0.5$ (top left), 1.0 (top right), 2.0 (bottom left) and 5.0 (bottom right) and $Re_\varepsilon = 1500$ estimated from the particle distributions calculated with 3 different methods with grid resolution of $N = 256$, namely the Lagrangian method (solid blue), the Eulerian method with energy contributions (dashed orange), and the Eulerian method without energy contributions (dashed-dotted green). The black line indicates the -5/3 slope of the carrier phase velocity spectra. 108

3.13 Spectral energy of the particle energy fluctuations against the wavenumber for $Stk = 0.5$ (top left), 1.0 (top right), 2.0 (bottom left) and 5.0 (bottom right) and $Re_\varepsilon = 1500$ estimated from the particle distributions calculated with 2 different methods with grid resolution of $N = 256$, namely the Lagrangian method (solid blue) and the Eulerian method with energy contributions (dashed orange). The black line indicates the -5/3 slope of the carrier phase velocity spectra. 110

4.1 Instantaneous spatial distributions of particle concentration on a 2D slice through the flow for a range of different Stk, Re_λ, and Fr_l. Particle concentrations are calculated using a box counting method (Box size = $L/N = 0.025$). 125

4.2 Spectral energy of the particle number density fluctuations against the wavenumber for a range of Stokes numbers (left < 1.0, right > 1.0). Spectra are at constant $Re_\lambda = 111$, and $Fr_l = 0$. Left panel shows Stokes numbers less than 1.0 and right panel shows Stokes numbers greater than 1.0. 126

4.3 Spectral energy of the particle number density fluctuations against the wavenumber for a range of Stokes numbers and Reynolds numbers ($Re_\lambda = 57,\ 81,\ \&\ 111$). These spectra are at constant $Fr_l = 0$. 128

4.4 Spectral energy of the particle number density fluctuations against the wavenumber for a range of different Stokes numbers and Froude numbers ($Fr_l = 0.0,\ 2.0,\ \&\ 2.0$). These spectra are at constant $Re_\lambda = 111$. 130

4.5 Spectral energy of the particle number density fluctuations against the wavenumber for a range of Reynolds numbers ($Re_\lambda = 57,\ 80,\ \&\ 111$) and Froude numbers ($Fr_l = 0.0,\ 2.0,\ \&\ 2.0$). These spectra are at two different Stokes numbers $Stk = 1.0$, and 5.0. 131

4.6 Plots of parameter C_1 of Equation 4.15 as a function of Stokes number (see Equation 4.19) . Each different colour line represents a different Reynolds number (in this case all lines coincide as C_1 is independent of Reynolds number (Equation 4.19)). Each graph corresponds to a different Froude number Fr_l. 135

4.7 Plots of the exponent α of Equation 4.15 as a function of Stokes number (see Equation 4.20). Each different colour line represents a different Reynolds number. Each graph corresponds to a different liquid Froude number. 136

4.8 Plots of parameter C_2 of Equation 4.16 as a function of Stokes number (see Equation 4.21). Each different colour line represents a different Reynolds number. Each graph corresponds to a different Froude number Fr_l. 138
4.9 Plots of exponent β of Equation 4.16 as a function of Stokes number (see Equation 4.22). Each different colour line shows a different Reynolds number. Each graph corresponds to a different Froude number Fr_l. 139
4.10 Plots of parameter γ of Equation 4.17 as a function of Stokes number (see Equation 4.23). Each different colour line represents a different Reynolds number. Each graph corresponds to a different Froude number Fr_l. 141
4.11 Spectral energy of the particle number density fluctuations against the wavenumber for a range of different Stokes, Reynolds and Froude numbers. The raw spectra are plotted as well as the spectra calculated from the empirical model of Equation 4.17. Plots (a) – (g) are spectra calculated from the current study, plots (h) – (l) are spectra from Matsuda et al. [104, 105]. 142

5.1 Normalised particle concentration C/C_0(left) and normalised Q-Criterion Q/Q_σ (middle) in a slice of turbulence with $Re_\lambda = 90.0$ and $Stk = 1.0$. Low values are in blue and high values are in yellow. Superimposed image (right), the green channel represents particle concentration, while the red channel represents the Q-Criterion. The particle concentration was calculated using a box-counting method with a box width of 2η. 155
5.2 The left-hand plot displays the histogram of the Q-Criterion sampled at fluid particle positions and at inertial particle positions. The right-hand plot re-normalizes the frequency density values by dividing by the fluid frequency density, allowing a clearer comparison of the ratio of inertial particles to fluid particles. 156
5.3 Joint probability distribution of particle concentration C/C_0 and the Q-Criterion Q/Q_σ in turbulence, with colour representing the frequency density on a logarithmic scale (low - dark blue, high - bright yellow). The figure also includes the one-dimensional probability density functions (PDFs) for the Q-Criterion and particle concentration. 157

5.4 Joint probability density function of particle concentration C/C_0 and the Q-Criterion Q/Q_σ assuming independence between the two variables, calculated as the product of their one-dimensional probability density functions (PDFs). This figure represents the theoretical distribution if there was no correlation between particle concentration and Q-Criterion. Colour represents the frequency density on a logarithmic scale (low - dark blue, high - bright yellow). The figure also includes the one-dimensional probability density functions (PDFs) for the Q-Criterion and particle concentration. 159
5.5 Ratio ζ of the observed joint probability density function (PDF) of particle concentration C/C_0 and Q-Criterion Q/Q_σ to the PDF assuming independent variables, providing a measure of the correlation between these two variables. 160
5.6 Ratio ζ of the probability density functions (PDFs) for four selected particle concentrations: $C/C_0 \approx 0.0$ (voids), $C/C_0 \approx 1.0$ (mean concentration), $C/C_0 \approx 5.0$ (clusters), and $C/C_0 \approx 15.0$ (intense clusters), plotted against the Q-Criterion Q/Q_σ. 161
5.7 Normalised particle concentration C/C_0(left) and normalised Enstrophy $\varepsilon/\varepsilon_0$ (middle) in a slice of turbulence with $Re_\lambda = 90.0$ and $Stk = 1.0$. Low values are in blue and high values are in yellow. Superimposed image of the two quantities (right), the green channel represents particle concentration, while the red channel represents Enstrophy. The particle concentration was calculated using a box-counting method with a box width of 2η. 162
5.8 Ratio ζ of the probability density functions (PDFs) for four selected particle concentrations: $C/C_0 \approx 0.0$ (voids), $C/C_0 \approx 1.0$ (mean concentration), $C/C_0 \approx 5.0$ (clusters), and $C/C_0 \approx 15.0$ (intense clusters), plotted against the Enstrophy $\varepsilon/\varepsilon_0$. 163
5.9 Normalised particle concentration C/C_0(left) and normalised Q-Criterion with a time-delay of $0.5\tau\eta$ ($Q_{0.5\tau\eta}/Q_\sigma$) (middle) in a slice of turbulence with $Re_\lambda = 90.0$ and $Stk = 1.0$. Low values are in blue and high values are in yellow. Superimposed image of the two quantities (right), the green channel represents particle concentration, while the red channel represents the Q-Criterion. The particle concentration was calculated using a box-counting method with a box width of 2η. 165

5.10 Ratio ζ of the probability density functions (PDFs) for four selected particle concentrations: $C/C_0 \approx 0.0$ (voids), $C/C_0 \approx 1.0$ (mean concentration), $C/C_0 \approx 5.0$ (clusters), and $C/C_0 \approx 15.0$ (intense clusters), plotted against the Q-Criterion with a time-delay of $0.5\tau\eta$ ($Q_{0.5\tau\eta}/Q_\sigma$). 166
5.11 Normalised particle concentration C/C_0(left) and normalised Q-Criterion with a time-delay of $1.3\tau\eta$ ($Q_{1.3\tau\eta}/Q_\sigma$) (middle) in a slice of turbulence with $Re_\lambda = 90.0$ and $Stk = 1.0$. Low values are in blue and high values are in yellow. Superimposed image of the two quantities (right), the green channel represents particle concentration, while the red channel represents the Q-Criterion. The particle concentration was calculated using a box-counting method with a box width of 2η. 167
5.12 Ratio ζ of the probability density functions (PDFs) for four selected particle concentrations: $C/C_0 \approx 0.0$ (voids), $C/C_0 \approx 1.0$ (mean concentration), $C/C_0 \approx 5.0$ (clusters), and $C/C_0 \approx 15.0$ (intense clusters), plotted against the Q-Criterion with a time-delay of $1.3\tau\eta$ ($Q_{1.3\tau\eta}/Q_\sigma$). 168
5.13 Normalised particle concentration C/C_0(left) and normalised Q-Criterion with a time-delay of $2.6\tau\eta$ ($Q_{2.6\tau\eta}/Q_\sigma$) (middle) in a slice of turbulence with $Re_\lambda = 90.0$ and $Stk = 1.0$. Low values are in blue and high values are in yellow. Superimposed image of the two quantities (right), the green channel represents particle concentration, while the red channel represents the Q-Criterion. The particle concentration was calculated using a box-counting method with a box width of 2η. 169
5.14 Ratio ζ of the probability density functions (PDFs) for four selected particle concentrations: $C/C_0 \approx 0.0$ (voids), $C/C_0 \approx 1.0$ (mean concentration), $C/C_0 \approx 5.0$ (clusters), and $C/C_0 \approx 15.0$ (intense clusters), plotted against the Q-Criterion with a time-delay of $2.6\tau\eta$ ($Q_{2.6\tau\eta}/Q_\sigma$). 170
5.15 Normalised particle concentration C/C_0(left) and FTLE field with a time window of $15.1\tau\eta$ (middle) in a slice of turbulence with $Re_\lambda = 90.0$ and $Stk = 1.0$. Low values are in blue and high values are in yellow. Superimposed image of the two quantities (right), the green channel represents particle concentration, while the red channel represents the FTLE field. The particle concentration was calculated using a box-counting method with a box width of 2η. . . 172

5.16 Ratio ζ of the probability density functions (PDFs) for four selected particle concentrations: $C/C_0 \approx 0.0$ (voids), $C/C_0 \approx 1.0$ (mean concentration), $C/C_0 \approx 5.0$ (clusters), and $C/C_0 \approx 15.0$ (intense clusters), plotted against the FTLE estimated over a time-window of $15.1\tau\eta$. 173
5.17 Normalised particle concentration C/C_0(left) and FTLE field with a time window of $7.4\tau\eta$ (middle) in a slice of turbulence with $Re_\lambda = 90.0$ and $Stk = 1.0$. Low values are in blue and high values are in yellow. Superimposed image of the two quantities (right), the green channel represents particle concentration, while the red channel represents the FTLE field. The particle concentration was calculated using a box-counting method with a box width of 2η. . . 173
5.18 Ratio ζ of the probability density functions (PDFs) for four selected particle concentrations: $C/C_0 \approx 0.0$ (voids), $C/C_0 \approx 1.0$ (mean concentration), $C/C_0 \approx 5.0$ (clusters), and $C/C_0 \approx 15.0$ (intense clusters), plotted against the FTLE estimated over a time-window of $7.4\tau\eta$. 174
5.19 Normalised particle concentration C/C_0(left) and LAVD field over a time window of $15.1\tau\eta$ (middle) in a slice of turbulence with $Re_\lambda = 90.0$ and $Stk = 1.0$. Low values are in blue and high values are in yellow. Superimposed image of the two quantities (right), the green channel represents particle concentration, while the red channel represents the LAVD field. The particle concentration was calculated using a box-counting method with a box width of 2η. . . 176
5.20 Ratio ζ of the probability density functions (PDFs) for four selected particle concentrations: $C/C_0 \approx 0.0$ (voids), $C/C_0 \approx 1.0$ (mean concentration), $C/C_0 \approx 5.0$ (clusters), and $C/C_0 \approx 15.0$ (intense clusters), plotted against the LAVD over a time-window of $15.1\tau\eta$. . 177
5.21 Normalised particle concentration C/C_0(left) and LAVD field over a time window of $7.4\tau\eta$ (middle) in a slice of turbulence with $Re_\lambda = 90.0$ and $Stk = 1.0$. Low values are in blue and high values are in yellow. Superimposed image of the two quantities (right), the green channel represents particle concentration, while the red channel represents the LAVD field. The particle concentration was calculated using a box-counting method with a box width of 2η. . . 178
5.22 Ratio ζ of the probability density functions (PDFs) for four selected particle concentrations: $C/C_0 \approx 0.0$ (voids), $C/C_0 \approx 1.0$ (mean concentration), $C/C_0 \approx 5.0$ (clusters), and $C/C_0 \approx 15.0$ (intense clusters), plotted against the LAVD over a time-window of $7.4\tau\eta$. . 179

List of Tables

4.1 Simulation parameters used for both the Eulerian carrier fluid and the Lagrangian particle simulations. 122

5.1 Simulation parameters used for both the Eulerian carrier fluid and the Lagrangian particle simulations. 151

Chapter 1

Introduction

This chapter presents a review of the key concepts necessary for understanding the interaction between particles and turbulence, with a focus on particle clustering and preferential concentration. The discussion begins with the physics of turbulence, leading to an examination of homogeneous isotropic turbulence (HIT), which is used in this study as a reference case to investigate the mechanisms of particle clustering in turbulent flows. Following this, the relevant aspects of particle dynamics and turbulence-particle interaction are addressed. The computational approaches are then divided into two parts: the numerical simulation of turbulent flows and the numerical simulation of particle-laden flows. This framework provides the foundation for exploring the physical mechanisms that underlie aerosol dispersion and preferential concentration in turbulent environments. Finally, this chapter concludes with a summary of the current research, drawn from the literature review, and an outline of the thesis structure, providing a framework for understanding the scope and direction of the work.

1.1 The Problem Considered

The distribution of aerosols and inertial particles in turbulent flows significantly affects a wide range of natural and industrial processes. These particles do not distribute evenly in a flow but instead exhibit complex, non-uniform patterns of concentration. This variability can influence processes as diverse as cloud formation, combustion efficiency, pollutant transport, and even disease transmission. Understanding these non-uniform distributions is critical for predicting how aerosols behave in turbulent environments, as well as for designing systems to either exploit or mitigate their effects.

In atmospheric processes, for instance, the non-uniform distribution of droplets is essential for cloud dynamics and the initiation of rain. Within a cloud, turbu-

lence drives the motion of droplets, and under certain conditions, droplets cluster together, increasing the likelihood of collisions and coalescence. These interactions are nonlinear, meaning that even small changes in particle concentration can lead to significant shifts in the process, such as the rapid formation of rain in regions of high droplet concentration. The same non-uniform distributions play a role in pollutant transport in the atmosphere, where aerosols such as dust, soot, or chemical pollutants can become concentrated in certain areas, posing health and environmental risks. These clusters of particles can also be transported over long distances by turbulent air currents, influencing air quality far from the source of emission.

In industrial contexts, non-uniform particle distributions are equally significant. Processes such as spray coating, combustion, and chemical reactions often rely on the precise distribution of particles within a flow. Non-uniform distributions can lead to inefficiencies or defects. For example, in combustion systems, particle clustering can result in uneven burning, leading to hot spots that reduce overall efficiency or even cause structural damage to equipment. Similarly, in manufacturing processes involving powders or aerosols, the formation of particle clusters can lead to uneven coatings or incomplete reactions, which degrade the quality of the final product. Thus, understanding and controlling these distributions are crucial for optimizing industrial operations.

Another area of growing importance is the transmission of airborne diseases. Recent global health crises, such as the COVID-19 pandemic, have underscored the importance of understanding how aerosols, which may carry pathogens, are distributed in indoor environments. The non-uniform concentration of aerosols can lead to localized zones where the risk of transmission is significantly higher. Airflow patterns, ventilation systems, and room layout all influence how these aerosols disperse, and computational models are critical for predicting areas of higher risk. In this context, the study of aerosol behaviour is not merely academic but has direct implications for public health policies and the design of safer indoor environments.

These varied processes share a common feature: they are strongly influenced by the non-uniform distribution of particles within turbulent flows. The challenge, therefore, lies in understanding how and why these distributions form, and how they influence the systems they occur in. This is where the concept of preferential concentration becomes essential.

Preferential concentration refers to the tendency of inertial particles to cluster in specific regions of a turbulent flow while avoiding others. This behaviour arises from the fact that particles, due to their inertia, cannot follow the fluid motion perfectly. Instead, they deviate from the fluid streamlines, accumulating in low-

vorticity regions while being expelled from high-vorticity regions. The extent of this clustering is influenced by various factors, including the particle size, the flow's turbulence intensity, and the gravitational forces acting on the particles. When particles are of an optimal size—typically when the Stokes number is around unity—they interact most effectively with the turbulent eddies, resulting in the strongest clustering.

The focus of this study is to understand the mechanisms behind preferential concentration, with an emphasis on the computational modelling of these phenomena. While both experimental and computational methods have been used to study aerosol dispersion and particle clustering, computational approaches offer several unique advantages, particularly when it comes to extracting detailed physical insights.

Experimental studies, while essential for validating models and understanding real-world phenomena, face significant limitations when it comes to studying aerosol and particle behaviour in turbulent flows. The primary challenge in experiments is the difficulty of measuring particle positions and velocities with high spatial and temporal resolution in a turbulent environment. Turbulence, by its nature, involves a wide range of length and time scales, making it challenging to capture the full spectrum of particle behaviour. While modern experimental techniques such as particle image velocimetry (PIV) and laser diagnostics have improved our ability to track particles, these methods are often limited by the resolution of the instruments and the complexity of the flow.

In contrast, computational methods, particularly direct numerical simulation (DNS), allow researchers to resolve all relevant scales of the turbulent flow and extract detailed information about the particles' behaviour. DNS provides an unprecedented level of detail, offering insights into the exact interactions between particles and turbulent structures that would be impossible to observe experimentally. By simulating the fluid flow at high resolution, computational models can track individual particles, revealing how they respond to different flow features, such as vortices, shear layers, and stagnation points. Moreover, computational methods enable the study of a wide range of parameter spaces, including variations in particle size, flow intensity, and external forces such as gravity. This flexibility allows for a systematic exploration of the factors influencing preferential concentration, which would be prohibitively expensive and time-consuming to replicate experimentally.

However, computational methods also have their drawbacks. One of the main limitations is the computational cost associated with DNS. Resolving all relevant turbulent scales requires extremely fine grids and small time steps, leading to high computational demands, especially for flows with high Reynolds numbers. Addi-

tionally, while DNS is valuable for fundamental studies, its direct application to large-scale industrial or atmospheric flows is limited by the sheer scale of these systems. For practical applications, researchers often turn to large-eddy simulation (LES) or Reynolds-averaged Navier-Stokes (RANS) approaches, which model the largest turbulent scales while approximating the smaller ones. While these approaches reduce computational costs, they also introduce modelling uncertainties that must be carefully considered when interpreting the results.

Despite these limitations, computational models remain a powerful tool for studying aerosol dispersion and preferential concentration, especially when experimental methods fall short. In many cases, computational models can isolate specific physical mechanisms and test hypotheses that would be difficult or impossible to explore in an experimental setting. For example, the ability to control all parameters of the system—such as particle size, turbulence intensity, and boundary conditions—allows for a detailed investigation of how each factor influences particle clustering and void formation.

This study focuses on the computational analysis of preferential concentration, leveraging the strengths of DNS to explore the detailed physics behind aerosol and particle behaviour in turbulent flows. The goal is to provide a deeper understanding of how factors such as the Stokes number, Reynolds number, and gravitational forces interact to shape the distribution of particles in turbulence. The findings of this research will not only contribute to the fundamental understanding of preferential concentration but also provide practical insights for improving models of aerosol behaviour in natural and industrial systems.

This thesis aims to build a comprehensive computational framework to model and analyse aerosol dispersion and preferential concentration in turbulent flows. The emphasis is on understanding the detailed interactions between particles and the turbulent structures that lead to the formation of clusters and voids. By using DNS and related computational techniques, this study explores how different dimensionless parameters, such as the Stokes number, Reynolds number, and Froude number, influence particle distributions.

The research will also investigate the implications of preferential concentration for practical applications. In the context of aerosol transmission of diseases, understanding how particles concentrate in specific regions of a room can inform the design of ventilation systems that minimize the risk of airborne transmission. Similarly, in industrial processes involving aerosol dispersion, the ability to predict and control particle clustering can improve the efficiency and consistency of operations such as spray coating, combustion, and chemical reactions.

Moreover, this study will explore the scalability of computational models to more complex flow geometries and higher Reynolds numbers, addressing some of

the current limitations in applying DNS to large-scale systems. By doing so, this research aims to bridge the gap between detailed fundamental studies and practical applications, providing a framework for both understanding and controlling aerosol behaviour in turbulent environments.

In conclusion, this thesis addresses the critical need to understand the mechanisms governing aerosol dispersion and preferential concentration in turbulent flows. By focusing on computational methods, the study seeks to provide detailed physical insights that are difficult to obtain experimentally. The findings will have wide-ranging applications, from improving public health and safety to optimizing industrial processes involving particle-laden flows. Through the systematic exploration of particle-turbulence interactions, this research will contribute to both the theoretical and practical understanding of aerosol dynamics in complex flow environments.

1.2 Turbulence

1.2.1 Fundamentals of Turbulence

Unlike laminar flow, which is smooth and orderly, turbulence represents a complex and chaotic fluid flow phenomenon characterized by irregular motion and enhanced mixing. This contrast between laminar and turbulent flows is fundamental to fluid dynamics, with turbulence exhibiting a rich and intricate behaviour that deviates from the predictability of laminar flow patterns.

Turbulent flows are ubiquitous in everyday situations. Their irregularity is strikingly evident in natural phenomena such as the swirling patterns observed in smoke or the eddies formed in river currents [130]. These visible instances of turbulence highlight its presence and influence in our natural environment.

In the realm of engineering, turbulent flows are pervasive. They occur in various liquid or gas processing systems, such as pumps, compressors, and pipelines, and around vehicles, including airplanes, cars, ships, and submarines. These turbulent flows play critical roles in the efficiency and functionality of these systems and vehicles.

One of the hallmarks of turbulent flows is the presence of vortices, or swirling motions, also known as eddies, which vary in size and significantly influence the overall flow dynamics [155]. For example, the exhaust plume from a solid rocket motor exhibits turbulent motions at various scales, from large eddies to the smallest detectable by a camera. These vortices, or eddies, contribute to the complexity and dynamic nature of turbulence.

Turbulence significantly enhances the transport and mixing of fluids, far sur-

passing the efficiency of laminar flow. In practical applications, turbulence enhances the mixing and diffusion of momentum, heat, and mass, which is particularly beneficial in combustion engines and chemical reactors [159]. This property of turbulence facilitates the efficient dispersal of pollutants in the atmosphere or water bodies and ensures effective reactant mixing in combustion devices and chemical reactors [21]. However, turbulence increases wall shear stress and drag on aircraft wings and ship hulls, potentially impacting their performance and efficiency.

The transition from laminar to turbulent flow is influenced by the Reynolds number, a dimensionless quantity that compares inertial forces to viscous forces within the fluid. The Reynolds number (Re) is defined as:

$$\mathrm{Re} = \frac{\rho u_{char} L_{char}}{\mu}, \tag{1.1}$$

where ρ is the fluid density, u_{char} is the fluid velocity, L_{char} is a characteristic length, and μ is the fluid's dynamic viscosity. Understanding and calculating the Reynolds number is essential for predicting and managing the onset of turbulence in various systems.

Turbulence is inherently three-dimensional, with interactions between vortices occurring in all spatial directions [37]. This three-dimensionality adds to the complexity of turbulent flows. Furthermore, turbulence is not uniformly distributed in space and time; it exhibits intermittency. This means regions of high turbulence intensity are interspersed with relatively calm regions, a phenomenon observed in various turbulent flows, including atmospheric turbulence and boundary layer flows [54]. This intermittency underscores the unpredictable and fluctuating nature of turbulent flows.

The behaviour of both laminar and turbulent flows can be mathematically described by the Navier-Stokes equations. These fundamental equations of fluid mechanics are derived from Newton's second law and describe how the velocity field of a fluid evolves over time. The Navier-Stokes equations for an incompressible fluid (in vector form) are given by:

$$\rho\left(\frac{\partial \boldsymbol{u}}{\partial t} + \boldsymbol{u}\cdot\nabla\boldsymbol{u}\right) = -\nabla p + \mu\nabla^2\boldsymbol{u} + \boldsymbol{f}, \tag{1.2}$$

$$\nabla\cdot\boldsymbol{u} = 0, \tag{1.3}$$

here, $\boldsymbol{u}$ is the fluid velocity vector, ρ is the fluid density, p is the pressure, μ is the dynamic viscosity, and $\boldsymbol{f}$ represents any external forces acting on the fluid. The first equation represents the conservation of momentum, while the second

equation ensures the conservation of mass for an incompressible fluid.

Solving the Navier-Stokes equations for turbulent flows is particularly challenging due to the non-linear term $\boldsymbol{u}\cdot\nabla\boldsymbol{u}$, which represents the convective acceleration. This term introduces complexities that lead to the chaotic and unpredictable nature of turbulence. The difficulty in finding analytical solutions to these equations necessitates the use of numerical methods and simulations [113].

In the analysis of turbulent flows, the strain rate tensor and the rotation rate tensor characterize different aspects of fluid motion. The strain rate tensor S_{ij} describes the rate of deformation of fluid elements and is defined as:

$$S_{ij} = \frac{1}{2}\left(\frac{\partial u_i}{\partial x_j} + \frac{\partial u_j}{\partial x_i}\right), \tag{1.4}$$

this tensor provides a measure of how fluid particles are stretched, compressed, or sheared as they move, contributing to the overall deformation of the flow.

Complementing the strain rate tensor is the rotation rate tensor Ω_{ij}, which describes the rotational motion of fluid elements. It is given by:

$$\Omega_{ij} = \frac{1}{2}\left(\frac{\partial u_i}{\partial x_j} - \frac{\partial u_j}{\partial x_i}\right), \tag{1.5}$$

this tensor captures the local rotational effects within the flow, indicating the presence of vortices or rotational motion.

To distinguish between vortex-dominated and shear-dominated regions, the Q-criterion is commonly used. The Q-criterion is defined as:

$$Q = \frac{1}{2}\left(|\Omega_{ij}|^2 - |S_{ij}|^2\right), \tag{1.6}$$

where $|\Omega_{ij}|^2 = \Omega_{ij}\Omega_{ij}$ and $|S_{ij}|^2 = S_{ij}S_{ij}$. The criterion identifies vortices as regions where rotational effects dominate over strain-induced deformation, i.e., where $Q > 0$. This provides a useful tool for visualizing vortex structures in turbulent flows.

Closely related to the rotation rate tensor is the concept of vorticity, $\boldsymbol{\omega}$, which is a vector quantity representing the local rotation of fluid elements. Vorticity is defined as the curl of the velocity field:

$$\boldsymbol{\omega} = \nabla \times \boldsymbol{u}, \tag{1.7}$$

The vorticity vector provides insights into the intensity and orientation of rotational motion within the fluid. High vorticity regions typically correspond to intense swirling motions or vortices, which are a characteristic feature of turbulent flows.

1.2.2 Energy Cascade of Turbulence

The concept of the energy cascade is fundamental to understanding turbulence. In turbulent flows, energy is injected at large scales and transferred to progressively smaller scales through a process known as the energy cascade. This transfer of energy continues until it reaches the smallest scales, where it is dissipated as heat due to viscous forces. This cascading process is crucial for maintaining the dynamic nature of turbulence and plays a significant role in the overall energy balance within the fluid.

Kolmogorov's 1941 theory provides a theoretical framework for describing the behaviour of turbulent flows. According to Kolmogorov's first similarity hypothesis, at sufficiently high Reynolds numbers, the statistics of the large scales of turbulence are universal and independent of the fluid's viscosity. These large scales are influenced primarily by the energy input and the large-scale flow structure [54].

Kolmogorov's second similarity hypothesis pertains to the small scales of turbulence, where the effects of viscosity become significant. At these small scales, also known as the Kolmogorov scales, the turbulent motions are isotropic and homogeneous, meaning they are statistically similar in all directions. Kolmogorov introduced the concept of Kolmogorov length, time, and velocity scales to describe these smallest scales of turbulence. The Kolmogorov length scale (η) is given by:

$$\eta = \left(\frac{\nu^3}{\epsilon}\right)^{1/4}, \tag{1.8}$$

where ν is the kinematic viscosity and ϵ is the rate of dissipation of turbulent kinetic energy per unit mass. The Kolmogorov timescale (τ_η) and velocity scale (u_η) are similarly defined as:

$$\tau_\eta = \left(\frac{\nu}{\epsilon}\right)^{1/2}, \tag{1.9}$$

$$u_\eta = (\nu\epsilon)^{1/4}, \tag{1.10}$$

these scales provide a quantitative measure of the smallest eddies in turbulent flow and are critical for understanding the dissipation process [37].

Within the energy spectrum of turbulence, the inertial subrange is the range of scales where energy transfer occurs without significant loss due to viscosity. In this subrange, the energy spectrum follows a universal behaviour described by the famous $-5/3$ power law, indicating that the energy density ($E(k)$) at wavenumber k scales as:

$$E(k) \propto k^{-5/3}, \tag{1.11}$$

this scaling law reflects the self-similar nature of turbulence in the inertial subrange, where energy cascades from larger to smaller scales in a predictable manner [159].

As the energy cascade continues, it eventually reaches the dissipation range, where viscous forces dominate and convert the kinetic energy into heat. The transition from the inertial subrange to the dissipation range marks the point where the smallest eddies are efficiently dissipated, completing the energy cascade process [21].

The energy cascade and Kolmogorov scales is essential for various practical applications and for developing different modelling techniques in fluid dynamics. The concept of the energy cascade underpins many turbulence models, such as Large Eddy Simulation (LES). LES resolves the larger turbulent structures while modelling the smaller scales, making use of the energy cascade's predictable nature in the inertial subrange.

1.2.3 Statistical Description of Turbulence

Describing turbulence statistically is essential for understanding its complex, chaotic nature. Several statistical methods and tools are employed to analyse and predict turbulent flows. These methods provide insights into the behaviour of turbulence and enable the development of effective models for various applications.

One of the foundational approaches in the statistical description of turbulence is Reynolds decomposition. This technique separates flow variables into mean and fluctuating components. By expressing a flow variable $\phi(\boldsymbol{x}, t)$ at position $\boldsymbol{x}$ and time t as the sum of its mean $\langle\langle\phi\rangle\rangle(\boldsymbol{x}, t)$ and its fluctuating part $\phi'(\boldsymbol{x}, t)$, the analysis of turbulent flows becomes more manageable:

$$\phi(\boldsymbol{x}, t) = \langle\langle\phi\rangle\rangle(\boldsymbol{x}, t) + \phi'(\boldsymbol{x}, t), \tag{1.12}$$

The mean component represents the steady (or slower) part of the flow, while the fluctuating component captures the deviations caused by turbulence.

Building on this decomposition, the Reynolds-averaged Navier-Stokes (RANS) equations are derived, which govern the mean flow behaviour in turbulent conditions. These equations introduce additional terms known as Reynolds stresses, which represent the effects of turbulence on the mean flow. The RANS equations for an incompressible fluid are given by:

$$\rho\left(\frac{\partial\left\langle\left\langle u_i\right\rangle\right\rangle}{\partial t}+\left\langle\left\langle u_j\right\rangle\right\rangle\frac{\partial\left\langle\left\langle u_i\right\rangle\right\rangle}{\partial x_j}\right)=-\frac{\partial\left\langle\left\langle p\right\rangle\right\rangle}{\partial x_i}+\mu\frac{\partial^2\left\langle\left\langle u_i\right\rangle\right\rangle}{\partial x_j^2}-\frac{\partial\left\langle\left\langle u_i'u_j'\right\rangle\right\rangle}{\partial x_j},\tag{1.13}$$

where $\langle\langle u_i\rangle\rangle$ is the mean velocity, $\langle\langle p\rangle\rangle$ is the mean pressure, and $\langle\langle u_i'u_j'\rangle\rangle$ are the Reynolds stresses. These stresses are modelled to close the RANS equations and enable practical computations of turbulent flows [43].

The autocorrelation function measures the correlation between velocity fluctuations at different points in space and time. It is defined as:

$$R_{\boldsymbol{uu}}(\boldsymbol{r})=\frac{\langle\langle\boldsymbol{u}'(\boldsymbol{x})\boldsymbol{u}'(\boldsymbol{x}+\boldsymbol{r})\rangle\rangle}{\langle\langle\boldsymbol{u}'^2\rangle\rangle},\tag{1.14}$$

where $\boldsymbol{r}$ is the spatial separation, and $\langle\langle\cdot\rangle\rangle$ denotes an average over space and time. This function provides insights into the spatial and temporal coherence of turbulence. From the autocorrelation function, integral length scales L can be calculated, which represent the size of the energy-containing eddies in the flow:

$$L=\int_0^\infty R_{uu}(r)\,dr,\tag{1.15}$$

In addition to spatial scales, the integral time scale T is used to characterize the temporal structure of turbulence and is defined as:

$$T=\int_0^\infty R_{uu}(\tau)\,d\tau,\tag{1.16}$$

where τ is the time lag. These scales are important for describing the spatial and temporal structure of turbulence and for developing turbulence models [116].

Turbulent kinetic energy (TKE) describes the energy contained in the turbulent motion of the fluid. The TKE budget equation outlines the balance between production, dissipation, and transport of turbulent kinetic energy. Production terms represent the generation of TKE from the mean flow, dissipation terms account for the conversion of TKE into heat due to viscosity, and transport terms describe the redistribution of TKE within the flow. The TKE budget equation is expressed as:

$$\frac{\partial k}{\partial t}+\left\langle\left\langle u_j\right\rangle\right\rangle\frac{\partial k}{\partial x_j}=-\left\langle\left\langle u_i'u_j'\right\rangle\right\rangle\frac{\partial\left\langle\left\langle u_i\right\rangle\right\rangle}{\partial x_j}-\epsilon+\frac{\partial}{\partial x_j}\left(\nu\frac{\partial k}{\partial x_j}-\frac{\left\langle\left\langle u_i'p'\right\rangle\right\rangle}{\rho}-\frac{1}{2}\left\langle\left\langle u_i'u_j'u_j'\right\rangle\right\rangle\right),\tag{1.17}$$

where k is the turbulent kinetic energy, and ϵ is the rate of dissipation of TKE. This equation helps in predicting and modelling turbulent flows in various applications [37].

1.2.4 Homogeneous Isotropic Turbulence

A velocity field is statistically stationary if its moments are invariant under a shift in time, statistically homogeneous if its moments are invariant under a shift in space, and statistically isotropic if its moments are invariant under a rotation or reflection of the coordinate system [130].

Homogeneous Isotropic Turbulence (HIT) is a theoretical construct in fluid dynamics that greatly simplifies the study of turbulence. HIT is defined as a turbulent flow in which statistical properties are uniform in space and time (homogeneous) and exhibit no preferred direction (isotropic). This idealized form of turbulence eliminates the complexities associated with boundaries and directional biases, providing a clearer framework for analysing turbulent behaviours.

The properties of HIT make it a fundamental model in turbulence research. Because HIT assumes uniform statistical properties throughout the flow, it implies that the turbulence is the same at every point in the fluid. Isotropy means that the statistical properties are identical in all directions, which further simplifies the mathematical treatment of turbulence and analysis of turbulent properties. These properties allow researchers to focus on the intrinsic nature of turbulence without the complications introduced by varying conditions or directional influences [130].

A notable characteristic of HIT is that it will decay over time without an external energy source. In the absence of forcing, the turbulent kinetic energy (TKE) gradually diminishes as energy is transferred to smaller scales and dissipated as heat. According to Pope (2000), the rate of decay of TKE in HIT is described by the equation:

$$\frac{dK}{dt} = -\varepsilon, \tag{1.18}$$

where K is the total turbulent kinetic energy, and ε is the total rate of dissipation of TKE (this is opposed to k and ϵ which are local fluid properties). This equation highlights the direct relationship between the decay of TKE and the energy dissipation rate.

In wind tunnel experiments, homogeneous isotropic turbulence is approximated by observing the decaying turbulence downstream of a grid [72]. Hwang and Eaton [79] used jet actuators to produce near-isotropic turbulence without a mean flow inside a turbulence chamber. Homogeneous isotropic turbulence has also been achieved experimentally via the 'box of turbulence' method without a meanflow [96].

The Taylor microscale is another important concept in HIT. It provides an intermediate scale between the large energy-containing eddies and the small dissipative eddies, characterizing the scale at which viscous effects become significant.

The Taylor microscale λ is defined as:

$$\lambda = \left(\frac{15\nu u'^2}{\varepsilon} \right)^{1/2}, \tag{1.19}$$

where ν is the kinematic viscosity, u' is the root mean square of the velocity fluctuations, and ϵ is the rate of dissipation of turbulent kinetic energy. The Taylor microscale helps in bridging the gap between the inertial subrange and the dissipation range, providing insights into the transition from large to small scales in turbulence [159].

The Taylor Reynolds number Re_λ is defined using the Taylor microscale and provides a measure of the turbulence intensity at the intermediate scales. It is given by:

$$Re_\lambda = \frac{u'\lambda}{\nu}, \tag{1.20}$$

The Taylor Reynolds number is a dimensionless quantity that indicates the relative significance of inertial forces to viscous forces at the Taylor microscale and is used to characterize the turbulence level in HIT [130].

Mathematically, HIT is often described using statistical and spectral methods. The use of these methods allows for a detailed characterization of turbulence through quantities like the autocorrelation function, structure functions, and the energy spectrum. These tools help in quantifying the distribution of energy among different scales and understanding the transfer mechanisms at play within the turbulent flow [37].

The relevance of HIT in research and applications lies in its role as a simplified model that captures the essential features of turbulence. Studying HIT helps in developing and validating theories that can be applied to more complex, real-world turbulent flows. For instance, assumptions of HIT are useful in atmospheric sciences, oceanography, and engineering applications where the detailed structure of turbulence needs to be understood without the complications of boundaries or directional influences. Numerical simulations, such as Direct Numerical Simulation (DNS) and Large Eddy Simulation (LES), often use HIT to benchmark their results and improve turbulence models [113].

1.3 Particle Dynamics

1.3.1 Equation of Motion

If a particle is smaller than the smallest fluid scale, it can be considered a point particle [101]. The core of the point-particle approach in understanding the dynamics

of small particles in turbulent flows is encapsulated by the Maxey–Riley–Gatignol (MRG) equation of motion. This equation describes the forces acting on a small particle undergoing arbitrary motion in an unsteady nonhomogeneous flow [108]. A rigorous derivation of this equation necessitates a vanishing particle Reynolds number (Re_p), allowing for the linear superposition of different forces, and assumes extremely dilute particle concentrations to ignore interparticle effects. The particle Reynolds number is defined as

$$Re_p = \frac{\rho_f d_p |\boldsymbol{u} - \boldsymbol{v}_p|}{\mu}, \tag{1.21}$$

where ρ_f is the fluid density, d_p is the particle diameter, $\boldsymbol{u}$ is the fluid velocity, $\boldsymbol{v}_p$ is the particle velocity, and μ is the dynamic viscosity of the fluid. Despite these assumptions, the MRG equation is frequently used outside these ideal conditions, requiring careful assessment of the framework's limitations.

The MRG equation of motion is given by:

$$\begin{aligned} m_p \frac{d\boldsymbol{v}_p}{dt} = (m_p - m_f)\,\boldsymbol{g} + \\ m_f \left.\frac{D\boldsymbol{u}}{Dt}\right|_{\boldsymbol{y}(t)} - \\ \frac{1}{2} m_f \frac{d}{dt}\left\{ \boldsymbol{v}_p - \boldsymbol{u}[\boldsymbol{y}(t), t] - \frac{1}{10} a^2 \left.\nabla^2 \boldsymbol{u}\right|_{\boldsymbol{y}(t)} \right\} - \\ 6\pi a \mu \left\{ \boldsymbol{v}_p - \boldsymbol{u}[\boldsymbol{y}(t), t] - \frac{1}{6} a^2 \left.\nabla^2 \boldsymbol{u}\right|_{\boldsymbol{y}(t)} \right\} - \\ 6\pi a \mu \int_0^t d\tau \left(\frac{\frac{d}{dt}\left\{ \boldsymbol{v}_p - \boldsymbol{u}[\boldsymbol{y}(t), t] - \frac{1}{6} a^2 \left.\nabla^2 \boldsymbol{u}\right|_{\boldsymbol{y}(t)} \right\}}{[\pi \nu (t-\tau)]^{\frac{1}{2}}} \right), \end{aligned} \tag{1.22}$$

where m_p is the mass of the particle, $\boldsymbol{v}_p$ is the velocity of the particle, t is time, m_f is the mass of the fluid displaced by the particle, $\boldsymbol{g}$ is the gravitational acceleration vector, $\frac{D\boldsymbol{u}}{Dt}$ is the material derivative of the fluid velocity field, $\boldsymbol{u}[\boldsymbol{y}(t), t]$ is the fluid velocity at the particle position $\boldsymbol{y}(t)$, $a = d_p/2$ is the radius of the particle, μ is the dynamic viscosity of the fluid, $\nabla^2 \boldsymbol{u}$ is the Laplacian of the fluid velocity field, and ν is the kinematic viscosity of the fluid.

This equation accounts for various forces acting on the particle, including the buoyancy force, fluid acceleration, added mass force, Stokes drag, and history force. The buoyancy force $(m_p - m_f)g_i$ is the net gravitational force considering buoyancy. The fluid acceleration term $m_f \left.\frac{D\boldsymbol{u}}{Dt}\right|_{\boldsymbol{y}(t)}$ represents the force due to the

fluid's acceleration. The added mass force

$$-\frac{1}{2}m_f\frac{d}{dt}\left\{\boldsymbol{v}_p-\boldsymbol{u}_i[\boldsymbol{y}(t),t]-\frac{1}{10}a^2\,\nabla^2\boldsymbol{u}\big|_{\boldsymbol{y}(t)}\right\},$$

accounts for the inertia of the fluid surrounding the particle. Stokes drag

$$-6\pi a\mu\left\{\boldsymbol{v}_p-\boldsymbol{u}[\boldsymbol{y}(t),t]-\frac{1}{6}a^2\,\nabla^2\boldsymbol{u}\big|_{\boldsymbol{y}(t)}\right\},$$

describes the viscous resistance of the fluid. The history force

$$-6\pi a\mu\int_0^t d\tau\left(\frac{\frac{d}{dt}\left\{\boldsymbol{v}_p-\boldsymbol{u}[\boldsymbol{y}(t),t]-\frac{1}{6}a^2\,\nabla^2\boldsymbol{u}\big|_{\mathbf{y}(t)}\right\}}{[\pi\nu(t-\tau)]^{\frac{1}{2}}}\right),$$

accounts for the past velocities' effect on the current motion due to fluid memory effects. All the terms proportional to Laplacian of velocity ($\nabla^2\boldsymbol{u}$) are the Faxén correction terms which account for the non-uniformity in the flow across the particle's length.

For small heavy particles, gravity and drag are the dominant forces [97]. The drag force is often modelled by correcting the Stokes formula to account for finite Re_p. Schiller [149] proposed a correction that has been widely adopted, particularly for finite Reynolds numbers. Although these corrections were derived under homogeneous and steady conditions, they have shown good performance in simple cellular configurations [19] and low-Re turbulence where $Re_p = O(1)$ [109]. However, in high-Re turbulence, the probability of extreme events tends to be underestimated Saw et al. [147].

Unsteady forces within the MRG equation, such as added mass, fluid acceleration, and the history force, become significant even when the particle-to-fluid density ratio (ρ_p/ρ_f) is much greater than one, particularly when the particle diameter (d_p) is comparable to the Kolmogorov scale (η) [97]. The relevance of the history term, which accounts for past fluid acceleration effects on particle motion, has been highlighted in studies of particle kinematics [36] and clustering Olivieri et al. [120]. Recent efficient computational approaches have improved the calculation of the history term Prasath et al. [132].

In cases of extremely small Reynolds numbers ($Re_p \ll 1$) and high particle-to-fluid density ratio ($\rho_p/\rho_f \gg 10$), the equation of motion for a small spherical particle simplifies significantly. Stokes' law provides a model for the drag force under these conditions, expressed as $\boldsymbol{F}_d = 3\pi\mu d_p(\boldsymbol{u}-\boldsymbol{v}_p)$. The gravity force, based on Archimedes' principle, is expressed as $\boldsymbol{F}_b = \frac{\pi d_p^3}{6}\rho_p\boldsymbol{g}$, reflecting the density difference between the particle and the fluid. Thus, under these assumptions, the

equation of motion for a small, spherical particle can be simplified to a balance between the drag force and the net gravitational force:

$$m_p \frac{d\boldsymbol{v}_p}{dt} = 3\pi\mu d_p(\boldsymbol{u}[\boldsymbol{y}(t), t] - \boldsymbol{v}_p) + \frac{\pi d_p^3}{6}\rho_p \boldsymbol{g}, \tag{1.23}$$

this can be rewritten more compactly by using the particle relaxation time τ_f:

$$\tau_p = \frac{\rho_p d_p^2}{18\mu}, \tag{1.24}$$

$$\frac{d\boldsymbol{v}_p}{dt} = \frac{1}{\tau_f}(\boldsymbol{u}[\boldsymbol{y}(t), t] - \boldsymbol{v}_p) + \boldsymbol{g}. \tag{1.25}$$

Additionally, particles in a fluid experience diffusion due to random thermal motion, known as Brownian motion. This molecular diffusion can be described by the Einstein relation for the diffusion coefficient D:

$$D = \frac{k_B T}{6\pi\mu d_p}, \tag{1.26}$$

where k_B is the Boltzmann constant, T is the absolute temperature, μ is the dynamic viscosity of the fluid, and d is the particle diameter. This equation provides a measure of the rate at which particles diffuse through a fluid due to thermal energy, offering insights into the microscopic dynamics of particle motion within fluids.

1.3.2 Preferential Concentration

Inertial particle or droplet distributions in turbulent flows often exhibit clustering in regions of high concentration and voids in regions of low concentration. This behaviour, known as preferential concentration, occurs due to particle inertia, which causes the dispersed phase to deviate from the fluid flow streamlines. This process is influenced by variables such as particle size and the properties of the fluid [154]. Understanding preferential concentration is crucial for a variety of natural and industrial processes. In atmospheric physics, it plays a role in cloud formation and rain initiation, while in chemical engineering, it impacts processes such as powder manufacturing. These processes often depend nonlinearly on particle concentration. For example, the general aerosol dynamic equation, which describes the evolution of droplet size distribution [55], underscores the significance of non-uniform particle concentration profiles. Moreover, preferential concentration affects various phenomena including droplet coalescence in clouds [163, 150, 95], droplet evaporation or condensation [137, 145], and gas-particle

phase reactions [70].

The mechanisms driving the clustering of inertial particles in fluid flows are complex and influenced by various factors, including the Stokes and Reynolds numbers. One common effect observed in flows with a mean velocity component is centrifuging. In the context of turbulence, Coleman and Vassilicos [32] proposed the 'sweep-stick' mechanism. This mechanism suggests that particles are swept along with and get stuck to the acceleration stagnation points of the fluid. However, an alternative perspective is offered by Bragg et al. [23], whose analysis also applies to arbitrary spatially correlated velocity fields. Crucially, their findings challenge the scale invariance of the radial distribution function, offering a different view on the underlying processes of particle clustering.

To understand the underlying physics and predict the preferential concentration of particles, researchers have developed several methods to correlate fluid properties with particle concentration. Among these properties, the Q-criterion has been widely used to identify vortex-dominated regions within a turbulent flow [6, 32]. The Q-criterion is based on the second invariant of the velocity gradient tensor and is used to distinguish between rotation-dominated (vortical) and strain-dominated regions [78]. Regions where the Q-criterion is positive are typically associated with vortical structures, where centrifugal forces can lead to particle clustering around the periphery of vortices.

Another important method is the Enstrophy, which quantifies the intensity of vorticity within the flow without considering the strain. Enstrophy is particularly useful for identifying regions with high rotational energy, which can influence the distribution of particles by expelling them from the vortex cores and concentrating them in regions of lower vorticity [52]. Oujia et al. [123] used neural networks to try to synthesise inertial particle concentrations from Enstrophy to varying degrees of success. These Eulerian-based approaches provide valuable insights into the correlation between fluid structures and particle concentration and can effectively frame coherent features of the instantaneous velocity field but lack objectivity Haller [66]. They are often limited by their reliance on instantaneous snapshots of the flow, which may not fully capture the temporal dynamics of particle clustering.

The mechanisms driving the clustering of inertial particles in fluid flows are complex and influenced by various factors, including the non-dimensional Stokes (Stk), Froude (Fr) and turbulent Reynolds numbers (Re_λ). The Stokes number (Stk) measures the ratio of particle inertia to fluid drag forces, indicating how quickly particles respond to changes in fluid velocity:

$$Stk = \frac{\tau_p}{\tau_f}, \tag{1.27}$$

where τ_p is the particle relaxation time (Equation 1.24), and τ_f is a representative timescale of the fluid, most often chosen as the Kolmogorov timescale τ_η. Many fluid timescales could be used, but the Kolmogorov timescale is often preferred due to its favourable analytical properties for small Stokes numbers ($Stk < 0.2$), where the Equilibrium Eulerian approach can be applied to theoretically derive particle velocities [8]. However it is noted that the Kolmogorov timescale may not be the appropriate timescale for representation of all relevant clustering processes and this remains an area of active research. The Froude number (Fr) is a ratio between is defined as a ratio of gravitational forces to inertial forces. In this thesis we define two Froude numbers, which are the reciprocals of the conventional definitions, as traditional Froude numbers become undefined when gravitational acceleration is zero, which was undesired for Chapter 4. The first Fr_f is the ratio of gravitational forces to fluid inertia, the second Fr_p is the ratio of gravitational forces to particle inertia, these are given in Equations 1.28 and 1.29 respectively:

$$Fr_l = \frac{g\tau_\eta}{u_\eta}, \tag{1.28}$$

$$Fr_p = Stk\ Fr_l = \frac{g\tau_p}{u_\eta}, \tag{1.29}$$

where g is the gravitational constant ($9.81\,\mathrm{m\,s^{-2}}$), τ_η is the Kolmogorov timescale (Equation 1.9) and u_η is the Kolmogorov velocity (Equation 1.10).

The preferential concentration of inertial particles in turbulent flows has been extensively studied with a primary focus on the dependence on the Stokes number (Stk), based on the Kolmogorov timescale of the fluid flow and a particle inertia timescale. This parameter, which measures the ratio of particle inertial forces to fluid viscous forces, plays a crucial role in determining how particles deviate from fluid streamlines and form clusters. Squires and Eaton [153] highlighted that particles with a Stokes number close to unity exhibit significant preferential concentration due to their optimal response time to turbulent eddies. Matsuda et al. [104] demonstrated that for $Stk < 2$, the turbulent clustering of droplets significantly influences radar reflectivity, indicating a strong dependence of clustering intensity on the Stokes number. Vaillancourt and Yau [163] reviewed various studies, emphasizing that particles with intermediate Stk are most likely to deviate from randomness and form clusters in turbulent flows.

Further studies, such as those by Shaw [150] and Lian et al. [95], provided experimental and numerical evidence showing that particle clustering is highly sensitive to Stokes number variations. Sahu et al. [145] examined the interaction between droplet dispersion and evaporation, noting that the degree of clustering and the resultant evaporation rates were significantly influenced by the Stokes

number. Haugen et al. [70] explored the impact of turbulence on mass transfer rates, demonstrating that particle clustering due to preferential concentration is maximized at $Stk \approx 1$, affecting surface reactions in turbulent environments.

Monchaux et al. [115] and Eaton and Fessler [46] discussed the underlying mechanisms of preferential concentration, such as the centrifuging of particles from vortical structures, which are most pronounced for particles with Stk around unity. Chun et al. [31] developed an analytical theory to predict particle clustering, confirming that the radial distribution function increases as an inverse power of interparticle separation for small Stokes numbers. Similarly, Bec [13] and Bec et al. [15] provided insights into the fractal nature of particle clustering at low Stk, with clustering intensity diminishing at higher Stokes numbers.

Gustavsson and Mehlig [64] and Bragg and Collins [22] compared statistical models for spatial patterns of heavy particles, elucidating the dependence of clustering behaviour on Stokes number across different turbulent flow regimes. Sundaram and Collins [158] and Coleman and Vassilicos [32] further explored the collision statistics of inertial particles, demonstrating that preferential concentration significantly enhances collision rates for particles with intermediate Stk.

Overall, these studies collectively highlight the critical role of the Stokes number in determining the preferential concentration of particles in turbulence. The observed clustering behaviour, which peaks at $Stk \approx 1$, underscores the importance of particle inertia in modulating their spatial distribution within turbulent flows, as corroborated by numerous experimental, numerical, and theoretical investigations.

While the impact of Stokes number on preferential concentration has been extensively studied, the influence of Reynolds number and gravitational forces on particle clustering in turbulence has received comparatively less attention. Ireland et al. [80, 81] conducted comprehensive simulations to investigate the effect of Reynolds number on inertial particle dynamics, both with and without gravitational effects. They found that higher Reynolds numbers, indicative of more intense turbulence, significantly alter particle behaviour and clustering patterns, particularly for particles with varying Stokes numbers. This study highlights the complexity of interactions at higher Reynolds numbers, where turbulence enhances particle dispersion and clustering through mechanisms not solely dependent on particle inertia.

The Reynolds number significantly influences the behaviour of particle clustering in turbulent flows. Ireland et al. [80] studied Reynolds numbers up to $Re_\lambda \approx 600$ and found that as the Reynolds number increases, regions of intense rotation and strain in the flow tend to form vortex sheets, which can eject inertial particles, particularly those with small Stokes numbers (Stk). This ejection re-

duces the tendency for clustering in these regions. For particles with higher Stokes numbers ($Stk \geq 10$), clustering is affected by a combination of inertial filtering and path-history effects, with increased Reynolds numbers generally enhancing clustering within the inertial range of turbulence [80]. This is because the influence of inertial filtering diminishes at high Reynolds numbers, where greater scale separation and increased turbulence intermittency lead to stronger clustering effects. However, for particles with lower Stokes numbers ($Stk \lessapprox 0.4$), clustering is largely independent of Reynolds number and is primarily driven by preferential sampling of specific turbulent structures [80]. Matsuda et al. [104] examined number density spectra for Reynolds numbers in the range $127 \leq Re_\lambda \leq 531$ at $Stk = 1.0$, finding that the spectra were mostly independent of Reynolds number for wavenumbers $\kappa\eta \geq 0.05$. However, at larger length scales ($\kappa\eta < 0.05$), clustering was shown to be highly dependent on Reynolds number. The combined effects of varying both Stokes number and Reynolds number were not explored in this study.

Matsuda et al. [105] investigated the combined effects of gravitational settling, Reynolds number, and Stokes number on turbulent droplet clustering and radar reflectivity factors. They found that the number density spectra were no longer independent of Reynolds number, even for $\kappa\eta \geq 0.05$, when the Stokes number was sufficiently large ($Stk > 2.0$). Their results showed that gravity significantly modulates clustering intensity, particularly for droplets with Stokes numbers greater than unity. This study, along with earlier work by Matsuda et al. [104], highlights the importance of gravity in modifying particle distributions in turbulent flows, which is essential for accurately modelling atmospheric processes.

Gravity exerts a complex influence on particle clustering and collisions in turbulent flows, with its effects varying based on particle size and Stokes number. Ireland et al. [81] demonstrated that for low-Stokes-number particles, gravity reduces clustering by shortening their interaction time with turbulent structures, thus diminishing preferential sampling and lowering the Lagrangian strain and rotation timescales. Conversely, for high-Stokes-number particles, gravity enhances clustering by modulating drift and diffusion, reducing the path-history effect. Overall, gravity tends to decrease relative velocities and accelerations, leading to fewer collisions between particles of the same size, but it increases collision rates between particles of different sizes due to faster settling speeds.

Onishi et al. [122] similarly found that gravity influences particle clustering by affecting droplet interactions. In monodisperse systems, gravitational sedimentation decreases relative velocities by reducing the interaction time with the turbulent fluid, despite a slight increase in the radial distribution function (RDF). This aerodynamic effect becomes prominent when the sedimentation rate of the droplets exceeds the fluid velocity fluctuations, though for cloud droplets, the

gravitational impact on collisions is often minimal, consistent with models that neglect this effect for monodisperse cloud droplets.

Woittiez et al. [174] further highlighted gravity's dual influence on clustering and collisions. For monodisperse droplets, gravity reduces the probability of collisions by limiting their interaction with turbulence. However, in bidisperse droplets, differing terminal velocities increase the collision kernel. Gravity plays a crucial role in preferential concentration, particularly for larger droplets interacting with large-scale turbulent structures. The interplay between turbulence and gravity is intricate, significantly affecting collision dynamics, especially for droplets of different sizes.

Bec et al. [18] added that gravity accelerates the settling of heavy particles in turbulence, causing them to settle faster than in still fluids by preferentially sampling downward-moving regions. While this promotes particle clustering, settling is shown to induce an effective horizontal two-dimensional dynamics which also reduces relative velocities, creating opposing effects on collision rates. While clustering increases the likelihood of collisions, reduced velocities can hinder them, requiring a balance between these factors for accurate modelling of particle collisions and coalescence in turbulent environments.

Vaillancourt and Yau [163] provided a review of particle-turbulence interactions, noting that while much is known about the role of particle inertia, the combined effects of Reynolds number and gravity on clustering are less well understood. Similarly, Haugen et al. [69] and Shaw [150] discussed the significance of Reynolds number and gravity, emphasizing the need for further investigation to fully comprehend their impact on particle concentration fields.

Reade and Collins [136] and Gustavsson and Mehlig [64] analysed how turbulence affects collision rates and spatial patterns of heavy particles, highlighting that Reynolds number influences these interactions by modifying the turbulence intensity and scales involved. Bragg and Collins [22] further elucidated these dynamics, demonstrating that higher Reynolds numbers can enhance clustering through increased turbulence intermittency and energy dissipation rates.

Experimental studies by Petersen et al. [127] and numerical investigations by Bec et al. [15] supported these findings, showing that particle clustering behaviour is significantly influenced by both turbulence intensity and gravitational forces. Sundaram and Collins [158] and Gualtieri et al. [61] also contributed to this understanding by examining collision statistics and anisotropic clustering in turbulent flows.

Lian et al. [95] and Reveillon and Demoulin [137] provided additional insights into how varying Reynolds numbers and gravitational forces affect droplet evaporation and dispersion, further emphasizing the need for more detailed studies.

Ayala, Rosa, Wang and Grabowski [5], Ayala, Rosa and Wang [4] and Durham et al. [44] also explored the combined effects of turbulence and gravity on particle behaviour, reinforcing the importance of considering these factors in models of particle-laden flows.

Among the studies that examine the combined effects of Stokes number, turbulent Reynolds number, and gravity, very few account for the full range of cluster and void length scales. Additionally, the empirical relation proposed by Matsuda et al. [104] attempts to predict particle concentration, but it is limited to the influence of the Stokes number at a constant Reynolds number and does not consider gravity, making it less applicable for practical use across a broad range of conditions.

Overall, while there has been progress in understanding the impact of Reynolds number and gravity on preferential concentration, this area remains less explored compared to the effects of the Stokes number. Further research is needed to fully elucidate these complex interactions and their implications for various natural and industrial processes.

1.3.3 Two-Way Coupling

The previous section looked at the forces on a particle, however particles can exert reactionary forces on the fluid. The concept of two-way coupling, which describes the back-reaction of inertial particles on the fluid, remains elusive and complex. The regime map proposed by Elghobashi [47] is often referenced to distinguish between one-way and two-way coupling based on the volume fraction, Φ_V. While this map provides a useful approximation for gas-solid systems [127], it is less applicable to solid-liquid systems, which show no turbulence modification below a volume fraction of $\Phi_V \sim 10^{-4}$ [129, 7].

The debate over whether turbulence is augmented or attenuated by particles is ongoing, with multiple competing mechanisms involved [8]. This controversy underscores the need for systematic studies that vary one parameter at a time to isolate specific effects.

Numerical efforts to model two-way coupling typically involve projecting the drag force exerted by particles back onto the fluid grid. However, when particles are not much smaller than the grid spacing, this approach can produce a nonsmooth force field [45]. To address this, Capecelatro and Desjardins [28] proposed a regularization procedure using a compact Gaussian stencil, which smooths the force field and improves accuracy.

A critical aspect of two-way coupling is the particle-fluid slip velocity, which is typically formulated based on the undisturbed fluid velocity. However, the nomi-

nal slip velocity is often higher than the actual slip velocity due to the self-induced disturbance created by the particle. This discrepancy is particularly significant at high particle concentrations, where the undisturbed state is no longer available. Recent approaches have used analytical solutions to a regularized point-force applied by the particle to address this issue [62, 76, 82]. Systematic comparisons with experiments and particle-resolved direct numerical simulations (PR-DNS) are necessary to validate these approaches.

Simulating homogeneous particle-laden turbulence poses significant challenges due to interscale energy transfers. While decaying turbulence simulations can avoid some of these issues, they quickly lead to weak turbulence intensity and are highly dependent on initial conditions.

Experimental studies on the modification of homogeneous turbulence by particles are relatively scarce, partly due to the difficulty of characterizing the underlying flow at significant volume fractions. The number density of particles varies as d_p^{-3}, complicating the separation of fluid tracers and small inertial particles through imaging techniques.

Recent systematic particle image velocimetry (PIV) and particle tracking velocimetry (PTV) measurements have shown a pivoting effect and an increase in kinetic energy (K) with particle loading [68]. This finding contrasts with the common view that sub-Kolmogorov particles attenuate turbulence and is consistent with a previous experimental study by Yang and Shy (2005). Two-way coupled point-particle direct numerical simulations (PP-DNS) have reported turbulence enhancement in the presence of gravity [52], while simulations in zero gravity have indicated turbulence attenuation [128].

The net change in kinetic energy (K) results from the competing effects of gravity and drag. Falling particles transfer potential energy to the flow, which is more effective at a Stokes number (Stk) of order one ($O(1)$) via clusters. Particles also act as sinks of fluid momentum by dragging the fluid and distorting the flow.

As particle loading increases, the source of fluid fluctuating energy shifts from hydrodynamic forcing to the relative motion between the carrier and dispersed phases. Capecelatro et al. [29] studied heavy particles falling at large loadings, leading to cluster-induced turbulence, which is distinct from turbulence-driven particle motion.

Particles can also act as heat sources, generating turbulence through thermal effects. Zamansky et al. [178] investigated the absorption of radiative flux and subsequent heat release by particles, leading to cluster formation and the generation of buoyant plumes. Frankel et al. [52] reported a reduced settling velocity due to the interplay between buoyant plumes and forced turbulence.

1.3.4 Gravitational Settling

The settling velocity v_g of a particle in a quiescent fluid is given by [75]:

$$v_g = g\tau_p, \tag{1.30}$$

where g is the gravitational acceleration. To characterise the settling of particles in a turbulent flow, the Froude number (Fr) is often used, however a slightly different but related non-dimensional parameter used is the settling parameter Sv:

$$Sv = \frac{v_g}{u'}, \tag{1.31}$$

where u' is the root mean square of the velocity fluctuations.

Theoretical mechanisms have been proposed to explain how turbulence can either enhance or hinder the gravitational settling of particles. Most studies report that turbulence enhances the settling of small dilute particles in homogeneous shearless turbulence [59]. This enhancement is often attributed to a phenomenon known as preferential sweeping, where particles preferentially sample the downward-moving regions of turbulent eddies [107, 169, 127]. Preferential sweeping has been invoked to explain field observations of snowfall speeds [118, 94] and, conversely, the reduced rising velocity of bubbles in turbulent water [1].

The effect of turbulence on different types of particles varies. Particles that are slightly lighter than the fluid are driven out of vortex cores by the added mass force, leading to upward preferential sweeping and increased rising velocity [143, 102]. This behaviour differs from the centrifuging effect of vortex cores; instead, particle concentration correlates more with downward fluid fluctuations than with high-strain regions [127].

For significant settling enhancement, both the Stokes number (Stk) and the settling parameter (Sv) should be of order unity [58]. There is debate over which velocity scale governs this enhancement. Some studies suggest that enhancement is proportional to the root-mean-square of fluid velocity fluctuations [77], while others, like Tom and Bragg [160], propose that preferential sweeping is influenced by a range of velocity scales that increase with Stk.

The extent of settling enhancement has been a topic of extensive research. Early experiments indicated large differences, complicating the validation of numerical simulations [20]. Quantifying the fall speed of microscopic particles presents challenges: in wind tunnels, the settling rate is much smaller than the flow speed; in tanks stirred by oscillating grids, circulations likely alter particle fallout; and in chambers stirred by randomly actuated jets, intense turbulence is created with negligible mean flow and shear. Using the latter setup, Good et al. [58] and Pe-

tersen et al. [127] reported large maximum settling velocities, exceeding $2.5\tau_p g$ in very dilute regimes. Such massive settling enhancement has significant implications for particle transport in natural and industrial settings.

Despite these findings, the limits of the point-particle (PP) approach are evident. Settling velocities observed in experiments often exceed predictions from PP-DNS under matching conditions Good et al. [59]. This discrepancy highlights the limitations of the point-particle approach even in nominally one-way coupled flows, where the particles are assumed to have negligible effect on the fluid.

1.3.5 Interactions Between Particles

The interactions between particles in a turbulent flow are complex and multifaceted, significantly impacting the dynamics of the system. One of the primary interactions is collision and agglomeration. Several mechanisms drive particle collisions in turbulent flows. For very small particles, Brownian motion, which results from random thermal fluctuations, is the dominant collision mechanism [53]. In contrast, larger particles are more likely to collide due to shear flow, where differences in velocity gradients cause particles to come into contact [158]. Additionally, differential settling occurs when particles of different sizes settle at different rates, leading to collisions [11].

Once particles collide, agglomeration can occur, where particles stick together to form larger aggregates. This process is enhanced by turbulent mixing, which increases the frequency of collisions by providing the necessary kinetic energy to overcome electrostatic repulsion [34]. However, high shear rates in turbulence can exert significant stress on these aggregates, causing them to fragment. The balance between agglomeration and breakup, determined by the relative strengths of cohesive forces and shear forces, dictates the overall particle size distribution. When cohesive forces, such as van der Waals forces, dominate, aggregates form. Conversely, when shear forces exceed these cohesive forces, breakup occurs [75].

Various inter-particle forces influence particle collisions and agglomeration. Van der Waals forces, which are short-range attractions between molecules, play a significant role in particle cohesion [84]. Electrostatic forces arise from surface charges on particles, leading to either repulsion or attraction depending on the nature of the charges [2]. Magnetic forces can also impact particle interactions. These forces collectively determine the likelihood of particles sticking together upon collision.

Fluid properties, such as viscosity and density, significantly affect particle interactions in turbulent flows. Higher viscosity increases the energy dissipation rate, potentially reducing collision frequencies by damping turbulent eddies [108].

Conversely, fluid density affects the inertia of particles, influencing their settling velocities and collision rates. For example, in a rainstorm, the viscosity and density of air play crucial roles in determining how raindrops form and grow as smaller droplets collide and merge [134].

The shape and surface roughness of particles also influence collision rates and outcomes. Irregularly shaped particles or those with rough surfaces have higher collision cross-sections, increasing the probability of contact. Moreover, surface roughness can enhance the sticking efficiency by providing more contact points for van der Waals forces to act upon.

The general aerosol dynamic equation describes aerosol growth, accounting for processes such as nucleation, coagulation, and condensation/evaporation . In the context of rain formation, smaller water droplets in clouds collide and coalesce to form larger raindrops through these dynamic processes. Particles can grow through condensation when water vapour condenses on their surfaces or shrink via evaporation when liquid water transitions back to vapour [91]. Understanding these dynamics is essential for predicting the size distribution and behaviour of aerosols in various environments.

1.4 Numerical Simulation of Turbulent Flows

An incompressible fluid flow can be fully described by a momentum conservation equation, the Navier-Stokes equation, and a mass conservation equation, the continuity equation Equation 1.2. Several approaches that differ in their completeness and level of description, accuracy and computational cost have been developed for the numerical solution of these equations [130].

The simplest approach from a conceptual point of view as well as the most accurate approach is the full resolution of all scales of motion, the Direct Numerical Simulation (DNS) [50]. However, its total computational cost is extremely high and increases rapidly with the Reynolds number $O(Re_\lambda^6)$ [130].

By using the Reynolds decomposition (Equation 1.12) to only resolve the mean flow, the computational cost can be drastically reduced, an approach known as Reynolds-Averaged Navier Stokes (RANS) [50] (Equation 1.13). A variety of methods for modelling the unresolved, turbulent, motions, which are usually only sufficiently accurate for specific application areas, have been devised [130]. Due to the non-linear nature of the Navier-Stokes equation, turbulence models should be considered engineering approximations and not scientific laws [50].

In Large-eddy Simulations (LES) only the largest turbulent structures, containing at least 80% of the turbulent kinetic energy, are resolved [130]. The separation between resolved and unresolved scales is achieved by a filtering operation. The

filtered Navier-Stokes equation is not closed and the subgrid Reynolds stresses need to be modelled [110]. One way of modelling the subgrid Reynolds stresses is to relate them to the resolved strain rate, which is the underlying principle of the most widely used subgrid model, the Smagorinsky model [50].

Whereas in the original Smagorinsky model the subgrid stresses are related to the resolved strain by a constant with a fixed value [130], Germano (1992) developped a subgrid model in which this constant is dynamically determined based on the assumption of similarity between different scales of motion. Pope [130] showed that not the assumption of scale similarity, but choosing a constant that is independent of the grid resolution is the reason why this dynamic model gives good results.

Another approach to modelling the subgrid-scale motions, the deconvolution method, is to estimate them from an inverted filter operation [50]. The deconvolution method belongs to a family of structural methods whose goal is to obtain an estimate of the unfiltered velocities, the most accurate as well as most computationally expensive of these being the explicit evaluation on an auxiliary grid [144].

The validity of a subgrid-scale model needs to be tested by comparison to experimental or DNS data, which is known as a posteriori test [110]. Another type of test that is commonly performed is the a priori validation, in which the filtered velocity is directly obtained from the DNS results [144]. Whereas a priori tests provide more insight into the physics of a given subgrid model, the validity of a subgrid model can only be ascertained a posteriori [110]. Typically subgrid models yield better results for homogeneous turbulence than in more complex flows [144].

1.4.1 Direct Numerical Simulation With Pseudo-Spectral Simulation

The pseudo-spectral method is a powerful numerical technique widely used in Direct Numerical Simulation (DNS) of turbulence due to its high accuracy in solving the incompressible Navier-Stokes equations. This method is particularly effective for turbulent flow simulations because it leverages the spectral representation of the governing equations, allowing for a more precise handling of the nonlinear interactions inherent in turbulence.

In the pseudo-spectral approach, the velocity and pressure fields are transformed into Fourier space, where the spatial derivatives are computed exactly through simple multiplication by wave numbers. This eliminates the need for finite-difference approximations, which can introduce numerical dispersion errors,

especially at high wave numbers. By representing the variables in terms of their Fourier coefficients, the method achieves spectral accuracy, meaning the error decreases exponentially as the grid resolution increases. This property is especially advantageous in turbulence, where a wide range of scales must be captured, from the largest eddies down to the smallest dissipative scales [26].

The governing equations for the flow are the incompressible Navier-Stokes equations are given in Equations 1.2 & 1.3. In the pseudo-spectral method, these equations are transformed into Fourier space using the Fourier transform, where the velocity field $\boldsymbol{u}(\boldsymbol{x},t)$ and the pressure $p(\boldsymbol{x},t)$ are expressed in terms of their Fourier transforms $\hat{\boldsymbol{u}}(\boldsymbol{\kappa},t)$ and $\hat{p}(\boldsymbol{\kappa},t)$ [26]. The Fourier transform is defined as:

$$\hat{f}(\boldsymbol{k},t) = \int_{\mathbb{R}^3} f(\boldsymbol{x},t) e^{-i\boldsymbol{\kappa}\cdot\boldsymbol{x}} d\boldsymbol{x}, \tag{1.32}$$

where $\boldsymbol{\kappa}$ is the wavenumber vector. Applying the Fourier transform to the Navier-Stokes equations, we obtain the governing equations in wave number space as:

$$\frac{\partial \hat{\boldsymbol{u}}(\boldsymbol{\kappa},t)}{\partial t} + i\boldsymbol{\kappa}\cdot\widehat{(\boldsymbol{u}\otimes\boldsymbol{u})}(\boldsymbol{\kappa},t) = -i\boldsymbol{\kappa}\hat{p}(\boldsymbol{\kappa},t) - \nu|\boldsymbol{\kappa}|^2\hat{\boldsymbol{u}}(\boldsymbol{\kappa},t), \tag{1.33}$$

the nonlinear term $\boldsymbol{u}\cdot\nabla\boldsymbol{u}$ becomes a convolution in Fourier space, making it computationally expensive to evaluate directly. To simplify this, the pseudo-spectral method computes the nonlinear terms in physical space by transforming the variables back to physical space, performing pointwise multiplication, and then transforming the result back to Fourier space. This combination of physical space operations for nonlinear terms and spectral operations for linear terms allows the method to retain spectral accuracy while reducing computational costs.

The incompressibility condition in Fourier space is given by:

$$\boldsymbol{\kappa}\cdot\hat{\boldsymbol{u}}(\boldsymbol{\kappa},t) = 0, \tag{1.34}$$

To enforce this, a projection operator

$$\mathbf{P}(\boldsymbol{\kappa}) = \mathbf{I} - \frac{\boldsymbol{\kappa}\boldsymbol{\kappa}^T}{|\boldsymbol{\kappa}|^2}, \tag{1.35}$$

is applied to the velocity field in Fourier space, which ensures that the solution remains divergence-free [26]. This is one of the big advantages of the pseudo-spectral method, that a separate pressure equation does not need to be solved.

The linear terms (such as viscous dissipation) are treated spectrally, and the time evolution of the velocity field in Fourier space is given by:

$$\frac{\partial \hat{\boldsymbol{u}}(\boldsymbol{\kappa}, t)}{\partial t} = \mathbf{P}(\boldsymbol{\kappa}) \left(-i\boldsymbol{\kappa} \cdot (\widehat{\boldsymbol{u} \otimes \boldsymbol{u}})(\boldsymbol{\kappa}, t) - \nu k^2 \hat{\boldsymbol{u}}(\boldsymbol{\kappa}, t) \right), \tag{1.36}$$

The pseudo-spectral method excels in simulations where periodic boundary conditions are appropriate, making it particularly well-suited for homogeneous, isotropic turbulence (HIT). In HIT, the turbulence exhibits no preferred direction or position, and all statistical properties are invariant under translations and rotations. These characteristics align perfectly with the periodic domains naturally imposed by the pseudo-spectral method, ensuring that the boundaries of the computational domain do not artificially influence the flow field [141]. The method also benefits from efficient de-aliasing techniques, such as the 2/3 rule, which prevent the buildup of numerical artifacts by truncating the highest wave numbers [125].

The computational efficiency of the pseudo-spectral method and its ability to handle a wide range of scales make it ideal for DNS, where both the largest turbulent eddies and the smallest dissipative scales must be resolved. However, one limitation of the pseudo-spectral method is its restriction to periodic boundary conditions, which precludes its use for problems involving complex geometries or flows with significant boundary layer effects.

1.4.2 Fast Fourier Transform

The Fast Fourier Transform (FFT) is an essential component in implementing the pseudo-spectral method for Direct Numerical Simulation (DNS) of turbulence. The FFT is a highly efficient algorithm for computing the discrete Fourier transform (DFT) and its inverse, which is crucial for transitioning between physical space and Fourier space during the simulation process. The primary advantage of the FFT is its computational efficiency, reducing the complexity of the DFT from $O(N^2)$ to $O(N \log N)$, where N is the number of grid points. This significant reduction in computational cost makes it feasible to handle the large data sets typical in DNS of turbulence.

In the context of the pseudo-spectral method, the FFT is used at each time step to switch between the two representations of the flow field. The nonlinear terms, such as the convective term $\boldsymbol{u} \cdot \nabla \boldsymbol{u}$, are evaluated in physical space, where pointwise multiplication is computationally simple. However, the Fourier space is more suitable for handling the linear terms, including the viscous dissipation and pressure gradient. Therefore, the FFT is employed to transform the velocity field $\boldsymbol{u}(\boldsymbol{x}, t)$ from physical space to Fourier space $\hat{\boldsymbol{u}}(\boldsymbol{\kappa}, t)$, where the spatial derivatives and linear terms are computed spectrally. The inverse FFT is then applied to return to physical space after the linear terms have been updated.

The efficiency of the FFT is particularly important in DNS because turbulence requires resolving a wide range of scales, from the largest energy-containing eddies down to the smallest dissipative structures. This results in a large number of grid points in three-dimensional simulations, where the computational domain must capture the full spectrum of turbulent motions. The $O(N \log N)$ complexity of the FFT allows for practical DNS of large systems, making it possible to achieve high resolution and spectral accuracy without prohibitive computational costs.

1.4.3 Gibbs oscillations

A notable issue with spectral methods is the Gibbs phenomenon [156]. When Fourier series are truncated, they fail to fully capture the high-wavenumber components of the spectrum related to discontinuities in physical space, such as square waves, leading to numerical artifacts [27]. One approach to mitigate these effects is the use of spectral filters that dampen the contributions from higher wavenumbers [27]. More advanced techniques attempt to detect discontinuities directly, but this significantly increases computational demands [156].

1.4.4 Time Stepping

In Direct Numerical Simulation (DNS) of turbulence, time-stepping schemes are critical for advancing the flow field solution from one time step to the next while maintaining accuracy and stability. Among the various methods available, the fourth-order Runge-Kutta (RK4) scheme is widely used due to its balance between precision and computational efficiency [130]. The RK4 method is a multi-stage, explicit time integration scheme that allows for accurate resolution of the temporal evolution of the velocity field in DNS, particularly when using the pseudo-spectral method for spatial discretization.

The RK4 method operates by computing several intermediate steps (or stages) within each time step to achieve higher-order accuracy. The general form of the RK4 scheme for solving ordinary differential equations, such as the time-dependent Navier-Stokes equations, is given by:

$$\boldsymbol{k}_1 = f(\boldsymbol{u}^n, t^n), \tag{1.37}$$

$$\boldsymbol{k}_2 = f\left(\boldsymbol{u}^n + \frac{\Delta t}{2}\boldsymbol{k}_1, t^n + \frac{\Delta t}{2}\right), \tag{1.38}$$

$$\boldsymbol{k}_3 = f\left(\boldsymbol{u}^n + \frac{\Delta t}{2}\boldsymbol{k}_2, t^n + \frac{\Delta t}{2}\right), \tag{1.39}$$

$$\boldsymbol{k}_4 = f(\boldsymbol{u}^n + \Delta t\boldsymbol{k}_3, t^n + \Delta t), \tag{1.40}$$

$$\boldsymbol{u}^{n+1} = \boldsymbol{u}^n + \frac{\Delta t}{6}(\boldsymbol{k}_1 + 2\boldsymbol{k}_2 + 2\boldsymbol{k}_3 + \boldsymbol{k}_4), \tag{1.41}$$

where $\boldsymbol{u}^n$ represents the velocity field at the current time step t^n, $\boldsymbol{u}^{n+1}$ is the velocity field at the next time step, and Δt is the size of the time step. The function $f(\boldsymbol{u}, t)$ corresponds to the right-hand side of the governing equations, which, in this case, is the Navier-Stokes equations in Fourier space (Equation 1.36). The intermediate values $\boldsymbol{k}_1, \boldsymbol{k}_2, \boldsymbol{k}_3$, and $\boldsymbol{k}_4$ are calculated at different stages within the time step to improve accuracy.

The RK4 method achieves fourth-order accuracy in time, meaning that the error per time step decreases as $O(\Delta t^4)$. This high level of accuracy makes it suitable for simulations that require precise time evolution, such as DNS of turbulence, where capturing the detailed dynamics of turbulent eddies over a range of time scales is essential [130].

Despite its accuracy, explicit Runge-Kutta methods, including RK4, are subject to stability constraints. One of the main limitations is the Courant-Friedrichs-Lewy (CFL) condition, which restricts the maximum allowable time step size based on the grid resolution and the flow velocity. The CFL condition for an explicit time-stepping scheme can be expressed as:

$$\Delta t \leq \frac{\text{CFL}}{\max(u) \cdot \Delta x}, \tag{1.42}$$

where Δx is the spatial grid spacing, $\max(u)$ is the maximum velocity magnitude in the domain, and the CFL number is typically less than one to ensure stability [27]. In DNS of turbulence, where a fine grid resolution is required to resolve the smallest scales of motion (such as those on the order of the Kolmogorov scale η), the CFL condition often imposes a strict upper limit on the time step size. Consequently, the RK4 method must be used with relatively small time steps to ensure numerical stability, especially in simulations involving high Reynolds numbers [130].

Another important consideration in the application of the RK4 method to DNS is the separation of linear and nonlinear terms in the governing equations. In the

pseudo-spectral method, the Navier-Stokes equations consist of linear terms, such as viscous dissipation ($\nu\nabla^2\boldsymbol{u}$), and nonlinear terms, such as advection ($\boldsymbol{u}\cdot\nabla\boldsymbol{u}$). The RK4 method handles both terms explicitly, advancing the solution for both components over each time step [27]. In some cases, semi-implicit schemes are used, where the linear terms are treated implicitly to relax the CFL constraint, while the nonlinear terms are treated explicitly using an RK4 scheme. Alternatively an Exponential integrator alternative of the RK4 method can be used where the viscosity term is solved exactly [33]. These approaches allows for larger time steps without compromising stability [93].

The RK4 method is well-suited to DNS because it balances the need for accuracy with manageable computational costs. Although higher-order Runge-Kutta methods or implicit schemes could potentially offer even greater accuracy or stability, RK4 remains a popular choice due to its simplicity and ease of implementation. Its explicit nature also makes it straightforward to parallelize, which is critical for large-scale DNS simulations of turbulence, where computational efficiency is a primary concern [130].

1.5 Numerical Simulation of Particle Flows

The most accurate approach for simulating the movement of solid particles in turbulent flows is fully-resolved Direct Numerical Simulation (DNS), where the fluid flow around each particle is computed exactly using a method to resolve the interface between the particles and the fluid [101]. However, this method becomes computationally prohibitive when applied to the large number of particles typically encountered in practical applications [8]. Moreover, fully-resolved DNS requires a finely resolved grid to capture the fluid dynamics accurately, which restricts its feasibility to particles significantly larger than the Kolmogorov length scale, η [101].

Alternative approaches are generally classified into two categories: Lagrangian point-particle methods and Eulerian methods. In Lagrangian point-particle methods, the trajectory of individual particles is tracked using a Lagrangian frame of reference, whereas in Eulerian methods, particle concentration and velocity fields are computed on a fixed grid [101]. Both approaches rely on the approximation of particles as point particles, either explicitly in Lagrangian methods or implicitly through the assumptions used in deriving the Eulerian equations [8]. While these methods are less computationally demanding than fully-resolved DNS, they introduce assumptions that may limit accuracy, particularly for flows where the particle size approaches or exceeds the turbulence scales.

1.5.1 Lagrangian Point-Particle Method

In Lagrangian point-particle methods, the trajectory of individual particles is calculated based on their motion [8]. Typically, this is done using the equation of motion described in Equation 1.22, which is often simplified to the most significant terms in Equation 1.25 [48]. Unlike Eulerian methods, Lagrangian methods are well-suited to handling polydisperse particle distributions and are not constrained by particle inertia [8]. Additionally, Lagrangian methods are effective for simulating low-concentration particle flows, where the continuum assumption breaks down [49]. Although Lagrangian methods can be used for particles with any Stokes number, Eulerian methods are typically more computationally efficient for small Stokes number particles [8]. A key advantage of Lagrangian point-particle methods is their ability to represent particles with varying velocities within the same control volume, a feature generally unavailable in Eulerian methods [8].

One limitation of the Lagrangian point-particle approach is the assumption that particles are small compared to the smallest turbulence scales, specifically the Kolmogorov length scale η. This approximation can lead to inaccuracies when the particle size becomes comparable to or exceeds η, as the method does not resolve the detailed fluid-particle interactions. In such cases, the point-particle model fails to capture effects like the distortion of the surrounding fluid or the finite-size influence on the local flow field, which could affect particle dynamics [108]. This limitation highlights the need for caution when applying Lagrangian point-particle methods to larger particles.

Another important consideration in Lagrangian methods is the treatment of interactions between the particles and the fluid, as well as between the particles themselves. In low-concentration flows, the one-way coupling assumption, where particles are influenced by the fluid but do not affect it, is typically sufficient. However, in denser particle-laden flows, two-way coupling, where the particles exert forces on the fluid and alter the flow field, becomes necessary. For very high concentrations, four-way coupling must be considered, accounting for both fluid-particle interactions and direct particle-particle collisions. These additional couplings introduce significant computational complexity and necessitate more sophisticated models, but are essential for accurately simulating high-concentration multiphase flows [47].

Since the particle's position in a Lagrangian framework typically does not align with the nodes of the Eulerian fluid mesh, an interpolation of the fluid velocity at the particle's position is required [9]. The most accurate interpolation under periodic boundary conditions is achieved by summing spectral coefficients over all wavenumbers, which provides an exact solution:

$$f(x) = \sum_{k=-N/2}^{N/2} \hat{f}_k e^{ikx}, \tag{1.43}$$

where $\hat{f}_k$ are the Fourier coefficients and N is the number of grid points [9]. However, this approach is computationally expensive and rarely applied in practice [83].

Van Hinsberg et al. [164] conducted a thorough comparison of various interpolation methods using both theoretical error analysis and validation with direct numerical simulations (DNS) of homogeneous isotropic turbulence. Among the methods tested, linear interpolation exhibited the highest error, while B-spline interpolation was found to be the most accurate.

Linear interpolation estimates the velocity at a particle's position by weighting the values at the nearest grid points. For a function $f(x)$ in one dimension, linear interpolation is given by:

$$f(x) \approx f(x_1) + \frac{f(x_2) - f(x_1)}{x_2 - x_1}(x - x_1), \tag{1.44}$$

While simple and computationally inexpensive, linear interpolation introduces significant error, particularly in turbulent flows where small-scale features need to be resolved accurately.

B-spline interpolation, on the other hand, provides higher-order accuracy by using smooth basis functions. For cubic B-spline interpolation in one dimension, the interpolated value is calculated using:

$$f(x) = \sum_i N_i^3(x) f(x_i), \tag{1.45}$$

where $N_i^3(x)$ are the cubic B-spline basis functions. This method significantly reduces the error compared to linear interpolation, making it more suitable for DNS of turbulence. The B-spline interpolation was found to be the most accurate in their comparison [164].

Hermite interpolation is another higher-order method that takes into account both the values and the derivatives of the function at the grid points. The cubic Hermite interpolation between two points x_1 and x_2 can be expressed as:

$$f(x) = h_{00}(t)f(x_1) + h_{10}(t)f'(x_1)(x_2 - x_1) + h_{01}(t)f(x_2) + h_{11}(t)f'(x_2)(x_2 - x_1), \tag{1.46}$$

where $t = \frac{x - x_1}{x_2 - x_1}$ is the normalized distance between x_1 and x_2, and the Hermite basis functions $h_{ij}(t)$ ensure smooth transitions between grid points. While

Hermite interpolation provides high accuracy, it comes with a significant computational cost due to the need to compute and store derivative information.

An analysis of the acceleration spectrum of inertial particles revealed that all interpolation schemes introduced high-frequency oscillations, even with spectral interpolation, due to discretization error rather than the interpolation itself [164].

Ireland et al. [83] also evaluated interpolation schemes in DNS of homogeneous isotropic turbulence and concluded that B-spline interpolation offers the best compromise between accuracy and computational efficiency [83].

In large-scale DNS, the computational cost of Lagrangian point-particle methods can be reduced through parallelization techniques, which are crucial for handling the large number of particles required in many simulations. Lagrangian methods are inherently suited to parallelization, as the particle trajectories can be computed independently of one another, apart from the relatively infrequent updates needed for fluid-particle or particle-particle interactions. By distributing the particle computations across multiple processors, modern high-performance computing (HPC) platforms can significantly mitigate the computational burden. This scalability is one of the key reasons Lagrangian point-particle methods remain viable for DNS of particle-laden turbulence, even in high-Reynolds-number flows or simulations with large particle counts [8].

1.5.2 Eulerian Methods

Eulerian methods, which handle particle concentration fields or probability distributions rather than tracking individual particles, offer significant computational efficiency, particularly in two-way coupling simulations between the particulate and carrier phases. This is primarily because the grids for both phases can be aligned, simplifying the computation of momentum transfer between particles and the fluid. However, while efficient, Eulerian methods have limitations, especially in their ability to capture the detailed dynamics of individual particles. This results in a loss of information about the behavior of specific particles, which Lagrangian methods can model more precisely.

An often underemphasized aspect of Eulerian methods is the importance of the chosen numerical schemes, which critically impact the accuracy of the simulation results. One key challenge arises from the physical diffusion properties of particles in air. For larger particles, physical diffusion is extremely low, as indicated by the high Schmidt number, which can be orders of magnitude greater than unity [35]. This means that while diffusion in the carrier phase is relatively significant, it is almost negligible for the particulate phase. This disparity can lead to numerical instabilities in the partial differential equations governing the particle phase if not

appropriately handled. Although Direct Numerical Simulation (DNS) is effective for resolving the carrier fluid down to the smallest dissipative scales, applying DNS to the particle phase is impractical due to the much smaller scales involved.

To address the challenge of simulating advection in the absence of significant physical diffusion, various techniques have been developed. One common approach is to introduce artificial diffusion [173], which adds a small amount of diffusion into the governing equations to stabilize the simulation. This artificial diffusion dampens high-frequency fluctuations, making it possible to use higher-order numerical methods like pseudo-spectral methods. However, the accuracy of simulations becomes highly dependent on the choice of the artificial diffusivity. Introducing too much artificial diffusion can diminish the accuracy gains from using high-order schemes, leading to a trade-off between stability and precision.

Another class of methods involves upwind-biased schemes, which are designed to ensure numerical stability while minimizing numerical diffusion. The simplest linear upwind scheme that guarantees stability is the first-order upwind method [56], but this approach introduces significant numerical diffusion, reducing accuracy. To overcome this, more advanced non-linear upwind schemes, such as Total Variation Diminishing (TVD) and Weighted Essentially Non-Oscillatory (WENO) schemes, can be employed [98]. These schemes offer higher accuracy in regions with smooth solutions but revert to lower-order accuracy near discontinuities or shocks. The complexity of the problem increases in cases involving advection of multiple quantities, such as energy or second-order velocity moments, where different velocities must be considered. One approach to solving this multi-velocity problem is to solve a localized Riemann problem for each quantity, using upwind methods to account for the different velocities. The Roe Flux-Difference method [140] is a notable example of this technique.

Many Eulerian approaches only track a single velocity for the particulate phase in each grid cell [69]. While this reduces computational cost, it fails to capture important particle transport phenomena such as crossing trajectories. Crossing trajectories occur when two particles, which may be close to each other or even occupy the same location (if collisions are not modeled), move with different velocities [87]. This limitation can be addressed by advanced models that account for second-order velocity moments. For instance, an anisotropic Gaussian closure model was developed to simulate the particulate phase by also transporting the second-order velocity moments, which allows the model to capture crossing trajectories [167]. These models, often referred to as mesoscopic approaches, provide a more detailed representation of the particulate phase. Variations of these mesoscopic models have been developed [51] and tested in a range of studies [88, 90].

These methods as well as equations are discussed in more detail in Section 3.3.2.2

1.5.3 Numerical Simulation of Preferential Concentration

Simulations of particle preferential concentration in turbulent flows typically employ either Lagrangian or Eulerian methods, each with distinct advantages and limitations. Lagrangian methods have been widely adopted for studying preferential concentration because they can capture the complex dynamics of particle clustering [106]. However, Lagrangian simulations require a large number of computational particles to produce statistically reliable results, making them computationally expensive. Haugen et al. [69] showed the effects of random noise on particle number spectra by varying the number of Lagrangian particles, they used 10 times the number of particles than fluid mesh points, and highlighted the difficulty in exploring weak clustering at large wavelengths. Additionally, because the particle positions do not coincide with the grid points used for simulating the fluid, interpolation is required to extract fluid velocities at particle positions, which further adds to the computational cost.

In contrast, Eulerian methods simulate concentration or probability fields rather than individual particles. This makes them computationally more efficient, especially in two-way coupling scenarios where interactions between the particulate and carrier fluid phases need to be resolved. Eulerian approaches are particularly effective when the grids for both phases align, simplifying the computation of momentum transfer between particles and fluid. However, these methods face significant limitations when it comes to simulating individual particle dynamics. The most critical shortcoming of Eulerian methods is their inability to handle the "crossing trajectories" phenomenon, where two particles can occupy the same location but have different velocities—a common occurrence in turbulent particle-laden flows [87]. Most Eulerian methods assign a single velocity to the particulate phase in each grid cell, which can result in inaccurate representation of particle dynamics.

To overcome this, mesoscopic approaches have been developed. An example is the anisotropic Gaussian closure model, which transports second-order velocity moments to allow for crossing trajectories [167]. These advanced Eulerian models extend the traditional approach by incorporating more detailed information about the velocity distributions of particles within a grid cell. This mesoscopic approach, and its variations [51, 88, 90], provides a better balance between computational efficiency and physical accuracy. Despite these advances, Lagrangian methods remain the more accurate choice when particle clustering and individual particle dynamics are the primary focus of the simulation.

Accurately quantifying preferential concentration is essential for understanding how particles cluster in turbulent flows. Several methods have been developed

to analyze this phenomenon. Radial distribution functions (RDFs) are commonly used to quantify particle clustering by measuring how the concentration of particles changes with distance from a reference particle. RDFs provide important insights into the spatial arrangement of particles, especially at lower Stokes numbers [5, 14, 148, 31, 177]. However, RDFs are typically limited to pairwise interactions and assume spherical symmetry in the particle distribution. This assumption may not always hold, especially in flows where particle clusters exhibit irregular shapes. To address this, some studies have employed angular distribution functions, which capture the angular relationships between particle pairs [61].

Voronoi tessellation is another widely used method for quantifying preferential concentration. This technique assigns a volume to each particle by partitioning the domain into Voronoi cells, which enables the calculation of local particle concentrations. By measuring the variance in the volumes of these cells, researchers can identify and quantify clusters, providing a direct measure of concentration in both numerical simulations and experimental studies [124, 114, 157, 6]. Voronoi tessellation is particularly valuable because it does not assume any symmetry in the particle distribution, allowing for a more accurate identification of non-uniformities in particle concentration.

Spectral methods offer a distinct approach by analyzing the spatial distribution of particles in terms of their length scales. These methods can be divided into Fourier transforms and wavelet transforms. Fourier transforms focus on the power spectrum of particle concentrations and are effective in identifying the dominant clustering scales in turbulent flows [41, 86, 104, 146, 69, 3]. However, Fourier transforms provide only a global overview of clustering and lack spatial localization, which limits their utility in capturing localized particle clustering. Wavelet transforms overcome this limitation by offering localized insights into particle concentration across different scales [10, 106]. Wavelet transforms are particularly useful for analyzing intermittent or spatially varying clustering phenomena, providing a more detailed view of how and where particles cluster within the flow.

1.6 Summary

The background section of this thesis has covered several key areas that form the foundation for understanding aerosol behaviour in turbulent flows, as well as the numerical methods used to study these systems. A central theme is the role of turbulence, a chaotic and irregular fluid phenomenon that contrasts sharply with laminar flow. Turbulence enhances mixing and transport processes across a wide range of systems, from natural environments to industrial settings. A detailed discussion of the characteristics of turbulence was provided in Section 1.2, em-

phasizing the presence of vortices and eddies that transfer energy through the well-known energy cascade, from larger to smaller scales, until dissipation occurs at the Kolmogorov scale. This fundamental understanding of the energy cascade is crucial for analysing fluid dynamics in systems where aerosol particles are dispersed.

Turbulence was further explored through its statistical description, including the Reynolds decomposition and the Reynolds-Averaged Navier-Stokes (RANS) equations, which describe how turbulence impacts mean flow fields. The turbulence kinetic energy budget and the concept of homogeneous isotropic turbulence (HIT) were introduced as important theoretical models that simplify the analysis of turbulence. These models allow for the development of turbulence theories and simulation techniques that are essential for understanding how turbulent flows interact with particles.

Building on this, Section 1.3 went into particle dynamics within turbulent flows, particularly focusing on the motion of small particles, such as aerosols. The Maxey-Riley-Gatignol (MRG) equation of motion was presented as a key tool for modelling the forces acting on particles in non-homogeneous flows. The equation accounts for a variety of forces, including buoyancy, added mass, drag, and history effects. Despite being derived under idealized conditions, the MRG equation is frequently applied in real-world turbulent environments to model particle motion, providing a critical foundation for simulating aerosol behaviour in fluid systems. The MRG equation is often simplified further into a Stokes drag with gravity.

A major focus of this thesis is on the phenomenon of preferential concentration, where inertial particles cluster in specific regions of turbulent flows. This behaviour, caused by the particles' inertia, leads to their deviation from fluid streamlines. The Stokes number has been established as the key parameter influencing preferential concentration, with extensive research showing that particles with a Stokes number near unity exhibit the strongest clustering. These particles respond optimally to turbulent eddies, which drives their aggregation into concentrated regions.

However, despite the wealth of research on the Stokes number, the effects of the Reynolds and Froude numbers on preferential concentration have received comparatively less attention. The Reynolds number, indicative of the intensity of turbulence, and the Froude number, which quantifies the relative influence of gravitational forces, play critical roles in shaping particle behaviour in realistic turbulent environments. Yet, the exact impact of these dimensionless parameters on clustering remains poorly understood. Current models often fail to fully capture how high Reynolds numbers alter the dynamics of particle concentration, particularly in complex flows where turbulence is intense. Similarly, while the

Froude number is important in systems where gravitational forces interact with turbulence—such as atmospheric aerosols or sedimentation processes—its effect on preferential concentration has been inadequately studied. This thesis will address these gaps by investigating the combined effects of these parameters on particle clustering.

Furthermore, the underlying mechanisms of preferential concentration remain an active area of research. Competing theories such as the 'sweep-stick' mechanism, where particles are swept into regions of low vorticity and settle into zones of near-zero fluid acceleration that are then convected by the fluid, or the centrifuging effect of vortices, offer plausible explanations for clustering. Yet, no consensus has been reached, particularly in high-Reynolds-number or gravity-influenced flows. The precise interactions between turbulence, particle inertia, and gravitational forces remain unclear, underscoring the need for further investigation into these mechanisms.

To model these complex behaviours, Section 1.4 & Section 1.5 reviewed several numerical methods for simulating turbulent flows and particle-laden systems. Direct Numerical Simulation (DNS) was highlighted as the most accurate method, resolving all scales of turbulence, but its high computational cost limits its practicality in large-scale applications. Large Eddy Simulation (LES) and RANS models were introduced as alternatives that sacrifice some accuracy for computational feasibility by resolving only the largest scales of turbulence. The pseudo-spectral method used in DNS was described in detail, including its reliance on Fourier transforms and spectral accuracy in handling the nonlinear interactions characteristic of turbulence.

Section 1.5 also explored the methods for simulating particle-laden flows, focusing on Lagrangian and Eulerian approaches. The Lagrangian point-particle method, which tracks individual particle trajectories, is highly effective for low-concentration flows but becomes computationally expensive at higher particle concentrations. Eulerian methods, which treat particles as a continuous phase, offer a more efficient approach for dense particle systems but are less accurate for resolving individual particle dynamics. These numerical techniques are crucial for studying the detailed behaviour of aerosol particles in turbulent environments, particularly where both large-scale and small-scale interactions need to be resolved.

In summary, the background section has laid the groundwork for a detailed study of aerosol dispersion and particle preferential concentration in turbulent flows. The subsequent chapters will build on this foundation, using advanced numerical methods to explore how turbulence, inertia, and gravitational forces interact to shape the behaviour of particle-laden flows. This research will provide new insights into the parametric dependence of particle clustering on dimensionless

numbers and the underlying mechanisms that drive preferential concentration.

1.7 Current Contribution

This thesis presents a comprehensive study of aerosol dispersion and particle preferential concentration in turbulent flows, emphasizing the development and application of computational modelling techniques. The research consists of several key contributions that advance our understanding of particle-turbulence interactions and offer efficient methods for predicting particle behaviour in both natural and industrial systems. Among the primary contributions are the development of an Eulerian method using the Roe-flux scheme, an investigation into the effects of Reynolds and Froude numbers on preferential concentration using spectral methods, the proposal of an empirical relation for particle concentration spectra under various conditions, and an in-depth analysis of the correlation between turbulent structures and particle clusters, particularly on large length scales.

A major contribution of this thesis is the development of an Eulerian method based on the Roe-flux scheme. Traditional studies of preferential concentration often rely on Lagrangian particle tracking, where individual particles are traced as they move through the turbulent flow. While this method is effective for capturing the detailed trajectories of particles, it can be computationally expensive, particularly when simulating large numbers of particles in highly turbulent environments. In contrast, the Eulerian method developed in this thesis offers a more efficient alternative by modelling the dispersed particle phase as a continuous field and solving the relevant transport equations directly on a grid. The Roe-flux scheme provides a numerically stable way to account for complex particle-fluid interactions, and the incorporation of second-order velocity moments in the Eulerian framework allows for an accurate representation of particle behaviour at higher Stokes numbers. This method reduces the need to track millions of individual particles while still capturing the essential physics of preferential concentration, making it especially useful for large-scale simulations where computational efficiency is a priority.

This thesis also explores the combined effects of the Reynolds number (Re_λ) and Froude number (Fr) on preferential concentration, with a focus on how these parameters influence particle behaviour across a range of length scales. Previous studies often focused solely on the Stokes number (Stk) as the primary factor governing particle-turbulence interactions. However, this research demonstrates that the Reynolds and Froude numbers play a significant role in shaping particle clustering, particularly at larger scales. Through direct numerical simulations (DNS) and spectral analysis, it was found that the intensity of particle clustering

is strongest at Stk near unity, but both Re_λ and Fr have profound effects on the distribution of particles. For example, at small Stokes numbers, the influence of Reynolds number is minimal, but for larger particles with higher inertia, increasing Re leads to more complex and varied clustering patterns. The role of gravity, quantified by the Froude number, further modulates these patterns, with gravity enhancing clustering at larger scales and diminishing it at smaller scales. These results provide a deeper understanding of how turbulence, particle inertia, and gravitational forces interact to affect particle distribution, offering valuable insights for atmospheric science and industrial processes that involve particle-laden flows.

An additional key contribution of this thesis is the development of an empirical relation for predicting particle concentration spectra under a variety of conditions. Spectral methods are widely used to analyse how energy and particle concentration are distributed across different length scales in turbulence. While the spectra for fluid turbulence are well-established, deriving accurate models for particle concentration spectra in particle-laden flows remains a challenge. This thesis addresses this gap by systematically analysing particle concentration spectra across a range of Stokes, Reynolds, and Froude numbers, leading to the development of an empirical model that can predict the spectra under different conditions. The proposed model is particularly effective for intermediate and large Stokes numbers, where particle inertia interacts most strongly with turbulent eddies. This empirical relation provides a practical tool for researchers and engineers who need to model particle-laden flows in large systems where DNS may be computationally infeasible. The model has potential applications in fields such as atmospheric science, chemical engineering, and environmental studies, where accurate predictions of particle clustering are essential for system design and optimization.

Another contribution is the detailed investigation into the correlation between turbulent structures and particle clusters, particularly at large length scales. Preferential concentration arises when inertial particles are ejected from high-vorticity regions and accumulate in low-vorticity regions, forming clusters and voids. However, the exact relationship between turbulent structures and these particle clusters has not been fully understood. This thesis addresses this gap by analysing how different turbulence metrics, such as the Q-Criterion, Enstrophy, and Lagrangian-averaged vorticity deviation (LAVD), correlate with particle clustering. The results show that LAVD, which measures the rotational coherence of turbulent structures, is the most reliable predictor of large-scale particle clustering. Regions of strong rotational coherence, as captured by LAVD, are most conducive to particle cluster formation, while areas of high vorticity and low rotational coherence correspond to voids where particle concentration is low. These findings provide

new insights into the dynamic relationship between fluid turbulence and particle distributions, particularly at large length scales, where the formation of clusters can significantly impact processes such as pollutant dispersion or aerosol mixing in industrial applications.

This thesis represents an advancement in our understanding of aerosol dispersion and particle preferential concentration in turbulent flows. By developing and applying efficient computational methods, such as the Eulerian method with Roe-flux and second-order velocity moments, and by investigating the effects of Reynolds and Froude numbers on particle clustering, this research provides both theoretical and practical tools for improving predictions of particle behaviour in complex systems. The empirical relation for particle concentration spectra offers a valuable model for researchers and practitioners, while the detailed analysis of the correlation between turbulent structures and particle clusters sheds light on the fundamental mechanisms driving preferential concentration. These findings have wide-ranging applications in fields such as atmospheric science, industrial fluid dynamics, and environmental engineering, where understanding and controlling particle behaviour is essential for optimizing processes and mitigating risks.

Chapter 2

Computational and Experimental Study of Aerosol Dispersion in a Ventilated Room

This work is published in Downing et al. [42] with the collaboration of the University of Bristol, it has been adapted to form the basis of this Chapter.

2.1 Abstract

For many respiratory diseases, a primary mode of transmission is inhalation via aerosols and droplets. The COVID-19 pandemic has accelerated studies of aerosol dispersion in indoor environments. Most studies of aerosol dispersion present computational fluid dynamics results, which rarely include detailed experimental verification, and many of the computations are complex, making them hard to scale to larger spaces. This study presents a comparison of computational simulations and measurements of aerosol dispersion within a typical ventilated classroom. Measurements were accomplished using a custom-built low-cost sensor network composed of 15 commercially available optical particle sizers, which provided size-resolved information about the number concentrations and temporal dynamics of 0.3 µm to 40 µm diameter particles. Measurement results are compared to the computed dispersal and loss rates from a steady-state Reynolds-Averaged Navier-Stokes k-epsilon model. The results show that a newly developed aerosol-transport-model can accurately simulate the dispersion of aerosols and faithfully predict measured aerosol concentrations at different locations and times. The computational model was developed with scalability in mind such that it may be adapted for larger spaces. The experiments highlight that the fraction of aerosol recycled in the ventilation system depends on the aerosol droplet size

and cannot be predicted by the recycled-to-outside air ratio. Moreover, aerosol recirculation is not negligible, as some computational approaches assume. Both modelling and measurements show that, depending on the location within the room, the maximum aerosol concentration can be many times higher than the average concentration, increasing the risk of infection.

2.2 Introduction

The use of ventilation systems is prevalent in many areas of day-to-day life including in road vehicles, trains, aeroplanes and office buildings and public places. Good ventilation is vital in maintaining good health, but current air quality regulations are not as developed as, for example, for food safety [117]. Wargocki indicated that health risks increase when the ventilation rate in homes is below 0.4 air changes per hour (ACH) [170]. Many high-rise and office buildings are now equipped with Heating, Ventilation and Air-Conditioning (HVAC) systems, which control the movement of air within a building. HVAC systems use mechanical ventilation that utilizes fans and ducts to inject outside air and circulate room air, consuming a large amount of energy. HVAC systems currently consume around 12% of the worldwide final energy use [57]. Air recirculation can be used to reduce the operating costs of HVAC systems, with some of the building air mixed with outside air from outside and resupplied to the room. Mixing of outside air with inside air already at temperature reduces the energy requirements for HVAC systems to heat or cool the ventilation air to a comfortable temperature [60]. However, such air recirculation increases the possibility that aerosols and contaminants can spread around a building.

With the COVID-19 pandemic, the dispersal and removal of aerosol within rooms and large spaces have become important topics of study. For many respiratory diseases, such as COVID-19 and influenza, a dominant mode of transmission is via aerosols comprising liquid droplets [172, 152]. The aerosol size distribution affects droplet dispersion in space, residence time in air, and deposition efficiency in the respiratory tract [175]. For example, large droplet sizes (diameter $> 100\,\mu m$) tend to quickly sediment out of the air (i.e. seconds), whereas smaller aerosol droplets (diameter $< 100\,\mu m$) may remain airborne for long periods (i.e. hours) and may present greater infection risk[133]. Moreover, viral load carried by droplets may depend on droplet size [111], highlighting the importance of aerosol dispersion due to airflow and its dependence on droplet size.

Computational modelling of aerosol dispersion in large spaces is challenging due to computational resource limitations, in particular when time-dependent computations are attempted in open spaces with complex geometries. The full

range of timescales and lengthscales of the physics of airflow and aerosol droplet dispersion is impossible to resolve. Therefore, different assumptions are required to deliver computations that may provide an efficient and accurate prediction of aerosol dispersion physics. One modelling approach for aerosol transport is the use of a purely diffusive model, without any information of the local airflow characteristics, which uses the turbulent eddy diffusivity to provide enhanced diffusion due to turbulence. This technique has successfully been compared with experiments for both instantaneous and continuous release of aerosol for a variety of ventilation rates [166]. However, a shortfall of this method is that some dispersion characteristics cannot be captured if a significant convective flow is present in a room due to the ventilation duct placement resulting in an advection dominated regime. Additionally, this method does not account for varying aerosol droplet size.

Many studies of aerosol dispersion utilise computational fluid dynamics (CFD) and either are not evaluated by comparison with experiments [73, 103, 179, 63, 135, 39, 38, 126], or include minimal experimental verification (for example using a tracer gas of SF6 to verify CFD results rather than aerosols) [85] or use different fluids in an equivalent geometry [131]. Many studies do not investigate the dependence of dispersion on aerosol droplet size distribution, as such calculations can be computationally expensive. In addition, it is challenging to generate aerosols with wide size distributions and measure the transport and loss rates of particles of varying size in ventilated rooms. Therefore, understanding the dynamics of the size distribution of dispersed aerosols is crucial for the evaluation of disease transmission risk, and studies are required to robustly investigate the dependence of aerosol dispersal and loss on droplet size.

In this study, we aim to provide computational and experimental results for aerosol dispersion within a ventilated room and investigate the effect of particle size on dispersion. In particular, the effect of ventilation air recycling ratio on aerosol concentration decay rate is considered. We concentrate on particles smaller than 10 µm diameter and will not consider the effect of evaporation in order to simplify the evaluation of the dispersion models. As droplet size has a large impact on aerosol dispersion, the potential impact of evaporation on dispersion cannot always be neglected and must be evaluated carefully. After exhalation, droplets can decrease significantly in size to around 20-40% of their initial diameter as they equilibrate with the ambient environment [165]. The time for full equilibration of a 10 µm droplet can be around 1 s [40]. This short time is far less than the timescales of dispersion we are interested in this study. The effect of evaporation on the experiments was lessened by using a high weight percent of salt (20%) in the solution. This ensures that aerosol's dry diameter was still a significant

portion of the initial wet diameter.

We present computational and experimental results for aerosol dispersion within a ventilated room. The inlet and outlet ventilation flowrates to the room were measured and used as inputs for the computational fluid dynamics (CFD) model. Aerosols were periodically generated in the room and their dispersion was measured experimentally using an array of low-cost sensors. Aerosol dispersion was simulated using a computational model that accounts for the local mean flow characteristics in the room and, with a modified aerosol-transport-model, the effects of turbulence on aerosol dispersion. The comparison between measurements and model predictions provide insight into how well a simplified computational model can represent aerosol dispersion in an indoor room environment and whether such an approach may be amenable to computational investigations of aerosol dispersion in larger scale environments (e.g. in buildings).

2.3 Methodology

This section presents the experimental arrangement and the tools that were used to obtain the measurements. It also presents the computational fluid dynamics models for the gas phase and the aerosol particles.

2.3.1 Experimental Methods

2.3.1.1 Experimental Room Set-Up

The test room used for the experiments and computational work was a typical classroom at the University of Bristol. The room is a cuboid with length 9.0 m, width 5.6 m and height 2.6 m. The room had desks and chairs (4 of each) as well as three people working within, each wore a face mask. For all experiments the windows were kept shut, and door use was kept to a minimum to ensure an enclosed environment. Further measures were not taken as the amount of aerosol purposefully generated provided a sufficient signal above background noise. The room had two swirl diffusers in the ceiling that provided the ventilation air inlets, and one square grill in the ceiling for the ventilation outlet. The inlets were 56 cm in diameter and the outlet was 53 cm in length and width. Figure 2.1 shows the placement of the ventilation ducting in the ceiling of the test room (indicated by WS401 in the figure) and the adjoining corridor.

The total ventilation rate to the room was 11.3 air changes per hour (ACH), according to the room data sheet provided by the facilities management unit, and air flow measurements obtained with a hot-wire probe at the square grill room outlet. The false ceiling of the room had a large void in which outside and

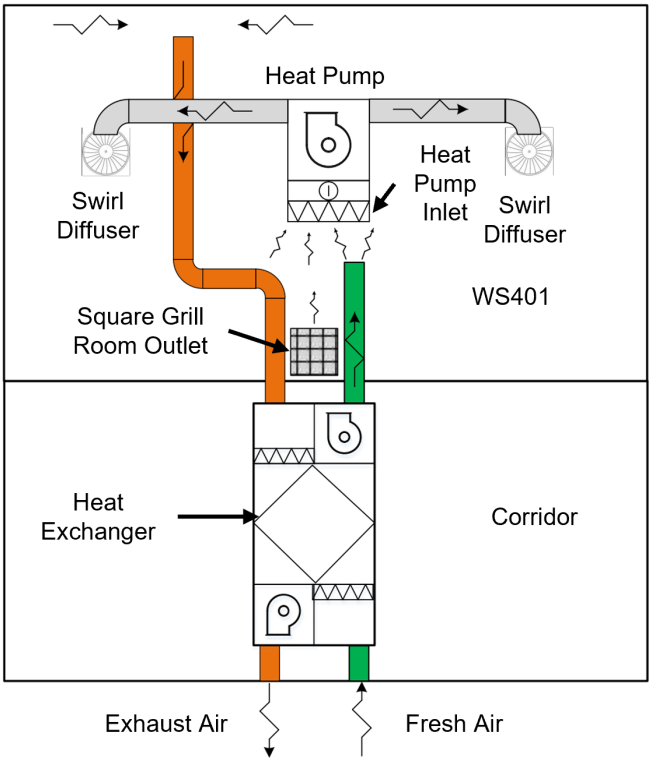


Figure 2.1: Top-down view of the false ceiling with ducting placement. Outside air flows into the false ceiling via the heat exchanger (green line) where is mixes with air being brought up from WS401 from the square grill. This mixed air is then drawn into the heat pump inlet where it enters WS401 via the swirl diffusers. The experimental room was WS401 in this diagram.

recirculated air mixed, resulting in 7.5 ACH outside air drawn in from the outside with the remaining 3.8 ACH drawn as recycled air. We recognise that 11.3 ACH is a high flowrate, however this room was chosen for practicality and not because of the air-change rate. This air-change rate may have been different in other rooms, and we did not have the opportunity to perform the experiment elsewhere. The fraction of aerosol recycled differs from the fraction of air recycled and is particle size dependent. Due to the placement of the square grill outlet adjacent to the inlet of the heat pump that feeds the swirl diffusers, it is conceivable that aerosols coming from the room to the ceiling void via this outlet may be recycled more easily than the air. The heat pump may also have some internal filters which will affect the amount of recycled aerosol. Initial assumptions are that all the aerosols (from outside air and recycled air) are filtered out and none are recycled, an assumption we shall revisit later in the discussion.

2.3.1.2 Aerosol Generation

It was desirable to produce a high aerosol number concentration to resolve an increase in aerosol concentration relative to the background concentration. In

addition, generation of a broad aerosol size distribution is desirable to quantify size dependent dispersion and loss rates. A typical 500 mL domestic mini snow mountain ultrasonic humidifier (SmartDevil) was used to generate 0.5 µm to 10 µm diameter particles from a 20-weight percent aqueous NaCl solution (water activity 0.93 [112]). The droplet size distribution generated by the humidifier (shown in Figure 2.2) was measured with an aerodynamic particle sizer (APS, TSI 3321, TSI Inc., Shoreview, MN) connected to the humidifier using 1 m of conductive silicon tubing in a straight line. The particles were released almost directly into the silicon tubing with the air outside the tubing being still. During transport from the humidifier to the APS only a portion of the aerosol would have fully evaporated, thus Figure 2.2 represents a distribution slightly larger than what would have been recorded by the low-cost sensor network. The effect of evaporation on the distribution was lessened by using a high weight percent of salt (20%) in the solution.

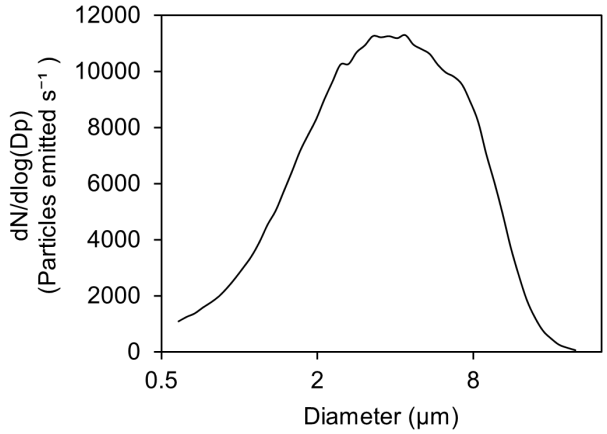


Figure 2.2: Droplet size distribution (measured by an APS) from the 500 mL humidifier, as measured close to the humidifier exit, so that the droplets had not evaporated.

To generate short term responses from the low-cost aerosol sensors, the generator was operated for short periods of time ranging from 10-60 s. The duration of these pulses was recorded for use as inputs to the computational model. The generator was kept at the same position throughout all experiments (Figure 2.3).

2.3.1.3 Aerosol Measurements

Aerosol number concentrations and size distributions (0.3 µm to 40 µm diameter) across the room were measured using a network of sensors consisting of 15 optical particle counters (Alphasense OPC N-3). The sampling frequency was 1 Hz. The uncertainty of the droplet concentration measurements of the optical particle counters has a maximum coincidence probability of 0.84% at 0.106 particles cm^{-3} and

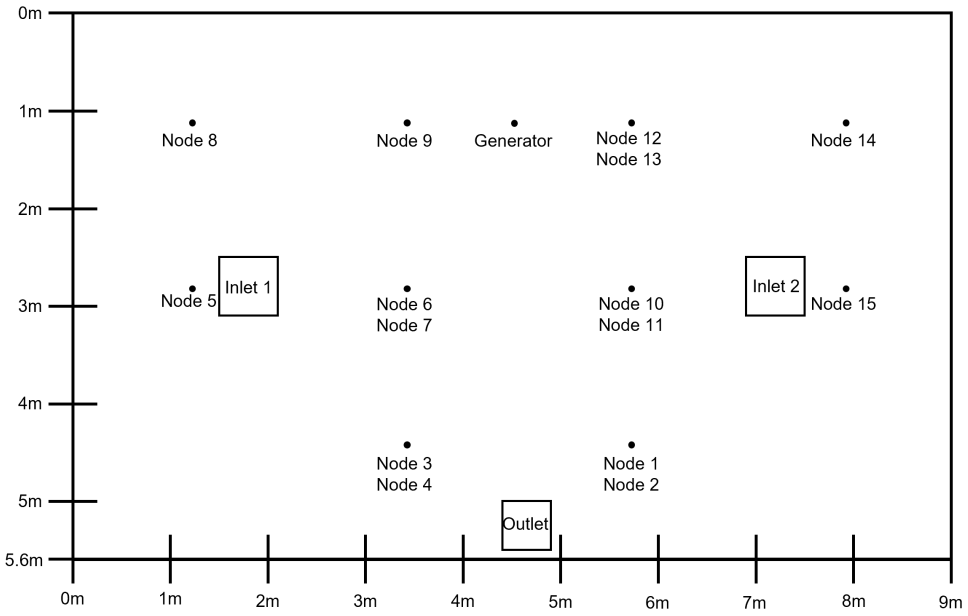


Figure 2.3: Top-down view of the room and sensor placements within the test room. All nodes are at a height of 1.6 m apart from Nodes 1, 3, 6, 10 & 12, which are at a height of 1.2 m. Diagram to scale.

0.24% at 0.500 particles cm^{-3}. If the OPCs fluctuated between detecting particles and not (for example fluctuating between reporting 0 particles and 1 particle), then that size-bin was not used; this only happened for size bins greater than 10 µm for which the samples are limited by Poisson arrival statistics due to the low number concentration of larger aerosol particles. Analysis was therefore limited to droplet sizes less than 10 µm.

Each optical particle counter was connected to a Raspberry Pi. The Raspberry Pis of all sensors were connected to an Intel NUC via Wi-Fi, allowing all the data from the network to be stored in a single location. The sensors were distributed across 10 pylons within the room. The positions are shown in Figure 2.3. The optical particle sizers were placed either at a height of 1.6 m (average height for the mouth when standing) or 1.2 m (average height for the mouth when sitting). All data were analysed in a custom-written Python script. The data were smoothed by taking a rolling average of the previous 30 seconds of data. This one-sided averaging was preferred over centred averaging as it preserves the start time of pulses.

2.3.2 Computational Methods

2.3.2.1 Fluid Dynamics Modelling

To compare experimental to computational results, a CFD model of the air flow in the room was created using the OpenFOAM package [171]. The room geometry

was simplified as explained below to keep computational cost to a minimum. The computational room was set up as a cuboid with height 2.6 m and floor dimensions of 9.0 m by 5.6 m, closely matching the physical room. Internal features of the room, such as desks, chairs and people, were not included in the computational domain.

The floor, ceiling and walls of the room were modelled as no-slip boundary conditions. The computational domain was divided into cells that were 10 cm in height, length and breadth. Two ventilation inlets and one outlet in the ceiling were modelled to represent the experimental room as closely as tractable. Although the square outlet has length and width of 53 cm, it was defined as a pressure outlet with a length and width of 60 cm to fit into the 10 cm cube cells. Air velocity measurements were obtained with a RS-8880 Hotwire Anemometer at different locations across the outlet, which provided a spatially averaged velocity that was multiplied by the outlet area to confirm that the outflow flowrate was 11.3 ACH ($0.41\,\mathrm{m^3\,s^{-1}}$). The inlets to the room were two spiral diffusers which had an outer diameter of 56 cm and an inner diameter of 18 cm. The measured air velocity magnitude at the outer diameter was $6\,\mathrm{m\,s^{-1}}$. In the computational domain, the inlets were modelled as a square annulus with a 60 cm outer diameter and a 20 cm inner diameter, such that it fitted into the 10 cm cells. The boundary conditions at the inlets were defined with a downward flowrate that would match the measured ACH, which led to a downward inlet area averaged velocity of $0.64\,\mathrm{m\,s^{-1}}$. To match the measured velocity magnitude at the inlets, a rotational speed of 150 rpm in the clockwise direction (from top-down perspective) was added to the boundary conditions of the inlets.

The fluid flow within the room was calculated with a steady-state Reynolds-Averaged Navier-Stokes (RANS) k-epsilon model [92]. This computational method separates the velocity and pressure fields into a time-averaged (mean) component and a fluctuating component. The method then calculates the mean flow field and not the fluctuating velocity field, ensuring that a steady-state solution can be obtained. However, due to the non-linearity of the Navier-Stokes equations, the fluctuating field influences the mean field, resulting in a requirement for a turbulent closure problem. This non-linearity is treated by creating two extra fields, the turbulent kinetic energy (k) and the turbulent kinetic energy dissipation rate (epsilon (ε)). The turbulent kinetic energy is the square magnitude of the velocity fluctuations (Equation 2.1) and, therefore, was quantified experimentally, and will be compared in the results section to the computations.

$$k = \frac{1}{2}\left(\left\langle\left\langle(u - \langle\langle u\rangle\rangle)^2\right\rangle\right\rangle + \left\langle\left\langle(v - \langle\langle v\rangle\rangle)^2\right\rangle\right\rangle + \left\langle\left\langle(w - \langle\langle w\rangle\rangle)^2\right\rangle\right\rangle\right), \tag{2.1}$$

where k is the turbulent kinetic energy, u, v, w are the velocities in the x, y and z directions respectively and $\langle\langle u \rangle\rangle$ represents a space and time average.

Figure 2.4 shows the top-down view of the grid size with the computed air flow at a height of 1.6 m across the room. The simulation used around 130,000 cells, which required 1 CPU hour to reach steady state, although availability of extra CPU cores will shorten the simulation time.

To evaluate the fluid flow simulation, the turbulent kinetic energy (TKE) was measured at several locations in the room and compared with the calculated turbulent kinetic energy from the CFD simulation at the equivalent locations in the computational domain. Turbulent kinetic energy was used as a guideline to assess the CFD simulation since it is an important parameter for the determination of the turbulent diffusion of aerosols (Equation 2.3). Evaluation of the air flow velocities across the room was not undertaken due to the simplified room geometry in the computational domain. The turbulent kinetic energy was estimated from the measured velocity magnitude using a RS-8880 hotwire anemometer.

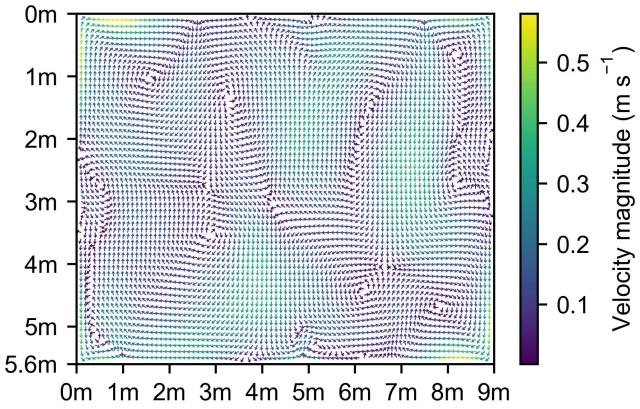


Figure 2.4: Top-down view of the velocity field at a height of 1.6 m. Grid size is 10 cm as seen in the figure and the velocity magnitude is according to the colour scale. (Figure 2.3 shows the room features for comparison.)

2.3.2.2 Aerosol Modelling

Using a RANS k-epsilon model, it is possible to transport passive scalars (such as trace molecular concentrations). The mean convection velocity of the scalar is given by the mean air velocity field from the RANS calculations. The fluctuating velocity field of the air flow also creates a fluctuating convection velocity of the scalar, which is often described as turbulent diffusion [138]. The turbulent diffusion effect is often modelled as Fickian diffusion with a turbulent diffusivity. In the RANS k-epsilon model, the turbulent kinematic viscosity is given as [92]:

$$\nu_t = C_\mu \frac{k^2}{\varepsilon} \tag{2.2}$$

where ν_t is the turbulent kinematic viscosity ($\mathrm{m^2\,s^{-1}}$), C_μ is the dimensionless model coefficient for the turbulent viscosity with a default value of 0.09 that has been empirically fitted from experiments in boundary layer flows. k is the turbulent kinetic energy ($\mathrm{m^2\,s^{-2}}$) and ε is the turbulent kinetic energy dissipation rate ($\mathrm{m^2\,s^{-3}}$). To relate the turbulent kinematic viscosity with the turbulent diffusivity, a dimensionless turbulent Schmidt number is used [25]:

$$Sc_t = \frac{\nu_t}{K} \tag{2.3}$$

where Sc_t is the turbulent Schmidt number and K is the turbulent diffusivity ($\mathrm{m^2\,s^{-1}}$). The simplest model for the turbulent Schmidt number, which has been used in this study, is to assume a constant value of $Sc_t = 1$.

Aerosols are not passive scalars, but have inertia and forces, such as weight and drag, which result in divergence from the fluid flow streamlines. The extent to which aerosols may divert from the fluid streamlines is quantified by the Stokes number [24]:

$$Stk = \frac{\rho_p\, d_p^2}{18\, \mu_g} \frac{1}{\tau_f} \tag{2.4}$$

where Stk is the Stokes number (dimensionless), ρ_p is the density of the aerosol particles ($\mathrm{kg\,m^{-3}}$), d_p is the droplet diameter (m), μ_g is the dynamic viscosity of the gas (Pa s), and τ_f is the fluid response time (s). ρ_p was assumed to be $2100\,\mathrm{kg\,m^{-3}}$ for pure NaCl assuming the aerosol particles are fully dried to form crystalline particles [71], justified by the measured 35% RH of the room. $\mu_g = 18.3\ \mu\mathrm{N\,s\,m^{-2}}$ for air at 23 °C [12].

For $Stk \ll 1$, it can be assumed that the aerosol particles closely follow the fluid streamlines [162]. If the total mass of a particle is low, then momentum transfer from the particles to the fluid can be neglected with minimal error. Under these assumptions, aerosols can be assumed to act as passive scalars. Due to the difficulty of calculating the timescale τ_f for the turbulent air flow, which may be different at different regions of the room, exact values of the Stokes numbers were not calculated. However, it was assumed that $Stk \ll 1$ due to the small size of particles (0.5 µm to 9.5 µm) and the low total mass of injected particles.

For $Stk \ll 1$, it can be assumed that the aerosol particles closely follow the fluid streamlines [162]. If the total mass of a particle is low, then momentum transfer from the particles to the fluid can be neglected with minimal error. Under these assumptions, aerosols can be assumed to act as passive scalars. The fluid timescale

τ_f can be estimated from the turbulent kinetic energy (k) and dissipation rate (ε); however, due to spatial variations in turbulence intensity throughout the room, determining a representative average is challenging. However, it was assumed that $Stk \ll 1$ due to the small size of particles (0.5 µm to 9.5 µm) and the low total mass of injected particles.

When modelling aerosol transport, the RANS mean velocity field was used for convection and the turbulent diffusivity for diffusion computations. It was assumed that turbulent diffusion would be far greater than any Fickian/molecular diffusion effects, thus these were not modelled. Since the experiments in the room lasted for a time scale of hours, the model also would have to simulate the aerosol transport for such a length of time.

5 µm salt particles have a terminal velocity in air of $5.6\,\mathrm{m\,h^{-1}}$. With a room height of just 2.6 m, a significant number of aerosol particles might be expected to sediment out onto the floor over the course of an hour. As such, the mean velocities from the RANS model were adjusted for the calculation of aerosol convection, and an additional downward velocity that was equal to the terminal velocity of the particles was added to the RANS model to account for long-term sedimentation. The terminal velocity of the aerosol particles is defined as:

$$v_T = \frac{\rho_p \, d_p^2}{18 \, \mu_g} \, g \tag{2.5}$$

where v_T is the terminal velocity ($\mathrm{m\,s^{-1}}$) and g is the gravitational acceleration of $9.81\,\mathrm{m\,s^{-2}}$.

Modelling aerosol transport as a passive scalar with convection and turbulent diffusion implies that the transport equations are linear. This means that scaling the aerosol concentration by a constant factor does not alter the dispersion dynamics, only the absolute concentration values, resulting in a free parameter when carrying out the simulations, which is the aerosol injection rate. The aerosol injection rate could be selected equal to the experimental injection rate. However, measuring the aerosol concentration by the generator could produce erroneous results as these particles may have only partially evaporated. As such a different method of estimating the aerosol injection rate within the simulation was chosen. The aerosol injection rate was chosen to be a fixed value so that the mean aerosol concentration of the experiment and the simulation matched.

Since any particle losses due to diffusion to the walls of the room were assumed negligible, the only particle losses were due to sedimentation or convection via the air flow vent. As discussed previously, the flow into the room consisted of a mixture of outside and recycled air. Using the experimental values of the recycle ratio of particles, described later, recycling of air and particles was also implemented into

the computational model to improve accuracy.

The aerosol transport model was custom written in Julia using the fluid flow results from OpenFOAM. The aerosol transport model used the same 130,000 cells as the CFD (Figure 2.4). 10 different aerosol particle sizes were tracked in the simulation for around 1 hour, requiring approximately 4 hours of computational time using a graphics processor. With additional processing power, the different aerosol sizes could be simulated in parallel reducing the computational time.

The CFD and aerosol transport simulations were also repeated on 5 cm grid cells. Figure 2.5 shows there was a minimal difference in the number concentration profiles between the 5 cm (fine) and 10 cm (coarse) grids. Because computational and experimental results agree well, a 10 cm grid was used.

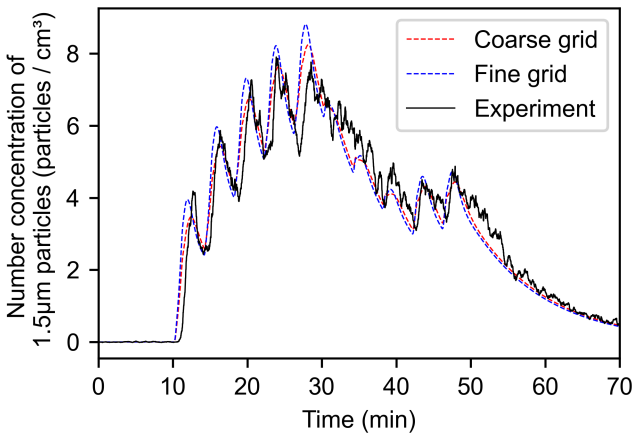


Figure 2.5: Time dependent aerosol particle number concentration computed at node 1 of a 5 cm grid (blue) and a 10 cm grid (red).

2.4 Results

2.4.1 Evaluation of Fluid flow Computation

The hot-wire measurements are expected to underestimate the TKE, a consequence of the finite response time of the hot-wire, which depends on the thickness of the wire; thicker wires 'filter out' higher frequency velocity fluctuations resulting in a lower magnitude estimate of TKE. As a result, we expect that the measured TKE to be systematically lower than the computed values from the CFD model. At the different room locations, the experimental TKEs were in the range of $3.2 \times 10^{-3}\,\mathrm{m^2\,s^{-2}}$ to $9.4 \times 10^{-3}\,\mathrm{m^2\,s^{-2}}$ and the computational TKEs were in the range of $5.2 \times 10^{-3}\,\mathrm{m^2\,s^{-2}}$ to $1.1 \times 10^{-2}\,\mathrm{m^2\,s^{-2}}$, in line with expectations for slightly lower experimental TKEs than the CFD values to within an order of magnitude (around 60%).

2.4.2 Aerosol Characteristics

2.4.2.1 Model & Experiment

The computations were compared to the aerosol concentration measurements at different locations and times within the room in order to assess the ability of the model to predict the dispersion of the aerosols. An experiment was designed that injected multiple sequential short pulses of aerosols that lasted for varying time lengths. Figure 2.6 shows the times when the aerosol generator was turned on and off during the experiment. The pulsed injection facilitates the detectors to observe the short timescale aerosol pulse dispersion due to diffusion and convection and the slow timescale decay of the aerosol due to droplet sedimentation and ventilation. After the pulsed aerosol injection, sufficient time is allowed for the aerosol concentrations to decay to background levels.

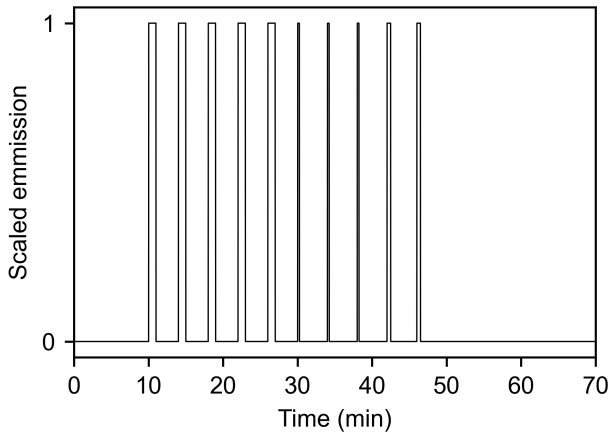
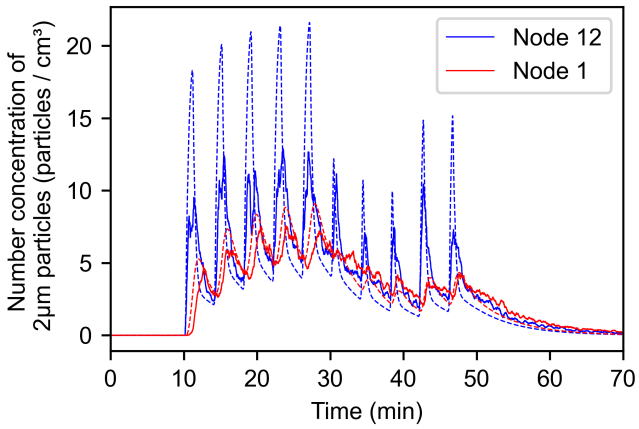


Figure 2.6: Aerosol injection pulses used in the experiment. 0 indicates the aerosol generator was switched off; 1 indicates the aerosol generator was switched on. The temporal sequence of the pulse included five 1-minute pulses followed by three 15-second pulses and finally two 30-second pulses.

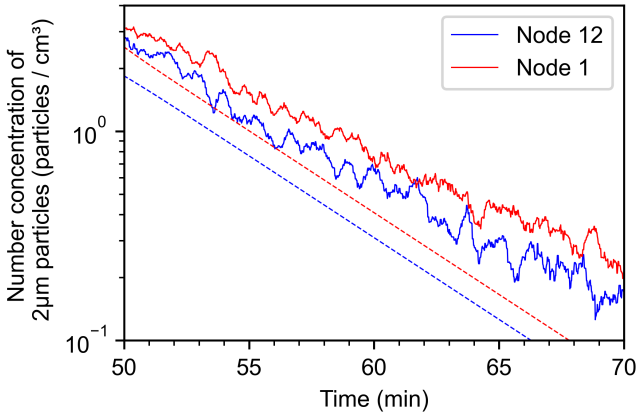
In total 165 different time series aerosol concentrations were recorded and analysed using 15 different sensors, each with 11 size bins of useable data. Figure 2.7 reports the concentration of 2.0 µm particles recorded at nodes 12 and 1, which were located near the aerosol generator and far away, respectively. (See Figure 2.3 for the sensor placements.) Both the model (dashed lines) and experiment (solid lines) for node 12 (blue) show larger peaks than node 1 (red), and the time delay between the aerosol injection pulse and the measurement initiation by the detector is shorter for node 12, consistent with expectations since node 12 is closer. Good agreement can be seen between model and experimental results for both nodes. Remaining small differences between model and experiment can be accounted for when it is recognised that the model predicts average behaviour whereas tempo-

ral changes to the instantaneous velocity field can cause large variations in the measured signal.

The model predicts a faster decay rate of particle concentration than the experiment, as can be seen beyond 50 minutes. This first modelling approach did not allow recycling of particles through the ventilation duct and, thus, any aerosol particles leaving the room through the ventilation exhaust grid are permanently removed from the simulation.



(a)



(b)

Figure 2.7: Model (dashed) and experimental (solid) temporal concentrations for 2.0 µm particles for Node 12 (placed near the aerosol generator, blue) and Node 1 (placed far from the aerosol generator, red). This model assumes no aerosol recirculation by the ventilation system. Model particle concentration rates were scaled by matching the mean of the model and experiment. (a) Shows the full response (b) Shows the response after 50 minutes on a logarithmic scale.

2.4.2.2 Aerosol Particle Recycling

As discussed in the previous section, the model overpredicts the decay rate of 2.0 µm particles. One potential explanation for this observation is that some par-

ticles are recycled through the ventilation duct due to the placement of the outlet (Figure 2.1). To investigate the number of recycled particles, the aerosol generator was temporarily placed in the ceiling of the room near the exhaust vent and the amount of aerosol entering the room was measured using the sensor network. It was found that all particles greater than 5.85 µm were completely filtered, while varying amounts of smaller particles returned into the room.

An approach to quantify the amount of recycled aerosol particles in the room is to computationally calculate the decay rates and compare these to the experimental values. After around two minutes of aerosol injection, the particles become well-mixed in the room, and it can be assumed that the aerosol concentration is reasonably uniform throughout the room. By fitting an exponential decay to the data at the time that the aerosol is well-mixed across the room (specifically for the data after 55 minutes in Figure 2.7), the size-dependent decay rate can be inferred and is reported in Figure 2.8.

Under a well-mixed assumption, a theoretical decay rate can be modelled taking into account the ventilation rate, the amount of recycled aerosol and the sedimentation rate of the aerosol. Diffusional losses of aerosol to the walls of the room are neglected in this simple model as it is assumed that turbulent diffusion approaches zero in the laminar boundary layer of the walls and particle Brownian diffusion is insignificant for the considered sizes of aerosol particles ($> 0.5\,\mu m$). The sedimentation rate of the aerosol was taken to be the terminal velocity of the particle multiplied by the floor area and the aerosol concentration. The derived equation for the decay is given below as:

$$\frac{dC}{dt} = -\frac{(Q\,(1-R) + v_T A_{floor})}{V_{room}}\,C, \tag{2.6}$$

where C is the well-mixed aerosol concentration in the room (m^{-3}), t is time (s^{-1}), Q is the total ventilation rate of the room ($0.41\,m^3\,s^{-1}$), R is the recirculation ratio of particles in the ventilation system (unitless), v_T is the particle terminal velocity given by Equation 2.5 ($m\,s^{-1}$), A_{floor} is the total floor area of the room ($50.4\,m^2$), and V_{room} is the volume of the room ($131\,m^3$).

The theoretical decay rate for 100% recycled aerosol (R=1 in Equation 2.6, green) and 0% recycled aerosol (R=0 in Equation 2.6, red) is shown in Figure 2.8 for different particle sizes. The simulations and experiments reported in Figure 2.8 are consistent with the measurements with the aerosol source positioned in the ceiling with large aerosol particle sizes well described when assuming no recycling of aerosol (red). However, the experimental data show significant deviation from this line for small particle sizes, also consistent with the ceiling experiment and substantial recycling of small particles into the room.

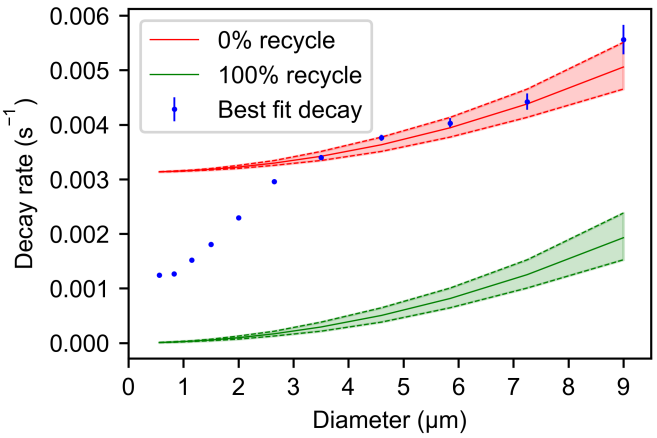


Figure 2.8: Experimental decay rates (blue) along with theoretical decay rates assuming 0% recycled particles (red, solid) and 100% recycled particles (green, solid) for different particle sizes. The error bar of the experimental data represents the standard error of the exponential fit. The error in the theoretical decay rates (distance between the two dashed lines) represents the width of the bin size of the low-cost sensors.

By using Figure 2.8, it is possible to estimate the recycle ratio of aerosol based on the decay rate model (Equation 2.6), which is presented in Figure 2.9. A line (red) was fitted to the calculated recycling ratios using Equation 2.6 (blue crosses) and, as expected, the amount of recycled aerosol increases as the particle size decreases since smaller particles more efficiently pass through the ventilation filter. An important consequence of Figure 2.9 is that the decay rate of aerosols cannot be simply predicted by using the air changes of the room. The CFD flow field may be recalculated using these recycling ratios to deliver an experimentally informed model, as seen in the next section.

2.4.2.3 Experimentally Informed Computational Model

The flow field was recalculated using the experimentally determined recycling ratios plotted in Figure 2.9. The results from the revised model for 2.0 µm particles at nodes 1 and 12 are presented in Figure 2.10, which can be compared directly to the results of the model that ignores recirculation (see Figure 2.7). This comparison shows that the model with recirculation of aerosol matches the experimental data much better than the model without recirculation, especially in the time region after 55 minutes. The experimentally informed model predicts a slower decay rate of aerosol particle concentration due to the recycled aerosol.

Figure 2.11 shows the effect of aerosol size on aerosol dispersion in the room. Figure 2.11a shows the temporal response for the concentration of 1.5 µm particles and Figure 2.11b that of 7.25 µm particles. For 7.25 µm particles, the aerosol

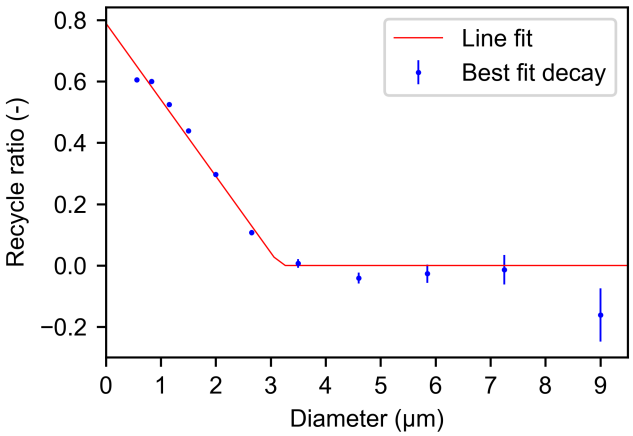
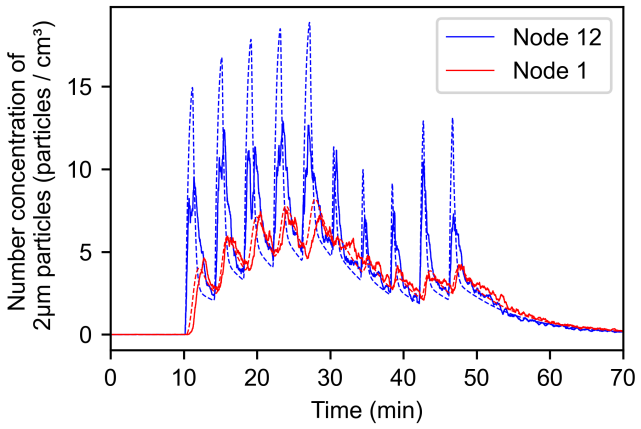


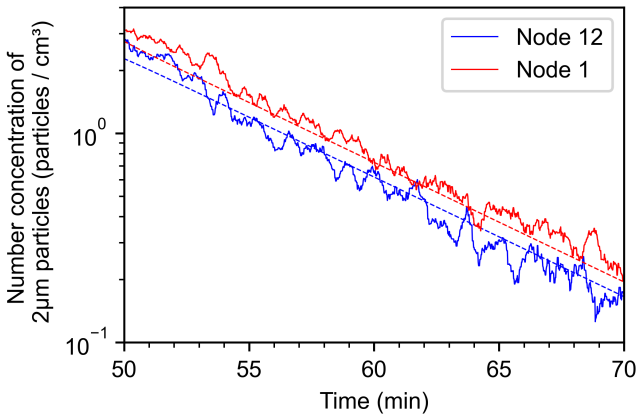
Figure 2.9: Calculated recycling ratios (blue) as a function of particle size based on results of Figure 2.8, and best fit line (red) used in the computations with the Experimentally Informed CFD Model. Arrow heads represent the uncertainty. For the linear portion $r^2 = 0.97$.

concentration does not rise as much compared to the 1.5 µm particles due to the slower decay rates of 1.5 µm particles and fewer 7.25 µm generated.

Aerosol mass concentration is a key parameter used to quantify air quality. Figure 2.12 shows the measured PM_{10} (total particle mass of all particles less than 10 µm in diameter) temporal responses across the low-cost sensor network and the comparison to model predictions. When comparing aerosol concentrations between experiment and simulation there are two types of error to consider, these are temporal errors and concentration errors. Quantitative assessments of the accuracy of the simulations have not been undertaken as it would mean assigning a weight to these two errors. However, it is still possible to draw conclusions from these data by qualitatively comparing the location and strength of the pulses and their decays. We observe very good agreement between model and experiment for all sensors; both long-term decay rate and short-term diffusion of the aerosol are well captured for all measurement nodes and the duration of the pulses causing different magnitude peaks is also well captured. There are four locations, which show the worst temporal and pulse strength match between model and experiments, which are nodes 6, 7, 10 & 11. These nodes are located at the centre of the room (Figure 2.3) where the two large airflow vortical structures, generated from the inlet swirl diffusers, interact. It is not surprising that this location has the lowest agreement with experimental data since the simplicity of the CFD calculation does not capture the complexity of the local flow. The mixing at this central region of the airflow is perhaps not captured well by a RANS k-epsilon model. However, it is more likely that this is caused by the lack of some geometrical features of the room in the computational domain, which existed in the experiment



(a)



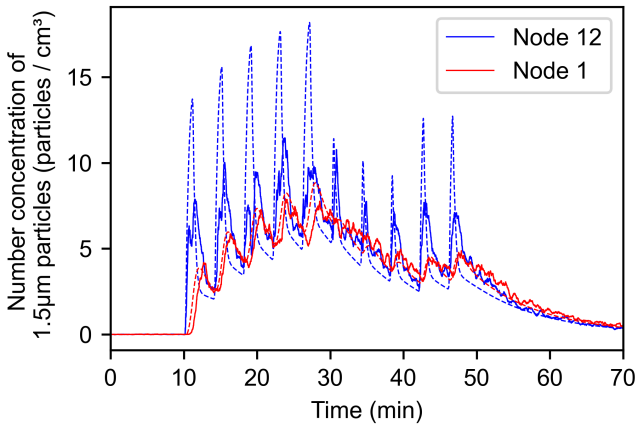
(b)

Figure 2.10: Model (dashed) and experimental (solid) temporal responses for the concentration of the 2.0 µm particles for Node 12 (blue) and Node 1 (red). This model uses the recycling ratios defined in Figure 2.8. Model and experimental values were scaled together by matching their median values. (a) Shows the full response (b) Shows the response after 50 minutes on a logarithmic scale.

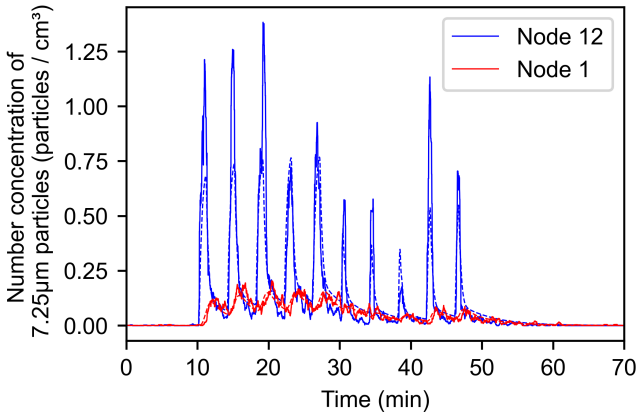
such as tables and chairs. Another area of interest are nodes 3, 4 & 5 compared to their counterparts 1, 2 & 15. The left-hand side of the room (Figure 2.3) has worse agreement with experimental results than the right-hand side. This could be due to the slight off-centre outlet (Figure 2.3) or more likely the combined rotational velocities of both diffusers being better captured on the right hand side.

2.4.3 Discussion

When experimental data are used to inform the computational model on the recycling ratios in the room from the ventilation system, the agreement between model and experiments is very good in both space and time (Figure 2.12). This provides evidence that the proposed simplified approach for the CFD calculation of the air flow and aerosol transport is sufficient to predict aerosol transport in



(a)



(b)

Figure 2.11: Time-dependent experimental measurements (solid) and model predictions (dashed) of aerosol number concentration at Node 12 (blue) and Node 1 (red) for (a) 1.5 µm and (b) 7.25 µm particles.

large spaces, at least as large as the room size of the current study. From our results, we see that proximity to the initial aerosol injection event results in extreme maximum aerosol exposure that quickly dissipates. A more surprising result is the amount of time that aerosols reside in the room. For a ventilation rate of 11.3 ACH, it takes around 30 mins for concentration levels of 2 µm to reach 5% of the peak (based on decay rate in Figure 2.8), and therefore everyone in the room would have significant exposure to the initial aerosol injection event. This is longer than what simple calculation would predict, and this behaviour could provide better models for exposure and disease transmission risks. However, it is noted that the experimentally evaluated recycling ratio depends on the geometry of the room and the ventilation system and this evaluation must be repeated for different geometries.

Many existing computational studies of aerosol transport do not investigate the effect of particle size on aerosol transport. Figures 2.8 and 2.11 demonstrate that

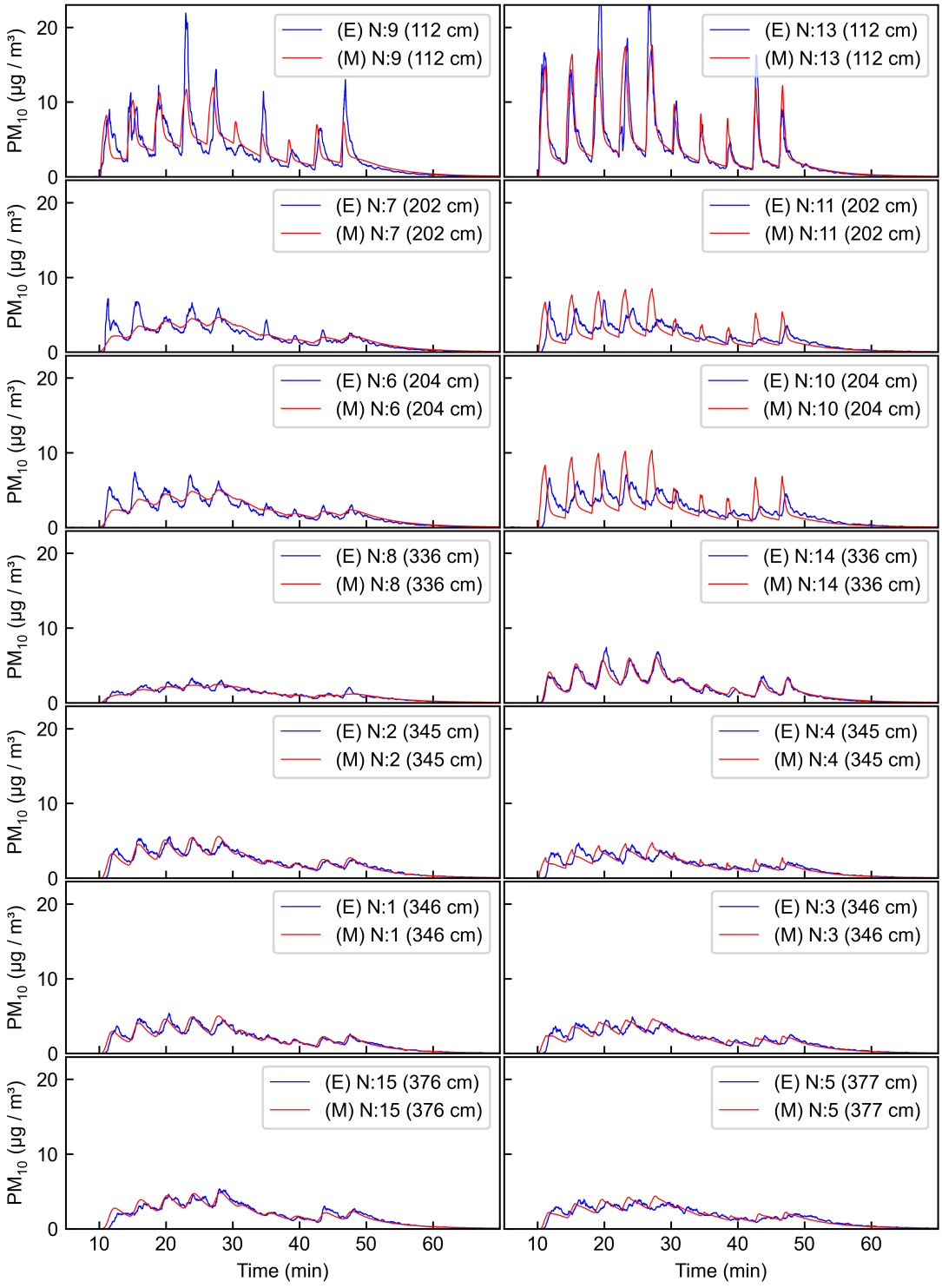


Figure 2.12: Showing PM_{10} for all nodes (except Node 12). Nodes are ordered based on distance from the aerosol generator. Blue (E) lines are the experimental values, orange (M) lines are the CFD model with recycling. All graphs have the same axis scales.

particle size has a significant effect on dispersion and decay rates. Consequently, the effect of particle size should not be neglected in computational models. In our

experimental setup, there are two reasons for the large differences between the behaviour of different aerosol particle sizes. Under a fixed ventilation rate, aerosol dispersion for particle diameters greater than 3 µm is dominated by the varying sedimentation rate with size (Figure 2.8). However, for diameters less than 3 µm, the variable recycling rates of aerosols in the ventilation ducting accounts for the large variation in the aerosol dispersion for different particle sizes. There is no simple way to estimate aerosol recycling ratios without an experimental measurement. Based on pure airflow measurements, we might expect all aerosols to have a recycling ratio of R=0.34, (7.5 ACH outside air, 11.3 ACH total ventilation). However, based on Figure 2.9, the recycling ratios of aerosols for this room vary between R=0.6 and R=0.0 depending on particle size. By observing Figure 2.1, it is possible to reason that most of the aerosol is expected to enter the heat pump inlet due to the placement of the room outlet. In hindsight, this is a poor design in terms of aerosol filtration as it allows higher recycling of aerosol than air. The decline of the recycling ratio of aerosol down to R=0.0 is most likely due to some internal filtration in the heat pump unit, however no specifications for the heat pump were found. This lack of specification is common for most ventilation systems, as manufacturers do not need to provide detailed filtration specifications. These results provide significant conclusions for future aerosol dispersion CFD modelling, indicating that any simulations performed without experimental verification or extensive filtration and ventilation information may be invalid. This size dependent recycle is unlikely to be significant for rooms with industrial ventilation with HEPA filters, but, for typical rooms, such as workspace offices and classrooms, this effect should not be ignored.

Subsequent work should focus on applying and verifying this combined experimental and modelling approach to other test rooms, such as larger rooms with more complex ventilation arrangements. Our approach was computationally efficient due to the steady velocity calculation and the simplicity of the aerosol transport model. Thus, it is well suited for spaces even larger than the room of the current study, and as the transport of aerosol is largely dominated by turbulent diffusion, high resolution in the velocity is not required. Additional work could develop a disease transmission risk based on the room and exposure times, evaluating the effectiveness of practices such as the 2-meter rule. More research should be performed to consider different ventilation rates, assessing the effectiveness of reducing aerosol dispersion and exposure. Finally, to reduce the computational costs and simplify the analysis, we assumed that the aerosol was already dry with no diameter change due to evaporation. Aerosol generated by vocalization contain water and salts and undergo some evaporation upon initial discharge depending on particle size and RH. As such the experiment should also be repeated with lower

salt concentrations and the computations repeated with evaporation included.

2.5 Conclusion

A combined experimental and computational approach has been developed to predict aerosol dispersion around a room. It is possible to predict the temporal and spatial aerosol concentrations within the room for different particle sizes with good accuracy. The results show that depending on location within the room the peak concentration of aerosol can be many times more than the average concentration. Additionally, depending on room layout, the number of air changes per hour may not be representative of the decay rate of aerosol particles, as they may be recycled, and this recycling ratio depends on size. This shows that the number of air changes per hour is an insufficient metric for determining the safety of a room in terms of disease transmission unless additional information about air filtration is known. This study also shows that modelling aerosols as a pure scalar is insufficient for large particles because over long times (hours), sedimentation can play a major role.

After studying aerosol dispersion in ventilated rooms, the next logical step is to explore the broader principles governing particle behaviour in turbulent flows. This leads to the investigation of particle preferential concentration, which also affects aerosol dispersion in various environments. The study shifts focus from a specific real-world setting (a classroom) to the underlying turbulence dynamics that influence aerosol behaviour, which will be explored using both Eulerian and Lagrangian methods.

Chapter 3

Spectral Characteristics of Particle Preferential Concentration in Turbulence Computed by Eulerian and Lagrangian Methods

This work is published in Downing and Hardalupas [41], it has been adapted to form the basis of this Chapter.

3.1 Abstract

This study conducts a comprehensive analysis of the Fourier spectra characteristics of particle preferential concentration in turbulent flows obtained by Eulerian and Lagrangian modelling approaches for different Stokes numbers. Particle preferential concentration is characterized by clusters and voids in the spatial particle distributions formed in turbulent flows and can significantly influence processes such as droplet coalescence, evaporation, and gas-particle reactions. The research primarily focuses on comparing the performance of two Eulerian models (one with and one without second-order velocity moments) and one Lagrangian model, which are used to predict particle dispersion. Key findings include the impact of artificial diffusion in Eulerian methods, the superiority of methods incorporating second-order velocity moments contributions at higher Stokes numbers, and the sensitivity of the Lagrangian method to Poisson statistics. Notably, the study reveals minimal variation in mean velocity spectra across different Stokes numbers, as opposed to the marked variations in particle concentration, momentum, and energy spectra. Grid resolution emerges as a crucial factor in enhancing spectral energy predictions in Eulerian methods. The research underscores the nuanced

distinctions between Eulerian and Lagrangian methods in modelling preferential concentration, providing a detailed spectral comparison of particle concentration, velocity, momentum, and energy, highlighting the importance of method selection based on specific modelling needs.

3.2 Introduction

Droplets or particles dispersing in turbulent flows often form clusters of high concentration and voids of low concentration at various locations. This phenomenon, known as preferential concentration, results from droplet inertia causing deviations from background fluid streamlines, a process influenced by factors such as particle size and fluid properties [154]. This phenomenon is critical in many natural and industrial processes, such as rain formation, powder manufacturing, and others that depend nonlinearly on particle concentration. For instance, the general aerosol dynamic equation (GDE), which describes the evolution of a droplet size distribution [55], highlights the impact of non-uniform particle concentration profiles. Additionally, preferential concentration significantly influences processes like droplet coalescence in clouds [163, 150, 95], droplet evaporation or condensation [137, 145], and gas-particle phase reactions [70].

The aim of this research is to compare the effectiveness of three distinct modelling approaches (two Eulerian and one Lagrangian) in predicting key properties of particle preferential concentration. While the study includes traditional analysis of particle concentration spectra, it also extends current understanding to explore the Fourier spectra of additional properties such as particle momentum, mean velocity, total energy, and velocity fluctuations. This extension offers a more nuanced comparison of the methods used and the dynamics at play. We will assess the effects of artificial diffusion and Stokes number variability on these properties, with a focus on the contributions of second order velocity contributions in Eulerian methods. The influence of computational grid resolution on spectral energy predictions in Eulerian simulations will also be investigated, further enriching the scope of our analysis.

Simulations of particle preferential concentration in turbulent flows employ either Lagrangian or Eulerian methods. The Lagrangian approach tracks the path of individual particles, offering a closer representation of reality and has been popular for preferential concentration calculations. However, it faces limitations such as statistical uncertainty due to a limited number of computational particles and computational inefficiencies from the required interpolation onto the carrier fluid to extract fluid velocities. In contrast, Eulerian methods, which handle concentration or probability fields rather than individual particles, offer computational

efficiency and are better suited for two-way coupling between the particulate and carrier phases. This is largely due to the ease of computing momentum transfer when the grids for both phases align. Despite their efficiency, Eulerian methods have a notable disadvantage: they cannot fully capture the same physical system as Lagrangian methods, especially in terms of individual particle dynamics.

The choice of numerical schemes in Eulerian methods, though often overlooked in published research, plays a crucial role in determining the accuracy of the obtained results. A key factor to consider is the physical diffusion of particles in air, which can be significantly small for larger particle sizes [35]. This leads to the Schmidt number for the particles being orders of magnitude greater than unity, implying negligible physical diffusion in the particle phase, as opposed to the carrier phase. This discrepancy can cause the partial differential equations used in modelling to become numerically unstable, a challenge often not addressed in studies employing Eulerian methods. While Direct Numerical Simulation (DNS) is effective for simulating the carrier fluid down to energy dissipation scales due to viscosity, its application to the particulate phase is hindered by the much smaller relevant scales, rendering DNS impractical. Large Eddy Simulation (LES) provides an alternative approach by resolving the larger turbulent scales while modelling the smaller subgrid-scale motions. This significantly reduces computational cost compared to DNS while still capturing key turbulent structures. However, LES introduces additional modelling uncertainties in the subgrid-scale turbulence and may struggle with accurately representing small-scale particle dynamics.

To counter this, various techniques have been developed for simulating advection in the absence of physical diffusion. One such technique is artificial diffusion [173], which introduces a minimal level of diffusion into the physical equations to attain numerical stability. Although this approach dampens higher wavenumber fluctuations, enabling the use of high-order methods like pseudo-spectral methods, the accuracy of simulations heavily relies on the chosen value of artificial diffusivity, potentially diminishing the benefits of high-order numerical schemes.

Another approach involves upwind-biased schemes. The only linear upwind scheme that guarantees stability is the first-order scheme [56], which, however, introduces substantial numerical diffusion. More advanced non-linear upwind schemes, such as Total Variation Diminishing (TVD) or Weighted Essentially Non-Oscillatory (WENO) schemes, can achieve higher accuracy in regions with smooth solutions [98]. However, in the vicinity of shocks, these schemes revert to lower order accuracy. The complexity increases for advection problems involving energy or second-order moments of velocity, where multiple velocities need to be considered for different advected quantities. One solution to this multi-velocity challenge is solving a localized Riemann problem, where all velocities are addressed

using upwinding. The Roe Flux-Difference method [140] is an example of such an approach.

Many Eulerian methods only provide a single velocity for the particulate phase in each grid cell [69]. Whilst these methods are computationally cheaper, they fail to capture a key phenomenon with particle transport, which is the crossing trajectories of some particles. Crossing trajectories occurs when two particles can be very close to each other (even at the same location if collisions are not modelled) but have different velocities [87]. To address this limitation, an anisotropic Gaussian closure model was developed for simulating the particulate phase which also transports the second order velocity moments thus allowing for crossing trajectories [167]. These detailed Eulerian methods are refereed mesoscopic approaches and variations have been developed [51] and tested [88, 90].

The mechanisms driving the clustering of inertial particles in fluid flows are complex and influenced by various factors, including the Stokes and Reynolds numbers. One common effect observed in flows with a mean component is centrifuging. In the context of turbulence, Coleman and Vassilicos [32] proposed the 'sweep-stick' mechanism. This mechanism suggests that particles are swept along with and get stuck to the acceleration stagnation points of the fluid. However, an alternative perspective is offered by Bragg et al. [23], whose analysis also applies to arbitrary spatially correlated velocity fields. Crucially, their findings challenge the scale invariance of the radial distribution function, offering a different view on the underlying processes of particle clustering.

Several methods are available for analysing and quantifying preferential concentration. Among these, radial distribution functions (RDFs) are commonly used, providing valuable insights into the structural aspects of clustering. RDFs are particularly applicable to both empirical and theoretical models at lower Stokes numbers [5, 4, 14, 148, 31, 177]. However, RDFs are not without limitations. They typically focus on pairwise interactions and often assume spherical symmetry, neglecting the factor of shape. To address this, some studies employ angular distribution functions, offering a more comprehensive perspective on particle interactions [61].

Voronoi tessellation is another technique used in this field. It involves assigning volumes around individual particles and is particularly favoured in experimental methods and numerical simulations. These assigned volumes are used to calculate local particle concentrations, identify clusters, and measure concentration variance [124, 114, 157, 6].

Additionally, spectral methods offer a distinct approach. These methods can be further divided into Fourier and wavelet transforms. Fourier transforms, used in various studies [104, 146, 69, 3], focus on the power spectra of particle densities,

effectively delineating the length scales of particle clusters. While Fourier transforms provide a global overview and are relatively straightforward to interpret, wavelet transforms, employed in other research [10, 106], offer localized insights, presenting more detailed data.

In this study, we employ an analytical approach akin to that used by Haugen et al. [69], concentrating on comparing the particle concentration spectra in preferential concentration scenarios. Our analysis involves both Eulerian and Lagrangian methods set against the backdrop of periodic DNS homogenous isotropic turbulence. While focusing on incompressible turbulence, we broaden the scope of the Eulerian method by incorporating a model that accounts for second-order velocity moments, utilizing an anisotropic Gaussian approach. This enhancement is crucial for accurately capturing the crossing trajectories phenomenon.

Kong et al. [90], conducted a similar investigation employing an anisotropic Gaussian model. However, their study did not examine the impact of varying Stokes numbers on model performance, nor did it provide spectra for particle velocity fluctuations. These aspects are essential for understanding the conditions under which such models are necessary and effective. Our study aims to fill these gaps by offering a more comprehensive analysis of model performance across different Stokes numbers, including spectra for particle velocity fluctuations.

Furthermore, our investigation goes beyond particle concentration spectra, encompassing additional properties such as particle velocity and momentum. This comprehensive approach allows for a more thorough assessment of the Eulerian method's capabilities. We also introduce a numerical scheme based on the Roe Flux-Difference with TVD, offering an approach to address the complexities inherent in these simulations. This method is compared to Lagrangian results in 3D homogenous isotropic turbulence, focusing on one-way coupling. A key aspect of our comparison is the particle concentration spectra from different methods, providing valuable insights into the accuracy of each method across various length scales.

3.3 Numerical Method

3.3.1 Carrier Fluid Simulations

The carrier fluid simulations are conducted using the incompressible Navier-Stokes equations, augmented with a forcing term to achieve stationary homogenous isotropic turbulence. A linear forcing function, directly proportional to the velocity, was selected for its ease of implementation and physical relevance [100]. The initial velocity field introduces randomness to the turbulence. With the application of

linear forcing, the longer velocity waves become unstable and do not settle into any equilibrium state. This ensures that the velocity field maintains an appropriate level of randomness [100]. The governing equations, expressed in Einstein notation, are as follows:

$$\frac{\partial u_i}{\partial t} + \frac{\partial u_i u_j}{\partial x_j} = -\frac{1}{\rho_f}\frac{\partial p}{\partial x_i} + \nu\frac{\partial^2 u_i}{\partial x_j^2} + \frac{\varepsilon}{\langle u_j^2 \rangle}u_i, \tag{3.1}$$

$$\frac{\partial u_j}{\partial x_j} = 0, \tag{3.2}$$

where u_i represents the carrier fluid velocity in the i-th direction, x_i is the spatial coordinate in the i-th direction, t denotes time, ρ_f is the carrier fluid density, p the pressure, ν the kinematic viscosity, and ε the mean turbulent kinetic energy dissipation rate. The summation is over the index j, and angled brackets denote a spatial average.

Throughout the simulation, the mean turbulent kinetic energy dissipation rate (ε), the fluid density (ρ_f), and the kinematic viscosity (ν) are kept constant. The carrier fluid simulation, which is executed independently of the particulate phase due to one-way coupling, is stored for subsequent analysis. These simulations are performed in a three-dimensional periodic cube with side length L. The pseudo-spectral method is employed for the carrier fluid, utilizing N equidistant grid points in each direction, resulting in a grid spacing Δ. A crucial parameter in turbulence simulations is the Kolmogorov length scale, η. To meet the criteria for Direct Numerical Simulation (DNS), the ratio η/Δ should be greater than 0.45 [130]. The specific details of the simulation setup are: $Re_\varepsilon = L^{\frac{4}{3}}\varepsilon^{\frac{1}{3}}/\nu = 1500$, $Re_\lambda = 45.9$, $N = 256$, $\Delta/L = 3.90 \times 10^{-3}$, $\eta/L = 4.14 \times 10^{-3}$, and $L_{Int}/L = 0.12$, where L_{Int} is the integral length scale.

Figure 3.1 presents a 2D slice extracted from this simulation, illustrating the instantaneous kinetic energy distribution. This serves as an exemplar of the fluid flow characteristics within the simulation.

3.3.2 Particle Simulations

3.3.2.1 Lagrangian Simulations

The Lagrangian particle simulations are conducted under the assumption of one-way coupling. The particles are treated as point spheres with negligible mass loading, and the influence of gravity is not considered. The Stokes drag model is employed as the friction model. Based on these assumptions, the equations of motion for an individual particle are formulated as follows:

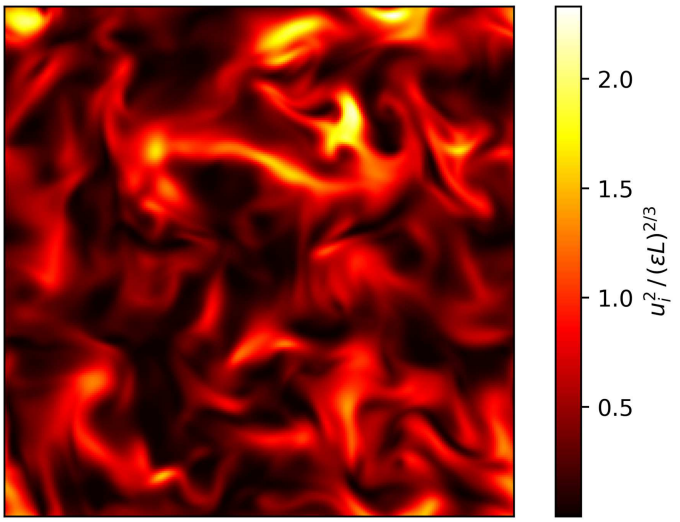


Figure 3.1: An example instantaneous kinetic energy distribution in a 2D slice of a 3D Direct Numerical Simulation (DNS) fluid simulation at $Re_\varepsilon = 1500$.

$$\frac{dx_{p,i}}{dt} = v_{p,i}, \tag{3.3}$$

$$\frac{dv_{p,i}}{dt} = \frac{1}{\tau_p}\left(u_i - v_{p,i}\right), \tag{3.4}$$

$$\tau_p = \frac{\rho_p d^2}{18\rho_f \nu}, \tag{3.5}$$

where $x_{p,i}$ denotes the position of an individual particle p in the spatial coordinate i, $v_{p,i}$ represents the velocity of the particle p in the same coordinate, τ_p is the particle relaxation time, ρ_p the particle material density, and d the particle diameter.

The Stokes number Stk of a particle is defined as the ratio of the particle relaxation time τ_p to a characteristic timescale of the carrier fluid. For the scaling of particle preferential concentration, the Kolmogorov timescale τ_η is often used as this characteristic timescale and Stk is defined in Equation 3.6.

$$Stk = \frac{\tau_p}{\tau_\eta} = \tau_p\sqrt{\frac{\varepsilon}{\nu}} \tag{3.6}$$

3.3.2.2 Eulerian Conservation Equations

The developed Eulerian simulations are based on the conservation of properties from an ensemble of particles with the same mass and diameter within a control volume. In all subsequent equations, physical diffusion has been omitted under the assumption that all particles exhibit large Schmidt numbers, as per Cunningham

[35]. If many particles are present within a control volume, then the conservation of particle number density is:

$$\frac{\partial n}{\partial t} + \frac{\partial n\overline{v_j}}{\partial x_j} = 0, \tag{3.7}$$

where n is the number density of particles within a control volume and v_j is the velocity of the particulate phase. $\overline{v_j}$ represents a conditioned average over all the realisations of different particle instances present at that location in space [51]. The conservation of momentum is considered next. Temporarily ignoring the momentum transfer between the particulate phase and the carrier phase we have:

$$\frac{\partial n\overline{v_i}}{\partial t} + \frac{\partial n\overline{v_i v_j}}{\partial x_j} = 0, \tag{3.8}$$

many Eulerian methods treat $\overline{v_i v_j}$ as $\overline{v_i}\,\overline{v_j}$ which neglect the conservation of the higher moments of particle velocity. This can be a good approximation for small particle sizes and reduces computational complexity but, for large sizes, can give inaccurate results for the formation of clusters and voids in a turbulent flow. To conserve the second moment of particle velocity another set of conservation equations are required, these can be thought of as conservation of 'directional' kinetic energy:

$$\frac{\partial n\overline{v_i v_k}}{\partial t} + \frac{\partial n\overline{v_i v_k v_j}}{\partial x_j} = 0, \tag{3.9}$$

$$\frac{\partial n\overline{v_i v_k}}{\partial t} + \frac{\partial \left(n\overline{v_i v_k}\,\overline{v_j} + n\overline{v_i v_j}\,\overline{v_k} + n\overline{v_j v_k}\,\overline{v_i} - n\overline{v_i}\,\overline{v_k}\,\overline{v_j}\right)}{\partial x_j} = 0, \tag{3.10}$$

Equation 3.9 leads to a moment closure problem, as each transport of the velocity moment requires information about the higher moments. By assuming that the 3rd order fluctuations are negligible and taking them to be zero, Equation 3.9 can be turned to Equation 3.10, making the system of equations closed. Equations 3.7, 3.8 & 3.10 form a system of 10 partial differential equations in 3D space. We now introduce the conserved quantities for the particulate phase, namely the particle number density n, the particle momentum p_i in direction i, and the particle 'directional' kinetic energy E_{ik} in directions i & k, which are defined as:

$$p_i = n\overline{v_i}, \tag{3.11}$$

$$E_{ik} = \frac{1}{2} n\overline{v_i v_k}, \tag{3.12}$$

substituting Equations 3.11 & 3.12 into Equations 3.7, 3.8 & 3.10 as well as

including the contributions of Stokes drag to the conservation of particle momentum and particle 'directional' kinetic energy, the final conservation equations used become:

$$\frac{\partial n}{\partial t} + \frac{\partial p_j}{\partial x_j} = 0, \tag{3.13}$$

$$\frac{\partial p_i}{\partial t} + \frac{\partial 2E_{ij}}{\partial x_j} = \frac{nu_i}{\tau_p} - \frac{p_i}{\tau_p}, \tag{3.14}$$

$$\frac{\partial E_{ik}}{\partial t} + \frac{\partial \left(\frac{nE_{ik}p_j + nE_{ij}p_k + nE_{jk}p_i - p_i p_j p_k}{n^2} \right)}{\partial x_j} = \frac{p_k u_i + p_i u_k - 4E_{ik}}{2\tau_p}, \tag{3.15}$$

equations 3.14 and 3.15 show that higher orders of velocity moments decay faster. Specifically, Equation 3.14 features a decay coefficient of $1/\tau_p$ whereas Equation 3.15 is characterized by a higher decay coefficient of $2/\tau_p$. This pattern continues with each successive higher order moment of velocity, where the decay coefficient increases incrementally. For example, third-order moments would have a decay coefficient of $3/\tau_p$, and so on. This provides evidence that at small Stokes numbers the 'directional' kinetic energy terms can be neglected as the velocity fluctuations will decay very quickly. For intermediate Stokes numbers, it also suggests that neglecting the 3rd order velocity moments is an appropriate assumption as these moments will decay even faster.

One method to stabilize the numerical calculations for the equations involves the use of explicit artificial diffusion. However, as outlined in the introduction, the Roe-flux numerical scheme chosen for this study inherently ensures stability through upwind biasing. Therefore, the stabilization is not dependent on the Stokes number, since the diffusion effect is implicitly managed by the numerical scheme. The Roe-flux scheme can be used with or without the 'directional' kinetic energy terms.

3.3.2.3 Eulerian Roe-Flux Splitting

The numerical method developed for the particulate phase conservation equations is an adaptation of the Roe-flux difference method [140]. This method ensures the correct upwind procedure is followed, even though there are multiple 'speeds' potentially travelling in different directions due to the presence of the particle 'directional' kinetic energy. In general, Roe-flux methods have the following procedure in 1D advection problems:

$$\frac{\partial \boldsymbol{U}}{\partial t} + \frac{\partial \boldsymbol{F}}{\partial x} = 0, \tag{3.16}$$

$$\frac{\partial \boldsymbol{U}}{\partial t} \approx \frac{1}{\Delta}\left(\boldsymbol{F}_{i+\frac{1}{2}} - \boldsymbol{F}_{i-\frac{1}{2}}\right), \tag{3.17}$$

$$\boldsymbol{F}_{i+\frac{1}{2}} = \frac{1}{2}\left(\boldsymbol{F}^{L}_{i+\frac{1}{2}} + \boldsymbol{F}^{R}_{i+\frac{1}{2}}\right) - \frac{1}{2}\left|\mathbf{A}_{i+\frac{1}{2}}\right|\left(\boldsymbol{U}^{R}_{i+\frac{1}{2}} - \boldsymbol{U}^{L}_{i+\frac{1}{2}}\right), \tag{3.18}$$

where $\boldsymbol{U}$ is a vector of conserved variables, $\boldsymbol{F}$ is a vector of the fluxes of the conserved variables, subscripts $i+\frac{1}{2}$ represents the boundary between grid cell i and $i+1$, superscripts L and R represents the quantity calculated on the left- or right-hand side of the boundary, and $\mathbf{A}_{i+\frac{1}{2}}$ is a Jacobian of the system that is calculated from the left and right fluxes. The vertical bars are an operation that diagonalizes the matrix, takes the absolute values of the eigenvalues, and then reforms the matrix. The Jacobian needs to satisfy three conditions to solve the localised Riemann problem, it needs to be diagonalisable with real eigenvalues, the scheme should be conservative, and it needs to be consistent with the initial problem [140]. These are summarised below:

$$\mathbf{A}_{i+\frac{1}{2}} = \mathbf{P}_{i+\frac{1}{2}}\mathbf{\Lambda}_{i+\frac{1}{2}}\mathbf{P}^{-1}_{i+\frac{1}{2}}, \tag{3.19}$$

$$\boldsymbol{F}^{R}_{i+\frac{1}{2}} - \boldsymbol{F}^{L}_{i+\frac{1}{2}} = \mathbf{A}_{i+\frac{1}{2}}\left(\boldsymbol{U}^{R}_{i+\frac{1}{2}} - \boldsymbol{U}^{L}_{i+\frac{1}{2}}\right), \tag{3.20}$$

$$\mathbf{A}_{i+\frac{1}{2}} = \frac{\partial \boldsymbol{F}}{\partial \boldsymbol{U}} \quad \text{if} \quad \boldsymbol{U}^{R}_{i+\frac{1}{2}} = \boldsymbol{U}^{L}_{i+\frac{1}{2}}, \tag{3.21}$$

whilst these equations are only given for one dimension, it is easy to expand them to three dimensions with the use of operator splitting. The form of matrix $\mathbf{P}$ and $\mathbf{\Lambda}$ for the particulate phase conservation equations is given in Appendix A. This yields a numerically stable scheme that is upwind biased. The choice of how to calculate $\boldsymbol{U}^{R}_{i+\frac{1}{2}}$ and $\boldsymbol{U}^{L}_{i+\frac{1}{2}}$ determines the order of accuracy of the scheme and the effect of numerical diffusion. A simple choice of scheme that results in first order accuracy is $\boldsymbol{U}^{R}_{i+\frac{1}{2}} = \boldsymbol{U}_{i+1}$ and $\boldsymbol{U}^{L}_{i+\frac{1}{2}} = \boldsymbol{U}_{i}$. For a simple scalar advection case, it can be shown that this Roe-Flux scheme is equivalent to the first order upwind scheme. We choose a TVD flux limiting scheme that increases the order of accuracy to second order in regions of smooth solutions whilst still providing numerical stability. An overview of the scheme is given below [139]:

$$\boldsymbol{U}^R_{i+\frac{1}{2}} = \boldsymbol{U}_i - \frac{1}{2}\phi\left(r_{i+1}\right)\left(\boldsymbol{U}_{i+2} - \boldsymbol{U}_{i+1}\right), \tag{3.22}$$

$$\boldsymbol{U}^L_{i+\frac{1}{2}} = \boldsymbol{U}_i + \frac{1}{2}\phi\left(r_i\right)\left(\boldsymbol{U}_{i+1} - \boldsymbol{U}_i\right), \tag{3.23}$$

$$r_i = \frac{\boldsymbol{U}_i - \boldsymbol{U}_{i-1}}{\boldsymbol{U}_{i+1} - \boldsymbol{U}_i}, \tag{3.24}$$

$$\phi\left(r\right) = \max\left[0, \min\left(2r, 1\right), \min\left(r, 2\right)\right], \tag{3.25}$$

The grid choice for the Roe-Flux method is an important consideration. A simple first approach is to use the same grid as the carrier fluid simulation, eliminating the need for interpolation of the carrier fluid velocities to the particulate phase. Figure 3.8, discussed in detail in Section 3.4, shows a brief sensitivity analysis of the grid size on the particle number density.

3.4 Results

In the subsequent section, we compare the performance of the anisotropic gaussian Eulerian method for the particulate phase with that of a standard Lagrangian method and another Eulerian method that does not include 'directional' kinetic energy terms. For details on the carrier flow simulations, refer to 3.3.1. The comparison begins with a qualitative assessment, where we visually analyse slices of the particle number density generated by each method. Additionally, an error metric δ is employed for a more quantitative evaluation, defined as:

$$\delta = \sqrt{\langle\langle (n - n_L)^2 \rangle\rangle}, \tag{3.26}$$

in this context, n_L represents the number density calculated using the Lagrangian approach. The metric δ calculates the root mean squared error between the number density n obtained by a given method and a reference number density n_L derived from the Lagrangian approach. The Lagrangian method is also subjected to this error metric by running a second Lagrangian simulation with the same carrier fluid but different initial random particle placements. This allows us to quantify the inherent variance of the Lagrangian method due to random Poisson statistics. Since different realisations of the Lagrangian simulation—with identical flow fields but varying initial particle distributions—naturally produce fluctuations in number density, the expected error between such realisations is approximately 1.0. This serves as a baseline, indicating the level of variation introduced purely by randomness. A value significantly lower than 1.0 would be unexpected, as it would suggest a level of agreement beyond the statistical vari-

ance of the method itself. The error δ could be reduced by increasing the number of simulated particles, thereby decreasing statistical noise.

The Lagrangian simulation utilized 167 million particles. Following this, we compare the particle number density spectra of the different methods, which is defined as:

$$\left\langle\left\langle n^2 \right\rangle\right\rangle = \int_0^\infty \mathrm{E}_n(\kappa)\mathrm{d}\kappa, \tag{3.27}$$

here, κ represents the wavenumber, and $\mathrm{E}_n(\kappa)$ is the spectral energy encompassing all contributions between κ and $\kappa + \mathrm{d}\kappa$. Four distinct Stokes numbers (0.5, 1.0, 2.0, and 5.0) are simulated to cover a broad range of particle behaviour, facilitating a comprehensive comparison of the methods. The same carrier fluid simulation is used for each particulate phase simulation, ensuring consistency and ease of comparison across different methods and Stokes numbers. Other spectra are also investigated such as the particle momentum $\mathrm{E}_p(\kappa)$, velocity $\mathrm{E}_v(\kappa)$, energy $\mathrm{E}_E(\kappa)$, and energy fluctuations $\mathrm{E}_C(\kappa)$, which are defined as:

$$\left\langle\left\langle p_x^2 + p_y^2 + p_z^2 \right\rangle\right\rangle = \int_0^\infty \mathrm{E}_p(\kappa)\mathrm{d}\kappa, \tag{3.28}$$

$$\left\langle\left\langle v_x^2 + v_y^2 + v_z^2 \right\rangle\right\rangle = \int_0^\infty \mathrm{E}_v(\kappa)\mathrm{d}\kappa, \tag{3.29}$$

$$\left\langle\left\langle E_{xx}^2 + E_{yy}^2 + E_{zz}^2 \right\rangle\right\rangle = \int_0^\infty \mathrm{E}_E(\kappa)\mathrm{d}\kappa, \tag{3.30}$$

$$\left\langle\left\langle \left(E_{xx} - \frac{p_x^2}{n} \right)^2 \right\rangle\right\rangle = \int_0^\infty \mathrm{E}_C(\kappa)\mathrm{d}\kappa, \tag{3.31}$$

Computing spectra for Eulerian simulations is straightforward, thanks to the regular mesh on which these simulations are conducted. We directly perform the Fourier transform on this mesh using the fast Fourier transform (FFT) method, which efficiently provides us with all the necessary wavenumbers. In contrast, computing spectra from Lagrangian simulations offers different approaches. A common method is to take a box-averaged value or to 'bin' the particles into a mesh, as discussed by Jin et al. [86]. This approach creates a number density field from the Lagrangian data, allowing the Fourier transform to be applied using FFT. This technique is also beneficial for obtaining spectra of other properties such as momentum and energy, as these too can be 'binned' similarly. Haugen et al. [69] introduced a correction method for spectra derived from the FFT of Lagrangian simulations, aimed at eliminating the impact of white noise on the number density spectra. This technique has not been incorporated into the current study for two main reasons. Firstly, the contribution of noise in our work is reduced owing to the

utilization of a substantial number of particles (167 million). Secondly, Haugen et al. did not detail how this correction could be applied to spectra beyond number density.

Alternatively, the particle number density spectra can be computed without discretizing it onto a mesh. This method, outlined by Matsuda et al. [104], involves modelling the particles as direct delta functions and summing their contributions in Fourier space. However, this method cannot utilize the FFT algorithm and is prohibitively slow for large numbers of particles and wavenumbers. Its distinct advantage lies in its independence from a mesh, allowing it to capture clustering on length scales much smaller than the mesh size.

Figure 3.2 showcases an example spectrum of particle number density from both Eulerian methods and the Lagrangian method, using the two approaches (box-averaged and direct Dirac delta). For lower wavenumbers (larger length scales), the two Lagrangian spectra concur, as expected. However, at higher wavenumbers (smaller length scales), the direct Dirac delta spectrum is notably more elevated due to the sub-mesh particle clustering, which the box-averaged approach filters out.

Given our interest in spectra beyond number density, the computational efficiency of the box-averaged approach, and the observation that Eulerian methods only match at lower wavenumbers (elaborated in Section 3.4.2), we have opted to use the box-averaged approach for analysing the Lagrangian spectra in our study.

3.4.1 Instantaneous Particle Concentration Spatial Distributions

Figure 3.3 displays the particle number density slices for Stokes number 0.0 (known as fluid particles) and $Re_\varepsilon = 1500$, comparing both Eulerian methods (with and without energy contributions) to the Lagrangian method. Fluid particles do not deviate from the carrier fluid streamlines and should therefore not be subjected to preferential concentration. This is clearly shown in Figure 3.3 where both Eulerian methods show a uniform particle concentration. It is also clear here to see the downside to the Lagrangian method, as what should be a uniform concentration is instead shown to be 'grainy' which is a result from the Poisson statistics and the inherent randomness of the Lagrangian method with a limited non-infinite number of particles. In practical applications, the finite number of particles can lead to "grainy" results. However, with sufficient computational resources to increase the particle count, the smoothness of the outcomes will enhance.

Figure 3.4 displays the particle number density slices for Stokes number 0.5 and $Re_\varepsilon = 1500$, comparing both Eulerian methods (with and without energy

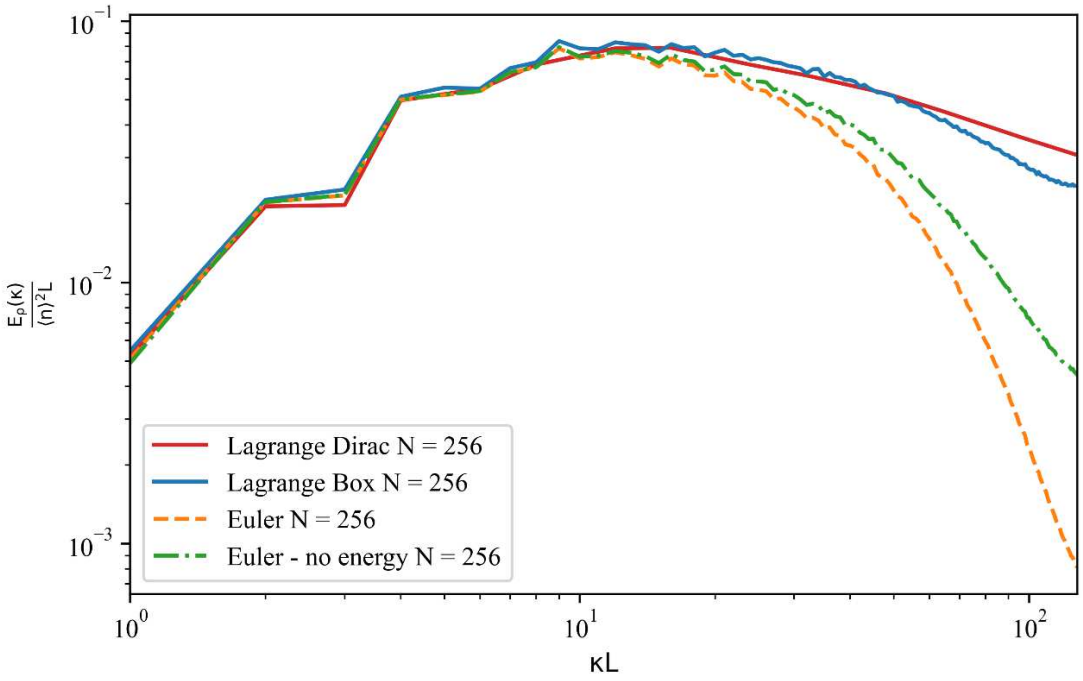


Figure 3.2: Spectral energy of the particle number concentration against the wavenumber for $Stk = 1.0$ and $Re_\varepsilon = 1500$ estimated from the particle distribution calculated with 4 different methods, the direct spectrum from the Lagrangian method (solid red), the box-averaged Lagrangian method (solid blue), the Eulerian method with energy contributions (dashed), and the Eulerian method without energy contributions (dashed-dotted).

contributions) to the Lagrangian method. At this Stokes number, there is no discernible difference in the concentration slices between the Eulerian methods, regardless of whether they incorporate 'directional' kinetic energy terms. This observation is quantitatively supported by both methods yielding the same error δ value ($\delta = 2.13$), defined according to Equation 3.26. It is important to note that δ is an error metric used to compare two methods, where a value of 1.0 signifies optimal performance, reflecting the natural variance inherent in the Lagrangian methods (Equation 3.26). This lack of difference between the Eulerian methods is anticipated and corroborated by Equation 3.15, which indicates that for small Stokes numbers (indicative of short particle relaxation times), the impact of 'directional' kinetic energy terms diminishes rapidly.

When juxtaposing the Eulerian methods with the Lagrangian method, the distinct advantages of each become apparent. The Lagrangian method exhibits random noise, which hinders precise determination of number density at specific points. This characteristic is also reflected in the δ value ($\delta = 0.96$) when comparing a Lagrangian simulation to another with different initial conditions for the particulate phase. In contrast, the Eulerian methods are prone to numerical diffusion, leading to more blurred imagery. Nonetheless, the location and size of

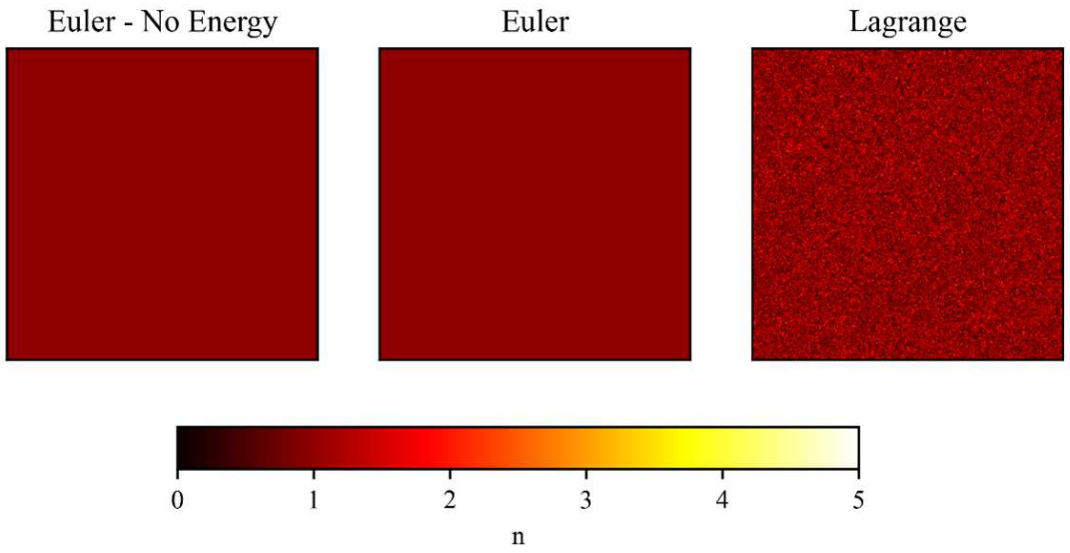


Figure 3.3: Instantaneous particle concentration spatial distribution on a 2D slice for $Stk = 0.0$ (Fluid particle) and $Re_\varepsilon = 1500$ calculated with 3 different methods. Left is the Eulerian method without energy contributions, middle is the Eulerian method with energy, right is the Lagrangian approach.

voids and clusters remain discernible and are consistently identifiable across the different methods.

Figure 3.5 presents the particle number density slices for Stokes number 1.0 and $Re_\varepsilon = 1500$, comparing the Eulerian methods (both with and without energy contributions) to the Lagrangian method. At this Stokes number, the impact of including 'directional' kinetic energy terms in the Eulerian method becomes visually apparent. The inclusion of these energy terms results in a slightly more blurred image for the Eulerian method with energy, suggesting an increase in particle dispersion. This observation is supported by the error δ values; the Eulerian method without energy contributions registers a δ value of 2.60, while the inclusion of energy contributions lowers this value to 2.45. This improvement indicates that even at $Stk = 1.0$, the energy contributions are having a significant effect.

Comparing Figures 3.5 and 3.4 reveals that some of the particle clusters present at lower Stokes numbers have been dispersed, a phenomenon likely attributable to the crossing trajectories. This comparison underscores the influence of Stokes number on the behaviour of particulate matter in the flow, as well as the effectiveness of energy contributions in the Eulerian method at different Stokes numbers.

Figure 3.6 presents the number density slices for Stokes number 2.0 and $Re_\varepsilon = 1500$, comparing both the Eulerian methods (with and without energy contributions) and the Lagrangian method. The influence of 'directional' kinetic energy terms on the Eulerian simulations is now markedly evident. Similar to observations for Stokes number 1.0, these energy terms contribute to the dispersion of

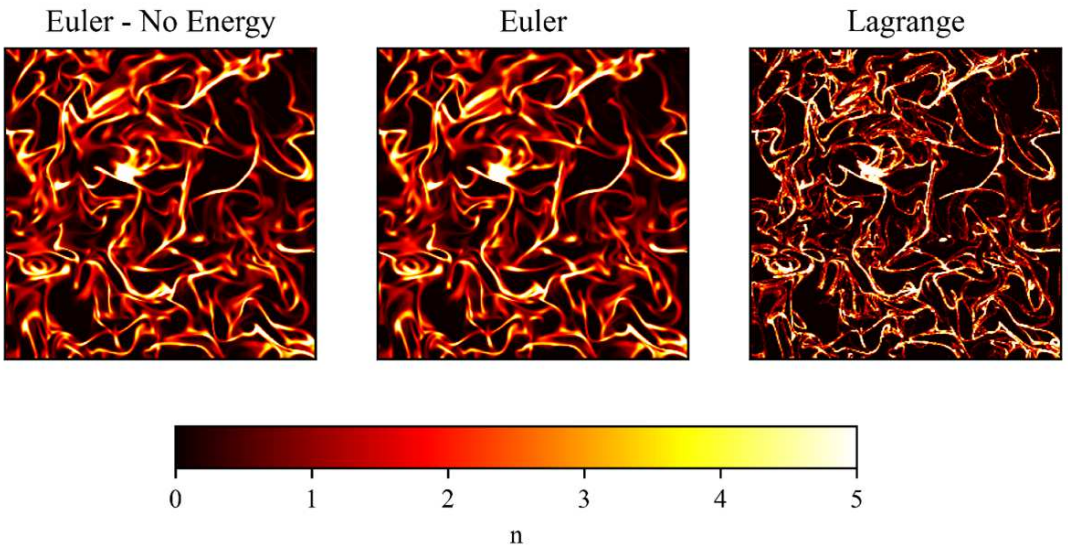


Figure 3.4: Instantaneous particle concentration spatial distribution on a 2D slice for $Stk = 0.5$ and $Re_\varepsilon = 1500$ calculated with 3 different methods. Left is the Eulerian method without energy contributions (error metric $\delta = 2.13$), middle is the Eulerian method with energy ($\delta = 2.13$), right is the Lagrangian approach ($\delta = 0.96$).

particle clusters. However, the effect is more pronounced for Stokes number 2.0, where it not only disperses the clusters but also alters their locations.

This comparison highlights that for larger particle sizes, the exclusion of 'directional' kinetic energy terms in Eulerian methods is not a suitable approximation when compared to the Lagrangian method. This is further evidenced by the error δ values; the Eulerian method without energy has a δ value of 2.59, which significantly improves to 1.71 with the inclusion of energy. Notably, the Eulerian method incorporating the 'directional' kinetic energy terms still maintains a good visual alignment with the Lagrangian results, especially in terms of the locations of clusters and voids.

Figure 3.7 displays the particle number density slices for Stokes number 5.0 and $Re_\varepsilon = 1500$, comparing the Eulerian methods (both with and without energy contributions) and the Lagrangian method. The impact of 'directional' kinetic energy terms on the Eulerian simulations is strikingly apparent in this case. The Eulerian method that excludes these energy terms fails to disperse the clusters adequately at this larger Stokes number, leading to a misrepresentation of the concentration field. This is quantitatively underscored by the δ values; the Eulerian method without energy contributions shows a δ value of 2.96, which is significantly improved to 1.06 when energy terms are included.

Despite the improvement, there are noticeable visual differences between the Eulerian method with energy and the Lagrangian method. While the overall

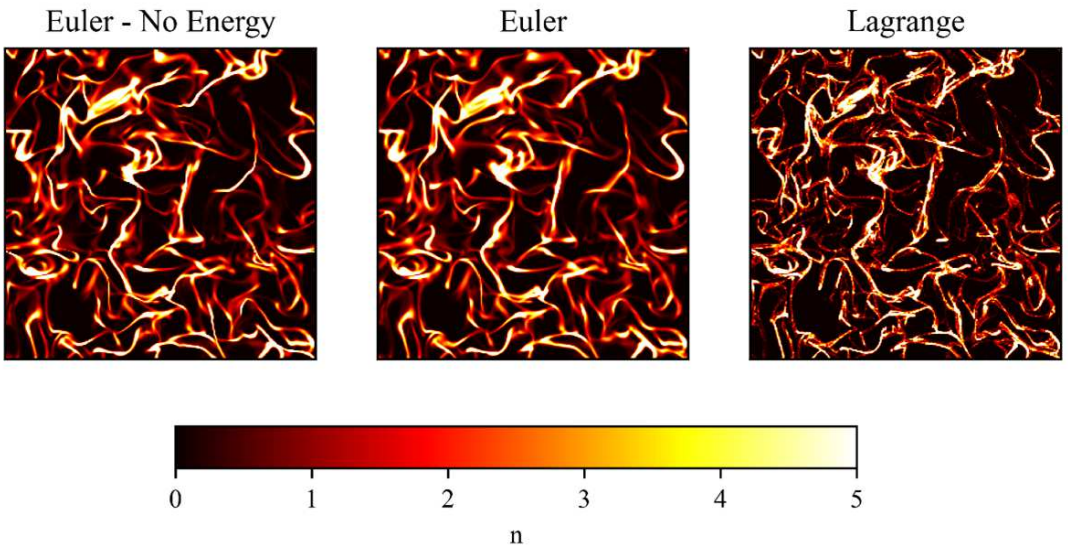


Figure 3.5: Instantaneous particle concentration spatial distribution of a 2D slice for $Stk = 1.0$ and $Re_\varepsilon = 1500$ calculated with 3 different methods. Left is the Eulerian method without energy contributions ($\delta = 2.60$), middle is the Eulerian method with energy ($\delta = 2.45$), right is the Lagrangian approach ($\delta = 1.03$).

structures of the concentration fields appear similar, the differences at these larger sizes suggest that third-order velocity moments may start to have a significant impact. This factor could account for the observed discrepancies between the two methods.

3.4.2 Effect of Grid Resolution

Figure 3.8 illustrates the number density spectra for Stokes number 2.0 and $Re_\varepsilon = 1500$, comparing the Eulerian methods (with and without energy contributions) to the Lagrangian method. This figure also highlights the influence of grid resolution on the Eulerian results. Echoing findings for Stokes number 5.0, it is evident that including energy is crucial for the Eulerian method to align with the spectral energy calculated by the Lagrangian method.

Upon doubling the grid resolution (from 256 to 512), both Eulerian methods exhibit a reduced impact from numerical diffusion, sustaining their spectral energy across a broader range of higher wavenumbers. For the Eulerian method devoid of energy contributions, a finer grid resolution diminishes its agreement with the Lagrangian solution. This discrepancy is attributed to the decreased effect of numerical diffusion, leading to more distinctly defined clusters. Notably, the Eulerian method without energy does not show convergence with increasing resolution. In contrast, the Eulerian method that includes energy contributions demonstrates improved alignment with the Lagrangian solution at higher wavenumbers when

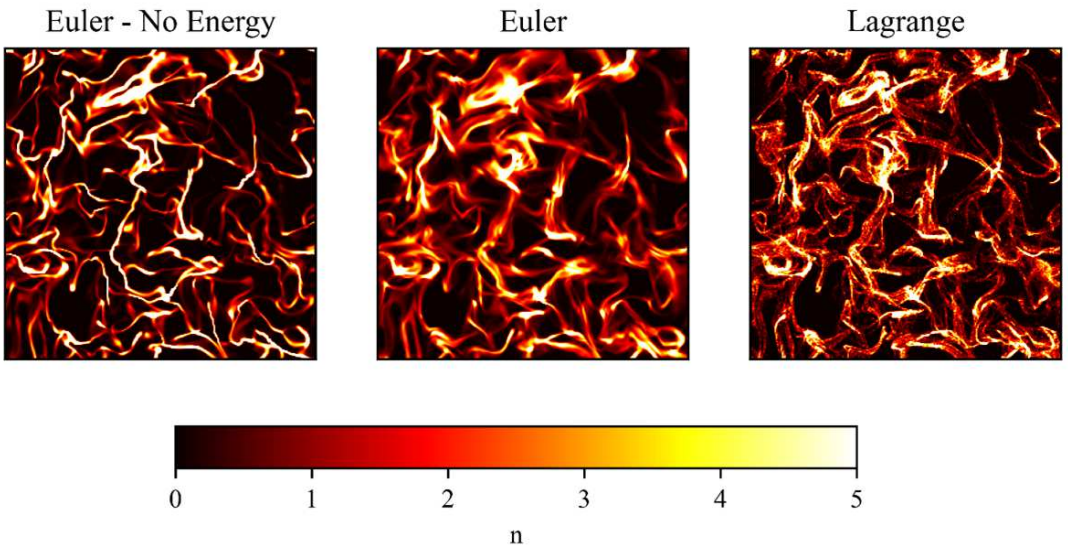


Figure 3.6: Instantaneous particle concentration spatial distribution of a 2D slice for $Stk = 2.0$ and $Re_\varepsilon = 1500$ calculated with 3 different methods. Left is the Eulerian method without energy contributions ($\delta = 2.59$), middle is the Eulerian method with energy ($\delta = 1.71$), right is the Lagrangian approach ($\delta = 0.97$).

the grid resolution is increased, owing to reduced numerical diffusion. However, due to the lack of any physical diffusion, convergence of Eulerian methods is not possible with a finite sized mesh. The inclusion of energy allows for cluster dispersion through crossing trajectories, explaining why the spectral energy at higher wavelengths is lower than that observed in the Eulerian method without energy.

Conversely, reducing the grid resolution (from 256 to 128/64), involved filtering the carrier fluid in wave space using a box filter. In these simulations, the lower wavenumbers maintained consistency, but the effects of numerical diffusion became significantly more pronounced. The precise impact of conducting carrier fluid simulations that are not fully resolved, as opposed to direct numerical simulations, remains uncertain and is beyond the scope of this paper.

3.4.3 Particle Concentration Spectra

Figure 3.9 illustrates the number density spectra across a range of Stokes numbers and $Re_\varepsilon = 1500$ estimated from the particle distributions calculated with grid resolution of $N = 256$ using three distinct evaluation methods: Lagrangian and two Eulerian approaches. The $-5/3$ slope shown in the figure is provided for comparison with the Kolmogorov energy spectrum; however, the number density is not expected to follow this slope. Both Eulerian methods align with the Lagrangian spectrum as the wavenumber approaches zero for all investigated Stokes numbers. This alignment shows that all methods are representing the same physical phe-

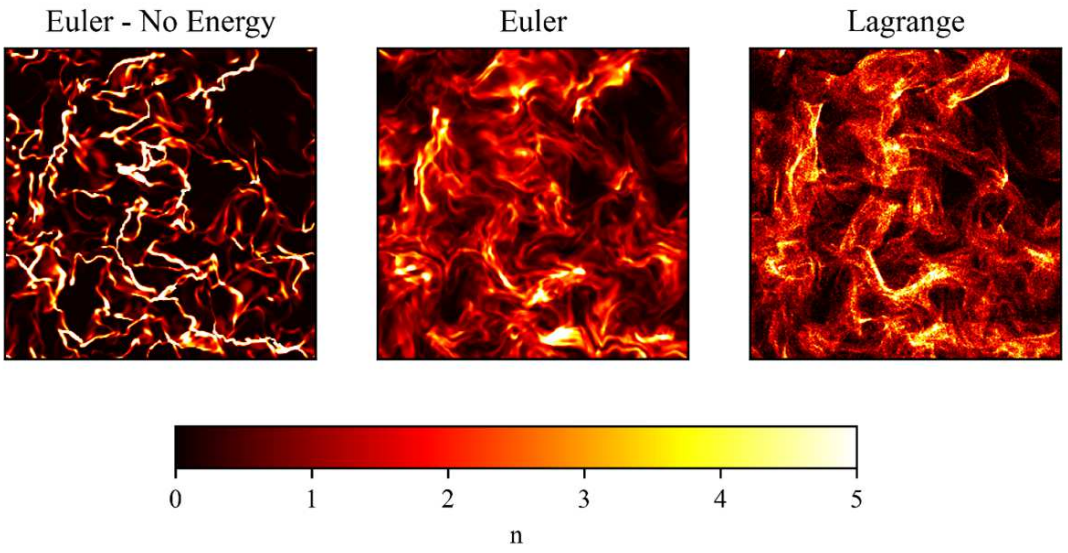


Figure 3.7: Instantaneous particle concentration spatial distribution of a 2D slice for $Stk = 5.0$ and $Re_\varepsilon = 1500$ calculated with 3 different methods. Left is the Eulerian method without energy contributions ($\delta = 2.96$), middle is the Eulerian with energy ($\delta = 1.06$), right is the Lagrangian approach ($\delta = 0.89$).

nomena. This is because the largest length scales of clusters and voids, associated with the smallest wavenumbers, are the least affected by the artificial diffusion inherent in the Eulerian methods and the random Poisson statistics affecting the Lagrangian method.

In the case of smaller Stokes numbers, specifically 0.5 and 1.0, the performance of both Eulerian methods aligns closely with the Lagrangian method up to a wavenumber of approximately 20. Beyond this point, the Eulerian methods show a marked decline, a trend indicative of diffusion effects. Notably, these effects are not inherent to the particulate phase but result from the artificial diffusion characteristics of Eulerian methods. As the Stokes number increases, the differences between the two Eulerian approaches become more pronounced, with divergence starting at lower wavenumbers.

Particularly, the Eulerian method incorporating energy contributions consistently demonstrates lower spectral energy compared to its counterpart without these contributions, a disparity that becomes more evident at higher wavenumbers. This outcome aligns with expectations, as energy contributions in the Eulerian method serve as a diffusing mechanism, facilitating the intermingling of particle clusters.

For Stokes number 2.0, the distinction between the two Eulerian methods is large. The method excluding energy contributions begins to predict higher spectral energies than the Lagrangian method, deviating at around a wavenumber of 8. This suggests more pronounced clustering. In contrast, the Eulerian method

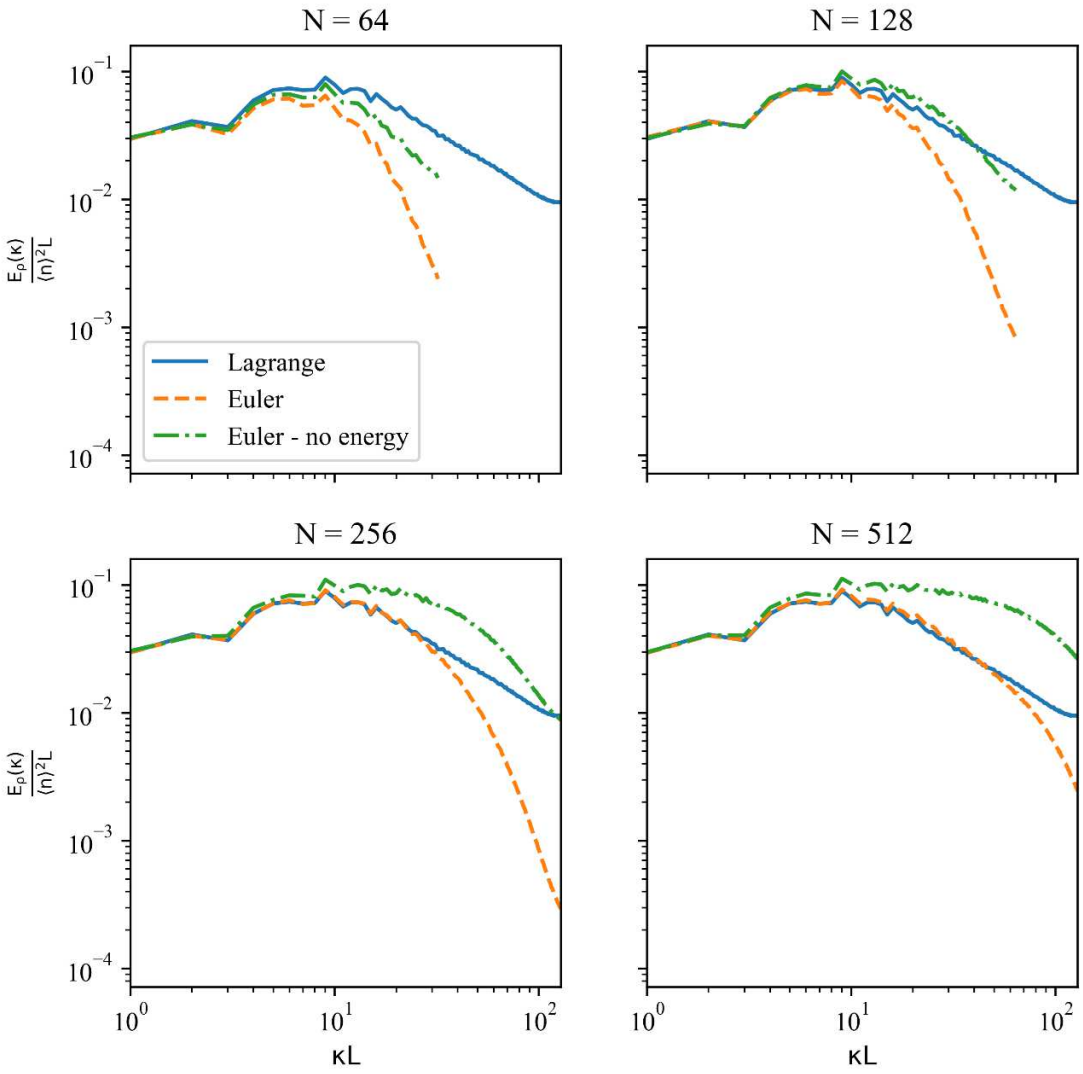


Figure 3.8: Spectral energy of the particle number concentration against the wavenumber for $Stk = 2.0$ and $Re_\varepsilon = 1500$ estimated from the particle distribution calculated with 3 different methods, namely the Lagrangian method (solid), the Eulerian method with energy contributions (dashed), and the Eulerian method without energy contributions (dashed-dotted). The four plots each have differing grid sizes $N = 64$ (top left), 128 (top right), 256 (bottom left) and 512 (bottom right).

with energy contributions maintains parity with the Lagrangian spectrum up to about wavenumber 30, after which diffusion effects become dominant.

The disparity is even more significant for Stokes number 5.0. Here, the Eulerian method without energy contributions struggles to match the Lagrangian spectrum, accurate only at the lowest wavenumbers. Conversely, the Eulerian method with energy contributions achieves a comparable spectrum up to a wavenumber of around 50.

Three primary factors contribute to the observed differences between the Eule-

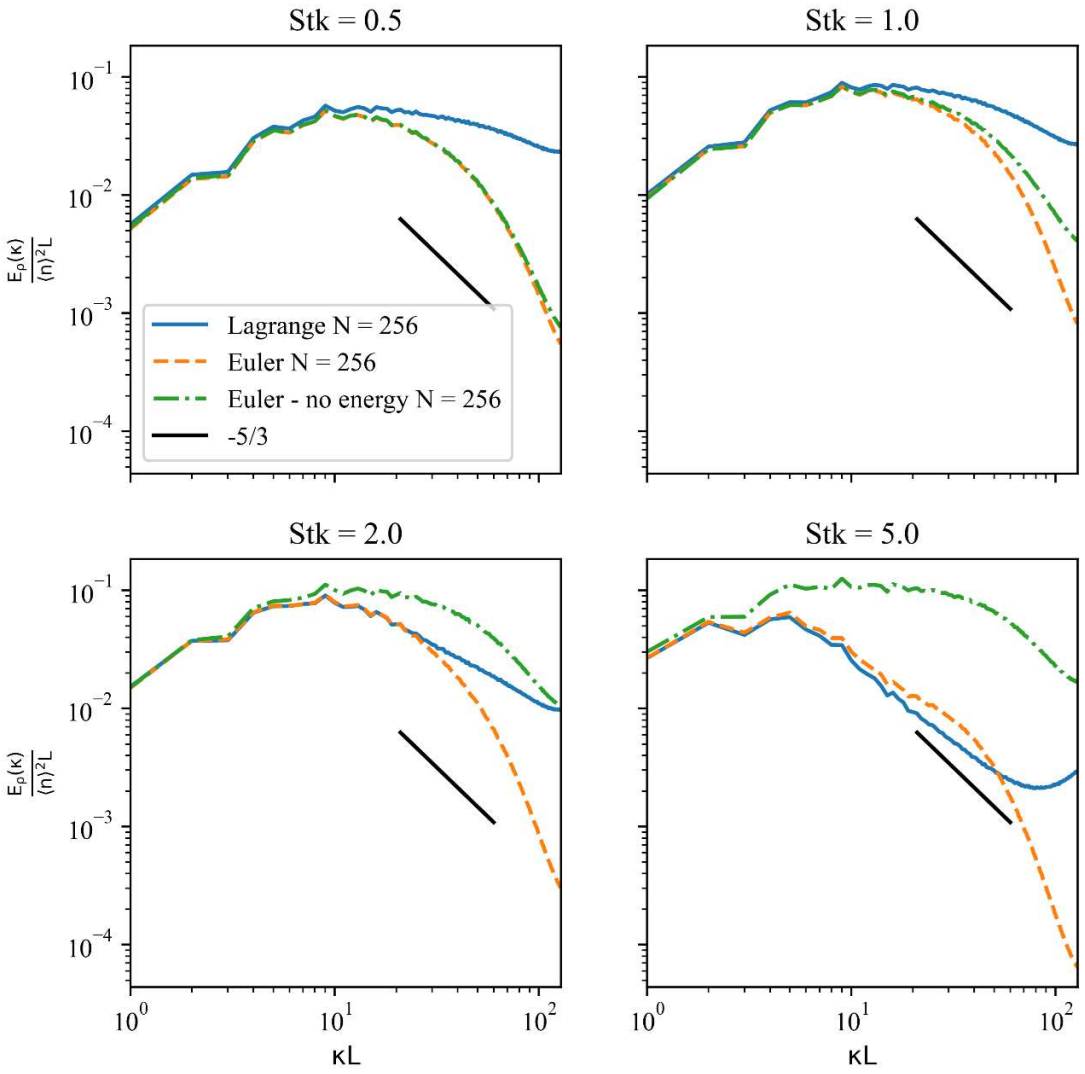


Figure 3.9: Spectral energy of the particle number concentration against the wavenumber for $Stk = 0.5$ (top left), 1.0 (top right), 2.0 (bottom left) and 5.0 (bottom right) and $Re_\varepsilon = 1500$ estimated from the particle distributions calculated with 3 different methods with grid resolution of $N = 256$, the Lagrangian method (solid blue), the Eulerian method with energy contributions (dashed orange), and the Eulerian method without energy contributions (dashed-dotted green). The black line indicates the -5/3 slope of the carrier phase velocity spectra.

rian spectrum with energy contributions and the Lagrangian spectrum. First is the Eulerian diffusion, as previously discussed. Second, the Poisson statistics of the Lagrangian particles result in increased spectral energy at higher wavenumbers. Lastly, the exclusion of third-order velocity moments in the Eulerian method likely leads to the slight elevation in spectral energy observed at wavenumbers around 20.

An unexpected finding is that the Eulerian method, when incorporating energy contributions, tends to perform increasingly well as the Stokes number rises

compared to how well it performs at low Stokes numbers, aligning more closely with the Lagrangian method for an extended range of wavenumbers, for example matching the Lagrangian method up to $\kappa L = 0.8$ for $Stk = 0.5$ but matching up to $\kappa L = 25$ for $Stk = 2.0$. Intuitively, one might anticipate the greatest alignment between the two methods (Lagrangian and Eulerian with energy) at lower Stokes numbers, where the particles behave more like tracer particles, as this is where the Eulerian equations have the least error by neglecting 3rd order velocity terms. We attribute this phenomenon to the effect of Eulerian numerical diffusion. At lower Stokes numbers, this diffusion represents the primary mechanism of dispersion, exerting a significant influence on the spectrum. However, at higher Stokes numbers, the predominant source of dispersion shifts to the crossing trajectories of the particles, thereby diminishing the relative impact of numerical diffusion.

For lower Stokes numbers, particles are more closely coupled to the fluid motion, and their dispersion is governed by all the turbulent structures of the carrier phase. However, as the Stokes number increases, the inertia of the particles allows them to 'escape' from the smallest turbulent eddies. This is evidenced in the figures, as the Stokes number increases the contribution of the lower wavelengths increases, resulting in larger structures of clusters. However, we can also see the contribution of the higher wavelengths significantly drop with increasing Stokes numbers, this results in the clusters being less 'sharp'. So we have two competing effects reliant on Stokes number, increased clustering at lower wavelengths but the enhanced dispersion at higher wavelengths. The changes to the spectra are non-trivial as the Stokes number changes, the peak of the spectrum shifts to the left as the Stokes number increases, and the slopes of the spectra on either side also change. A Stokes number of 1.0 has the highest energy spectrum which agrees with past literature that preferential concentration peaks at a Stokes number of 1.0. As the Stokes number increases beyond $Stk = 5.0$, we expect clustering to decrease in the Lagrangian method. In the Eulerian method with Energy, clustering is also expected to diminish; however, the influence of third-order velocity terms is likely to become more significant, potentially leading to greater differences with the Lagrangian method in the observed spectra.

3.4.4 Particle Momentum Spectra

Figure 3.10 presents the spectra of total particle momentum, equivalent to flux, for various Stokes numbers, for the Lagrangian approach and two Eulerian approaches. These spectra exhibit trends consistent with those obtained from the particle number concentration analysis from Section 3.4.3. Specifically, the Eulerian methods are affected by artificial diffusion, not intrinsic to the particulate

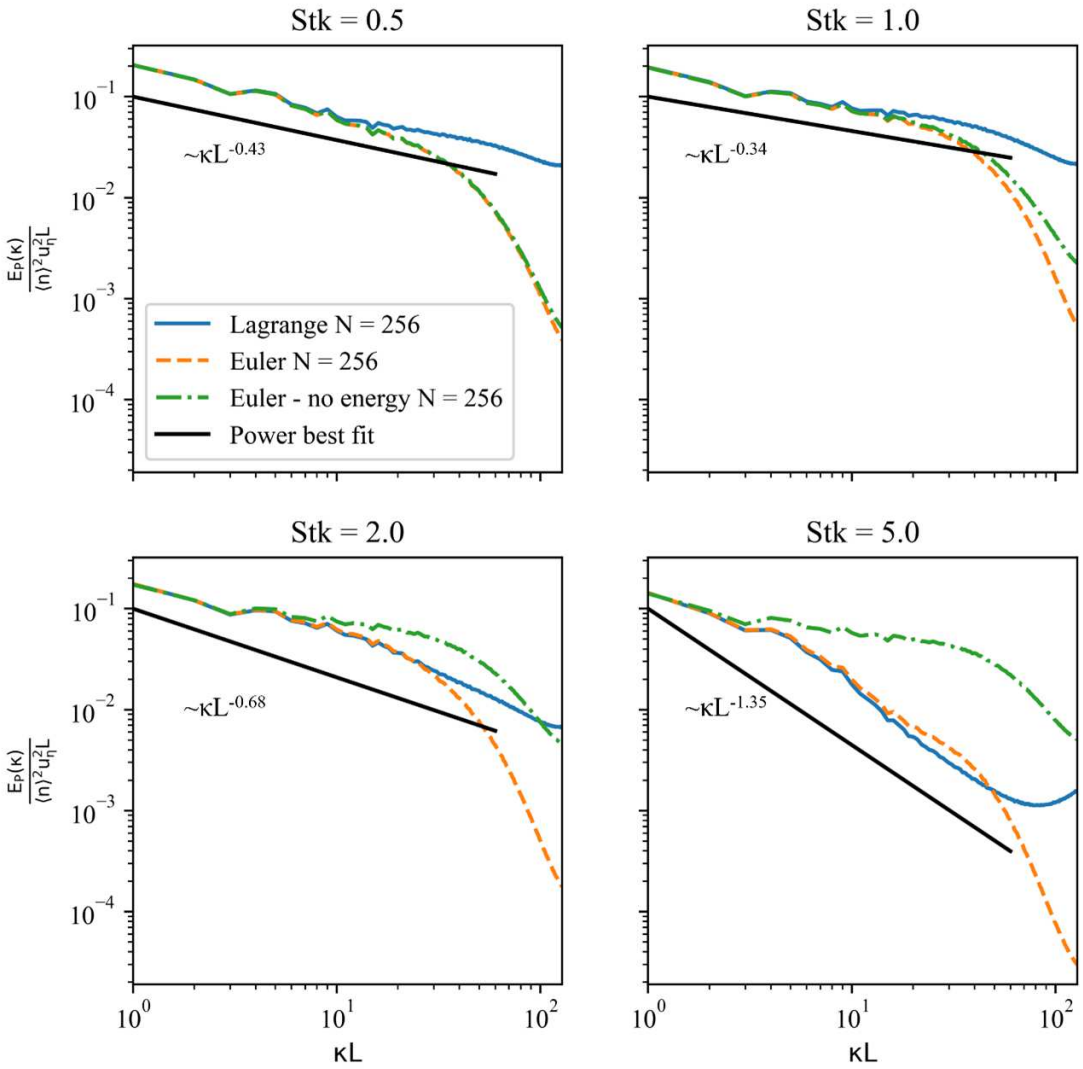


Figure 3.10: Spectral energy of the total particle momentum (flux) against the wavenumber for $Stk = 0.5$ (top left), 1.0 (top right), 2.0 (bottom left) and 5.0 (bottom right) and $Re_\varepsilon = 1500$ estimated from the particle distributions calculated with 3 different methods with grid resolution of $N = 256$, the Lagrangian method (solid blue), the Eulerian method with energy contributions (dashed orange), and the Eulerian method without energy contributions (dashed-dotted green). The black line indicates the best power law fit.

phase, resulting in a decrease in spectral energy at higher wavenumbers. Conversely, the Lagrangian spectra are influenced by Poisson statistics, leading to an increase in spectral energy at these wavenumbers. As observed at the number concentration spectra, the Eulerian method incorporating energy contributions outperforms its counterpart without these contributions, with this difference becoming more pronounced at higher Stokes numbers.

The definition of particle momentum, as delineated in Equation 3.11, indicates that the number concentration and particle velocity both contribute to the momentum. This correlation explains the clear alignment observed with the number

concentration spectra. However, a notable distinction in the momentum spectra, as opposed to the number concentration spectra, is the behaviour at lower wavenumbers. Across all Stokes numbers, we observe the disappearance of the spectrum peak, replaced by a monotonically decreasing trend. This observation suggests that the differences between the methods in the momentum spectra are likely rooted in the number density spectra, rather than any additional discrepancies introduced by the Eulerian methods compared to their performance in the number concentration spectra. The Lagrangian momentum spectra exhibit an almost power law, with the best fitting powers being -0.43, -0.34, -0.68 & -1.35 for $Stokes = 0.5, 1.0, 2.0\&5.0$ respectively.

3.4.5 Particle Velocity Spectra

Figure 3.11 displays the spectra of the conditionally averaged particle velocity (Equation 3.7) across a range of Stokes numbers, focusing exclusively on the Eulerian methods. The $-5/3$ slope shown in the figure is provided for comparison with the Kolmogorov energy spectrum; The particle velocity is expected to follow the carrier fluid spectra for small stokes numbers. The exclusion of the Lagrangian method is due to its inability to define a velocity field at all locations. Specifically, in areas devoid of particles, the Lagrangian method results in an undefined velocity, in contrast to the Eulerian methods which, working with a continuous concentration, can establish a defined velocity everywhere. To facilitate a comparison of the Eulerian methods, the velocity spectrum for the background flow of the turbulent fluid is also provided.

Notably, both Eulerian methods exhibit a high degree of agreement with each other. The disparity between them is considerably less pronounced than what was observed in the particle number concentration and momentum spectra. The primary difference manifests as a marginal decrease in spectral energy at higher wavelengths and for higher Stokes numbers. As the Stokes number approaches zero, the particle velocity is expected to converge towards that of the carrier fluid. This trend is observable at a Stokes number of 0.5 for the lower wavenumbers, indicating alignment with theoretical expectations.

Unlike the carrier fluid, the particle velocity lacks a physical diffusion or viscosity term. Consequently, the spectrum for the carrier fluid decreases at a much more rapid rate than that of the particulate phase across all examined Stokes numbers. This observation suggests that the velocity cascade in the particulate phase can sustain higher wavenumbers, even though they are continuously decaying towards the carrier fluid values. It is important to note that this observation also applies to a Stokes number of 0.5, where there are still significant deviations from

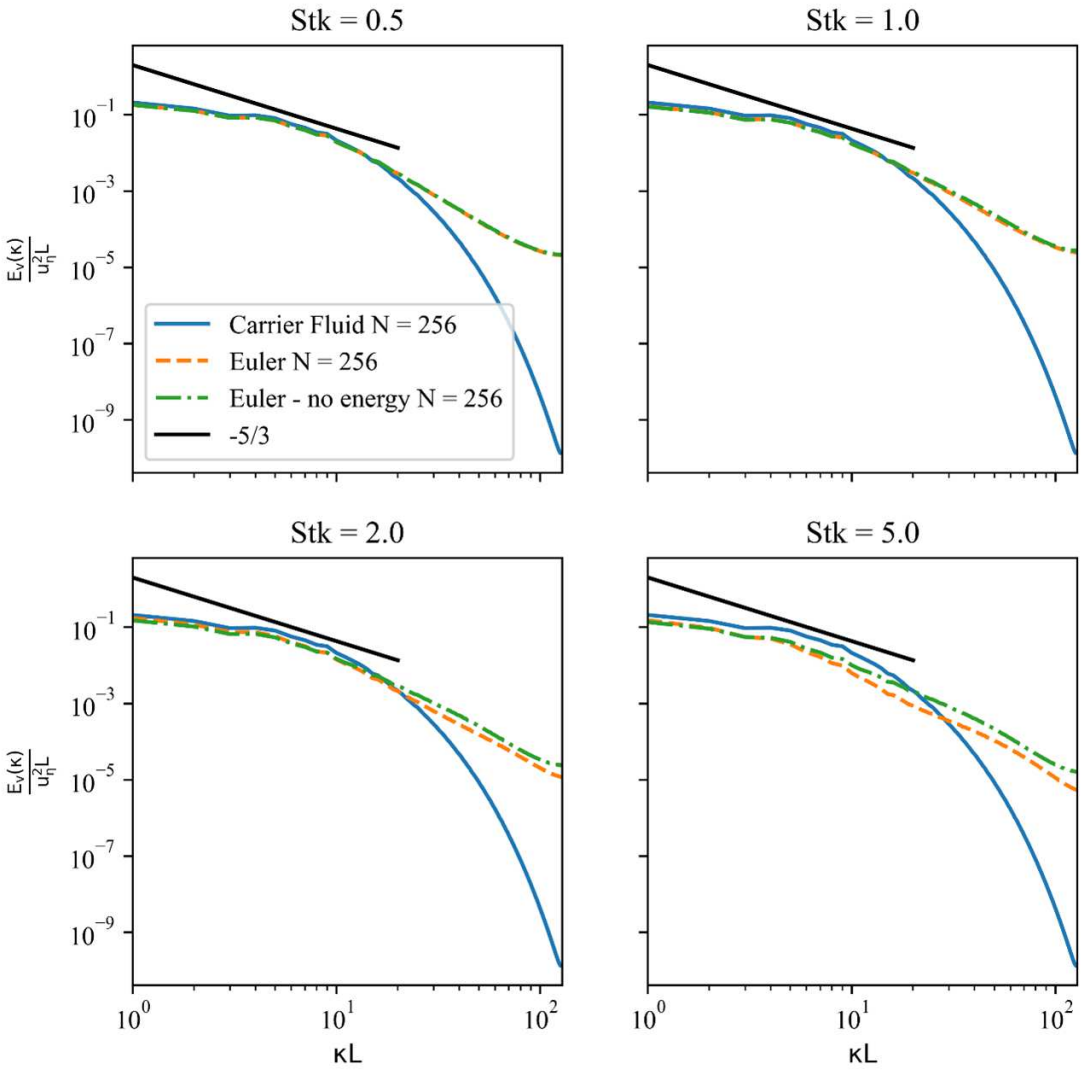


Figure 3.11: Spectral energy of the conditionally averaged particle velocity against the wavenumber for $Stk = 0.5$ (top left), 1.0 (top right), 2.0 (bottom left) and 5.0 (bottom right) and $Re_\varepsilon = 1500$ estimated from the particle distributions calculated with 2 different methods with grid resolution of $N = 256$, the Eulerian method with energy contributions (dashed orange), and the Eulerian method without energy contributions (dashed-dotted green). The background carrier fluid velocity spectrum (solid blue) is also plotted for comparison. The black line indicates the -5/3 slope of the carrier phase velocity spectra.

the carrier fluid. These deviations result in considerable amounts of preferential concentration, as illustrated in Figure 3.4.

In contrast to the particle number concentration and momentum spectra, the velocity spectrum exhibits minimal variation across different Stokes numbers. A consistent trend observed is a slight decrease in the overall velocity spectral energy across all wavenumbers as the Stokes number increases. This behaviour aligns with theoretical expectations. As the Stokes number increases, it leads to more pronounced temporal filtering of the carrier velocity field. Consequently, this

results in a reduced energy transfer from the carrier fluid to the particulate phase.

3.4.6 Particle Energy Spectra

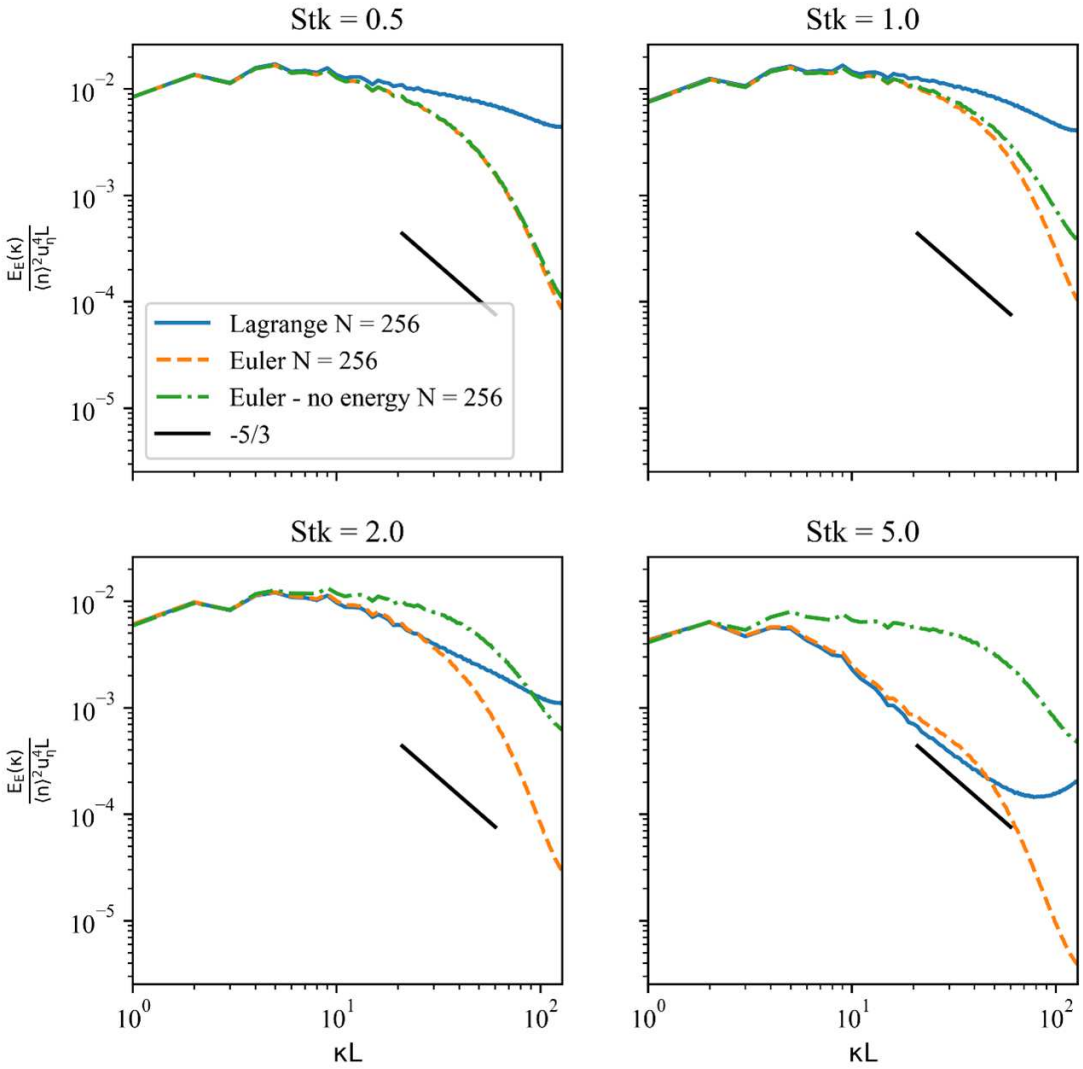


Figure 3.12: Spectral energy of the total particle energy (momentum flux) against the wavenumber for $Stk = 0.5$ (top left), 1.0 (top right), 2.0 (bottom left) and 5.0 (bottom right) and $Re_\varepsilon = 1500$ estimated from the particle distributions calculated with 3 different methods with grid resolution of $N = 256$, namely the Lagrangian method (solid blue), the Eulerian method with energy contributions (dashed orange), and the Eulerian method without energy contributions (dashed-dotted green). The black line indicates the -5/3 slope of the carrier phase velocity spectra.

Figure 3.12 illustrates the spectra of total particle energy for a range of Stokes numbers, comparing the Lagrangian approach to the two Eulerian approaches. The $-5/3$ slope shown in the figure is provided for comparison with the Kolmogorov energy spectrum; however, the total particle energy is not expected to

follow this slope. Mirroring the trends observed in the concentration and momentum spectra (Sections 3.4.3 and 3.4.4, respectively), the general patterns are consistent. Specifically, the Eulerian methods exhibit a decrease in spectral energy at higher wavenumbers due to artificial diffusion, which is not an inherent characteristic of the particulate phase. In contrast, the Lagrangian spectra are influenced by Poisson statistics, leading to an increase in spectral energy at these higher wavenumbers. Similar to the findings in the number concentration spectra, the Eulerian method that incorporates energy contributions performs better than the method without these contributions, particularly at higher Stokes numbers. The definition of total particle energy, as outlined in Equation 3.30, suggests that the trends in total particle energy are largely reflective of the trends observed in number concentration. This is because the velocity spectra, as discussed in Section 3.4.5, do not exhibit the same level of diffusion. Additionally, unlike the momentum spectra, the data for total particle energy does not display a monotonically decreasing trend.

Figure 3.13 focuses on the spectra of total particle velocity fluctuations, a component of total particle energy. The $-5/3$ slope shown in the figure is provided for comparison with the Kolmogorov energy spectrum; however, the total particle velocity fluctuations are not expected to follow this slope. In this analysis, the Eulerian method without energy contributions is omitted, as it inherently lacks velocity fluctuations. This figure elucidates the extent of occurrence of crossing trajectories within the particulate phase. As anticipated, both methods demonstrate that an increase in Stokes number leads to a significant rise in crossing trajectories, evident in the general increase of spectral energy across all wavenumbers. Despite its importance, the fluctuating part of the total energy constitutes a relatively small percentage of the total, contributing 2%, 3%, 9%, and 20% for Stokes numbers 0.5, 1.0, 2.0, and 5.0, respectively. For Stokes numbers 1.0, 2.0, and 5.0, the Eulerian method shows a marginally higher spectral energy compared to the Lagrangian method at smaller wavelengths. This discrepancy arises because the Lagrangian method cannot define velocity fluctuations in scenarios with zero or only one particle, and its accuracy in measuring fluctuations decreases with fewer particles. In this analysis, the energies illustrated are derived from the 'parallel' second order velocity components as defined in Equations 3.30 and 3.31. While the 'perpendicular' energies or cross-velocity moments were also examined, their results closely mirrored those of the 'parallel' energy spectra, albeit consistently exhibiting lower spectral energies. This similarity in trends led us to primarily focus on the 'parallel' energies for a clearer representation of the overall energy patterns.

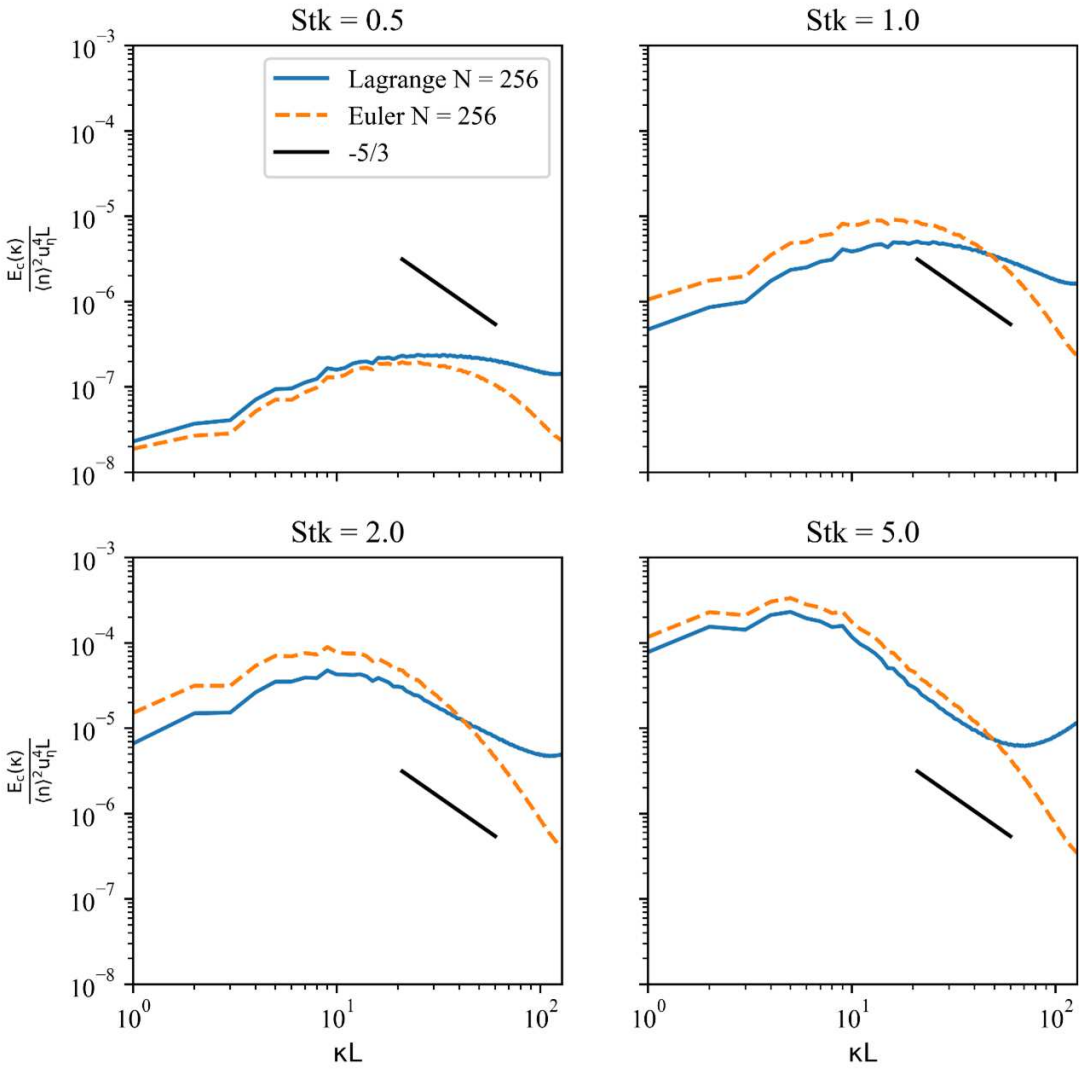


Figure 3.13: Spectral energy of the particle energy fluctuations against the wavenumber for $Stk = 0.5$ (top left), 1.0 (top right), 2.0 (bottom left) and 5.0 (bottom right) and $Re_\varepsilon = 1500$ estimated from the particle distributions calculated with 2 different methods with grid resolution of $N = 256$, namely the Lagrangian method (solid blue) and the Eulerian method with energy contributions (dashed orange). The black line indicates the -5/3 slope of the carrier phase velocity spectra.

3.5 Conclusions

This study presents an in-depth analysis based on Fourier spectra of the characteristics of particle preferential concentration across various Stokes numbers in isotropic turbulence calculated using both Eulerian and Lagrangian methods. Two distinct Eulerian methods were compared: one incorporating 'directional' kinetic energy terms, accounting for the 2nd order velocity moments of the particulate phase, and the other excluding these terms. This distinction is crucial for facilitating the occurrence of crossing trajectories in the particle dispersion, which are

prevalent in particle preferential concentration scenarios involving larger particle sizes.

The study reveals that both Eulerian methods are affected by artificial diffusion, an effect not inherent to the particulate phase. This diffusion, predominantly attributed to the particle number concentration, influences other spectra intrinsically linked to it. Notably, the Eulerian methods with energy contributions consistently outperform those without such contributions, particularly at higher Stokes numbers. This advantage arises from their ability to include energy contributions, enabling the accurate representation of crossing trajectories and proper dispersion of particle clusters, formed during the interaction with turbulence. A point of further study would be the investigation of the effect of the 3rd order velocity moments and the impact of their inclusion. As they will decay faster than the 2nd order moments, we predict they will only have a significant effect for the largest Stokes numbers.

Conversely, the Lagrangian method, while not affected by artificial diffusion, is limited by its sensitivity to Poisson statistics. Additionally, it faces challenges in defining a particle velocity field uniformly in space and in accurately capturing velocity fluctuations in areas of low concentration. However, in the low wavenumber range of the spectra, the Lagrangian method and the Eulerian method with energy contributions exhibit similar performance.

A notable finding is the minimal variability in conditionally averaged velocity spectra across different Stokes numbers, in contrast to the more significant variations observed in particle concentration, momentum, and energy spectra. This suggests that, while Stokes number variability greatly influences energy transfer and diffusion effects, its impact on mean particle velocity is relatively minor. Furthermore, the study highlights the critical role of grid resolution in Eulerian methods. Improved resolution diminishes numerical diffusion, enhancing spectral energy predictions in the method incorporating second-order velocity fluctuations. However, the Eulerian method without energy contributions does not converge with increased resolution, and its accuracy diminishes.

The research emphasizes the analysis of periodic, homogeneous isotropic turbulence using an equidistant grid. It posits that the transition to studying anisotropic or wall-bounded flows would not necessitate alterations in the foundational methods and numerical approaches, given that the initial assumptions do not rely on the fluid flow's isotropy. Nevertheless, an important consideration for future work is the application to non-regular grid systems. The Roe-flux numerical scheme, as applied in this study, is specifically designed for equidistant velocity grids. To extend this scheme to non-regular grids, it would require appropriate modifications to ensure accuracy and validity.

In conclusion, this research elucidates the nuanced differences between Eulerian and Lagrangian methods in modelling particle preferential concentration in turbulent flows, emphasizing the importance of selecting the appropriate method based on specific modelling requirements. It provides detailed spectral comparisons not only for particle concentration but also for other crucial properties relevant to preferential concentration.

While Chapter 3 discusses spectral characteristics using different methods, the next chapter builds on this analysis by introducing additional key parameters (Reynolds, Stokes, and Froude numbers). The findings from the spectral characteristics of particle concentration can be extended to explore how these additional parameters influence particle behavior in turbulent flows, providing a more comprehensive understanding of particle clustering.

Chapter 4

Spectral Analysis of Preferential Concentration in Turbulent Flows: Parametric Dependence on Reynolds, Stokes, and Froude Numbers

This work has been submitted and is under review for the Journal of Multiphase Flow, it has been adapted to form the basis of this Chapter.

4.1 Abstract

Understanding the preferential concentration of inertial particles in turbulent flows is crucial for a wide range of natural and industrial processes. This study advances our understanding of turbulence-particle interactions by systematically evaluating the combined effects of Reynolds number (Re_λ), Stokes number (Stk), and Froude number (Fr) on particle clustering through direct numerical simulations (DNS). Our analysis demonstrates that particle clustering intensity peaks at $Stk \approx 1$, where particles optimally interact with turbulent eddies. While previous research often overlooks the influence of Reynolds number, our findings reveal that this assumption holds for small Stk, but for larger Stk, Reynolds number significantly impacts clustering behaviour. Gravitational effects, quantified by Fr, also play a critical role in clustering dynamics. For $Stk \ll 1$, gravity's impact is minimal for $Fr < 5.0$; however, as Stk increases, gravity enhances large-scale clustering and modulates small-scale clustering—diminishing it for intermediate $Stk \approx 1$ and enhancing it for $Stk \gg 1$. Here, large-scale clustering refers to particle aggregation

at scales comparable to the largest energy-containing eddies, while small-scale clustering involves particle aggregation at the dissipative scales of turbulence. We introduce a novel empirical model that accurately predicts particle concentration spectra across a wide range of conditions, validated against current and previous studies. This model provides a practical tool for analysing particle-laden turbulent flows in large spaces and has substantial implications for atmospheric science, chemical engineering, and environmental studies, offering improved predictions of droplet clustering in clouds, particulate dispersion in reactors, and pollutant transport.

4.2 Introduction

Particles and droplets in turbulent flows tend to cluster in regions with high concentration while forming voids in areas of low concentration, a phenomenon known as preferential concentration. This occurs because the inertia of particles causes them to deviate from the fluid's streamlines [154]. Several factors, including particle size and fluid properties, influence this process. Preferential concentration is vital to many natural and industrial systems. For instance, in atmospheric physics, it influences rain formation, while in chemical engineering, it affects processes such as powder manufacturing. Many of these processes rely on nonlinear interactions with particle concentration. The general aerosol dynamic equation, which models the evolution of droplet size distribution, highlights the importance of non-uniform particle concentrations [55]. Furthermore, preferential concentration plays a critical role in phenomena such as droplet coalescence in clouds [163, 150, 95], evaporation or condensation of droplets [137, 145], and gas-particle phase reactions [70]. However, measuring and simulating preferential concentration in large domains presents substantial challenges for both experimental and computational methods.

The clustering of inertial particles in fluid flows is governed by a variety of complex mechanisms, with key influences from factors such as the Stokes and Reynolds numbers. In flows with a mean velocity component, a commonly observed effect is centrifuging. Within the context of turbulence, Chen et al. [30] introduced the 'sweep-stick' mechanism, and Oka and Goto [119] later expanded on this concept with the 'generalised sweep-stick' mechanism. According to these models, particles are swept along with the flow and become trapped at the acceleration stagnation points of the fluid. An alternative perspective is provided by Bragg et al. [23], whose analysis applies to velocity fields with arbitrary spatial correlations. Their work challenges the idea of scale invariance in the radial distribution function, offering new insights into the processes driving particle clustering. In addition,

other research has explored inertial-range scaling [14, 16, 3]. For further details, Bec et al. [17] provide a comprehensive review of these topics.

There are several approaches for analyzing and quantifying preferential concentration, with radial distribution functions (RDFs) being among the most widely used. RDFs provide significant insights into the structural characteristics of clustering and are particularly useful for empirical and theoretical models at lower Stokes numbers [5, 14, 148, 31, 177]. However, RDFs have certain limitations. They primarily capture pairwise interactions and often assume spherical symmetry, which overlooks the actual shape and spatial configuration of particle clusters. To overcome these limitations, some studies utilize angular distribution functions, which offer a more detailed understanding of particle interactions [61].

Voronoi tessellation is another method commonly employed to quantify preferential concentration. This technique involves assigning volumes to individual particles, making it particularly useful in both experimental studies and numerical simulations. By calculating the local particle concentrations from these assigned volumes, it allows for the identification of clusters and the measurement of concentration variance [124, 114, 157, 6].

Spectral methods provide an alternative means of analysing preferential concentration and can be categorized into Fourier and wavelet transforms. Fourier transforms, employed in various studies [41, 86, 104, 146, 69, 3], focus on the power spectra of particle concentration, effectively capturing the length scales of particle clusters. The Fourier spectrum of number density is connected to the radial distribution function through a Fourier transform and an offset. However, there is no universally accepted analytical model for the number density spectrum $E_\rho(\kappa)$, especially when accounting for a range of Stokes, Reynolds, and Froude numbers [104]. Such a model would be invaluable for estimating clustering across varying conditions. Matsuda et al. [104] proposed an empirical model that predicts the number density spectrum for different Stokes numbers, though it applies under conditions without gravitational influence and at a single Reynolds number, $Re_\lambda = 204$. While Fourier transforms provide a global perspective and are relatively simple to interpret, wavelet transforms, used in other studies [10, 106], offer more localized insights, allowing for a finer resolution of spatial variations in particle clustering. This localized approach provides more detailed information about clustering behaviour across different scales.

The preferential concentration of inertial particles in turbulent flows has been extensively investigated, with much of the research focusing on the dependence of clustering on the Stokes number (Stk), which is derived from the ratio of the particle inertia timescale to the Kolmogorov timescale of the fluid flow. This parameter, which quantifies the balance between particle inertial forces and fluid

viscous forces, is critical in determining how particles deviate from fluid streaklines and form clusters. Squires and Eaton [154] demonstrated that particles with a Stokes number near unity exhibit pronounced preferential concentration, as their response time aligns optimally with turbulent eddies. Matsuda et al. [104] showed that for $Stk < 2$, turbulent clustering of droplets significantly affects radar reflectivity, highlighting the strong dependence of clustering intensity on the Stokes number. Vaillancourt and Yau [163] reviewed multiple studies, emphasizing that particles with intermediate Stk are most likely to deviate from random distribution and form clusters in turbulent flows.

Additional research, including studies by Shaw [150] and Lian et al. [95], has provided both experimental and numerical evidence demonstrating that particle clustering is highly sensitive to changes in the Stokes number. Sahu et al. [145] investigated the interaction between droplet dispersion and evaporation, showing that the degree of clustering and the associated evaporation rates were strongly influenced by the Stokes number. Haugen et al. [70] explored the effects of turbulence on mass transfer rates, revealing that particle clustering driven by preferential concentration is most pronounced at $Stk \approx 1$, significantly impacting surface reactions in turbulent environments.

Monchaux et al. [115] and Eaton and Fessler [46] explored the mechanisms driving preferential concentration, such as the centrifuging of particles from vortical structures, which is most pronounced for particles with Stk near unity. Chun et al. [31] developed an analytical theory to predict particle clustering, confirming that the radial distribution function increases as an inverse power of the interparticle separation for small Stokes numbers. Similarly, Bec [13] and Bec et al. [15] provided insights into the fractal nature of particle clustering at low Stk, noting that clustering intensity decreases at higher Stokes numbers.

Gustavsson and Mehlig [64] and Bragg and Collins [22] compared statistical models for the spatial distribution of heavy particles, clarifying how clustering behaviour depends on the Stokes number across different turbulent flow regimes. Sundaram and Collins [158] and Coleman and Vassilicos [32] also examined the collision statistics of inertial particles, demonstrating that preferential concentration significantly enhances collision rates for particles with intermediate Stk.

These studies collectively emphasize the crucial role of the Stokes number in governing the preferential concentration of particles in turbulence. Clustering behaviour, which peaks at $Stk \approx 1$, highlights the importance of particle inertia in shaping their spatial distribution within turbulent flows, as evidenced by a wide range of experimental, numerical, and theoretical investigations.

The Reynolds number significantly influences the behaviour of particle clustering in turbulent flows. Ireland et al. [80] studied Reynolds numbers up to

$Re_\lambda \approx 600$ and found that as the Reynolds number increases, regions of intense rotation and strain in the flow tend to form vortex sheets, which can eject inertial particles, particularly those with small Stokes numbers (Stk). This ejection reduces the tendency for clustering in these regions. For particles with higher Stokes numbers ($Stk \geq 10$), clustering is affected by a combination of inertial filtering and path-history effects, with increased Reynolds numbers generally enhancing clustering within the inertial range of turbulence [80]. This is because the influence of inertial filtering diminishes at high Reynolds numbers, where greater scale separation and increased turbulence intermittency lead to stronger clustering effects. However, for particles with lower Stokes numbers ($Stk \lessapprox 0.4$), clustering is largely independent of Reynolds number and is primarily driven by preferential sampling of specific turbulent structures [80]. Matsuda et al. [104] examined number density spectra for Reynolds numbers in the range $127 \leq Re_\lambda \leq 531$ at $Stk = 1.0$, finding that the spectra were mostly independent of Reynolds number for wavenumbers $\kappa\eta \geq 0.05$. However, at larger length scales ($\kappa\eta < 0.05$), clustering was shown to be highly dependent on Reynolds number. The combined effects of varying both Stokes number and Reynolds number were not explored in this study.

Matsuda et al. [105] investigated the combined effects of gravitational settling, Reynolds number, and Stokes number on turbulent droplet clustering and radar reflectivity factors. They found that the number density spectra were no longer independent of Reynolds number, even for $\kappa\eta \geq 0.05$, when the Stokes number was sufficiently large ($Stk > 2.0$). Their results showed that gravity significantly modulates clustering intensity, particularly for droplets with Stokes numbers greater than unity. This study, along with earlier work by Matsuda et al. [104], highlights the importance of gravity in modifying particle distributions in turbulent flows, which is essential for accurately modelling atmospheric processes.

Gravity exerts a complex influence on particle clustering and collisions in turbulent flows, with its effects varying based on particle size and Stokes number. Ireland et al. [81] demonstrated that for low-Stokes-number particles, gravity reduces clustering by shortening their interaction time with turbulent structures, thus diminishing preferential sampling and lowering the Lagrangian strain and rotation timescales. Conversely, for high-Stokes-number particles, gravity enhances clustering by modulating drift and diffusion, reducing the path-history effect. Overall, gravity tends to decrease relative velocities and accelerations, leading to fewer collisions between particles of the same size, but it increases collision rates between particles of different sizes due to faster settling speeds.

Onishi et al. [122] similarly found that gravity influences particle clustering by affecting droplet interactions. In monodisperse systems, gravitational sedimentation decreases relative velocities by reducing the interaction time with the

turbulent fluid, despite a slight increase in the radial distribution function (RDF). This aerodynamic effect becomes prominent when the sedimentation rate of the droplets exceeds the fluid velocity fluctuations, though for cloud droplets, the gravitational impact on collisions is often minimal, consistent with models that neglect this effect for monodisperse cloud droplets.

Woittiez et al. [174] further highlighted gravity's dual influence on clustering and collisions. For monodisperse droplets, gravity reduces the probability of collisions by limiting their interaction with turbulence. However, in bidisperse droplets, differing terminal velocities increase the collision kernel. Gravity plays a crucial role in preferential concentration, particularly for larger droplets interacting with large-scale turbulent structures. The interplay between turbulence and gravity is intricate, significantly affecting collision dynamics, especially for droplets of different sizes.

Bec et al. [18] added that gravity accelerates the settling of heavy particles in turbulence, causing them to settle faster than in still fluids by preferentially sampling downward-moving regions. While this promotes particle clustering, gravity also reduces relative velocities, creating opposing effects on collision rates. While clustering increases the likelihood of collisions, reduced velocities can hinder them, requiring a balance between these factors for accurate modelling of particle collisions and coalescence in turbulent environments.

Vaillancourt and Yau [163] reviewed particle-turbulence interactions and noted that although much is understood about the role of particle inertia, the combined effects of Reynolds number and gravity on clustering remain less well understood. Haugen et al. [69] and Shaw [150] echoed this sentiment, stressing the need for further investigation to fully comprehend the impact of these factors on particle concentration fields.

Reade and Collins [136] and Gustavsson and Mehlig [64] analysed the effects of turbulence on collision rates and the spatial distribution of heavy particles, showing that Reynolds number influences these interactions by altering turbulence intensity and the relevant scales. Bragg and Collins [22] expanded on these dynamics, demonstrating that higher Reynolds numbers enhance clustering by increasing turbulence intermittency and energy dissipation rates.

Experimental studies by Petersen et al. [127] and numerical investigations by Bec et al. [15] confirmed that particle clustering is strongly influenced by both turbulence intensity and gravitational forces. Sundaram and Collins [158] and Gualtieri et al. [61] also contributed to this understanding by studying collision statistics and anisotropic clustering in turbulent flows.

Lian et al. [95] and Reveillon and Demoulin [137] provided further insights into how varying Reynolds numbers and gravitational forces impact droplet evapora-

tion and dispersion, emphasizing the need for more detailed investigations. Ayala, Rosa, Wang and Grabowski [5] and Durham et al. [44] also explored the combined effects of turbulence and gravity on particle behaviour, reinforcing the importance of incorporating these factors into models of particle-laden flows.

Overall, while significant progress has been made in understanding the effects of Reynolds number and gravity on preferential concentration, the combined influence of these factors on the number density spectra across a wide range of Stokes numbers remains less explored. Further research is needed to fully unravel these complex interactions and their implications for various natural and industrial processes.

This study seeks to address the gaps identified in the existing literature by systematically investigating the combined effects of Reynolds number, Stokes number, and Froude number on the number density spectra of particles in turbulent flows. Unlike previous research, which primarily focused on the Stokes number, this work examines the relatively underexplored joint influence of Reynolds number and gravitational forces in conjunction with Stokes number on particle clustering. Using direct numerical simulations (DNS), this study offers a comprehensive analysis of how these parameters interact to shape particle concentration fields.

A key innovation in this study is the development of a new empirical model that accurately predicts the power spectrum of particle number density fluctuations across a wide range of Reynolds, Stokes, and Froude numbers. This model serves as a practical tool for estimating concentration fields in large domains, where direct simulations are often infeasible due to the high computational demands. By enabling the prediction of particle clustering behaviour under various flow conditions, this empirical model represents a substantial improvement over existing theoretical and numerical approaches.

Additionally, this study introduces a detailed spectral analysis method for evaluating particle clustering intensity at different scales, providing new insights into the mechanisms of preferential concentration in turbulence. Through the analysis of the power spectrum of particle number density fluctuations, this research reveals the scale-dependent nature of particle clustering, which holds important implications for understanding and modelling particle-laden flows in both natural and industrial contexts.

In conclusion, this study not only advances the understanding of turbulence-particle interactions by integrating the effects of Reynolds number and gravity but also develops practical tools for predicting particle concentration fields. The findings and methodologies presented here are expected to significantly contribute to fields such as atmospheric science, oceanography, and chemical engineering, where accurate modelling of particle behaviour in large-scale turbulent flows is

essential.

4.3 Numerical Method

4.3.1 Carrier Fluid Simulations

The carrier fluid is simulated using the incompressible Navier-Stokes equations with an additional forcing term to maintain statistically stationary homogenous isotropic turbulence. The equations for the carrier fluid in Einstein notation are:

$$\frac{\partial u_i}{\partial t} + \frac{\partial u_i u_j}{\partial x_j} = -\frac{1}{\rho_f}\frac{\partial p}{\partial x_i} + \upsilon \frac{\partial^2 u_i}{\partial x_j^2} + F_i, \tag{4.1}$$

$$\frac{\partial u_j}{\partial x_j} = 0, \tag{4.2}$$

where u_i is the carrier fluid velocity in the i-th direction, x_i is the spatial coordinate in the i-th direction, t denotes time, ρ_f is the carrier fluid density, p the pressure, υ the kinematic viscosity, and F_i forcing term in the i-th direction. The summation is over the index j.

Throughout the simulations, the fluid density (ρ_f), and the kinematic viscosity (υ) are kept constant. The carrier fluid simulations, which are performed independently from the particulate phase due to one-way coupling, is stored for subsequent analysis. The simulations are performed in a three-dimensional periodic cube with side length L. The simulations were run for a total of 54 integral timescales, with fluid data saved every 0.4 Kolmogorov timescales. The pseudo-spectral method is employed for the carrier fluid, utilizing N equidistant grid points in each direction, resulting in a grid spacing Δ [141, 153] and a 4-th order Runge-Kutta is used for the time integration with a time step of 0.04 Kolmogorov timescales. The forcing mechanism is to scale the wavenumbers of the fluid between 0.5 and 1.5 [168, 121]. This works by first integrating the equations without forcing, with resulting Fourier modes $\widehat{u_i^*}(\boldsymbol{\kappa}, t+\Delta t)$. Then, we multiply this result by a constant for Fourier modes with a wavenumber $|\boldsymbol{\kappa}|$ between 0.5 and 1.5. This is given below as:

$$\widehat{u_i}(\boldsymbol{\kappa})(t+\Delta t) = \widehat{u_i^*}(\boldsymbol{\kappa}, t+\Delta t)\sqrt{E_n(0)/E_n(t+\Delta t)}, \tag{4.3}$$

where $E_n(t+\Delta t)$ is the total energy of the modes with wavenumbers between 0.5 and 1.5 calculated by $\widehat{u_i^*}(\boldsymbol{\kappa}, t+\Delta t)$ and $\widehat{u_i}(\boldsymbol{\kappa})(t+\Delta t)$ is the final forced velocity profile. A linear forcing function, directly proportional to the velocity, can be used for its ease of implementation and physical relevance [100]; however the linear

forcing scheme requires twice as many grid points to resolve the smaller scales, reducing the attainable Reynolds number [142].

4.3.2 Inertial Particle Simulations

The Lagrangian particle simulations are conducted under the assumption of one-way coupling. The particles are treated as point spheres with negligible mass loading. Under these assumptions the Stokes drag model is employed as the friction model and the influence of gravity is considered [89]. Based on these assumptions, the equations of motion for an individual particle are formulated as follows:

$$\frac{dx_{p,i}}{dt} = v_{p,i}, \tag{4.4}$$

$$\frac{dv_{p,i}}{dt} = \frac{1}{\tau_p}\left(u_i - v_{p,i}\right) + g_i, \tag{4.5}$$

$$\tau_p = \frac{\rho_p d^2}{18\rho_f \upsilon}, \tag{4.6}$$

$$\tag{4.7}$$

where $x_{p,i}$ denotes the position of an individual particle in the spatial coordinate i, $v_{p,i}$ represents the velocity of the particle in the same coordinate, τ_p is the particle relaxation time, ρ_p the particle material density, g_i is the acceleration due to gravity in the i-th direction, and d the particle diameter.

The Stokes number Stk of a particle is defined as the ratio of the particle relaxation time τ_p to a characteristic timescale of the carrier fluid. For the scaling of particle preferential concentration, the Kolmogorov timescale τ_η is often used as this characteristic timescale and Stk is defined in Equation 4.8.

$$Stk = \frac{\tau_p}{\tau_\eta} = \tau_p\sqrt{\frac{\varepsilon}{\upsilon}}. \tag{4.8}$$

The Froude number Fr is defined as a ratio of gravitational forces to inertial forces. In this paper we define two Froude numbers, the first Fr_l is the ratio of gravitational forces to fluid inertia, the second Fr_p is the ratio of gravitational forces to particle inertia, these are given in Equations 4.9 and 4.10 respectively.

$$Fr_l = \frac{g}{\eta\tau_\eta^{-2}} = \frac{g\tau_\eta}{u_\eta}, \tag{4.9}$$

$$Fr_p = Stk \times Fr_l = \frac{g\tau_p}{u_\eta}. \tag{4.10}$$

The initial condition for the Lagrangian particles was an uniform random dis-

tribution, the time integration method used was a 4th order Runge-Kutta scheme that used cubic spline interpolation for fluid velocity measurements in both space and time. The particle simulation length was the same as the carrier fluid, namely 54 integral timescales and the timestep was also the same as the carrier fluid at 0.04 Kolmogorov timescales.

4.3.3 Simulation Conditions

The carrier fluid simulations were undertaken over a range of Taylor Reynolds numbers ($50 < Re_\lambda < 120$) in homogeneous isotropic turbulence. To meet the criteria for Direct Numerical Simulation (DNS) of turbulence flows, a crucial parameter is the Kolmogorov length scale, η, the grid spacing Δ, and their ratio η/Δ should be greater than 0.45 [130]. The number of grid points was kept constant at $N = 256$ per dimension, the domain length constant at $L = 6.28$ and the total number of simulation particles $N_p = 167$ million. The integral flow timescales for Reynolds numbers $Re_\lambda = 57$, 80, and 111 were $\tau_{Int} = 12.0\tau_\eta$, $15.0\tau_\eta$, and $20.0\tau_\eta$ respectively. More details on the simulation conditions as well as the carrier simulations and the inertial particle simulations are in Downing and Hardalupas [41].

Re_λ	N	Stk	Fr_l	η/Δ
57	256	[0.10, 0.25, 0.50, 1.00, 2.00, 5.00]	0.0	1.50
57	256	[0.10, 0.25, 0.50, 1.00, 2.00, 5.00]	2.0	1.50
57	256	[0.10, 0.25, 0.50, 1.00, 2.00, 5.00]	5.0	1.50
57	256	[0.07, 0.14, 0.37, 0.70, 1.40, 2.80, 3.71, 7.00]	0.0	1.50
80	256	[0.10, 0.25, 0.50, 1.00, 2.00, 5.00]	0.0	0.89
80	256	[0.10, 0.25, 0.50, 1.00, 2.00, 5.00]	2.0	0.89
80	256	[0.10, 0.25, 0.50, 1.00, 2.00, 5.00]	5.0	0.89
111	256	[0.10, 0.25, 0.50, 1.00, 2.00, 5.00]	0.0	0.59
111	256	[0.10, 0.25, 0.50, 1.00, 2.00, 5.00]	2.0	0.59
111	256	[0.10, 0.25, 0.50, 1.00, 2.00, 5.00]	5.0	0.59
111	256	[0.08, 0.13, 0.40, 0.64, 0.80, 1.29, 1.60, 2.57, 4.00, 6.43]	0.0	0.59

Table 4.1: Simulation parameters used for both the Eulerian carrier fluid and the Lagrangian particle simulations.

To ensure sufficient interactions between particles and turbulent structures during gravitational settling, the particle settling time (τ_S) across the computational domain must exceed the integral timescale (τ_{Int}). In simulations with the shortest settling times—corresponding to $Stk = 5.0$ and $Fr_l = 5.0$ (the largest particles under the strongest gravitational influence) — we obtain ratios of $\tau_S/\tau_{Int} = 1.75$, 1.30, and 1.14 at Reynolds numbers of 57, 80, and 111, respectively. This ensures that particles do not repeatedly encounter the same large eddies within the periodic domain, thereby avoiding unphysical clustering effects.

4.3.4 Spectra Analysis Methods

The main focus of this study is on the analysis of the power spectra (spectral density function) for the particle number density fluctuations of the particle concentration field. The power spectrum is defined as squared magnitude of the Fourier transform of the particle concentration field:

$$E_\rho(\kappa) = \frac{1}{\Delta\kappa L^3} \sum_{\kappa-\frac{\Delta\kappa}{2}\leq|\boldsymbol{\kappa}|<\kappa+\frac{\Delta\kappa}{2}} \langle\langle \widehat{n_p}(\boldsymbol{\kappa})\widehat{n_p}(\boldsymbol{\kappa})^* \rangle\rangle \,, \tag{4.11}$$

where $E_\rho(\kappa)$ is the power of the spectrum at wavenumber magnitude κ. It is calculated by the sum of the spectral density function in the region where the wavenumber magnitude κ lies within a slice of $\Delta\kappa$. The spectral density function is defined as the temporal average of the magnitude of the Fourier transform of the number density function $\widehat{n_p}(\boldsymbol{\kappa})$. The temporal averaging is performed by taking time slices across many different timesteps that are separated by integral flow timescales to minimise temporal correlations between slices.

The number density function in Fourier space is defined as:

$$\widehat{n_p}\left(\boldsymbol{\kappa}\right) = \iiint_{\boldsymbol{x}\in V_c} n_p(\boldsymbol{x}) \exp\left(-i\boldsymbol{\kappa}\cdot\boldsymbol{x}\right) d\boldsymbol{x}, \tag{4.12}$$

where $n_p(\boldsymbol{x})$ is the number density function at a position $\boldsymbol{x}$, and V_c is the total cubic domain of the simulation (periodic cube with side length L). The number density function $n_p(\boldsymbol{x})$ can be defined in many ways, and this influences the calculated power spectrum.

A common method is to take a box-averaged value or to 'bin' the particles into a mesh, as discussed by Jin et al. [86].

$$n_p(\boldsymbol{x}) = \mathrm{BoxCount}(\boldsymbol{x}), \tag{4.13}$$

this approach creates a number density field from the Lagrangian data, allowing the Fourier transform to be applied using FFT. This technique is also beneficial for obtaining spectra of other properties such as momentum and energy, as these too can be 'binned' similarly. This method can be completed in roughly $N\log(N)$ time, where N is the number of total grid points.

Alternatively, the particle number density spectra can be computed without discretizing it onto a mesh.

$$n_p(\boldsymbol{x}) = \sum_{j=1}^{N_p} \delta(\boldsymbol{x} - \boldsymbol{x}_{p,j}), \tag{4.14}$$

this method, outlined by Matsuda et al. [104], involves modelling the parti-

cles as direct delta functions and summing their contributions in Fourier space. However, this method cannot utilize the FFT algorithm and is prohibitively slow for large numbers of particles and wavenumbers. Its distinct advantage lies in its independence from a mesh, allowing it to capture clustering on length scales much smaller than the mesh size. This method requires $N_p \times N_\kappa$ calculations, where N_κ is the number of discrete wavenumber vectors $\boldsymbol{\kappa}$ in the shell of $\Delta\kappa$ (Equation 4.11). $\Delta\kappa$ was set to a value of $1/L$. This method is more inefficient than the box counting method, especially for many particles. However, it has a distinct advantage when trying to calculate the spectra at small distances of the order of the carrier fluid grid size or less. This is because there is no distortion of the particle number density function by binning, which gives a more accurate spectrum. As done in Matsuda et al. [104] we used the same method of eliminating white noise by removing the particle pair Fourier transform when the two particles are equal. Downing and Hardalupas [41] showed the effects on the particle number density spectra by using 'binning' and this direct approach. For this study the direct approach (Equation 4.14) is taken.

4.4 Results

4.4.1 Instantaneous spatial distributions of particle concentration

Figure 4.1 illustrates the instantaneous spatial distribution of particle concentration on a 2D slice through the flow for various Stokes numbers (Stk), Reynolds numbers (Re_λ), and Froude numbers (Fr_l). The particle concentrations are calculated using a box counting method (Box size $= L/N = 0.025$), which provides a clear visual representation of how these parameters influence particle clustering and void formation in turbulent flows.

The first row of Figure 4.1 (panels a, b, c) demonstrates the effect of varying Stokes number. As the Stokes number Stk increases from 0.25 to 1.0, the clusters of particles become more pronounced and the voids between them grow larger. However, when Stk increases further from 1.0 to 5.0, the intensity of these clusters begins to diminish, and the particles start to disperse more evenly across the 2D slice.

In the second row of Figure 4.1 (panels d, e, f), the impact of changing the Reynolds number is presented compared with the first row respectively (panels a, b, c). An increase in the Reynolds number leads to a significant variation in the size distribution of voids. Higher Reynolds numbers correspond to more turbulent and energetic flow conditions, which in turn cause a wider range of void sizes,

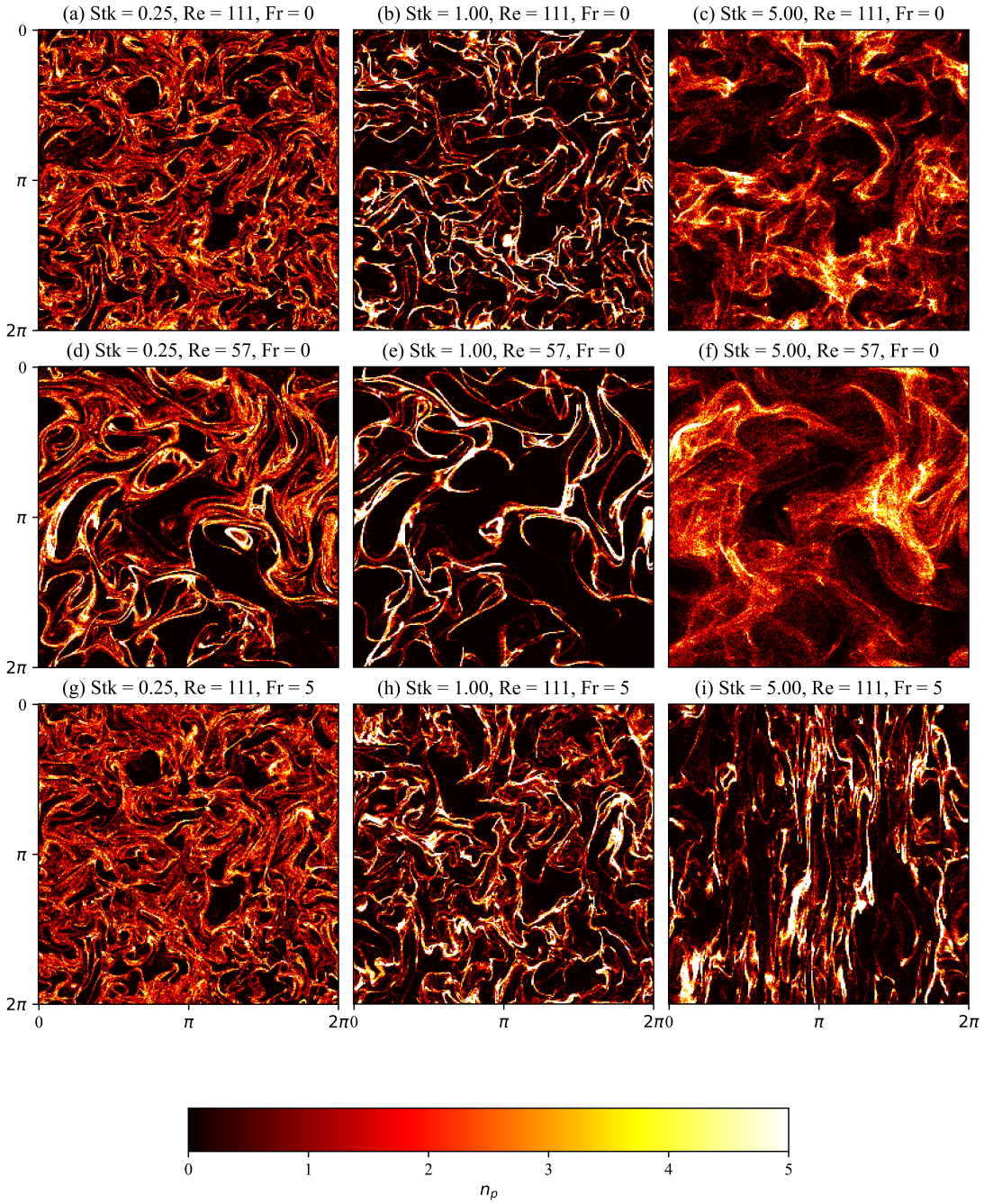


Figure 4.1: Instantaneous spatial distributions of particle concentration on a 2D slice through the flow for a range of different Stk, Re_λ, and Fr_l. Particle concentrations are calculated using a box counting method (Box size = $L/N = 0.025$).

indicating a more complex and heterogeneous distribution of particles.

The third row of Figure 4.1 (panels g, h, i) highlights the influence of the Froude number in comparison to the first row (panels a, b, c). At $Stk = 0.25$ (panels a and g), the addition of gravity results in negligible or no observable changes. However, at $Stk = 1.0$ (panels b and h), a slight difference is observed, with smaller voids and more cluster lines appearing in the presence of gravity.

The most significant contrast occurs at $Stk = 5.0$ (panels c and i), where, without gravity, the clusters are diffuse, but with the introduction of strong gravitational effects, the clusters align vertically with the gravitational force, becoming sharper, thinner, and less diffuse.

These observations highlight the intricate interplay between the Stokes, Reynolds, and Froude numbers in determining the spatial distribution of particles in turbulent flows. The box counting method employed here effectively captures these variations, providing a comprehensive understanding of how these parameters influence particle clustering and void formation.

4.4.2 Spectra of particle number density fluctuations for different Stokes numbers

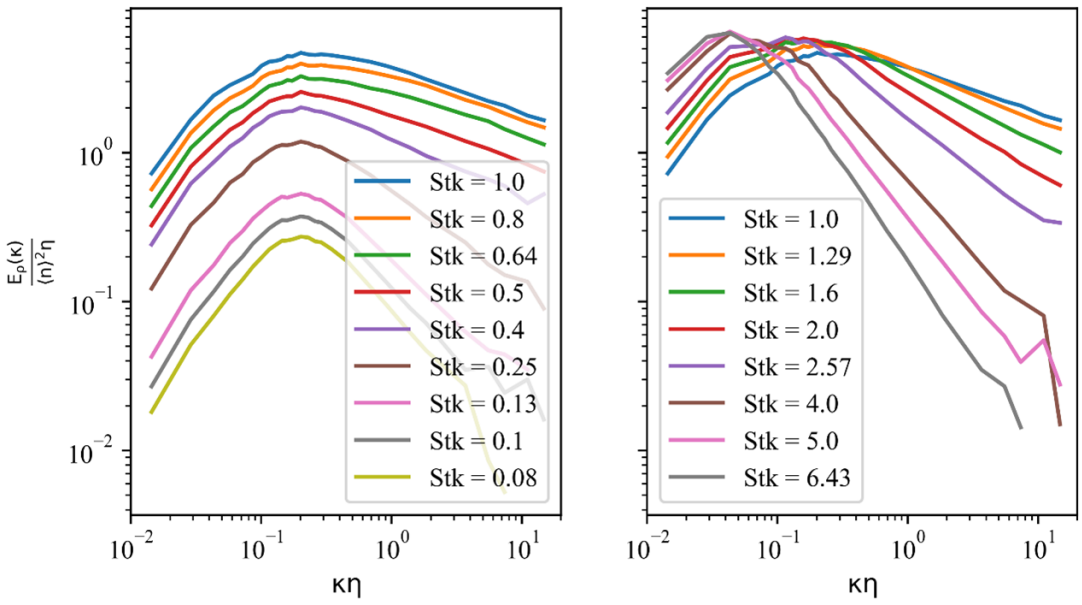


Figure 4.2: Spectral energy of the particle number density fluctuations against the wavenumber for a range of Stokes numbers (left < 1.0, right > 1.0). Spectra are at constant $Re_\lambda = 111$, and $Fr_l = 0$. Left panel shows Stokes numbers less than 1.0 and right panel shows Stokes numbers greater than 1.0.

Figure 4.2 presents the spectral energy of particle number density fluctuations plotted against the wavenumber for a range of different Stokes numbers, with the left panel showing Stokes numbers less than 1.0 and the right panel showing Stokes numbers greater than 1.0. These spectra are obtained at Reynolds number (Re_λ) of 111 and Froude number (Fr_l) of 0.

The overall shape of the power spectra follows the classic pattern of an increasing power law on the left-hand side (low wavenumber) and a decreasing power law on the right-hand side (high wavenumber). This characteristic shape underscores

the balance between particle clustering intensity and void formation across different scales of turbulence.

For Stokes numbers less than one, the peak of the spectral energy is consistently observed at around $\kappa\eta = 0.2$, aligning with previous findings by Matsuda et al. [104]. Note that with the factor of 2π from using a Fourier transform this is $2\pi\kappa\eta = 1.26$. This consistency indicates that the influence of turbulent eddies on particle clusters is relatively stable for low Stokes numbers. The particles are influenced by eddies across all scales, including the smallest Kolmogorov scale eddies. As the Stokes number approaches 1.0, the overall spectral power increases by over an order of magnitude, suggesting more intense clustering. The shape of the spectrum also flattens, implying subtle changes in the distribution of voids and clusters. The stationary peak at $\kappa\eta = 0.2$ suggests that the scale of voids remains consistent, while the increased power reflects higher clustering intensity.

For Stokes numbers greater than unity, there is a noticeable shift of the peak of the spectrum towards larger length scales. This shift occurs because particles with higher Stokes numbers effectively filter out the high spatial and temporal frequency components of the flow. These particles tend to be centrifuged out of eddies larger than a representative size, leading to preferential concentration. Simultaneously, they are dispersed by smaller eddies due to uncorrelated stirring effects. For particles with Stokes numbers less than unity, the representative size is smaller than the Kolmogorov scale, resulting in a consistent increase in power and a stable spectral shape. In contrast, for particles with Stokes numbers greater than unity, this representative size enters the inertial range. Consequently, there is a significant increase in spectral power at large scales due to enhanced centrifuging effects, while a steep drop-off in power at smaller scales occurs due to the dispersion effects of smaller eddies.

It is important to note that at high wavenumbers, there is some uncertainty in the spectral data due to the finite number of particles used in the simulations. This limitation can affect the accuracy of the spectral energy at smaller scales, particularly for extreme Stokes numbers.

4.4.3 Spectra of particle number density fluctuations for different Reynolds numbers

Figure 4.3 illustrates the spectral energy of particle number density fluctuations against the wavenumber for different Stokes numbers and varying Reynolds numbers ($Re_\lambda = 57,\ 81,\ \&\ 111$). These spectra are generated at a constant Froude number (Fr_l) of 0. Traditionally, it is assumed that the power spectrum of particle number density fluctuations is independent of the Reynolds number. This assump-

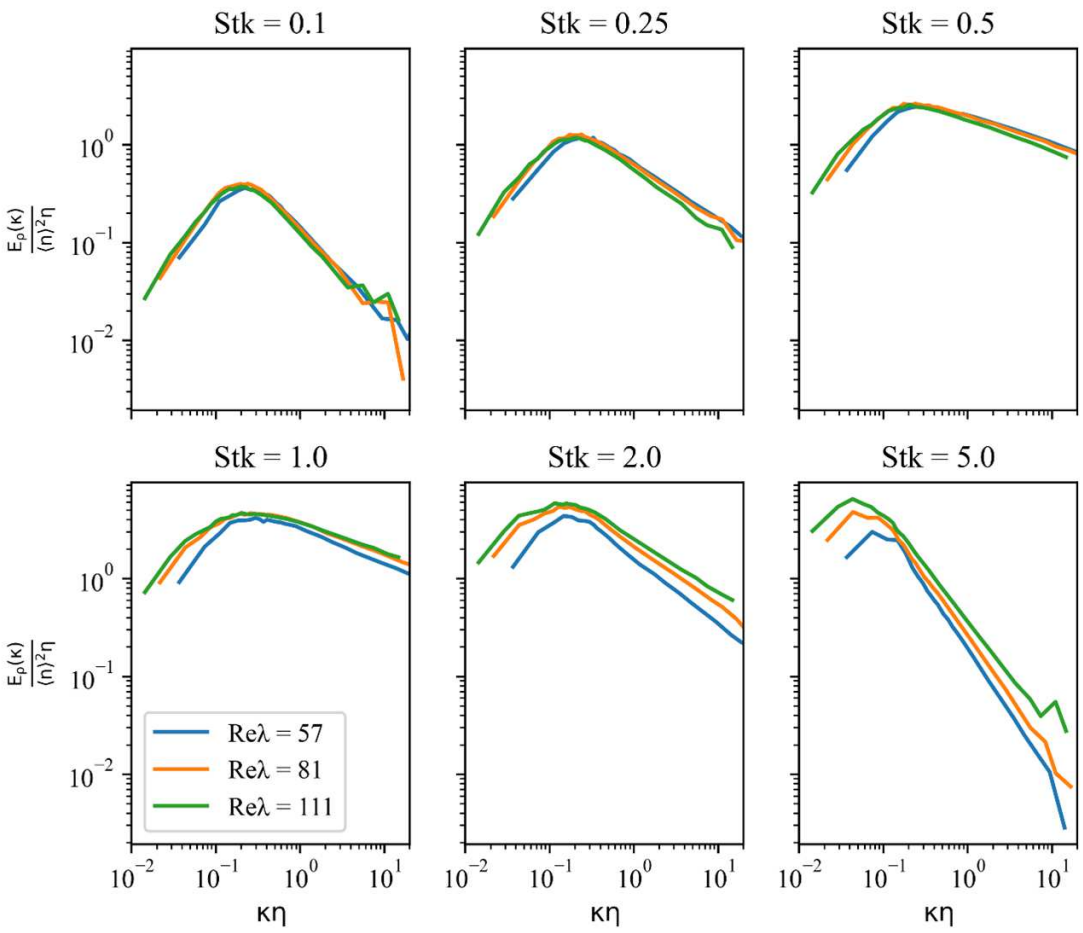


Figure 4.3: Spectral energy of the particle number density fluctuations against the wavenumber for a range of Stokes numbers and Reynolds numbers (Re_λ = 57, 81, & 111). These spectra are at constant $Fr_l = 0$.

tion is satisfied for particles with small Stokes numbers, ($Stk < 0.5$), provided the Reynolds number is sufficiently high. In these cases ($Re_\lambda = 81$ & 111), the spectral energy distribution remains relatively similar across different Reynolds numbers, indicating that the turbulence intensity does not significantly alter the clustering behaviour of low inertia particles. This is because, at high Reynolds numbers, the turbulence is sufficiently developed to exhibit a self-similar multi-scale nature, which ensures that the clustering of small inertia particles is influenced by a wide range of eddy scales.

However, for a lower Reynolds number of $Re_\lambda = 57$, deviations can be seen across all Stokes numbers, including the smaller ones. This suggests that at lower turbulence intensities, the independence of the power spectrum from the Reynolds number does not hold, and the clustering behaviour is more sensitive to changes in the Reynolds number. In such cases, flow turbulence may not be fully developed, and the range of active turbulent eddy scales is limited, leading to more pronounced effects of Reynolds number variations on particle clustering.

For larger Stokes numbers ($Stk = 2.0$ & 5.0), the power spectrum shows noticeable variations with changing Reynolds numbers. Specifically, the peak of the spectrum shifts to lower wavenumbers (to the left) and increases in power as the Reynolds number increases. This shift and increase in spectral power suggest that higher turbulence intensity enhances the clustering of particles with greater inertia, leading to more pronounced and larger-scale particle aggregates. This behaviour can be explained by the resonance condition, where particles with higher Stokes numbers interact more strongly with larger turbulent eddies in the flow, leading to enhanced clustering at larger scales [176].

Despite these changes in peak position and power of the spectra, the overall shape of the spectrum remains consistent throughout the range of Reynolds numbers examined. This consistent shape indicates that while the intensity and scale of clustering are influenced by the Reynolds number at higher Stokes values, the fundamental nature of the clustering process remains unchanged. This reflects the multi-scale self-similar nature of turbulence, where clusters of inertial particles form due to the interaction with a spectrum of eddy sizes, which is maintained across different Reynolds numbers.

These findings highlight the nuanced role of Reynolds number in the spectral energy distribution of particle number density fluctuations. While particles with small Stokes numbers exhibit a Reynolds number-independent clustering behaviour, at sufficiently high Reynolds numbers, particles with higher Stokes numbers are significantly affected by the turbulence intensity, resulting in larger and more intense clusters. This reinforces the importance of considering Reynolds number effects in studies of particle-laden turbulent flows, especially for particles with higher inertia. Matsuda et al. [104] presented a series of spectra for a variety of Reynolds numbers ($Re_\lambda = 127,\ 204,\ 322,\ \&\ 531$), but only at a single Stokes number ($Stk = 1.0$). Their results are consistent with the current study, where the high wavenumber part of the spectrum appears independent of Reynolds number. However, the low wavenumber part of the spectrum shows significant deviations as the Reynolds number changes, suggesting that the clustering at larger scales is more sensitive to changes in turbulence intensity. This aspect was not investigated further by Matsuda et al. [104] due to it being outside their relevant range for cloud reflectivity, and they did not explore the effect of Reynolds number at different Stokes numbers. Our findings extend their observations by demonstrating the critical role of Reynolds number across a range of Stokes numbers, emphasizing the need to account for turbulence intensity when analysing particle clustering in turbulent flows.

4.4.4 Spectra of particle number density fluctuations for different Froude numbers

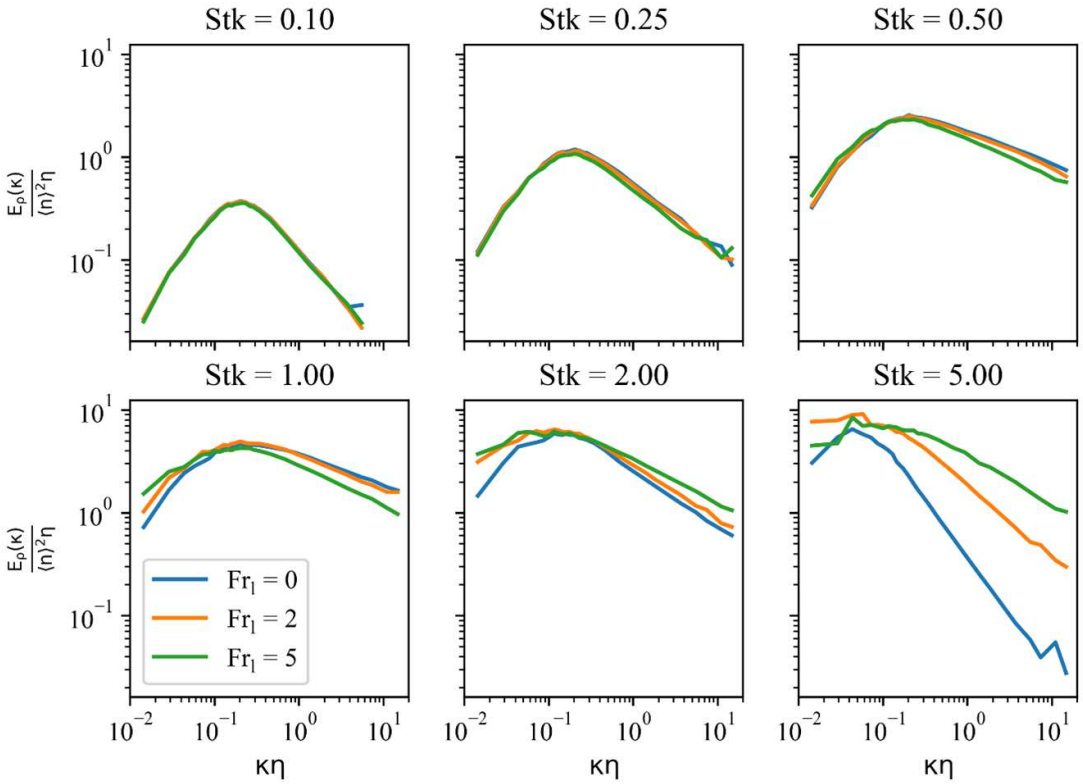


Figure 4.4: Spectral energy of the particle number density fluctuations against the wavenumber for a range of different Stokes numbers and Froude numbers ($Fr_l = 0.0,\ 2.0,\ \&\ 2.0$). These spectra are at constant $Re_\lambda = 111$.

Figure 4.4 depicts the spectral energy of particle number density fluctuations as a function of wavenumber for various Stokes and Froude numbers, based on DNS data at a Reynolds number (Re_λ) of 111 and Figure 4.5 depicts the spectral energy of particle number density fluctuations with changing Reynolds and Froude numbers for fixed Stokes at $Stk = 1.0$, and 5.0. The gravitational impact on particle clustering in turbulent flows is evident across different Stokes numbers (Stk).

For small Stokes numbers ($Stk < 0.5$), gravitational effects are minimal. The spatial distributions of particles for $Fr_l = 5.0$ closely resemble those for $Fr_l = 0.0$, with similar clustering and void areas observed (See Figure 4.1). This similarity is attributed to the weak inertial forces at low Stokes numbers, making particles more prone to follow the fluid motion rather than being influenced by gravity. As Stk increases, the influence of gravity becomes more pronounced. For large Stokes numbers ($Stk > 2.0$), the spatial distribution of particles for $Fr_l = 5.0$ shows clusters extending vertically, unlike the more prominent large-scale void

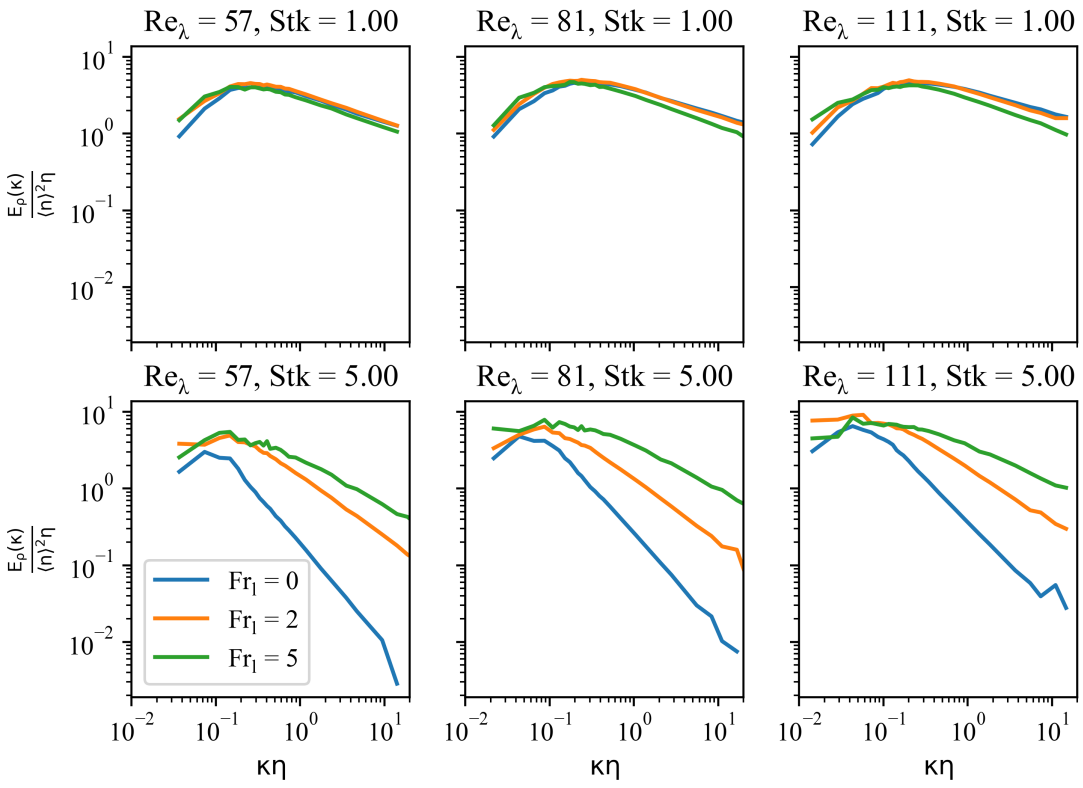


Figure 4.5: Spectral energy of the particle number density fluctuations against the wavenumber for a range of Reynolds numbers (Re_λ = 57, 80, & 111) and Froude numbers (Fr_l = 0.0, 2.0, & 2.0). These spectra are at two different Stokes numbers Stk = 1.0, and 5.0.

areas observed for $Fr_l = 0.0$. This vertical extension of clusters can be attributed to the gravitational settling effects, which dominate over the turbulent eddies' dispersive action (See Figure 4.1).

For all Stokes numbers, the particle number density spectrum at small wavenumbers (large length scales) is larger for increasing Fr_l, with the difference increasing significantly as Stk increases. This increase is due to the increased particle-turbulence interaction time, where gravitational settling lengthens the particle residence time in a large length-scale eddy, thus increasing cluster formation [5, 174]. This mechanism highlights the importance of gravity in modifying the residence time of particles within turbulent structures, leading to enhanced clustering at larger scales.

For intermediate and small Stokes numbers ($Stk \leq 1.0$), the spectrum of the particle number density fluctuations is diminished at high wavenumbers (small length scale), whereas for larger Stokes numbers ($Stk \geq 2.0$), the particle number density spectrum is enhanced at high wavenumbers. This trend aligns with the findings of Matsuda et al. [105], who observed similar spectral behaviour under varying Froude numbers.

We attribute the same mechanism to both the diminishing spectrum for small Stokes numbers and the enhancement for large Stokes numbers. Due to the settling velocities, particles of all sizes interact less with the small length-scale eddies. For small Stokes numbers, these small-scale eddies still cause clustering, so a decrease in the interaction time leads to a decrease in the power of the particle number density spectrum at high wavenumbers. However, for large Stokes numbers, the scale-dependent clustering mechanism Yoshimoto and Goto [176] implies that small-scale eddies attempt to disperse the particles. Consequently, reduced interaction time means less dispersion, resulting in an enhancement of the power of the particle number density spectrum at high wavenumbers. This finding underscores the importance of gravity on particle clustering, particularly for high Stokes numbers Gustavsson et al. [65].

As the Reynolds number increases from 57 to 111, we observe a consistent overall trend across all cases (see Figure 4.5). Notably, the effects of varying the Reynolds number and Froude number appear to compound, particularly at higher Stokes numbers ($Stk = 5.0$). As discussed in the previous section, increasing the Reynolds number can enhance clustering for large Stokes numbers, and from Figure 4.4, we see that stronger gravitational effects further amplify this clustering. This suggests an interplay between turbulence intensity and gravitational settling, both contributing to the preferential concentration of particles.

4.4.5 Empirical Relations

In this section, we develop a new empirical model for the power spectrum of particle number density fluctuations as a function of wavenumber, inspired by the work of Matsuda et al. [104]. The approach assumes that the power spectrum asymptotically approaches a power law as the wavenumber approaches both zero and infinity, as described by Equations 4.15 and 4.16. By smoothly connecting these two asymptotic regions, following the methodology proposed by Hill [74], we derive Equation 4.17.

$$\frac{E_\rho(\kappa)}{\langle n\rangle^2\eta} \approx C_1(\kappa\eta)^\alpha, \tag{4.15}$$

$$\frac{E_\rho(\kappa)}{\langle n\rangle^2\eta} \approx C_2(\kappa\eta)^\beta, \tag{4.16}$$

$$\frac{E_\rho(\kappa)}{\langle n\rangle^2\eta} = \frac{C_1(\kappa\eta)^\alpha}{\left(1+\frac{C_1}{C_2}^{\frac{2\gamma}{\alpha-\beta}}\right)^{\frac{\alpha-\beta}{2\gamma}}}, \tag{4.17}$$

In these equations, C_1, α, C_2, β, and γ are dimensionless parameters. Our model deviates from that suggested by Matsuda et al. [104] by considering not

only how these five parameters change with the Stokes number, but also how they simultaneously vary with the Reynolds number and Froude number. This extension allows the new model to remain valid over a range of Reynolds and Froude numbers, in addition to the original dependence on Stokes number. Consequently, the equations for these parameters take on different forms to accommodate these additional variables.

With this definition, we can describe any power spectrum using just five variables. By analysing how these variables change across the parameter space defined by the Stokes, Reynolds, and Froude numbers, we can begin to describe and predict the spectrum of particle number density fluctuations over a wide range of conditions.

To address the limitations of the standard Froude number, we define a modified Froude number (Fr_m) in Equation 4.18. Traditional Froude numbers are unsuitable for power laws because when gravity is zero ($Fr_l = 0$), the power spectrum remains defined, conversely this problem does not occur at zero Stokes or Reynolds numbers, the power spectrum has no meaningful interpretation. Thus, we redefine the Froude number to have a minimum value of 1. Additionally, it is formulated as an even function, since gravity can be reversed, and due to the symmetry of the problem, we expect the same power spectrum.

$$Fr_m = \sqrt{1 + Fr_p^2}, \tag{4.18}$$

$$C_1 = 33.25 Stk^{0.616} {Fr_m}^{0.554}, \tag{4.19}$$

$$\alpha = 65.26 \frac{Stk^{0.145}}{Re_\lambda^{0.658}} \log\left[1.192\left(1 + 0.002\frac{Re_\lambda^{0.992} Fr_m^{0.140}}{Stk^{0.736}}\right)\right], \tag{4.20}$$

$$C_2 = 0.0406 \frac{Re_\lambda^{0.464} Fr_m^{1.400}}{Stk^{0.923}} \frac{\left(1 + \frac{244.354}{Stk^{2.506} Fr_m^{1.200}}\right)^{0.960}}{\left(1 + 1.044\frac{Re_\lambda^{0.197} Fr_m^{0.176}}{Stk^{2.177}}\right)^{2.320}}, \tag{4.21}$$

$$\beta = -23.575 \frac{Stk^{0.213}}{Fr_m^{0.372}} \log\left[\frac{\left(1 + 2.270\frac{Fr_m^{0.031}}{Stk^{0.070}}\right)^{0.557}}{1.944\left(1 + 6.768 Stk^{5.133}\right)^{-0.008}}\right], \tag{4.22}$$

$$\gamma = \frac{9.033}{Re_\lambda^{0.412} Fr_m^{0.455}}, \tag{4.23}$$

Equations 4.19 to 4.23 provide the relationships of the five parameters as a function of Stokes, Reynolds, and Froude numbers. These formulas were derived using a least squares technique that minimised the difference between the empirical power spectrum and the computed power spectra across a variety of conditions, ranging from $Stk = 0.1 - 5.0$, $Re_\lambda = 57 - 111$, and $Fr_l = 0.0 - 5.0$. The least

squares technique used was a symbolic regression, which trialled formulas for the five parameters simultaneously within the wavenumber range $10^{-1} \leq \kappa\eta \leq 10^{2}$ across all simulation conditions. This contrasts with Matsuda et al. [104] which found formulas to each parameter separately by fitting straight lines in log-log space. The use of symbolic regression is the primary motivation for the modified Froude number (Fr_m) as this stabilised the symbolic search method.

By establishing these relationships, the model enables a comprehensive description and prediction of the power spectrum across diverse turbulent flow conditions. This advancement allows for the effective characterisation of particle clustering and void formation influenced by a wide range of turbulent flow parameters, enhancing our understanding and predictive capabilities in particle-laden turbulent flows at large scale spaces. This new model's validity over varying Reynolds and Froude numbers, in addition to Stokes number, represents a significant improvement over existing models such as Matsuda et al. [104], providing a more versatile and comprehensive tool for analysing and predicting particle-laden turbulence. Figures 4.6 – 9 provide plots on how C_1, α, C_2, β, and γ change over a wide range of conditions. We extend the limits of the model by plotting results up to $Stk = 10.0$, $Re_\lambda = 200$, $Fr_l = 10.0$ to show how the model looks under extrapolation.

Figure 4.6 presents the plots of parameter C_1 of Equation 4.15 as a function of Stokes, Reynolds, and Froude numbers. The parameter C_1 represents the left-hand side power law constant of the empirical model. According to Equation 4.19, C_1 follows a power law relationship with no dependence on the Reynolds number, simplifying its analysis. The graphs show a positive correlation between C_1 and Stokes number, indicating that as the particle size increases, the power spectrum of particle number density fluctuations for large scales also increases. This observation aligns with the findings from previous sections, where larger particles tend to cluster more intensely at larger scales due to the influence of larger eddies.

The positive correlation between C_1 and Stokes number can be attributed to the greater response of larger particles to the larger eddies of the turbulent flow. Larger particles, with higher inertia, interact more strongly with these larger eddies, leading to enhanced clustering and increased spectral energy at large scales. This mechanism is consistent with the findings of Yoshimoto and Goto [176] and aligns with the observations that larger eddies play a significant role in preferentially concentrating particles with higher Stokes numbers.

The relationship between C_1 and Froude number is also evident in Figure 4.6. As the Froude number increases, C_1 shows an upward trend, indicating that gravitational effects significantly influence particle clustering. This correlation can be explained by the gravitational settling mechanism, which increases the interaction time between particles and large-scale turbulent eddies. As gravity acts on the

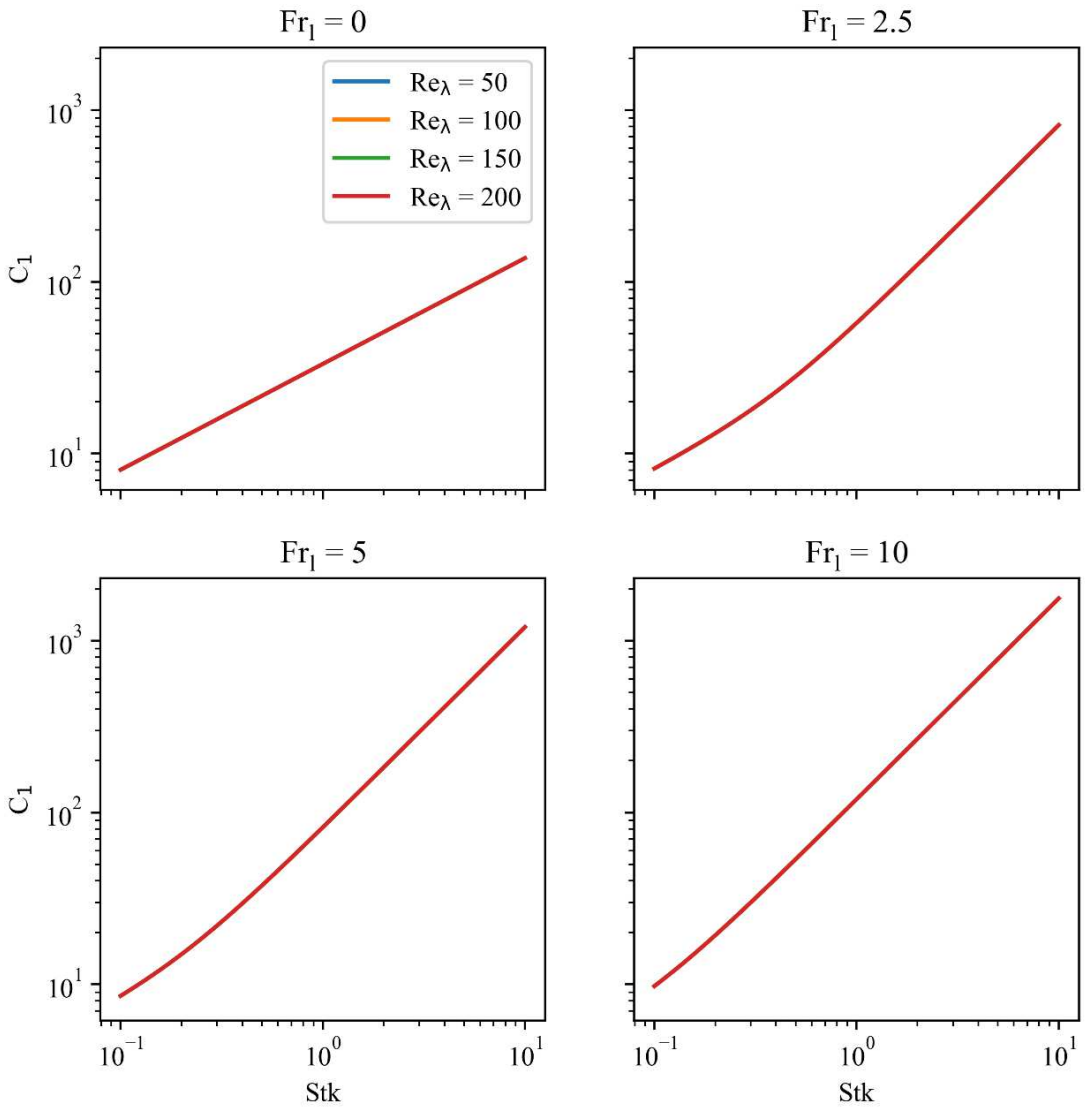


Figure 4.6: Plots of parameter C_1 of Equation 4.15 as a function of Stokes number (see Equation 4.19) . Each different colour line represents a different Reynolds number (in this case all lines coincide as C_1 is independent of Reynolds number (Equation 4.19)). Each graph corresponds to a different Froude number Fr_l.

particles, especially those with higher inertia (larger Stokes numbers), it enhances their residence time within large eddies, promoting more pronounced clustering at larger scales. This gravitational settling effect leads to an increase in C_1 as the Froude number increases, highlighting the critical role of gravity in modulating particle concentration spectra [5, 174, 65].

Figure 4.7 presents plots of the exponent α of Equation 4.15 as a function of Stokes, Reynolds, and Froude numbers. The parameter α represents the left-hand side power law exponent in the empirical model. As demonstrated in Figure 4.3, there is a noticeable dependence of the low wavenumber portion of the power spectra on the Reynolds number. Figure 4.6 shows that this dependence is not

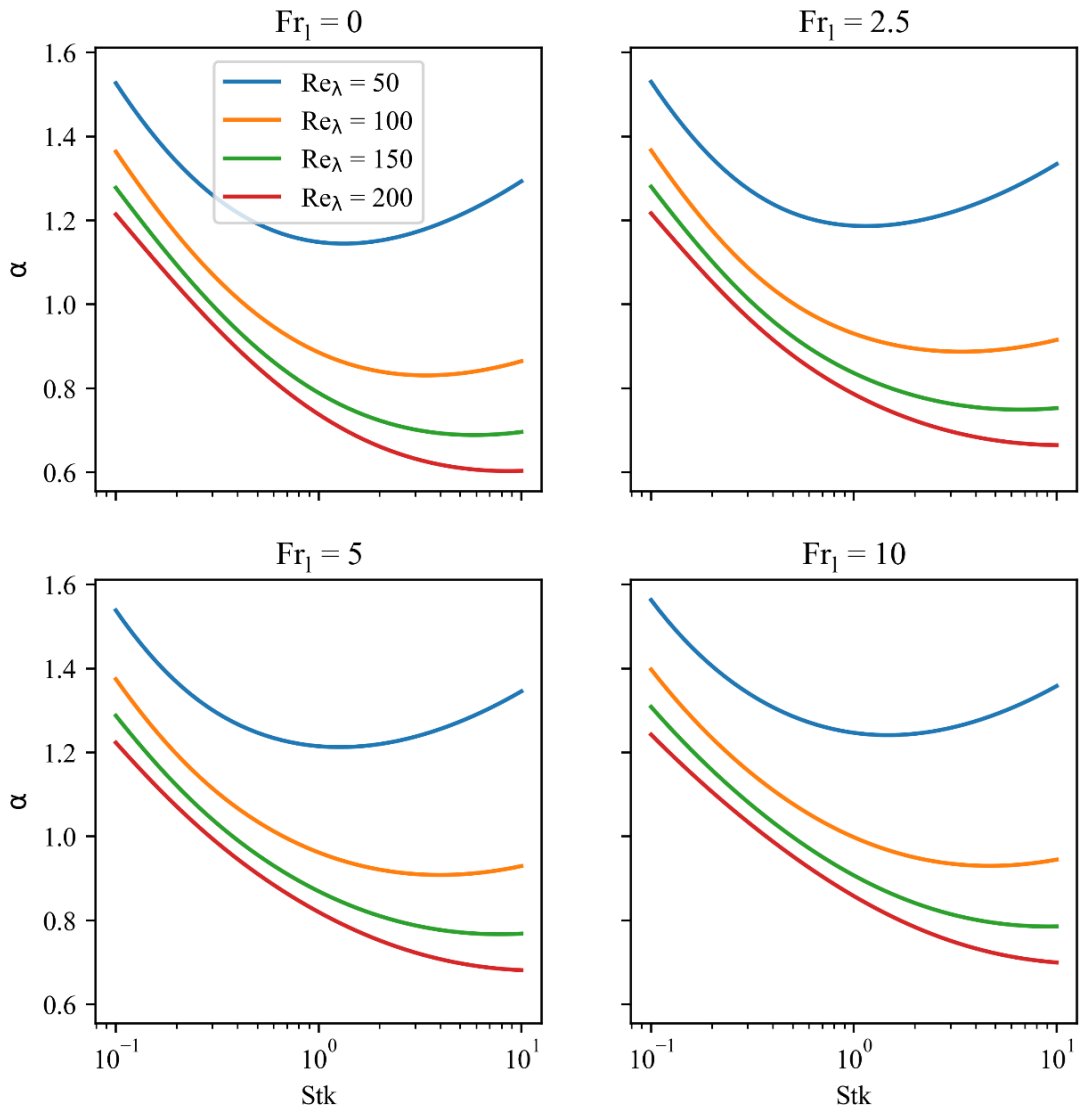


Figure 4.7: Plots of the exponent α of Equation 4.15 as a function of Stokes number (see Equation 4.20). Each different colour line represents a different Reynolds number. Each graph corresponds to a different liquid Froude number.

reflected in the power law constant (C_1), but rather in the exponent (α).

For moderate to high Reynolds numbers (above 100), α sharply decreases with increasing Stokes number before flattening out. This trend suggests a universal behaviour for large particles at large length scales when the Reynolds number is sufficiently high. The sharp decrease in the exponent corresponds to a flatter power spectrum, indicating that the energy distribution becomes more uniform across different scales. This phenomenon can be attributed to the greater interaction of larger particles with a wider range of turbulent eddy sizes, as described by Yoshimoto and Goto [176].

At low Reynolds numbers, α exhibits a distinct minimum as the Stokes number increases. This behaviour implies that for lower turbulence intensities, the particle

clustering dynamics are more complex and do not conform to the same universal behaviour observed at higher Reynolds numbers. The less developed flow turbulence at lower Reynolds numbers limits the range of the eddy scales, resulting in a more varied impact on particle clustering.

The decrease in α with increasing Reynolds number is significant. This trend may indicate that the dimensionless Stokes number and power spectrum of particle number density fluctuations relationships, which are based on Kolmogorov scales, might not be entirely appropriate for describing large-scale clustering. Instead, different length and time scales might be more relevant in this regime, suggesting the need for a revised framework to better capture these dynamics.

In contrast, the dependence of α on the Froude number is much less pronounced than its dependence on the Reynolds number. While gravitational effects play a crucial role in particle clustering, they do not significantly alter the exponent of the power law at the low wavenumber side of the spectrum. This indicates that the primary influence of gravity is on the clustering intensity and scale rather than on the distribution of energy across scales.

Thus, for the left-hand side power law, both the exponent (α) and the constant (C_1) are heavily dependent on the Stokes number. This behaviour is consistent with the findings of Matsuda et al. [104], which observed similar trends. However, in our model, the power law constant changes with the Froude number, while the power law exponent changes with the Reynolds number, highlighting the distinct influences of these parameters on particle clustering dynamics. These results underscore the complex interplay between particle inertia, turbulence intensity, and gravitational effects in shaping the spectral energy distribution of particle concentration fluctuations in turbulent flows.

Figure 4.8 presents plots of parameter C_2 of Equation 4.16 as a function of the Stokes, Reynolds, and Froude numbers. The parameter C_2 represents the right-hand side power law constant in the empirical model. The dependence of C_2 (see Equation 4.21) on Reynolds number is relatively insignificant at low Stokes numbers, and there is a positive correlation as the Stokes number increases. The positive correlation between C_2 and Reynolds number at higher Stokes numbers aligns with the observations in Figure 4.3. As shown in Figure 4.3, the Reynolds number has little effect on the power spectrum at low Stokes numbers but becomes increasingly significant at higher Stokes numbers.

The relationship between C_2 and Stokes number is complex and highly dependent on the Froude number. For low Froude numbers, C_2 exhibits a clear peak at around $Stk = 1.0$. This peak occurs because, at small Stokes numbers, increasing the Stokes number enhances the concentrating effect of small length scale eddies (high wavenumber). However, at larger Stokes numbers, further increases in the

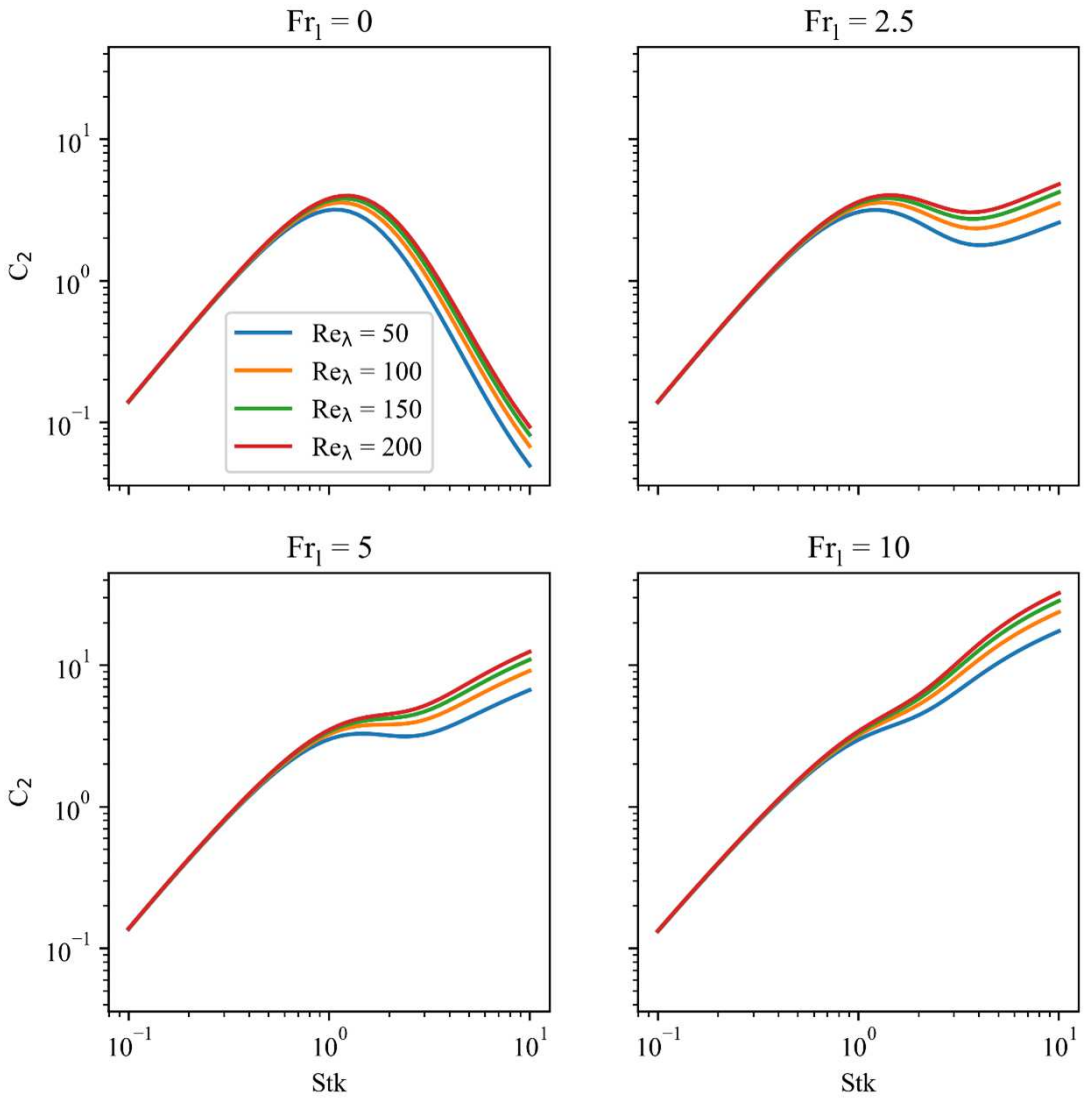


Figure 4.8: Plots of parameter C_2 of Equation 4.16 as a function of Stokes number (see Equation 4.21). Each different colour line represents a different Reynolds number. Each graph corresponds to a different Froude number Fr_l.

Stokes number enhance the dispersion properties of small-scale turbulent eddies, reducing the clustering effect. This behaviour is consistent with the findings of Matsuda et al. [104], where a similar dependence was observed.

As the influence of gravity increases (higher Froude numbers), the interaction time between particles and small-scale eddies decreases due to the settling velocity. This effect differs between large and small particles. For larger Stokes numbers, the settling velocity reduces the interaction time with small eddies, diminishing their dispersive effect and thereby enhancing clustering at high wavenumbers. For smaller Stokes numbers, reduced interaction time with small eddies means reduced clustering at these scales, as these particles are more prone to following fluid motion. This modulation by gravity enhances the clustering effect for larger

particles, while reducing it for smaller ones, consistent with the observations in Figure 4.4.

Overall, the parameter C_2 illustrates the intricate interplay between Stokes, Reynolds, and Froude numbers in defining the power spectra of particle number density fluctuations. While the dependence on Reynolds number is minimal at low Stokes numbers, it becomes more relevant at higher Stokes numbers, highlighting the role of turbulence intensity. Additionally, the Froude number significantly influences the relationship between C_2 and Stokes number, emphasizing the role of gravity in modulating particle clustering dynamics. This comprehensive understanding aids in predicting and analysing the behaviour of particle-laden turbulent flows under various conditions.

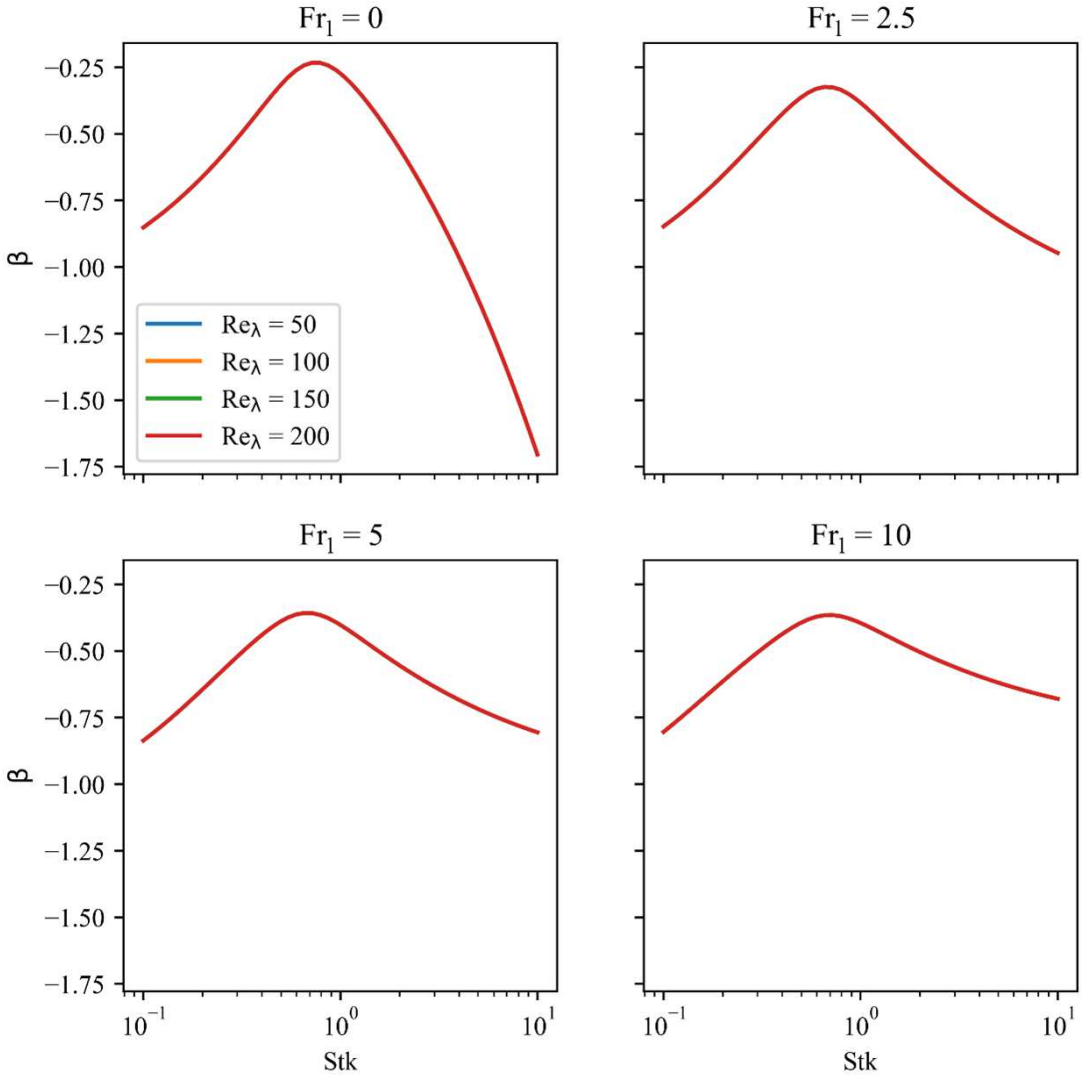


Figure 4.9: Plots of exponent β of Equation 4.16 as a function of Stokes number (see Equation 4.22). Each different colour line shows a different Reynolds number. Each graph corresponds to a different Froude number Fr_l.

Figure 4.9 presents plots of β as a function of Stokes, Reynolds, and Froude

numbers. The parameter β represents the right-hand side power law exponent in the empirical model. Notably, β is independent of the Reynolds number, indicating that variations in turbulence intensity do not significantly impact this exponent across the range of Reynolds numbers studied.

For all Froude numbers, there is a distinct peak in the value of β around Stokes number of 1. This peak can be attributed to the competing mechanisms of dispersion and concentration at the small scales of turbulence for different particle sizes. Similar to the argument for C_2, this peak at $Stk = 1.0$ reflects the balance between the clustering effect of small-scale eddies and the dispersive effect as particle inertia increases.

For small Froude numbers, β decreases sharply with increasing Stokes number, leading to results consistent with Matsuda et al. [104]. However, as the Froude number increases, this decrease of the value of β with increasing Stokes number becomes much more gradual. This indicates that as particles become larger, the power spectrum becomes flatter at high wavenumbers, reflecting a more uniform distribution of particle concentration. Higher gravitational effects modulate the influence of particle size on particle clustering dynamics, reducing the rate of decrease in the value of β. Gravitational forces counteract the dispersion caused by small-scale eddies, leading to a more gradual change in the power law exponent, for the same reasons as C_2.

Overall, the right-hand side power law (both the constant C_2 and exponent β) for high wavenumbers appears largely independent of the Reynolds number, except at the highest Stokes numbers, where there is a slight dependence on Reynolds number for the power law constant. However, the dependence on Froude number is very significant, especially at large Stokes numbers. This highlights the crucial role of gravity in modulating the spectral energy distribution at small scales, emphasizing the need to consider Froude number effects in studies of particle-laden turbulent flows.

Figure 4.10 presents the plots of parameter γ of Equation 4.17 as a function of Stokes, Reynolds number and Froude numbers (see Equation 4.23). The parameter γ describes the amount that the power spectrum is spread out around the transition point between the two power laws (how sharp this transition is). This parameter follows a simple power law with both the Reynolds number and the modified Froude number, indicating a clear relationship between these flow parameters and the spread of the spectrum.

As shown in Figure 4.10, the power spectra become more spread out (indicated by lower values of γ) with increasing Reynolds number and Froude number. The increased Reynolds number leads to a higher ratio of length scales between the smallest and largest eddies, which broadens the spectrum. This broadening re-

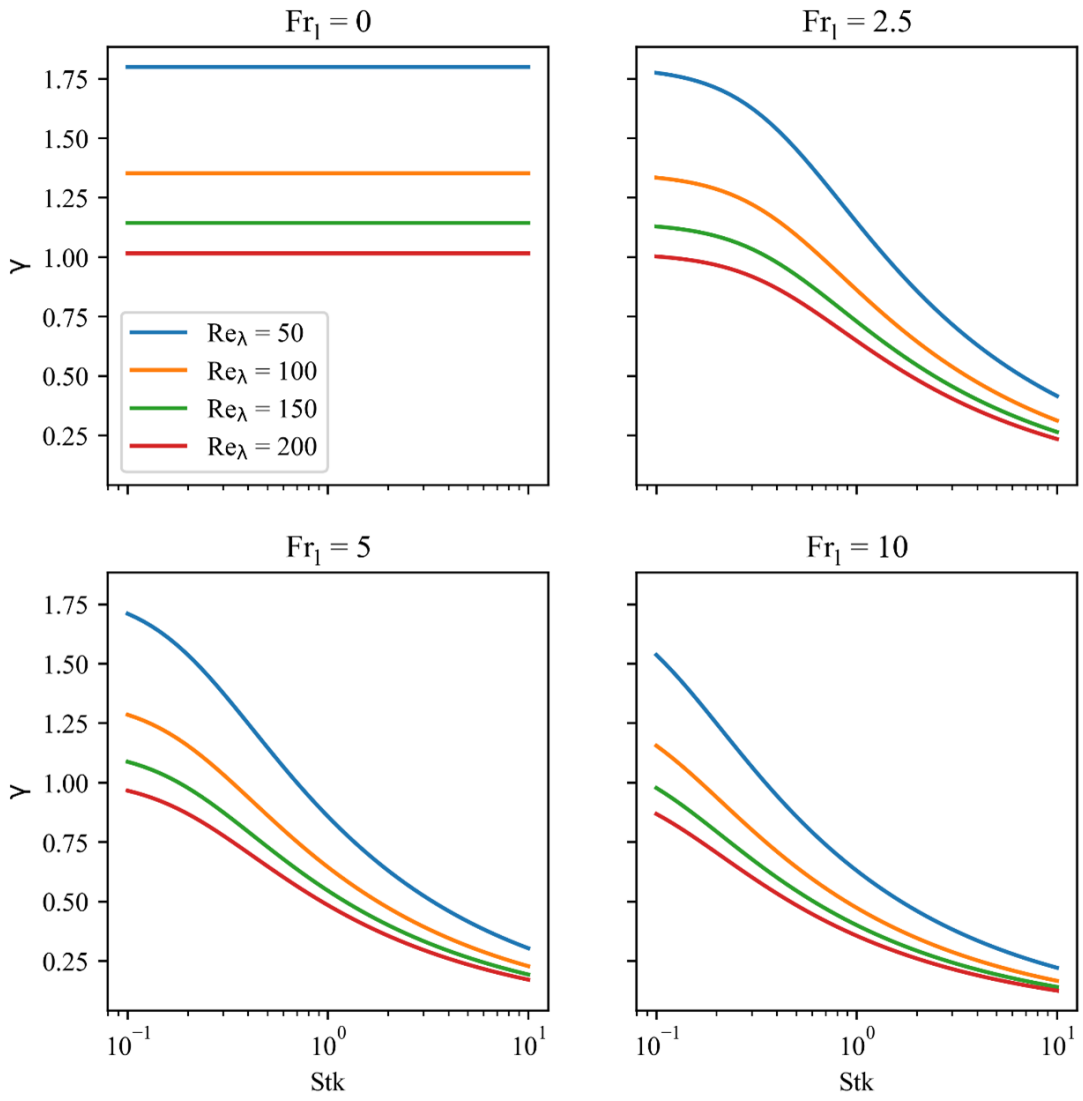


Figure 4.10: Plots of parameter γ of Equation 4.17 as a function of Stokes number (see Equation 4.23). Each different colour line represents a different Reynolds number. Each graph corresponds to a different Froude number Fr_l.

flects the enhanced range of turbulent eddies that contribute to particle clustering, resulting in a more extensive distribution of energy across different scales.

The influence of increasing Reynolds number is expected, since higher turbulence intensity introduces a wider range of eddy sizes, from the smallest Kolmogorov scales to the largest integral scales. This increased range directly contributes to a wider spectrum, indicating more complex and varied interactions among particles at different scales.

The effect of higher Froude numbers, however, is less straightforward. The observation that higher gravity results in a wider spectrum (lower γ) suggests that gravitational forces play a significant role in modulating the particle clustering dynamics. One possible explanation is that increased gravity breaks the isotropy

of the particle clusters in space (see Figure 4.1, high Stk and Fr_l), causing the spectrum to spread to wider range of scales. This anisotropy might lead to a more heterogeneous distribution of particle concentration, thus spreading the spectrum across a broader range of wavenumbers.

Overall, the dependence of γ on the Reynolds and Froude numbers highlights the complex interactions between turbulence intensity, gravitational forces, and particle clustering. While the relationship with Reynolds number aligns with the expected broadening of the spectrum due to a wider range of eddy sizes, the influence of gravity suggests additional mechanisms at play, potentially related to the anisotropy introduced by gravitational settling.

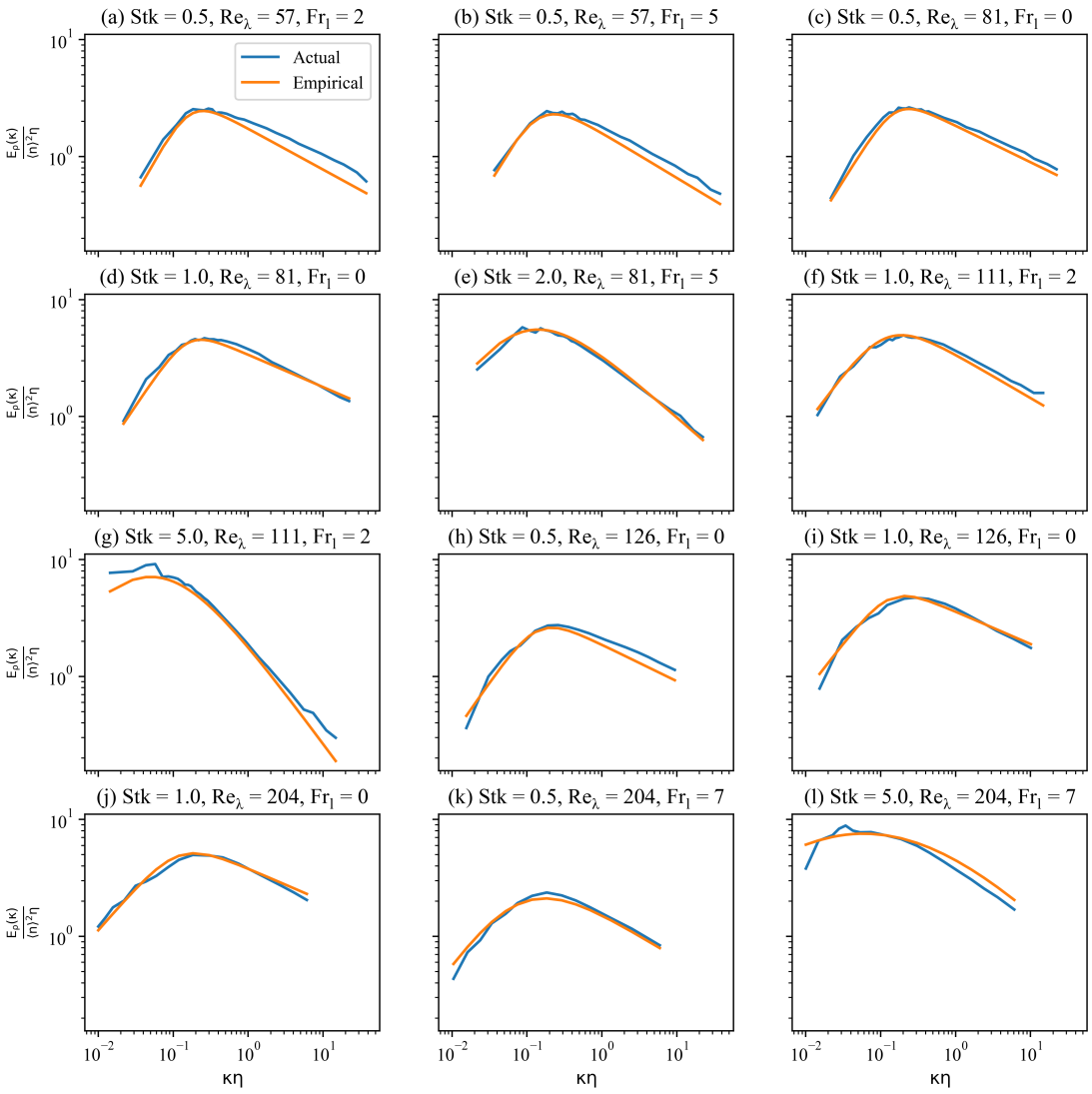


Figure 4.11: Spectral energy of the particle number density fluctuations against the wavenumber for a range of different Stokes, Reynolds and Froude numbers. The raw spectra are plotted as well as the spectra calculated from the empirical model of Equation 4.17. Plots (a) – (g) are spectra calculated from the current study, plots (h) – (l) are spectra from Matsuda et al. [104, 105].

Figure 4.11 presents the spectral energy of the particle number density fluctuations as a function of the wavenumber for various Stokes, Reynolds, and Froude numbers. Both the raw spectra obtained from turbulence simulations and the spectra calculated from the empirical model described by Equation 4.17 are plotted. Plots (a) – (g) depict the spectra calculated from the current study, while plots (h) – (l) show spectra from Matsuda et al. [104, 105], providing a comparison of the newly proposed empirical model to previous works. The performance of the model in extrapolating beyond the initial conditions ($Re_\lambda = 111$ and $Fr_l = 5$) is also validated, as seen in subplots (h) – (l), where it aligns well with the results of Matsuda et al. [104, 105].

Currently, the model is validated for homogeneous isotropic turbulence with the forcing mechanism defined in Equation 4.3. While different forcing methods could alter the low wavenumber part of the spectra, the right-hand side (high wavenumber) spectra are expected to remain relatively unchanged due to the assumption of universal turbulence energy cascade. However, anisotropic turbulence could significantly affect the spectra, potentially requiring further adjustments to the model.

The number of particles used in the simulation does not significantly influence the spectra, as demonstrated by Jin et al. [86]. This robustness enhances the empirical model's reliability across different simulation setups and particle counts.

This empirical model offers a valuable tool for estimating the characteristics of particle preferential concentration by providing accurate spectra predictions across a wide range of conditions. Practical applications of this model include atmospheric sciences, where it can aid in predicting droplet clustering in clouds, and industrial processes, such as improving the efficiency of particulate dispersion in reactors. Additionally, it can be used in environmental studies to estimate pollutant dispersion in turbulent flows, contributing to better air quality management and assessment.

Overall, the empirical model presented in this study, validated against both current and previous simulation results, provides a robust framework for understanding and predicting particle behaviour in turbulent flows. Its contribution is essential to applications where the large dimensions of the relevant geometries make detailed computational prediction of the flow and the particle clustering characteristics impractical due to high computational costs. This capability is crucial for advancing both theoretical and practical applications in various fields involving particle-laden turbulence.

4.5 Conclusions

The conclusions drawn from this study on the spectral analysis of particle preferential concentration characteristics in turbulent flows provide a comprehensive understanding of how various parameters influence particle clustering. The research systematically investigated the combined effects of Reynolds, Stokes, and Froude numbers on the preferential concentration of particles, offering novel insights and practical tools for predicting particle behaviour in turbulent environments, including geometries with large dimensions where detailed computational studies are impractical. The spectrum of particle number density fluctuations is used as the main form of analysis.

The findings confirm that preferential concentration dynamics are significantly influenced by the Stokes, Reynolds, and Froude numbers. Particle clustering intensity peaks around a Stokes number of unity, highlighting the optimal response times of particles to turbulent eddies. For Stokes numbers less than one, the spectral energy peaks consistently at specific wavenumber magnitudes, indicating stable clustering influenced by small eddies. Particles with Stokes numbers close to one exhibit the most pronounced preferential concentration, while those with higher Stokes numbers show a more dispersed distribution, reflecting reduced clustering intensity due to increased particle inertia. For Stokes numbers greater than one, spectral energy shifts to larger length scales (smaller wavenumber), reflecting the influence of larger eddies on particle clustering.

The role of the Reynolds number is crucial, as it alters particle clustering patterns significantly. Higher Reynolds numbers, indicative of more intense turbulence, lead to a wider range of void sizes and more complex particle distributions. Higher Reynolds numbers result in broader spectra, indicating a wider range of turbulent eddy interactions. For particles with lower Stokes numbers, clustering behaviour remains relatively independent of the Reynolds number at high turbulence intensities. However, for higher Stokes numbers, increased Reynolds numbers enhance clustering intensity and shift the spectral energy peak to larger length scales.

Gravitational effects, represented by the Froude number, play a pivotal role in modulating particle clustering. For small Stokes numbers, gravity has minimal impact on clustering behaviour. In contrast, at intermediate Stokes numbers, increased gravity enhances clustering at larger scales while reducing it at smaller scales. At high Stokes numbers, gravity enhances clustering at both large and small scales, underscoring its dominant influence on particle dispersion dynamics. These gravitational forces introduce anisotropy in particle clusters, broadening the spectrum and enhancing clustering intensity across various scales.

The practical applications of these findings extend to atmospheric sciences, oceanography, and chemical engineering. Accurate modelling of particle behaviour in turbulent flows is important for predicting droplet clustering in clouds, particulate dispersion in reactors, and pollutant dispersion in environmental studies. This research enhances predictive capabilities and informs the design and optimization of various industrial and environmental processes, in particular, for applications that involve large dimensions for which detailed computational predictions are impractical due to computational costs.

In summary, this study contributes to the understanding of turbulence-particle interactions by incorporating the effects of Reynolds number and gravity alongside the Stokes number. The findings offer insights into the mechanisms driving preferential concentration in turbulence and provide practical tools for predicting particle behaviour in various flow conditions. These contributions are expected to enhance the modelling of particle-laden turbulent flows in fluid mechanics and related disciplines.

With an in-depth exploration of preferential concentration and its dependency on key physical parameters, the focus now shifts towards understanding the physical mechanisms driving these phenomena. Chapter 5 naturally follows by diving into Lagrangian Coherent Structures (LCS) and their role in influencing particle behaviour, providing a more detailed physical explanation of particle clustering observed in the previous chapters.

Chapter 5

Investigating Preferential Concentration of Inertial Particles through Lagrangian Coherent Structures in Turbulent Flows

5.1 Abstract

Understanding how inertial particles cluster in turbulent flows is crucial for various natural and industrial applications. This research investigates the physical mechanisms of the formation of particle preferential concentration through interaction with fluid flow turbulence, particularly focusing on Lagrangian Coherent Structures (LCS). We employ Direct Numerical Simulations (DNS) to analyse the interaction between fluid dynamics and particle spatial and temporal distribution using both Eulerian and Lagrangian perspectives. The study examines the influence of the Q-Criterion, Enstrophy, and Lagrangian-averaged vorticity deviation (LAVD) of the fluid turbulence on particle clustering. Our results indicate that LAVD is the most reliable indicator of particle clustering, highlighting the significance of rotational coherence in turbulence. Furthermore, the introduction of a time delay into the correlation between fluid and particle motion reveals that past fluid states are better correlated with current particle distributions than simultaneous measurements. This research provides new insights into the dynamic processes governing particle behaviour in turbulent flows, offering potential applications in fields ranging from atmospheric science to chemical engineering.

5.2 Introduction

Inertial particle or droplet distributions in turbulent flows often exhibit clustering in regions of high concentration and voids in regions of low concentration. This behaviour, known as preferential concentration, occurs due to particle inertia, which causes the dispersed phase to deviate from the fluid flow streamlines. This process is influenced by variables such as particle size and the properties of the fluid [154]. Understanding preferential concentration is crucial for a variety of natural and industrial processes. In atmospheric physics, it plays a role in cloud formation and rain initiation, while in chemical engineering, it impacts processes such as powder manufacturing. These processes often depend nonlinearly on particle concentration. For example, the general aerosol dynamic equation, which describes the evolution of droplet size distribution [55], underscores the significance of non-uniform particle concentration profiles. Moreover, preferential concentration affects various phenomena including droplet coalescence in clouds [163, 150, 95], droplet evaporation or condensation [137, 145], and gas-particle phase reactions [70].

The mechanisms driving the clustering of inertial particles in fluid flows are complex and influenced by various factors, including the non-dimensional Stokes and Reynolds numbers. The Stokes number (Stk) measures the ratio of particle inertia to fluid drag forces, indicating how quickly particles respond to changes in fluid velocity (defined in Equation 7). The Reynolds number (Re_λ) characterizes the turbulence intensity in the flow. One common effect observed in flows with a mean velocity component is centrifuging. In the context of turbulence, Coleman and Vassilicos [32] proposed the 'sweep-stick' mechanism. This mechanism suggests that particles are swept along with and get stuck to the acceleration stagnation points of the fluid. However, an alternative perspective is offered by Bragg et al. [23], whose analysis also applies to arbitrary spatially correlated velocity fields. Crucially, their findings challenge the scale invariance of the radial distribution function, offering a different view on the underlying processes of particle clustering.

Various methods exist for analysing and quantifying preferential concentration in turbulent flows. Among them, radial distribution functions (RDFs) are widely used, particularly at lower Stokes numbers, offering insights into clustering [5, 4, 14, 148, 31, 177]. However, RDFs have limitations, such as focusing on pairwise interactions and assuming spherical symmetry. To address these, angular distribution functions provide a more comprehensive perspective [61].

Voronoi tessellation is another technique, often used in experimental and numerical simulations, that assigns volumes around particles to calculate local con-

centrations and identify clusters [124, 114, 157, 6]. Spectral methods, including Fourier and wavelet transforms, also offer insights into particle clustering. Fourier transforms provide a global overview [41, 86, 104, 69, 3] , while wavelet transforms present more detailed, localized data [10, 106].

The Stokes number (Stk), which measures the ratio of particle inertia to fluid viscous forces, plays a critical role in preferential concentration. Particles with Stk near unity exhibit significant clustering, as they respond optimally to turbulent eddies [154]. Studies have shown that clustering peaks at $Stk \approx 1$, influencing phenomena such as radar reflectivity and evaporation rates [104, 163, 150, 95, 145, 70, 115, 46, 31, 13, 15, 64, 22, 158, 32].

While the influence of Stokes number is well-documented, the effects of Reynolds number and gravitational forces on particle clustering are less understood. Ireland et al. [80] found that higher Reynolds numbers, indicating more intense turbulence, significantly alter particle behaviour and clustering patterns. Gravity also affects clustering, particularly for droplets with $Stk > 1$ [105, 163, 69, 150]. Additional studies have explored how turbulence and gravity influence collision rates and spatial patterns [136, 64, 22, 127, 15, 158, 61, 95, 137, 5, 44].

To understand the underlying physics and predict the preferential concentration of particles, researchers have developed several methods to correlate fluid properties with particle concentration. Among these properties, the Q-criterion has been widely used to identify vortex-dominated regions within a turbulent flow [6, 32]. The Q-criterion is based on the second invariant of the velocity gradient tensor and is used to distinguish between rotation-dominated (vortical) and strain-dominated regions [78]. Regions where the Q-criterion is positive are typically associated with vortical structures, where centrifugal forces can lead to particle clustering around the periphery of vortices.

Another important method is the Enstrophy, which quantifies the intensity of vorticity within the flow without considering the strain. Enstrophy is particularly useful for identifying regions with high rotational energy, which can influence the distribution of particles by expelling them from the vortex cores and concentrating them in regions of lower vorticity [52]. Oujia et al. [123] used neural networks to try to synthesise inertial particle concentrations from Enstrophy to varying degrees of success. These Eulerian-based approaches provide valuable insights into the correlation between fluid structures and particle concentration and can effectively frame coherent features of the instantaneous velocity field but lack objectivity Haller [66]. They are often limited by their reliance on instantaneous snapshots of the flow, which may not fully capture the temporal dynamics of particle clustering.

To address the limitations of Eulerian methods, more comprehensive approaches have been developed that adopt a Lagrangian perspective. Unlike the Eulerian ap-

proach, which examines fluid properties at fixed points in space, the Lagrangian perspective tracks the motion of individual fluid particles over time. This approach provides a more dynamic view of the flow, capturing how fluid particles and, by extension, inertial particles evolve as they move through the turbulent environment Toschi and Bodenschatz [161]. By analysing particle trajectories, the Lagrangian framework can reveal deeper insights into the mechanisms driving preferential concentration, such as how particles interact with coherent flow structures over time. Lagrangian Coherent Structures (LCS) are fundamental elements in fluid dynamics, representing organized, time-evolving structures within a flow that significantly influence the transport and mixing of particles Haller and Yuan [67].

Despite significant progress in understanding the relationship between fluid structures and particle distribution, many aspects of preferential concentration in turbulence remain poorly understood. Existing methods, while effective in certain contexts, often fall short in capturing the full complexity of particle dynamics, particularly when time-dependent effects are considered. The motivation for this study is to explore how various fluid properties, both from Eulerian and especially Lagrangian perspectives, influence the clustering of inertial particles in turbulent flows. By employing a combination of these methods, this research aims to provide a more comprehensive understanding of the correlation between fluid dynamics and particle spatial and temporal distribution, ultimately contributing to the development of more accurate predictive models.

5.3 Numerical Method

5.3.1 Carrier Fluid Simulations

The carrier fluid is simulated using the incompressible Navier-Stokes equations with an additional forcing term to maintain statistically stationary homogenous isotropic turbulence. The equations for the carrier fluid in Einstein notation are:

$$\frac{\partial u_i}{\partial t} + \frac{\partial u_i u_j}{\partial x_j} = -\frac{1}{\rho_f}\frac{\partial p}{\partial x_i} + \upsilon \frac{\partial^2 u_i}{\partial x_j^2} + F_i, \tag{5.1}$$

$$\frac{\partial u_j}{\partial x_j} = 0, \tag{5.2}$$

where u_i is the carrier fluid velocity in the i-th direction, x_i is the spatial coordinate in the i-th direction, t denotes time, ρ_f is the carrier fluid density, p the pressure, υ the kinematic viscosity, and F_i forcing term in the i-th direction.

The summation is over the index j.

Throughout the simulations, the fluid density (ρ_f), and the kinematic viscosity (υ) are kept constant. The carrier fluid simulations, which are performed independently from the particulate phase due to one-way coupling, is stored for subsequent analysis. The simulations are performed in a three-dimensional periodic cube with side length L. The pseudo-spectral method is employed for the carrier fluid, utilizing N equidistant grid points in each direction, resulting in a grid spacing Δ [141, 154] and a 4-th order Runge-Kutta is used for the time integration. The forcing mechanism is to scale the wavenumbers of the fluid between 0.5 and 1.5 [168, 121]. This works by first integrating the equations without forcing, with resulting Fourier modes $\widehat{u_i^*}(\boldsymbol{\kappa}, t+\Delta t)$. Then, we multiply this result by a constant for Fourier modes with a wavenumber $|\boldsymbol{\kappa}|$ between 0.5 and 1.5. This is given below as:

$$\widehat{u_i}(\boldsymbol{\kappa})(t+\Delta t) = \widehat{u_i^*}(\boldsymbol{\kappa}, t+\Delta t)\sqrt{E_n(0)/E_n(t+\Delta t)}, \tag{5.3}$$

where $E_n(t+\Delta t)$ is the total energy of the modes with wavenumbers between 0.5 and 1.5 calculated by $\widehat{u_i^*}(\boldsymbol{\kappa}, t+\Delta t)$ and $\widehat{u_i}(\boldsymbol{\kappa})(t+\Delta t)$ is the final forced velocity profile. A linear forcing function, directly proportional to the velocity, can be used for its ease of implementation and physical relevance [100]; however, the linear forcing scheme requires twice as many grid points to resolve the smaller scales, reducing the attainable Reynolds number [142].

5.3.2 Inertial Particle Simulations

The Lagrangian particle simulations are conducted under the assumption of one-way coupling. The particles are treated as point spheres with negligible mass loading. Under these assumptions the Stokes drag model is employed as the friction model and the influence of gravity is considered [89]. Based on these assumptions, the equations of motion for an individual particle are formulated as follows:

$$\frac{dx_{p,i}}{dt} = v_{p,i}, \tag{5.4}$$

$$\frac{dv_{p,i}}{dt} = \frac{1}{\tau_p}\left(u_i - v_{p,i}\right) + g_i, \tag{5.5}$$

$$\tau_p = \frac{\rho_p d^2}{18\rho_f \upsilon}, \tag{5.6}$$

$$\tag{5.7}$$

In these equations, $x_{p,i}$ denotes the position of an individual particle in the

spatial coordinate i, $v_{p,i}$ represents the velocity of the particle in the same coordinate, τ_p is the particle relaxation time, ρ_p the particle material density, g_i is the acceleration due to gravity in the i-th direction, and d the particle diameter.

The Stokes number Stk of a particle is defined as the ratio of the particle relaxation time τ_p to a characteristic timescale of the carrier fluid. For the scaling of particle preferential concentration, the Kolmogorov timescale τ_η is often used as this characteristic timescale and Stk is defined in Equation 5.8.

$$Stk = \frac{\tau_p}{\tau_\eta} = \tau_p \sqrt{\frac{\varepsilon}{\upsilon}}. \tag{5.8}$$

5.3.3 Simulation Conditions

The carrier fluid simulations were undertaken over a range of Taylor Reynolds numbers ($50 < Re_\lambda < 120$) in homogeneous isotropic turbulence. To meet the criteria for Direct Numerical Simulation (DNS) of turbulence flows, a crucial parameter is the Kolmogorov length scale, η, the grid spacing Δ, and their ratio η/Δ should be greater than 0.45 [130]. The number of grid points was kept constant at $N = 256^3$, the domain length constant at $L = 6.28$ and the total number of simulation particles $N_p = 167$ million.

Re_λ	N	Stk	Fr_l
90	256^3	1.0	0.0

Table 5.1: Simulation parameters used for both the Eulerian carrier fluid and the Lagrangian particle simulations.

5.3.4 Lagrangian Coherent Structures

Lagrangian Coherent Structures (LCS) are fundamental elements in fluid dynamics, representing organized, time-evolving structures within a flow that significantly influence the transport and mixing of particles [67]. These structures are identified through the Lagrangian framework, which focuses on tracking individual fluid particles over time, rather than analysing fluid properties at fixed spatial points as in the Eulerian perspective. At the core of the Lagrangian description is the concept of the flow map, which mathematically captures the movement of fluid particles within the flow.

The flow map, denoted by $\varphi_{t_0}^t(\boldsymbol{x}_0)$ provides a mathematical function that maps the initial position of a fluid particle $\boldsymbol{x}_0$ at an initial time t_0 to its position $\boldsymbol{x}(t)$ at a later time t. Mathematically, this is expressed as:

$$\varphi_{t_0}^t(\boldsymbol{x}_0) = \boldsymbol{x}(t; t_0, \boldsymbol{x}_0), \tag{5.9}$$

where $\boldsymbol{x}_0$ is the initial position of the particle at time t_0, and $\boldsymbol{x}\left(t; t_0, \boldsymbol{x}_0\right)$ represents the position of the particle at a subsequent time t. The flow map essentially describes the trajectory of each particle in the fluid, providing a complete description of how particles are transported by the velocity field over time.

The evolution of the flow map is governed by the velocity field $\boldsymbol{u}(\boldsymbol{x}, t)$ of the fluid, according to the differential equation:

$$\frac{d\boldsymbol{x}(t)}{dt} = \boldsymbol{u}\left(\boldsymbol{x}\left(t\right), t\right), \qquad \boldsymbol{x}\left(t_0\right) = \boldsymbol{x}_0, \tag{5.10}$$

this equation dictates how the position of a particle changes over time, driven by the local velocity of the fluid at each point along its trajectory. The solution to this equation, the flow map, provides a detailed picture of how fluid particles move through the flow, which is crucial for identifying Lagrangian Coherent Structures.

Lagrangian Coherent Structures can be broadly categorized into two main types: hyperbolic and elliptic LCS. Hyperbolic LCS are associated with regions in the flow where fluid particles experience significant stretching and folding. These structures act as transport barriers, delineating regions of the flow with different dynamic behaviours. For instance, repelling hyperbolic LCS disperse fluid particles away from each other, while attracting hyperbolic LCS draw particles together, often forming boundaries that separate different flow regions. These structures are essential for understanding how particles mix within the flow and how they organize into clusters or voids.

Elliptic LCS, in contrast, correspond to regions of rotational coherence within the flow. These structures typically form the cores of vortices or eddies, where fluid particles follow closed, circular paths with minimal stretching. Elliptic LCS are indicative of areas dominated by rotational motion rather than stretching, and they play a significant role in the stability of vortices within turbulent flows. The presence of elliptic LCS often leads to the trapping of fluid particles within these rotational structures, preventing their dispersion.

5.3.5 Finite-Time Lyapunov Exponent

The Finite-Time Lyapunov Exponent (FTLE) is a critical measure in fluid dynamics that quantifies the rate of separation of fluid particles over a finite time interval. It is a key tool for identifying Lagrangian Coherent Structures (LCS) within a flow, providing insight into regions where fluid elements experience the greatest stretching or compression. The FTLE essentially captures the exponential rate at which initially neighbouring fluid particles diverge from each other as they move through the flow, making it a valuable metric for understanding the dynamic behaviour of fluid systems.

Mathematically, the FTLE is defined based on the flow map $\varphi_{t_0}^t(\boldsymbol{x}_0)$, which describes the trajectory of fluid particles from an initial position $\boldsymbol{x}_0$ at time t_0 to their position $\boldsymbol{x}(t)$ at a later time t. The FTLE at a point $\boldsymbol{x}_0$ over a time interval $[t_0, t]$ is given by:

$$\sigma_{t_0}^t(\boldsymbol{x}_0) = \frac{1}{|t - t_0|} \ln \sqrt{\lambda_{max}\left(\mathbf{J}_{t_0}^t(\boldsymbol{x}_0)^T \mathbf{J}_{t_0}^t(\boldsymbol{x}_0)\right)}, \tag{5.11}$$

where $\mathbf{J}_{t_0}^t(\boldsymbol{x}_0) = \frac{\partial \varphi_{t_0}^t(\boldsymbol{x}_0)}{\partial \boldsymbol{x}_0}$ is the Jacobian matrix of the flow map, representing the gradient of the flow map with respect to the initial conditions. λ_{max} denotes the largest eigenvalue of the Cauchy-Green strain tensor, which is formed by the matrix $\mathbf{J}_{t_0}^t(\boldsymbol{x_0})^T \mathbf{J}_{t_0}^t(\boldsymbol{x}_0)$.

In practice, the Jacobian matrix of the flow map is estimated from finite differences by evolving fluid particles from a uniform grid along the time interval $|t - t_0|$.

The FTLE essentially measures how much the separation distance between neighbouring particles grows over time, normalized by the time interval $|t - t_0|$. A high FTLE value indicates that particles starting close to each other at time t_0 have diverged significantly by time t, which corresponds to regions of the flow with strong stretching and is indicative of hyperbolic LCS.

The FTLE can be computed both forward and backward in time. Forward FTLE identifies regions where particles are repelled from each other, which corresponds to repelling LCS. Conversely, backward FTLE identifies regions where particles converge, corresponding to attracting LCS. These measures are crucial for understanding the transport barriers within the flow and for mapping out the regions that will most significantly influence particle trajectories.

5.3.6 Lagrangian-Averaged Vorticity Deviation

The Lagrangian-Averaged Vorticity Deviation (LAVD) is a powerful measure in fluid dynamics used to identify rotationally coherent structures, particularly elliptic Lagrangian Coherent Structures (LCS), within a flow. Unlike hyperbolic LCS, which are associated with stretching and folding in the flow, elliptic LCS correspond to regions where fluid particles exhibit rotational motion with minimal stretching. These structures are crucial for understanding the dynamics of vortices and eddies in turbulent flows, as they help delineate regions where fluid particles are trapped within coherent rotational patterns over time.

The LAVD is calculated by averaging the deviation of the vorticity of fluid particles from the local mean vorticity along their trajectories over a finite time interval. Vorticity, a vector quantity, describes the local rotation of the fluid and

is given by the curl of the velocity field $\boldsymbol{u}(\boldsymbol{x}, t)$:

$$\boldsymbol{\omega}(\boldsymbol{x}, t) = \nabla \times \boldsymbol{u}(\boldsymbol{x}, t), \tag{5.12}$$

The LAVD at a point $\boldsymbol{x}_0$ over a time interval $[t_0, t]$ is defined as:

$$\mathrm{LAVD}_{t_0}^{t}(\boldsymbol{x}_0) = \int_{t_0}^{t} |\boldsymbol{\omega}(\boldsymbol{x}(s), s) - \langle\boldsymbol{\omega}\rangle(s)|\, ds, \tag{5.13}$$

where $\boldsymbol{x}(s)$ is the trajectory of the fluid particle that starts at $\boldsymbol{x}_0$ at time t_0 and moves with the flow until time t. $\boldsymbol{\omega}(\boldsymbol{x}(s), s)$ is the vorticity at the particle's position $\boldsymbol{x}(s)$ at time s. $\langle\boldsymbol{\omega}\rangle(s)$ is the spatially averaged vorticity over a neighborhood around $\boldsymbol{x}(s)$ at time s, taken to be the zero vector $\mathbf{0}$ for homogenous isotropic turbulence. ds represents the infinitesimal time increment along the particle trajectory.

The LAVD essentially measures how much the vorticity along a fluid particle trajectory deviates from the average vorticity of the surrounding fluid. By integrating this deviation over time, the LAVD quantifies the cumulative rotational coherence experienced by the particle. High LAVD values indicate that a fluid particle has remained within a region of strong, consistent rotation (relative to the mean vorticity) throughout the time interval. Such regions correspond to elliptic LCS, where fluid particles are likely trapped within coherent vortices or eddies, maintaining a stable, rotating motion.

In practical terms, LAVD is used to identify and visualize these elliptic LCS within the flow. Regions with high LAVD values mark the boundaries of coherent rotational structures, effectively delineating vortices where the rotation is strong and consistent over time. These structures are crucial for understanding how turbulence organises fluid motion, particularly in terms of how it traps fluid particles within vortical regions.

Unlike other measures of coherence, such as the Finite-Time Lyapunov Exponent (FTLE) which identifies hyperbolic LCS, the LAVD specifically targets rotational coherence, making it uniquely suited for studying the dynamics of vortices and rotational structures in turbulent flows. The LAVD provides a clear, quantitative tool for analysing the role of rotational motion in the organisation of fluid particles, offering insights into the persistence and stability of vortices and their influence on the overall behaviour of the flow.

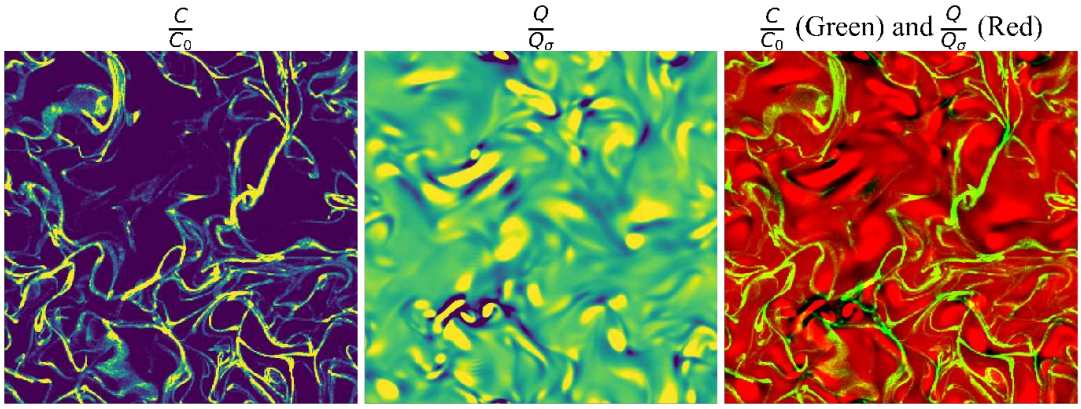


Figure 5.1: Normalised particle concentration C/C_0(left) and normalised Q-Criterion Q/Q_σ (middle) in a slice of turbulence with $Re_\lambda = 90.0$ and $Stk = 1.0$. Low values are in blue and high values are in yellow. Superimposed image (right), the green channel represents particle concentration, while the red channel represents the Q-Criterion. The particle concentration was calculated using a box-counting method with a box width of 2η.

5.4 Results

5.4.1 Influence of Q-Criterion

Figure 5.1 illustrates the normalised particle concentration, denoted as C/C_0, alongside the normalised Q-Criterion, Q/Q_σ. These two fields are superimposed within a slice of turbulence characterised by Reynolds number (Re_λ) of 90 and particle Stokes number (Stk) of 1.0 at the right hand side figure. In this figure, the green channel represents particle concentration, while the red channel represents the Q-Criterion.

The particle concentration was determined through a box-counting method, where the box width was set to 2η (with η being the Kolmogorov length scale). Upon examining this visualization, it becomes apparent that particle clusters display a subtle tendency to avoid regions of positive Q/Q_σ, instead gravitating towards areas characterised by negative Q/Q_σ. This behaviour aligns with observations reported in previous studies, such as those by Baker et al. [6] and Coleman and Vassilicos [32].

Figure 5.2 provides a more detailed examination of the relationship between inertial particles and the Q-Criterion. The left-hand plot presents a histogram of the Q-Criterion, sampled both at the positions of fluid particles (representing the entire domain) and at the positions of inertial particles. Notably, sampling the Q-Criterion at inertial particle positions is effectively equivalent to weighting the Q-Criterion histogram of the entire fluid domain by the particle concentration. This method of analysis is a well-established approach for comparing particle locations

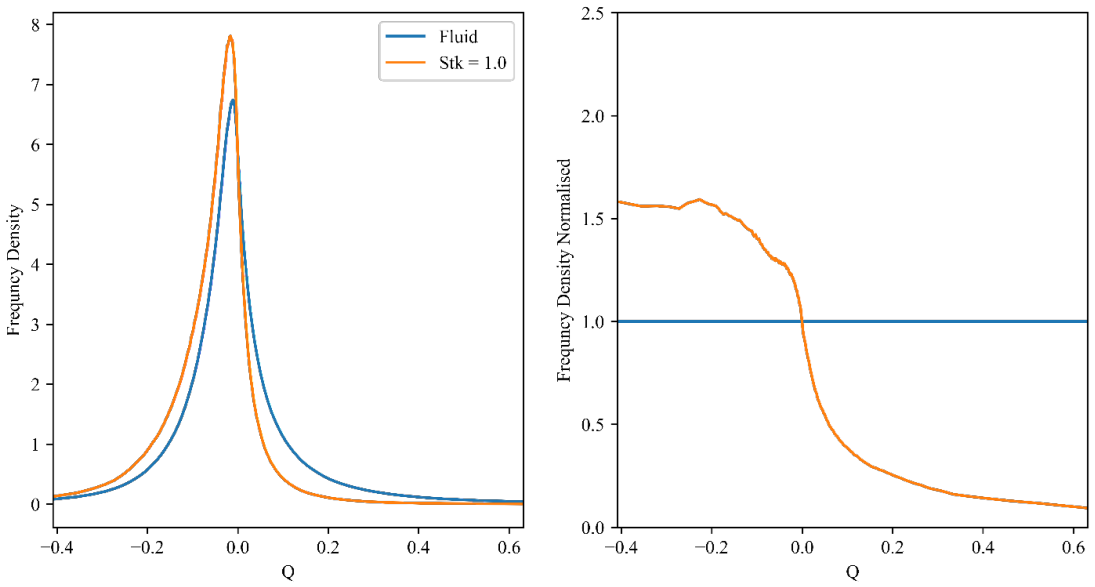


Figure 5.2: The left-hand plot displays the histogram of the Q-Criterion sampled at fluid particle positions and at inertial particle positions. The right-hand plot re-normalizes the frequency density values by dividing by the fluid frequency density, allowing a clearer comparison of the ratio of inertial particles to fluid particles.

to fluid properties, as employed in previous studies, such as those by Baker et al. [6] and Coleman and Vassilicos [32].

The left-hand plot confirms the qualitative observations made from the concentration slices of Figure 5.1, where it was noted that inertial particles tend to be underrepresented in regions of positive Q/Q_σ and overrepresented in regions of negative Q/Q_σ.

In the right-hand panel of Figure 5.2, the frequency density values are re-normalized to maintain a constant value for fluid particles. This normalisation facilitates a more straightforward comparison of the ratio of inertial particles to fluid particles, highlighting the sampling behaviour of the Q-Criterion by the inertial particles, independent of the non-uniform distribution of the Q-Criterion itself.

From this analysis, it becomes evident that inertial particles exhibit a strong preference for regions of negative Q/Q_σ. Specifically, the data show that inertial particles are observed up to 1.6 times more frequently in regions of negative Q/Q_σ than expected, while they are observed as little as 0.1 times in regions of positive Q/Q_σ. This significant change predominantly occurs when the Q-Criterion crosses the zero value, marking the transition from a strain-dominated regime to a rotation-dominated regime.

While Figure 5.2 provides a clear indication of the preference of inertial particles to accumulate in regions with negative Q/Q_σ, it does not fully capture how

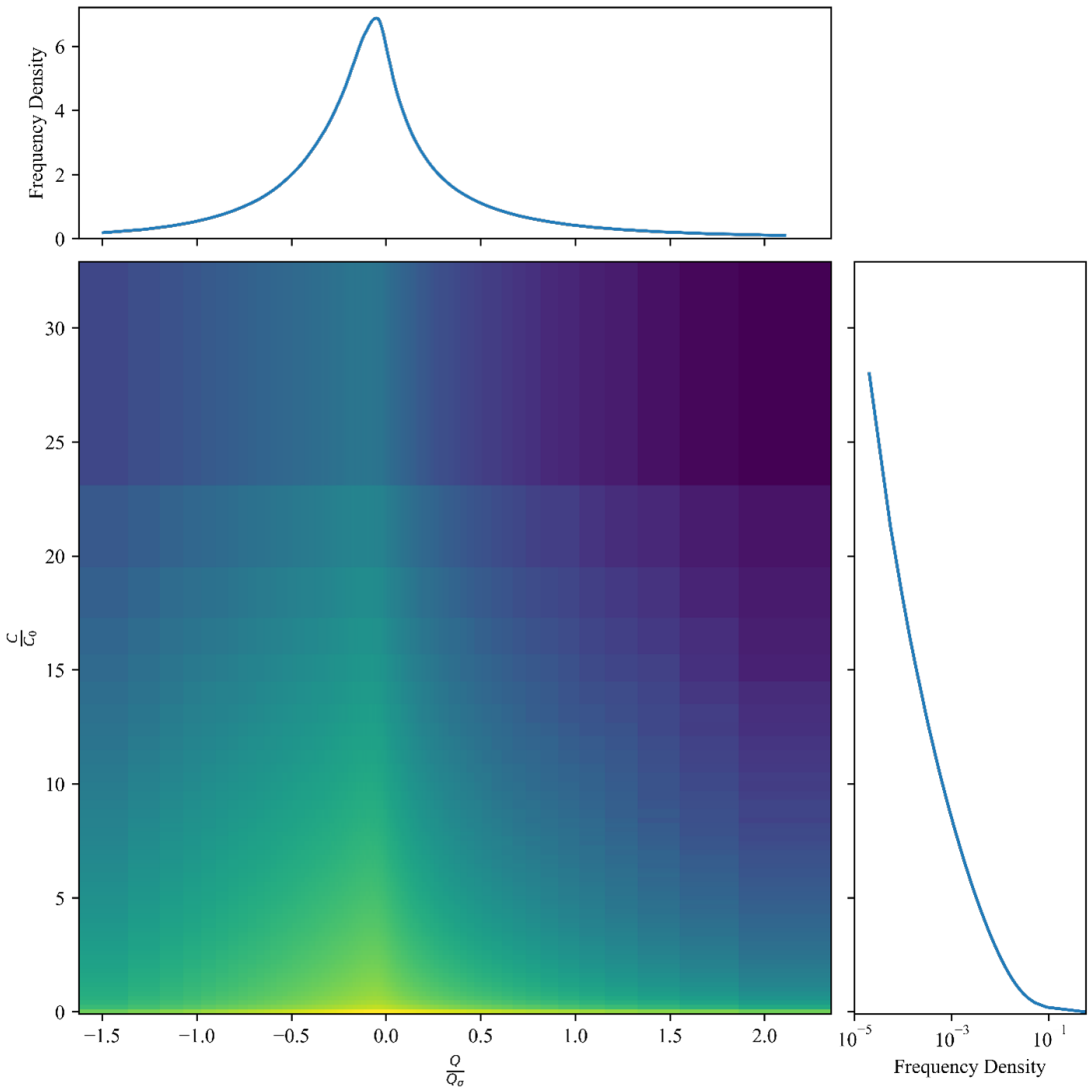


Figure 5.3: Joint probability distribution of particle concentration C/C_0 and the Q-Criterion Q/Q_σ in turbulence, with colour representing the frequency density on a logarithmic scale (low - dark blue, high - bright yellow). The figure also includes the one-dimensional probability density functions (PDFs) for the Q-Criterion and particle concentration.

particle concentration varies with the Q-Criterion. Specifically, it leaves unanswered questions about whether higher density particle clusters are more inclined towards regions of negative Q/Q_σ compared to lower density clusters, and how the distribution of voids behaves in relation to the Q-Criterion.

To address these questions, we present the joint probability distribution of particle concentration and the Q-Criterion in Figure 5.3, with the colour scale representing the frequency density on a logarithmic scale. Additionally, the figure includes the one-dimensional probability density functions (PDFs) for the Q-Criterion and particle concentration separately. It is worth noting that the Q-Criterion PDF in Figure 5.3 is identical to the one shown in Figure 5.2.

Upon analysing Figure 5.3, it is evident that the left-hand side (representing negative Q/Q_σ) generally appears lighter than the right-hand side (representing positive Q/Q_σ), indicating a tendency for particles to prefer negative Q/Q_σ regions. However, the precise relationship between particle concentration and the Q-Criterion remains ambiguous, particularly since a significant portion of the particle concentrations are zero, corresponding to large voids as seen in Figure 5.1. This suggests that while there is a general trend, the interplay between particle concentration and Q-Criterion is complex and not easily delineated from this data alone.

To further investigate the relationship between particle concentration and Q-Criterion, we compare the observed joint probability distribution to a distribution that would be expected if these two variables were independent. This comparison can be made by reconstructing a two-dimensional joint probability density function (PDF) using the one-dimensional PDFs of the Q-Criterion and particle concentration, assuming independence between them. Figure 5.4 displays the joint probability density function that would result from this assumption of independence, calculated as the product of the one-dimensional PDFs of the Q-Criterion and particle concentration.

While it is challenging to make an immediate, direct comparison between Figure 5.3 (which represents the actual, non-independent distribution) and Figure 5.4, certain distinctions are noticeable. For instance, in Figure 5.4, the left-hand side of the distribution (corresponding to negative Q/Q_σ) is noticeably darker for the highest particle clusters (around $C/C_0 \approx 30$) compared to Figure 5.3. This suggests that there is a deviation from the assumption of independence, particularly in the regions of highest particle concentration, where the correlation between particle clusters and negative Q/Q_σ becomes more pronounced.

To better understand the relationship between particle concentration and Q-Criterion, we examine the ratio of the observed joint probability density function (PDF) to the PDF assuming independent variables, denoted as ζ. This ratio is also called the copula [151], providing a measure of the association between the two variables. The copula (ζ) of a joint probability density function $f(x, y)$ is defined as:

$$\zeta(x, y) = \frac{f(x, y)}{\int_{-\infty}^{\infty} f(x, y)dx \int_{-\infty}^{\infty} f(x, y)dy}, \tag{5.14}$$

The copula fully captures the dependence structure between the random variables X and Y, independent of their marginal distributions. This separation allows us to analyse the joint behaviour of the variables without being influenced by their individual distributions. In particular, copulas are useful in identifying non-linear

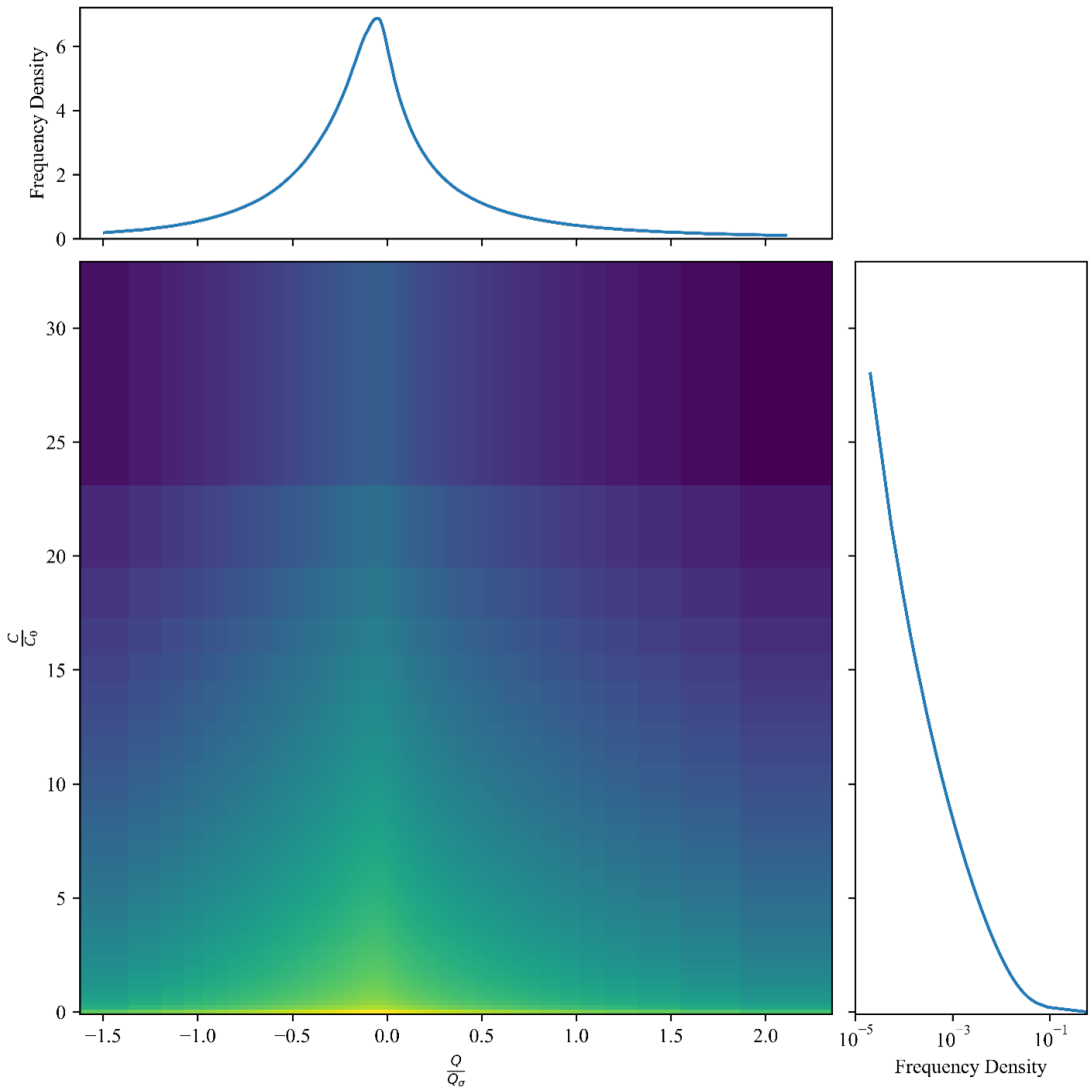


Figure 5.4: Joint probability density function of particle concentration C/C_0 and the Q-Criterion Q/Q_σ assuming independence between the two variables, calculated as the product of their one-dimensional probability density functions (PDFs). This figure represents the theoretical distribution if there was no correlation between particle concentration and Q-Criterion. Colour represents the frequency density on a logarithmic scale (low - dark blue, high - bright yellow). The figure also includes the one-dimensional probability density functions (PDFs) for the Q-Criterion and particle concentration.

dependencies, which traditional correlation measures might fail to capture.

By using copulas, we can model a wide range of dependence structures, including tail dependencies and asymmetries, making them particularly valuable in analysing particle clustering. Additionally, Sklar's theorem states that any joint distribution can be decomposed into its marginal distributions and a copula, reinforcing the fundamental role of copulas in multivariate probability modelling [151].

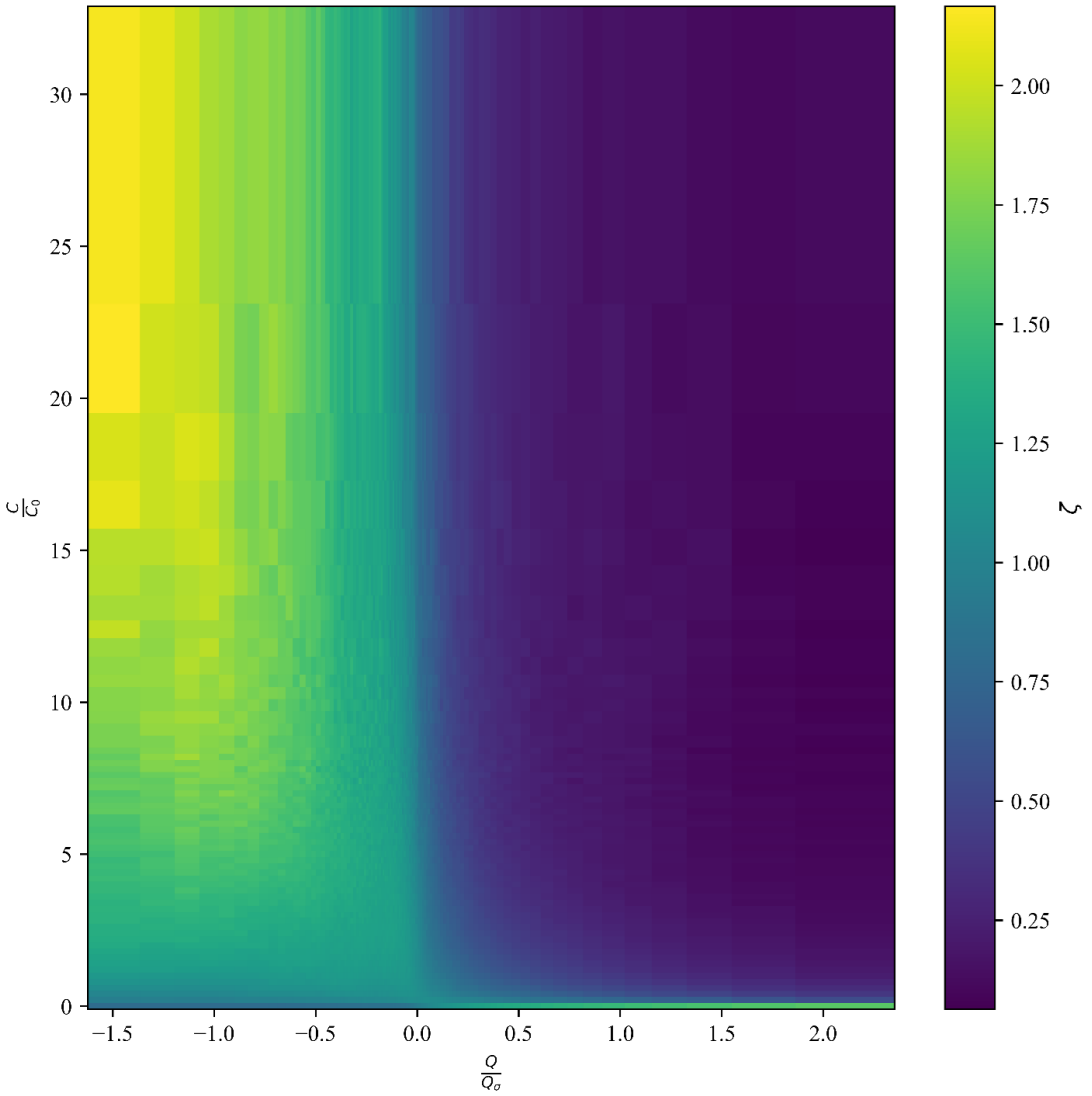


Figure 5.5: Ratio ζ of the observed joint probability density function (PDF) of particle concentration C/C_0 and Q-Criterion Q/Q_σ to the PDF assuming independent variables, providing a measure of the correlation between these two variables.

Figure 5.5 presents this ratio, offering a clear depiction of the correlation between Q-Criterion and particle concentration. The analysis reveals that voids, characterised by $C/C_0 \approx 0$, are positively correlated with positive Q/Q_σ values. This means that voids are more likely to occur in regions of positive Q/Q_σ and less likely in regions of negative Q/Q_σ. Conversely, particle clusters, defined by $C/C_0 > 1$, show a negative correlation with the Q-Criterion. This negative correlation becomes more pronounced as the concentration of the particle clusters increases, indicating that higher-density clusters are increasingly likely to be found in regions of negative Q/Q_σ. This pattern underscores the significant role of the Q-Criterion in influencing the spatial distribution of inertial particles within the turbulent flow.

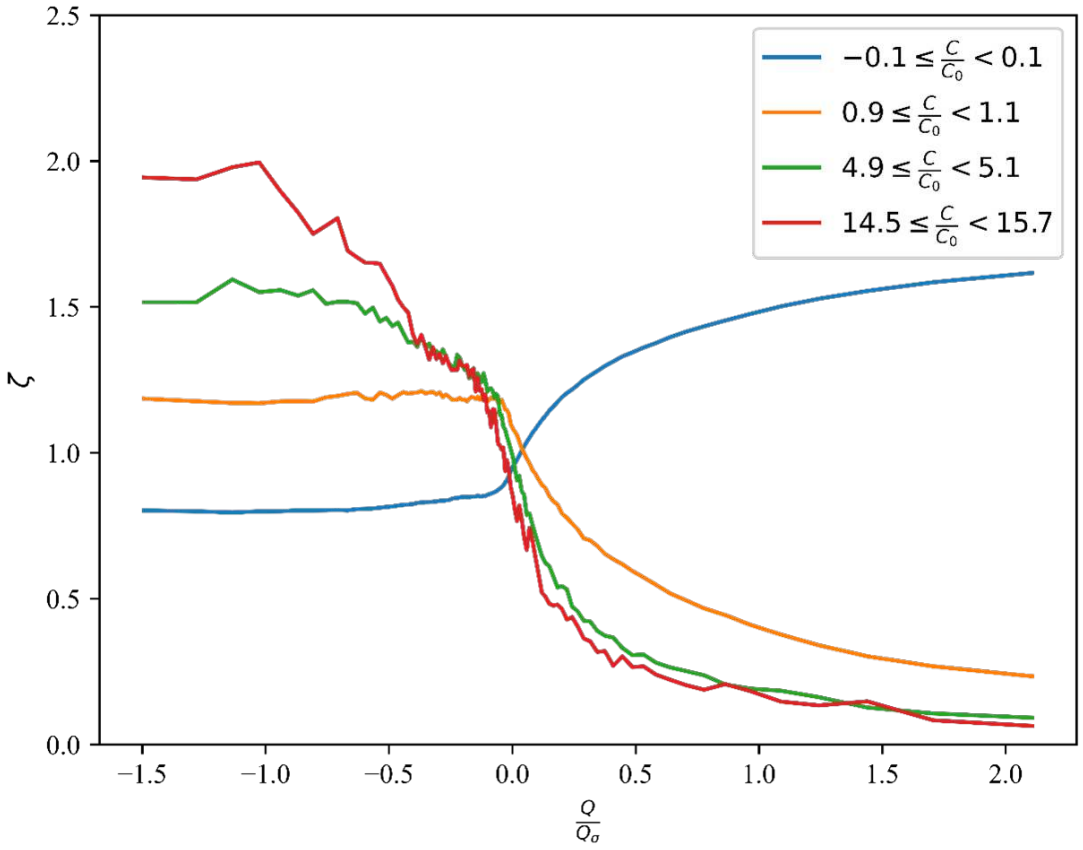


Figure 5.6: Ratio ζ of the probability density functions (PDFs) for four selected particle concentrations: $C/C_0 \approx 0.0$ (voids), $C/C_0 \approx 1.0$ (mean concentration), $C/C_0 \approx 5.0$ (clusters), and $C/C_0 \approx 15.0$ (intense clusters), plotted against the Q-Criterion Q/Q_σ.

To provide a clearer comparison of how the Q-Criterion affects different levels of particle concentration, we avoid the two-dimensional ratio ζ of Figure 5.5. Instead, we focus on four specific particle concentrations: $C/C_0 \approx 0.0$ representing voids, $C/C_0 \approx 1.0$ representing the mean concentration, $C/C_0 \approx 5.0$ for clusters, and $C/C_0 \approx 15.0$ for intense clusters. Figure 5.6 illustrates the ratio ζ of the PDFs for these four concentrations, effectively corresponding to four horizontal slices obtained from Figure 5.5. This approach allows for a more straightforward interpretation of the effect of Q-Criterion on different particle concentrations.

The results show that clusters with $C/C_0 > 5$ are significantly suppressed by positive Q/Q_σ values, with the ratio trending toward zero as Q/Q_σ exceeds 1.0. Compared to Figure 5.2, the effect on clusters is more pronounced here, as it is not averaged across all particles. Voids, on the other hand, are more prevalent in regions of positive Q/Q_σ, though this effect diminishes as Q/Q_σ increases, with the ratio peaking at just over 1.6 for $Q/Q_\sigma = 2$.

In contrast, when examining regions of negative Q/Q_σ, the effects are less pronounced. For lower concentrations ($C/C_0 \leq 1$), the ratio of the PDFs ap-

pears independent of the Q-Criterion, indicating that the formation of voids is not strongly influenced by negative Q regions, which are characterised by high strain. However, the ratio remains significant (around 0.8 for $C/C_0 \approx 0.0$), suggesting that voids still frequently occur at these negative Q/Q_σ regions.

For higher concentration clusters, the association with negative Q/Q_σ becomes more evident, with the effect intensifying as the cluster concentration increases. These findings suggest that while a negative Q/Q_σ is not the only condition for particle clustering, it is a necessary condition for the formation of such clusters.

5.4.2 Influence of Enstrophy

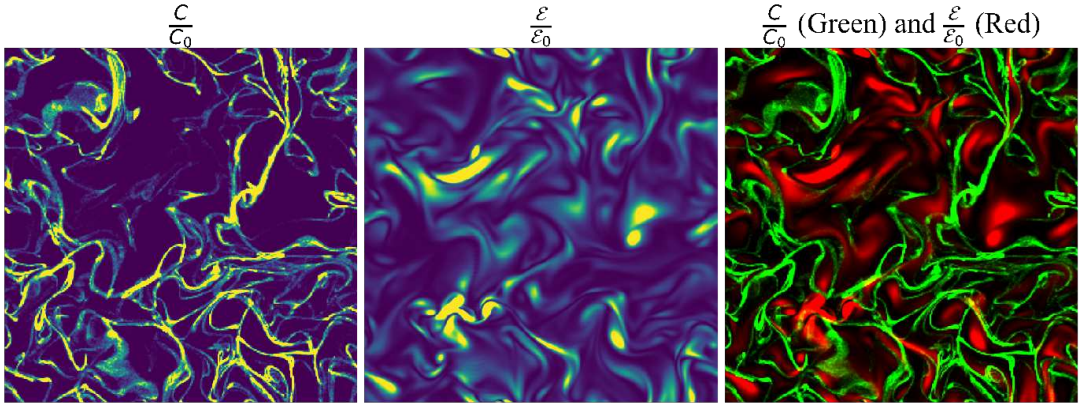


Figure 5.7: Normalised particle concentration C/C_0(left) and normalised Enstrophy $\varepsilon/\varepsilon_0$ (middle) in a slice of turbulence with $Re_\lambda = 90.0$ and $Stk = 1.0$. Low values are in blue and high values are in yellow. Superimposed image of the two quantities (right), the green channel represents particle concentration, while the red channel represents Enstrophy. The particle concentration was calculated using a box-counting method with a box width of 2η.

The Q-Criterion is derived from the difference between the rotation rate and the strain rate in turbulent flows. In the previous section (Section 5.4.1), particularly in Figure 5.6, it appeared that positive Q/Q_σ values (indicating rotation-dominated regions) had a more significant effect on particle concentration than negative Q/Q_σ values. This observation leads us to further explore the impact of rotation alone, which is quantified by the Enstrophy.

Unlike the Q-Criterion, which can be zero in regions where strain and rotation balance each other out, the Enstrophy focuses solely on the rotation rate. This distinction allows us to isolate the effect of rotational motion on particle concentration.

Figure 5.7 presents the normalised particle concentration C/C_0 alongside the normalised Enstrophy $\varepsilon/\varepsilon_0$, with these two fields overlaid at the right hand figure, where the green channel represents the particle concentration, while the red

channel represents the Enstrophy, within a slice of turbulence characterised by $Re_\lambda = 90$ and $Stk = 1.0$.

When comparing Figure 5.7 with Figure 5.1, it is evident that the maximum values of Enstrophy and the Q-Criterion generally coincide, which is expected due to the inherent relationship between rotation and Q-Criterion. However, from a visual inspection alone, it is challenging to determine whether the Enstrophy is more or less important than the Q-Criterion in influencing particle concentration. This motivates a more detailed quantitative analysis to draw definitive conclusions.

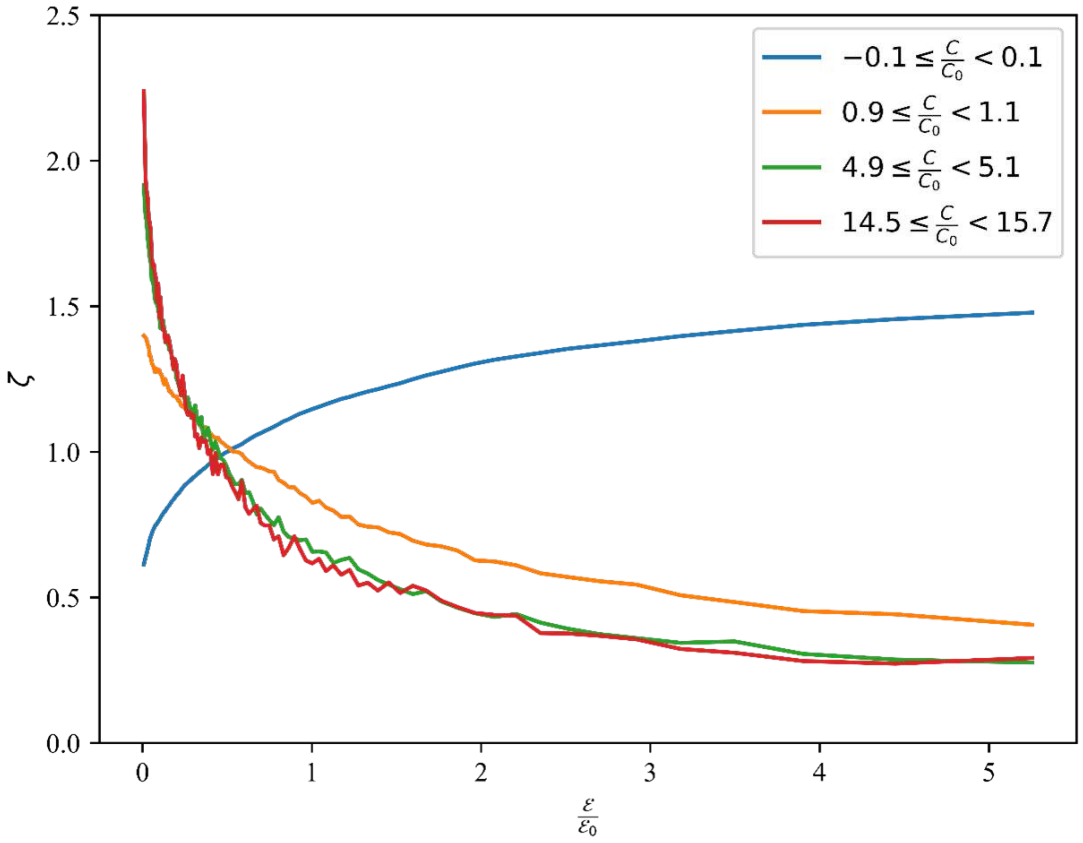


Figure 5.8: Ratio ζ of the probability density functions (PDFs) for four selected particle concentrations: $C/C_0 \approx 0.0$ (voids), $C/C_0 \approx 1.0$ (mean concentration), $C/C_0 \approx 5.0$ (clusters), and $C/C_0 \approx 15.0$ (intense clusters), plotted against the Enstrophy $\varepsilon/\varepsilon_0$.

Figure 5.8 presents the ratio ζ of the probability density functions (PDFs) against the Enstrophy $\varepsilon/\varepsilon_0$ for four different particle concentrations: $C/C_0 \approx 0.0$ (voids), $C/C_0 \approx 1.0$ (mean concentration), $C/C_0 \approx 5.0$ (clusters), and $C/C_0 \approx 15.0$ (intense clusters). The trends observed in Figure 5.8 indicate that particle clusters are significantly more likely to be found in regions of low Enstrophy, which aligns with the expected centrifuging effect where particles tend to avoid regions with high rotational motion. When compared to Figure 5.6, it is evident that clusters with $C/C_0 \approx 15.0$ are even more concentrated in areas of low Enstrophy,

with the ratio ζ peaking at 2.3, compared to a peak of 2.0 in areas of low Q/Q_σ.

This trend is also applicable to voids, as low Enstrophy regions exhibit a lower ratio ζ than low Q/Q_σ regions. These observations reinforce the findings from Figure 5.6, where the strength of the negative Q-Criterion appeared to have a limited effect on particle concentration.

However, for regions of high Enstrophy $\varepsilon/\varepsilon_0$, the suppression of clusters and the promotion of voids are not as pronounced as in regions with high positive Q-Criterion. Specifically, the PDF ratio ζ for clusters with $C/C_0 > 5.0$ stabilises around 0.2 in areas of high Enstrophy, in contrast to almost 0.0 in regions with a high Q-Criterion. This suggests that while both Enstrophy and Q-Criterion influence particle distribution, they do so with differing intensities, particularly in high rotation-dominated regions.

5.4.3 Time delay of Q-Criterion

In the previous Sections (5.4.1 and 5.4.2), we examined the relationship between the instantaneous Q-Criterion and Enstrophy with the instantaneous particle concentration. However, it is important to recognise that particles in a turbulent flow are subject to a time-delay in their response when compared to the surrounding fluid.

For very small particles, characterised by a Stokes number (Stk) much less than 1, the time-delay in particle velocities with the fluid flow is negligible and can be considered instantaneous for most practical purposes. Nonetheless, even for such small particles, the temporal evolution of particle concentrations, including the formation of voids and clusters, requires time, meaning that the current concentration field reflects the influence of the fluid dynamics over a preceding period.

In contrast, for larger particles ($Stk \geq 1$), both the particle velocities and concentrations exhibit a more significant time-delay in response to changes in the fluid. This delay necessitates an examination of the fluid properties at earlier times to better understand the current particle distribution.

To achieve this, it is not sufficient to merely consider the fluid properties at the same spatial coordinates in the past, using Eulerian coordinates, because the mean flow could have advected any evolving structures away from the region of interest. Instead, we employ Lagrangian coordinates, which track the fluid elements backward in time, allowing us to investigate how past fluid properties have influenced the present particle concentrations. This approach provides a more accurate understanding of the dynamic interaction between fluid and particles, accounting for the inherent time-delays in the system.

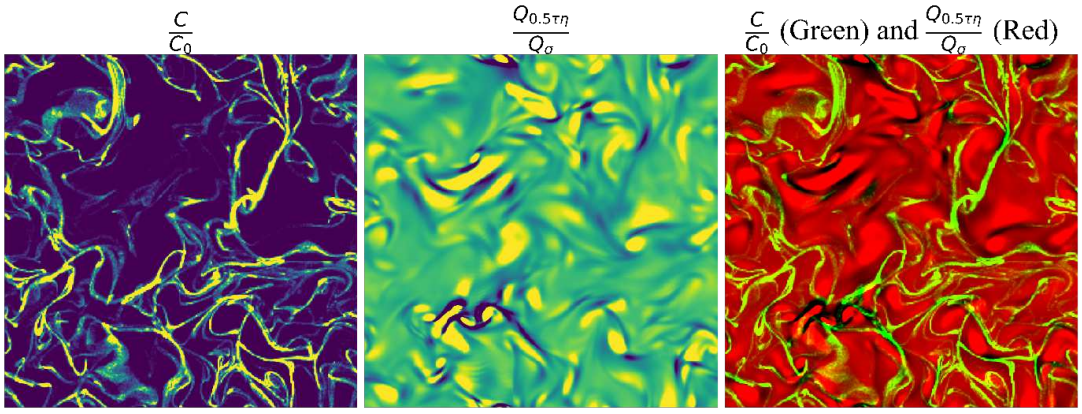


Figure 5.9: Normalised particle concentration C/C_0(left) and normalised Q-Criterion with a time-delay of $0.5\tau\eta$ ($Q_{0.5\tau\eta}/Q_\sigma$) (middle) in a slice of turbulence with $Re_\lambda = 90.0$ and $Stk = 1.0$. Low values are in blue and high values are in yellow. Superimposed image of the two quantities (right), the green channel represents particle concentration, while the red channel represents the Q-Criterion. The particle concentration was calculated using a box-counting method with a box width of 2η.

Figure 5.9 presents the normalised particle concentration C/C_0 alongside the normalised Q-Criterion $Q_{0.5\tau\eta}/Q_\sigma$ of the fluid at earlier time of 0.5 Kolmogorov timescale, using Lagrangian tracking to account for the time delay. The two fields are overlaid on each other, with the green channel representing particle concentration and the red channel representing the Q-Criterion. This visualization is obtained from a slice of turbulence with $Re_\lambda = 90.0$ and $Stk = 1.0$. This figure is similar to Figure 5.1, but with the crucial difference that a time delay has been introduced for the distribution of the Q-Criterion. The primary impact of the introduction of this time delay is the elongation of areas associated with high strain (negative $Q_{0.5\tau\eta}/Q_\sigma$), which is more evident in this visualization. However, for such a small-time difference, other effects are more subtle and harder to discern. The elongation of high-strain regions indicates that even a slight delay can influence the spatial distribution of $Q_{0.5\tau\eta}/Q_\sigma$, potentially affecting the alignment and interaction with particle clusters.

Figure 5.10 illustrates the ratio ζ of the probability density functions (PDFs) for the time-delayed distribution of the Q-Criterion, specifically with a delay of 0.5 Kolmogorov timescales. This figure allows the evaluation of how the time delay affects the correlation between Q-Criterion and particle concentration.

When compared to Figure 5.6, it is apparent that the ratio ζ is increased for clusters in regions of negative Q-Criterion. This suggests a stronger correlation between particle clusters and the time-delayed Q-Criterion than with the simultaneous Q-Criterion. The increased ratio indicates that considering the fluid's past

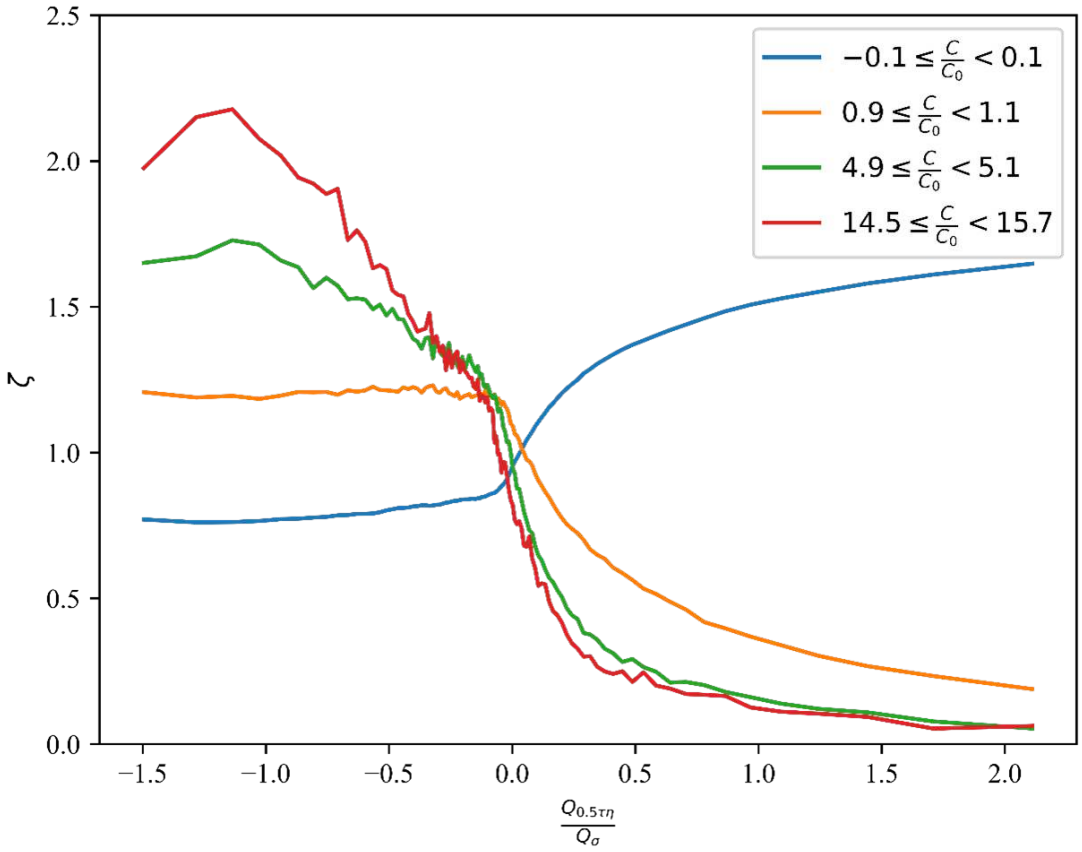


Figure 5.10: Ratio ζ of the probability density functions (PDFs) for four selected particle concentrations: $C/C_0 \approx 0.0$ (voids), $C/C_0 \approx 1.0$ (mean concentration), $C/C_0 \approx 5.0$ (clusters), and $C/C_0 \approx 15.0$ (intense clusters), plotted against the Q-Criterion with a time-delay of $0.5\tau\eta$ ($Q_{0.5\tau\eta}/Q_\sigma$).

state provides a better understanding of where particle clusters are likely to form, as the time-delayed Q-Criterion aligns more closely with the current distribution of these clusters.

Figure 5.11 presents a visualisation similar to Figure 5.9, but in this case, it depicts the normalised Q-Criterion $Q_{1.3\tau\eta}/Q_\sigma$ of the fluid at an earlier time of 1.3 Kolmogorov timescales, again using Lagrangian tracking to account for the time delay. The figure overlays the particle concentration C/C_0 and the Q-Criterion fields, with the green channel representing concentration and the red channel representing the Q-Criterion. In this figure, the elongation of the negative $Q_{1.3\tau\eta}/Q_\sigma$ regions, which correspond to high-strain areas, is more pronounced and easier to observe than in Figure 5.9. The increased time delay enhances the visibility of these elongated structures, making the association between particle clusters and regions of negative $Q_{1.3\tau\eta}/Q_\sigma$ more apparent. Some of the particle clusters now clearly align with these stretched regions of negative Q, indicating that these areas are favourable for cluster formation. However, it is also evident

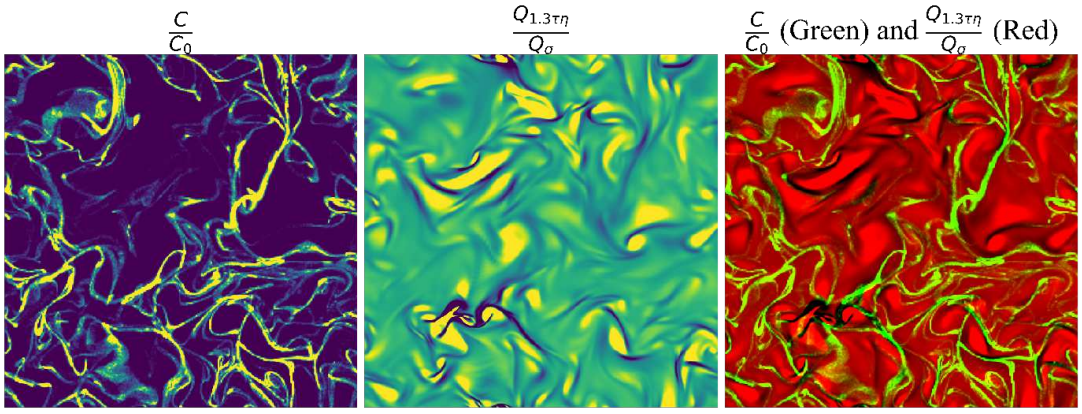


Figure 5.11: Normalised particle concentration C/C_0(left) and normalised Q-Criterion with a time-delay of $1.3\tau\eta$ ($Q_{1.3\tau\eta}/Q_\sigma$) (middle) in a slice of turbulence with $Re_\lambda = 90.0$ and $Stk = 1.0$. Low values are in blue and high values are in yellow. Superimposed image of the two quantities (right), the green channel represents particle concentration, while the red channel represents the Q-Criterion. The particle concentration was calculated using a box-counting method with a box width of 2η.

that some regions of highly negative $Q_{1.3\tau\eta}/Q_\sigma$ still correspond to voids, suggesting that while negative $Q_{1.3\tau\eta}/Q_\sigma$ is a strong indicator of cluster formation, it is not the sole determinant, and other factors may influence the presence of voids in these regions.

Figure 5.12 displays the ratio ζ of the probability density functions (PDFs) for the time-delayed Q-Criterion, this time with a delay of 1.3 Kolmogorov timescales. This allows us to further investigate how a longer time delay influences the correlation between the Q-Criterion and particle concentration.

When compared to Figure 5.10, the ratio ζ in Figure 5.12 shows a further increase for clusters in regions of negative Q-Criterion. This increase indicates an even stronger correlation between particle clusters and Q-Criterion when it is considered with a longer time delay. The higher ratio ζ suggests that the time-delayed Q-Criterion aligns more closely with the locations of particle clusters than the instantaneous Q-Criterion, reinforcing the idea that past fluid dynamics play a significant role in determining the present distribution of particle clusters in turbulence.

Figure 5.13 is similar to Figure 5.11, but with a time delay of 2.6 Kolmogorov timescales applied to the Q-Criterion $Q_{2.6\tau\eta}/Q_\sigma$. As in previous figures, the particle concentration C/C_0 and the time-delayed Q-Criterion fields are overlaid, with the green channel representing concentration and the red channel representing the Q-Criterion. With this extended time delay, the elongation of the negative $Q_{2.6\tau\eta}/Q_\sigma$ regions, corresponding to high-strain areas, becomes even more pro-

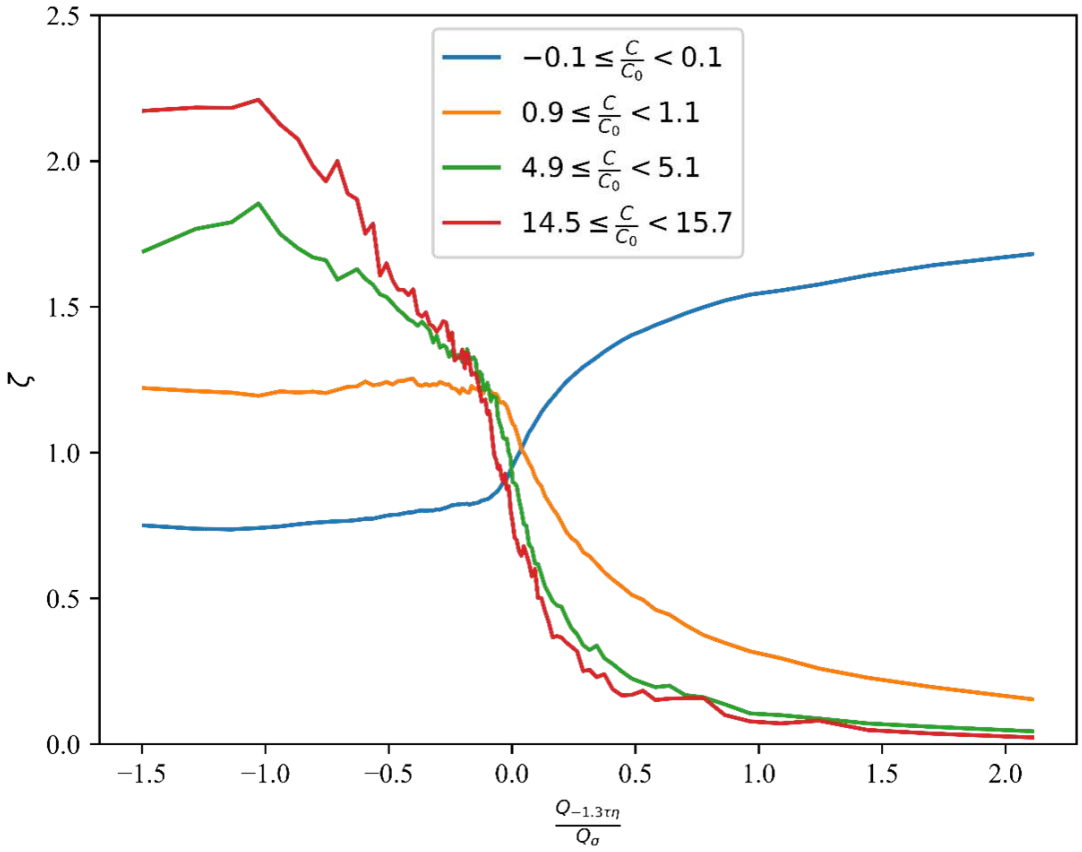


Figure 5.12: Ratio ζ of the probability density functions (PDFs) for four selected particle concentrations: $C/C_0 \approx 0.0$ (voids), $C/C_0 \approx 1.0$ (mean concentration), $C/C_0 \approx 5.0$ (clusters), and $C/C_0 \approx 15.0$ (intense clusters), plotted against the Q-Criterion with a time-delay of $1.3\tau\eta$ ($Q_{1.3\tau\eta}/Q_\sigma$).

nounced and visually distinct. The increased delay causes these regions to stretch further, with some areas becoming very thin. This enhanced elongation makes the alignment of particle clusters with these high-strain regions more apparent, emphasizing the influence of past fluid dynamics on the current distribution of particles. The thin, elongated structures highlight the temporal evolution of turbulence and its impact on the spatial distribution of particle clusters.

Figure 5.14 presents the ratio ζ of the probability density functions (PDFs) for the time-delayed Q-Criterion, this time with a delay of 2.6 Kolmogorov timescales. This figure allows for a comparison of how varying time delays affect the association between the Q-Criterion and particle concentration.

Compared to Figure 5.12, Figure 5.14 shows a decreased ratio ζ for clusters in regions of negative Q-Criterion. This reduction in ζ suggests that the strength of the correlation between particle clusters and the time-delayed Q-Criterion diminishes with a longer time delay. This observation indicates that the optimal time delay for maximizing the correlation between the Q-Criterion and particle

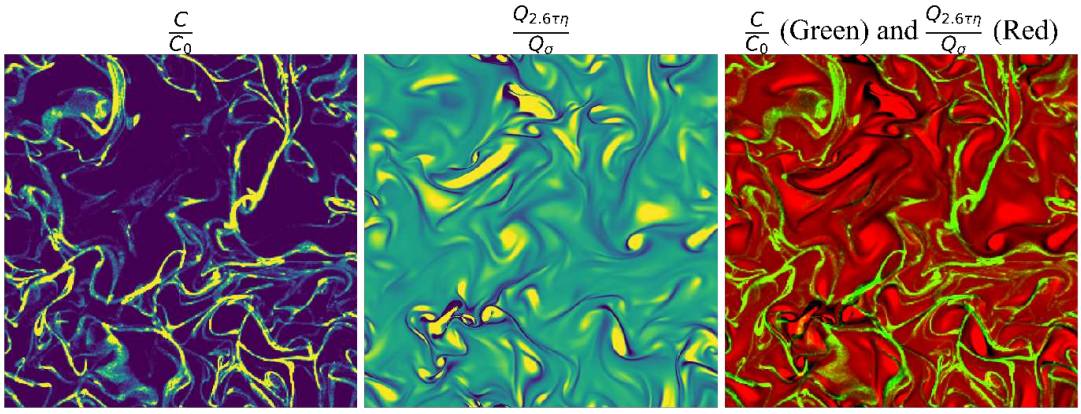


Figure 5.13: Normalised particle concentration C/C_0(left) and normalised Q-Criterion with a time-delay of $2.6\tau\eta$ ($Q_{2.6\tau\eta}/Q_\sigma$) (middle) in a slice of turbulence with $Re_\lambda = 90.0$ and $Stk = 1.0$. Low values are in blue and high values are in yellow. Superimposed image of the two quantities (right), the green channel represents particle concentration, while the red channel represents the Q-Criterion. The particle concentration was calculated using a box-counting method with a box width of 2η.

concentration is around 1 Kolmogorov timescale. Notably, this time scale is also commonly used in scaling the particle Stokes number, where maximum preferential concentration typically occurs at approximately $Stk = 1$. This alignment reinforces the importance of considering time delays when analysing the dynamics of particle clustering in turbulent flows.

While this study has focused on a Stokes Number of 1, it remains an open question whether a delay of $1\tau\eta$ is optimal for all particle sizes or if the best offset is related to the Stokes number. One possible explanation is that the optimal time delay might correspond to the particle response time, particularly for particles with a Stokes number close to 1. However, this scaling may only hold to a certain extent, as particles with much larger Stokes numbers exhibit different dynamics and may require a different approach.

Another plausible explanation is that the Kolmogorov timescale provides a useful relationship between particle velocity divergence and particle concentration, making this offset particularly effective for particles with smaller Stokes numbers. The Kolmogorov timescale might serve as a robust measure for linking these variables, especially in the context of moderate Stokes numbers, where particle clustering is most pronounced.

However, it is important to note that as the Reynolds number changes, the timescale that links particle velocity divergence with particle concentration may also shift. This relationship may not be universally fixed at 1 Kolmogorov timescale across different flow conditions. Further investigation is needed to determine

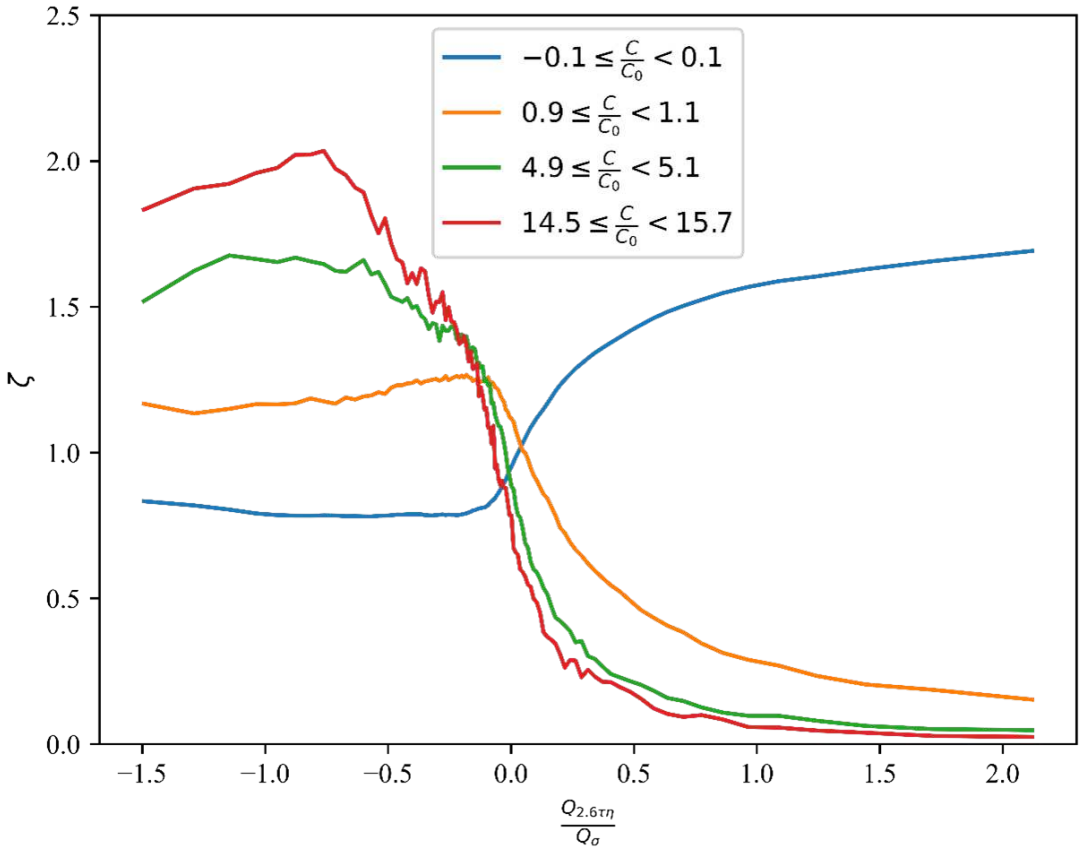


Figure 5.14: Ratio ζ of the probability density functions (PDFs) for four selected particle concentrations: $C/C_0 \approx 0.0$ (voids), $C/C_0 \approx 1.0$ (mean concentration), $C/C_0 \approx 5.0$ (clusters), and $C/C_0 \approx 15.0$ (intense clusters), plotted against the Q-Criterion with a time-delay of $2.6\tau\eta$ ($Q_{2.6\tau\eta}/Q_\sigma$).

whether the optimal time delay varies with changes in the Reynolds number or if it remains consistent across a range of turbulent flow regimes.

5.4.4 Finite-Time Lyapunov Exponent (FTLE)

In Section 5.4.3, we observed that introducing a Lagrangian time delay into the Q-Criterion provides a stronger correlation with particle concentration compared to using the simultaneous values of the Q-Criterion. This finding motivates us to explore Lagrangian Coherent Structures (LCS), which offer a more comprehensive understanding of fluid dynamics over time.

Lagrangian Coherent Structures (LCS) are defined as structures in a fluid flow that are responsible for organizing the trajectories of fluid particles over a finite time period. These structures can act as transport barriers, guiding the movement of particles and often defining the boundaries of eddies and other coherent flow patterns.

The lifetime of a particle cluster is variable and generally exhibits a probability

distribution function (PDF) with long tails, indicating that while most clusters have relatively short lifetimes, some can persist significantly longer. Notably, the lifetime of a cluster tends to increase with its size [99]. For particles with a Stokes number (Stk) of 1, the average cluster lifetime is approximately 4 Kolmogorov timescales, though this can extend to as much as 20 Kolmogorov timescales for the largest clusters [99]. Motivated by this variability in cluster lifetimes, we tested time windows corresponding to roughly one integral timescale (approximately 15 Kolmogorov timescales for the Reynolds number under consideration) and 0.5 integral timescales. The integral timescale provides a good approximation of the correlation time for the largest turbulent structures, ensuring that the most significant eddies are well-captured by the LCSs. However, it is important to consider that as the time window increases, the coherency of the LCSs tends to degrade due to the fractal nature of turbulence, which causes fluid particles to separate more rapidly over time. By selecting these timescales, we aim to strike a balance where the LCSs remain coherent enough to provide meaningful insights into the fluid dynamics while still encompassing the influence of larger-scale turbulent structures.

One popular method for identifying LCS is the use of the Finite-Time Lyapunov Exponent (FTLE). The FTLE measures how much fluid particles are either attracted to (in the case of backward FTLE) or repelled from (in the case of forward FTLE) a particular region over a finite time interval. The resulting FTLE field can often delineate the boundaries of eddies and other coherent structures in the flow. In our analysis, we focus on the backward FTLE, which identifies regions where fluid particles are attracted over time.

Figure 5.15 presents the normalised particle concentration C/C_0 alongside the Finite-Time Lyapunov Exponent (FTLE) field, calculated over a time window of 15.1 Kolmogorov timescales. The two fields are overlaid, with the green channel representing the particle concentration and the red channel representing the FTLE, providing a detailed view of a slice of turbulence characterised by $Re_\lambda = 90.0$ and $Stk = 1.0$.

The FTLE field identifies attracting boundaries where fluid particles converge over time. It is reasonable to infer that inertial particles may also be drawn to these regions, suggesting that these boundaries could play a role in the formation of particle clusters.

The structure of the FTLE field reveals visual similarities to the patterns formed by inertial particle clusters, particularly in the appearance of string-like, connected structures. However, the FTLE field contains many more such structures, especially in the regions identified as voids in the particle concentration field. This observation indicates that while the FTLE can capture the intricate dynam-

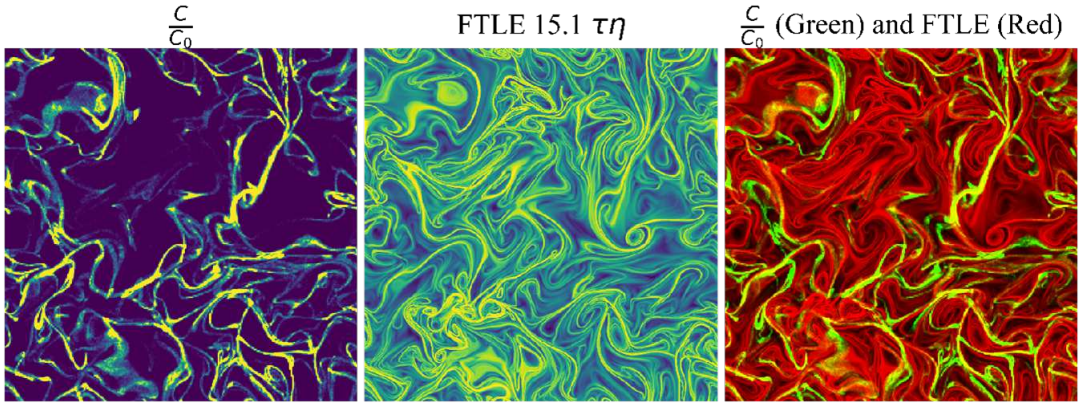


Figure 5.15: Normalised particle concentration C/C_0(left) and FTLE field with a time window of $15.1\tau\eta$ (middle) in a slice of turbulence with $Re_\lambda = 90.0$ and $Stk = 1.0$. Low values are in blue and high values are in yellow. Superimposed image of the two quantities (right), the green channel represents particle concentration, while the red channel represents the FTLE field. The particle concentration was calculated using a box-counting method with a box width of 2η.

ics of fluid attraction, it may identify coherent structures that do not directly correlate with particle clustering, highlighting the complexity of the interaction between particles and turbulent flow.

Figure 5.16 presents the ratio ζ of the probability density functions (PDFs) as a function of the Finite-Time Lyapunov Exponent (FTLE) estimated over a time window of 15.1 Kolmogorov timescales. The results indicate a correlation between particle clusters and areas of high FTLE, suggesting that clusters are more likely to form in regions with stronger attracting boundaries. However, this correlation is the weakest observed among the different fluid properties analysed so far, such as the Q-Criterion and Enstrophy.

Similarly, the correlation between particle voids and the FTLE is also weak, indicating that while the FTLE field does capture some aspects of particle clustering and void formation, it is not as strongly predictive of these phenomena as other fluid properties. This suggests that the FTLE, while useful in identifying coherent structures in the flow, may not fully account for the dynamics that govern the spatial distribution of inertial particles in turbulence.

The use of a time window of 15.1 Kolmogorov timescales in the previous analysis produced a FTLE field with an excessive number of structures. This high density of ridges is an artifact of the chaotic nature of turbulence, where longer time windows can exaggerate the complexity of the flow. To mitigate this effect, the time window, over which the FTLE field was evaluated, was reduced to 7.4 Kolmogorov timescales, which decreases the density of ridges in the FTLE field, providing a clearer and more interpretable visualization.

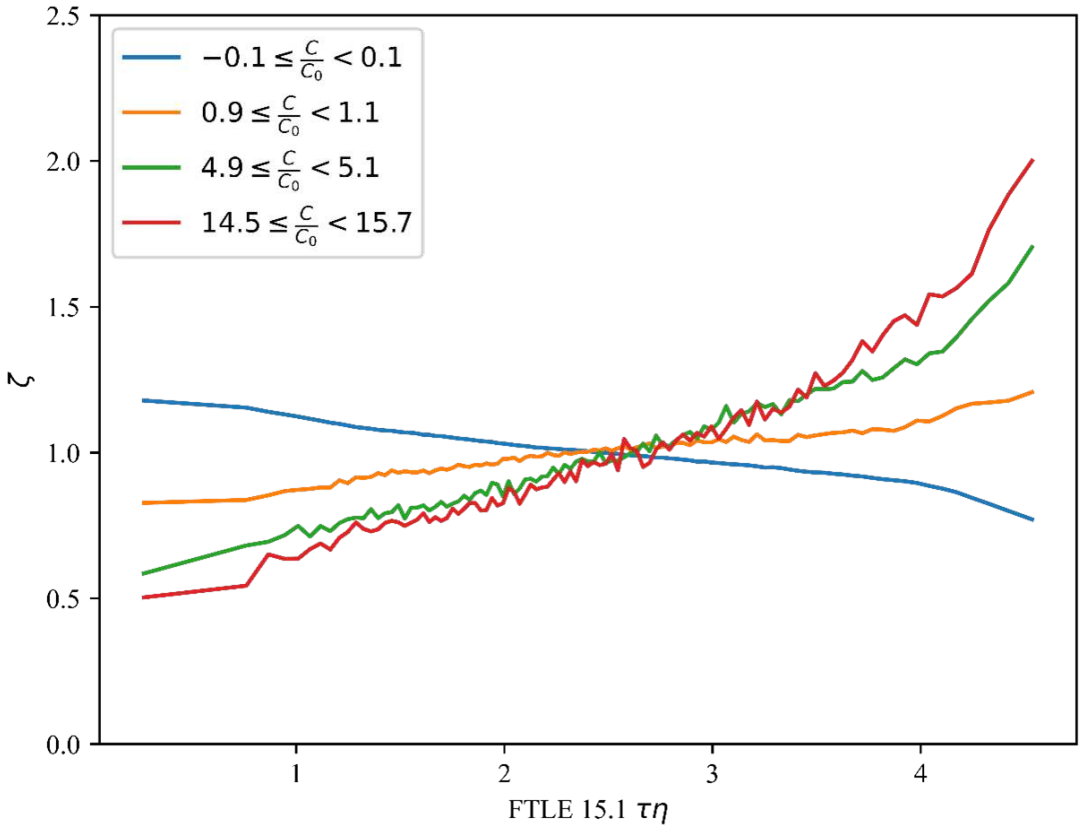


Figure 5.16: Ratio ζ of the probability density functions (PDFs) for four selected particle concentrations: $C/C_0 \approx 0.0$ (voids), $C/C_0 \approx 1.0$ (mean concentration), $C/C_0 \approx 5.0$ (clusters), and $C/C_0 \approx 15.0$ (intense clusters), plotted against the FTLE estimated over a time-window of $15.1\tau\eta$.

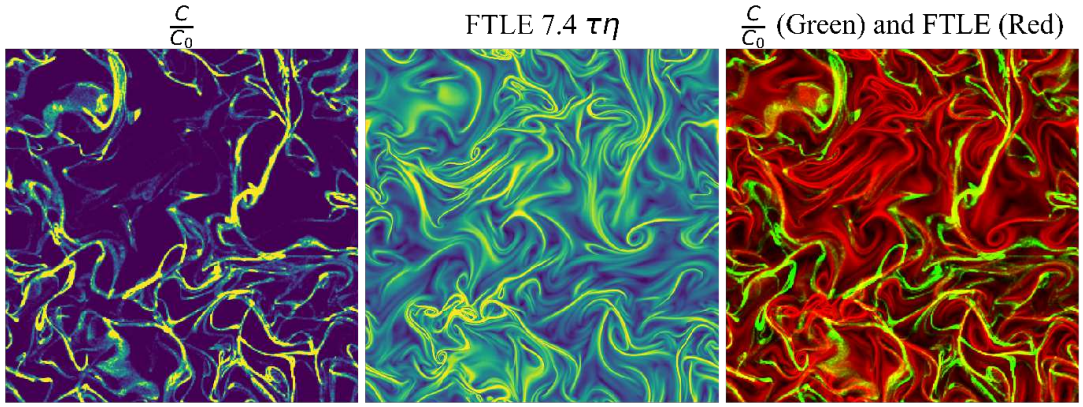


Figure 5.17: Normalised particle concentration C/C_0(left) and FTLE field with a time window of $7.4\tau\eta$ (middle) in a slice of turbulence with $Re_\lambda = 90.0$ and $Stk = 1.0$. Low values are in blue and high values are in yellow. Superimposed image of the two quantities (right), the green channel represents particle concentration, while the red channel represents the FTLE field. The particle concentration was calculated using a box-counting method with a box width of 2η.

Figure 5.17 shows the normalised particle concentration C/C_0 overlaid with the Finite-Time Lyapunov Exponent (FTLE) field, now calculated over a shorter time window of 7.4 Kolmogorov timescales.

When compared to Figure 5.15, it is evident that the FTLE field in Figure 5.17 is much smoother, with fewer and less intricate structures. This reduction in complexity makes it easier to identify key features of the flow and their association with particle concentration. The smoother FTLE field also offers a more straightforward analysis of the relationship between coherent structures in the flow and the spatial distribution of inertial particles.

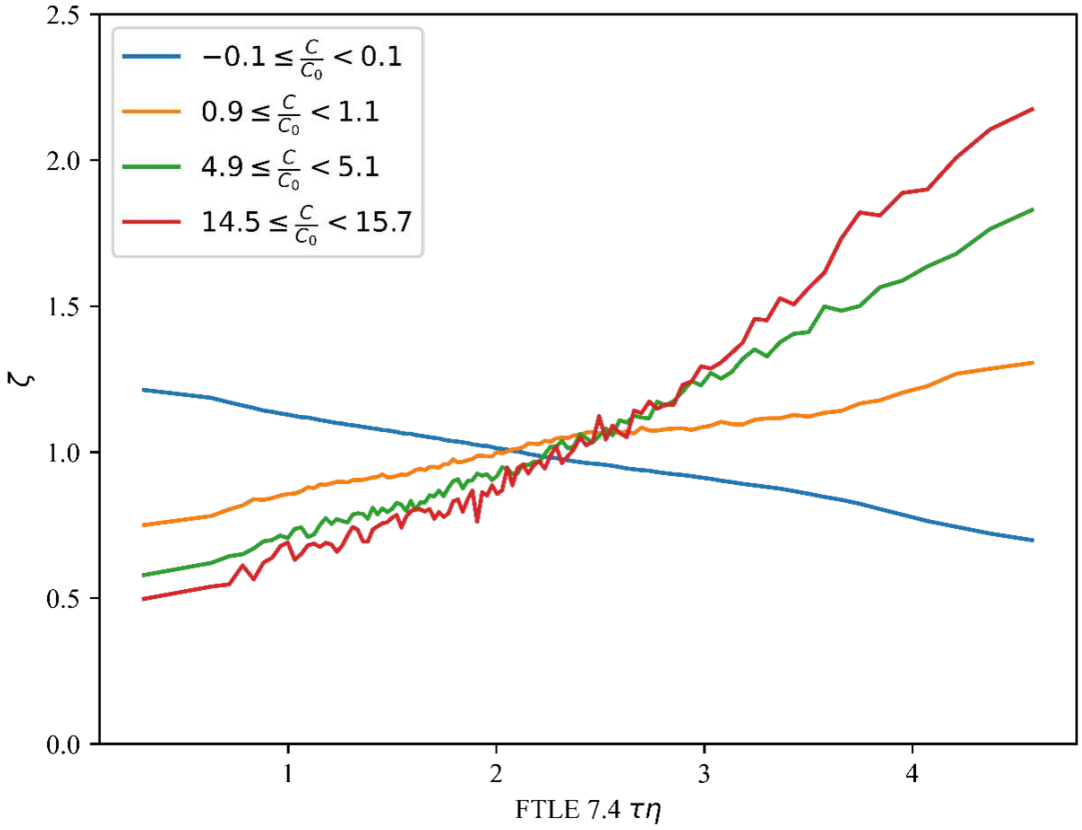


Figure 5.18: Ratio ζ of the probability density functions (PDFs) for four selected particle concentrations: $C/C_0 \approx 0.0$ (voids), $C/C_0 \approx 1.0$ (mean concentration), $C/C_0 \approx 5.0$ (clusters), and $C/C_0 \approx 15.0$ (intense clusters), plotted against the FTLE estimated over a time-window of $7.4\tau\eta$.

Figure 5.18 displays the ratio ζ of the probability density functions (PDFs) for the Finite-Time Lyapunov Exponent (FTLE), calculated over a reduced time window of 7.4 Kolmogorov timescales. This figure allows us to evaluate how the shorter time window affects the correlation between the FTLE and particle concentration. When compared to Figure 5.16, which used a longer time window of 15.1 Kolmogorov timescales, Figure 5.18 shows a slight increase in the correlation between particle clusters and the FTLE. This suggests that the smoother

FTLE field, resulting from the shorter time window, provides a somewhat better indication of where particle clusters are likely to form.

However, despite this improvement, the FTLE remains a less effective indicator of particle clusters compared to other fluid properties, such as the Q-Criterion or Enstrophy. While the FTLE can capture some aspects of the relationship between fluid dynamics and particle clustering, its predictive power is still limited relative to these other metrics, which more directly influence the spatial distribution of particles in turbulent flows.

5.4.5 Lagrangian-Averaged Vorticity Deviation (LAVD)

The Finite-Time Lyapunov Exponent (FTLE) is a measure of hyperbolic Lagrangian Coherent Structures (LCSs), which are regions in the flow where fluid particles either converge or diverge rapidly, often delineating boundaries that separate different flow regions. However, hyperbolic LCSs are not the only important structures in turbulent flows.

Elliptic LCSs, on the other hand, represent closed and nested material surfaces that serve as the Lagrangian equivalents of vortices. These are rotation-dominated regions where particle trajectories typically traverse the phase space without experiencing significant stretching or folding. Unlike hyperbolic LCSs, which are associated with stretching and folding, elliptic LCSs provide a more direct indication of coherent eddies within turbulence.

Elliptic LCSs are particularly relevant for understanding the long-term behaviour of vortices, which are expected to correlate strongly with voids in the particle concentration field due to centrifugal forces that tend to expel particles from these rotational regions. This makes elliptic LCSs a valuable tool for studying the spatial distribution of particles in turbulent flows.

A common and relatively straightforward method for quantifying the rotational coherence of the flow, and thus identifying elliptic LCSs, is the Lagrangian-averaged vorticity deviation (LAVD). The LAVD is a measure of how much the vorticity of fluid particles deviates from the average, over a finite time, and it effectively captures the rotational coherence of the flow. This makes LAVD a useful metric for identifying elliptic LCSs and understanding their relationship with particle clustering and void formation in turbulent environments.

Figure 5.19 presents the normalised particle concentration C/C_0 alongside the Lagrangian-averaged vorticity deviation (LAVD) field, calculated over a time window of 15.1 Kolmogorov timescales. These two fields are overlaid on each other, with the green channel representing particle concentration and the red channel representing the LAVD. The visualization is based on a slice of turbulence with

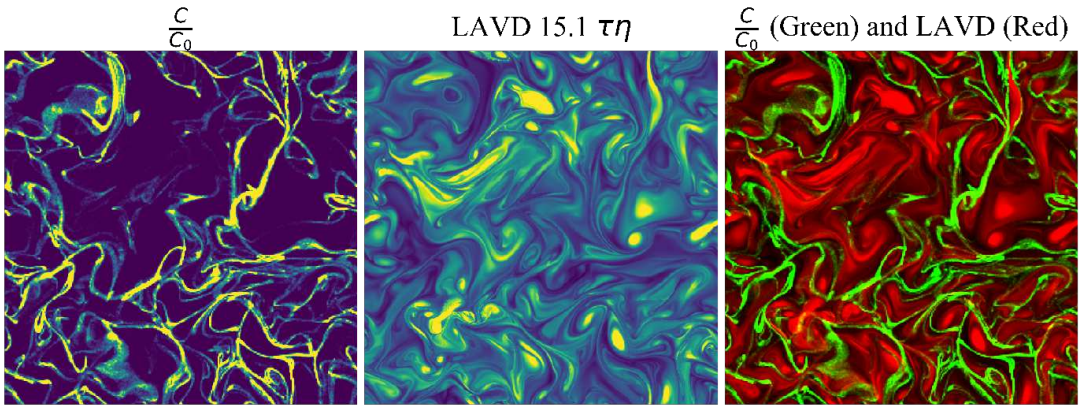


Figure 5.19: Normalised particle concentration C/C_0(left) and LAVD field over a time window of $15.1\tau\eta$ (middle) in a slice of turbulence with $Re_\lambda = 90.0$ and $Stk = 1.0$. Low values are in blue and high values are in yellow. Superimposed image of the two quantities (right), the green channel represents particle concentration, while the red channel represents the LAVD field. The particle concentration was calculated using a box-counting method with a box width of 2η.

$Re_\lambda = 90.0$ and $Stk = 1.0$. Qualitatively, the LAVD field allows for the identification of boundaries that correspond to coherent eddies in the flow. These boundaries, as highlighted by the LAVD, can be used to define the edges of these rotational structures within the turbulence. Most particle clusters appear to align with these boundaries between coherent eddies. This suggests that the edges of these rotational regions play a significant role in the spatial distribution of particles, likely due to the centrifugal effects that push particles away from the core of the eddies and towards the boundaries.

However, the relationship between eddy boundaries and particle clusters is not entirely straightforward. In some instances, the boundaries between coherent eddies may not be "stable" enough to maintain inertial particle clusters, leading to the merging of multiple eddies and the formation of a single void. Conversely, in other cases, a void may be well-defined by a single, stable eddy. It remains unclear what factors determine whether an eddy will contribute to the formation of a stable void or if it will combine with others to form a larger, more diffuse void.

Figure 5.20 presents the ratio ζ of the probability density functions (PDFs) for the Lagrangian-averaged vorticity deviation (LAVD) calculated over a time window of 15.1 Kolmogorov timescales. This figure provides a detailed analysis of the relationship between LAVD and particle concentration, particularly focusing on how this measure of rotational coherence correlates with particle clustering. The results show the strongest correlation observed yet between a fluid property and particle clusters. Specifically, at high LAVD values, particle clusters with

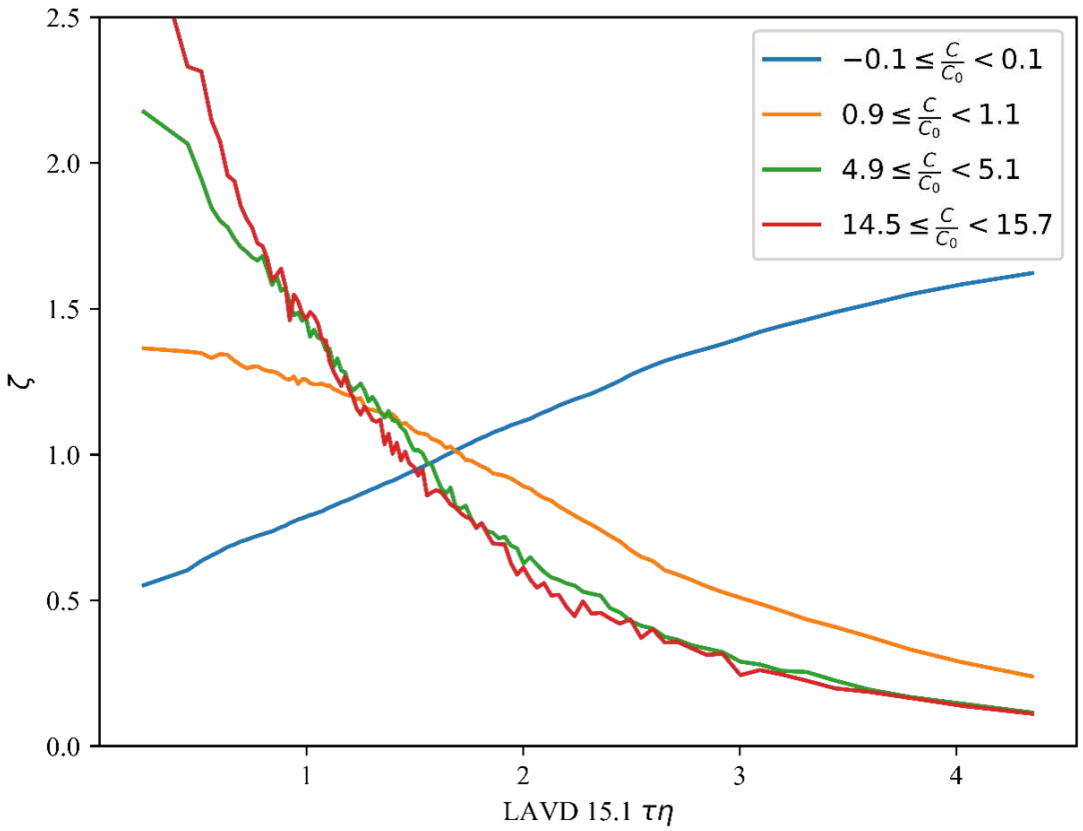


Figure 5.20: Ratio ζ of the probability density functions (PDFs) for four selected particle concentrations: $C/C_0 \approx 0.0$ (voids), $C/C_0 \approx 1.0$ (mean concentration), $C/C_0 \approx 5.0$ (clusters), and $C/C_0 \approx 15.0$ (intense clusters), plotted against the LAVD over a time-window of $15.1\tau\eta$.

$C/C_0 \geq 5.0$ are significantly diminished, and this reduction is largely independent of the particle concentration itself. Conversely, at low LAVD values, these particle clusters are strongly promoted, although this promotion is not entirely independent of particle concentration and becomes more pronounced as the concentration increases. These findings suggest that particle clusters are predominantly found in regions of the flow that have maintained low vorticity over a consistent period. This supports the idea that areas of low rotational activity are more conducive to the formation and persistence of particle clusters in turbulent flows.

Furthermore, voids are shown to have the strongest association with the LAVD field compared to any other fluid property discussed thus far. As noted in Figure 5.19, particle clusters often align with boundaries between eddies or groups of eddies. Consequently, voids remain significant at low LAVD values but are somewhat diminished. However, as the LAVD value increases, indicating stronger rotational coherence, the likelihood of voids also increases, suggesting a complex interplay between vorticity and spatial distribution of voids in the turbulent flow.

Figure 5.21 presents the normalised particle concentration C/C_0 alongside the

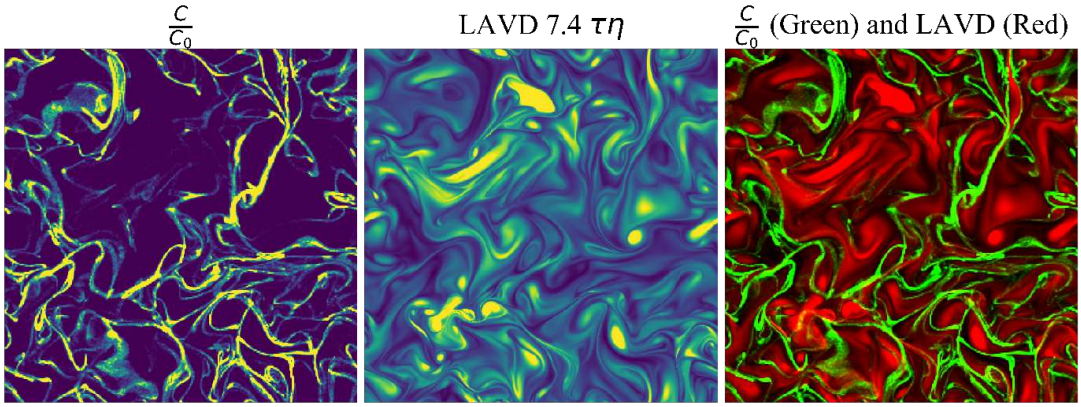


Figure 5.21: Normalised particle concentration C/C_0(left) and LAVD field over a time window of $7.4\tau\eta$ (middle) in a slice of turbulence with $Re_\lambda = 90.0$ and $Stk = 1.0$. Low values are in blue and high values are in yellow. Superimposed image of the two quantities (right), the green channel represents particle concentration, while the red channel represents the LAVD field. The particle concentration was calculated using a box-counting method with a box width of 2η.

Lagrangian-averaged vorticity deviation (LAVD) field, which is now calculated over a shorter time window of 7.4 Kolmogorov timescales. As with previous figures, these two fields are overlaid, with the green channel representing particle concentration and the red channel representing the LAVD. The visualization is based on a slice of turbulence characterized by $Re_\lambda = 90.0$ and $Stk = 1.0$. When comparing Figure 5.21 with Figure 5.19, which used a longer time window of 15.1 Kolmogorov timescales, only minimal differences are observed between the two LAVD fields. This similarity suggests that the LAVD field is relatively insensitive to changes of the time window used for its calculation, in contrast to the Finite-Time Lyapunov Exponent (FTLE) field, which showed more significant variations with different time windows.

The minimal changes between Figures 5.19 and 5.21 indicate that the LAVD is a more robust measure of Lagrangian Coherent Structures (LCSs) in homogeneous isotropic turbulence. This robustness makes LAVD a reliable metric for analysing the rotational coherence of turbulent flows and understanding the spatial distribution of particle concentrations and voids over time.

Figure 5.22 displays the ratio ζ of the probability density functions (PDFs) for the Lagrangian-averaged vorticity deviation (LAVD), calculated over a shorter time window of 7.4 Kolmogorov timescales. This figure allows us to compare the impact of different time windows on the relationship between LAVD and particle concentration. The results of Figure 5.22 are very similar to those of Figure 5.20, which used a longer time window of 15.1 Kolmogorov timescales. This similarity reinforces the observation that the LAVD field is less sensitive to changes of

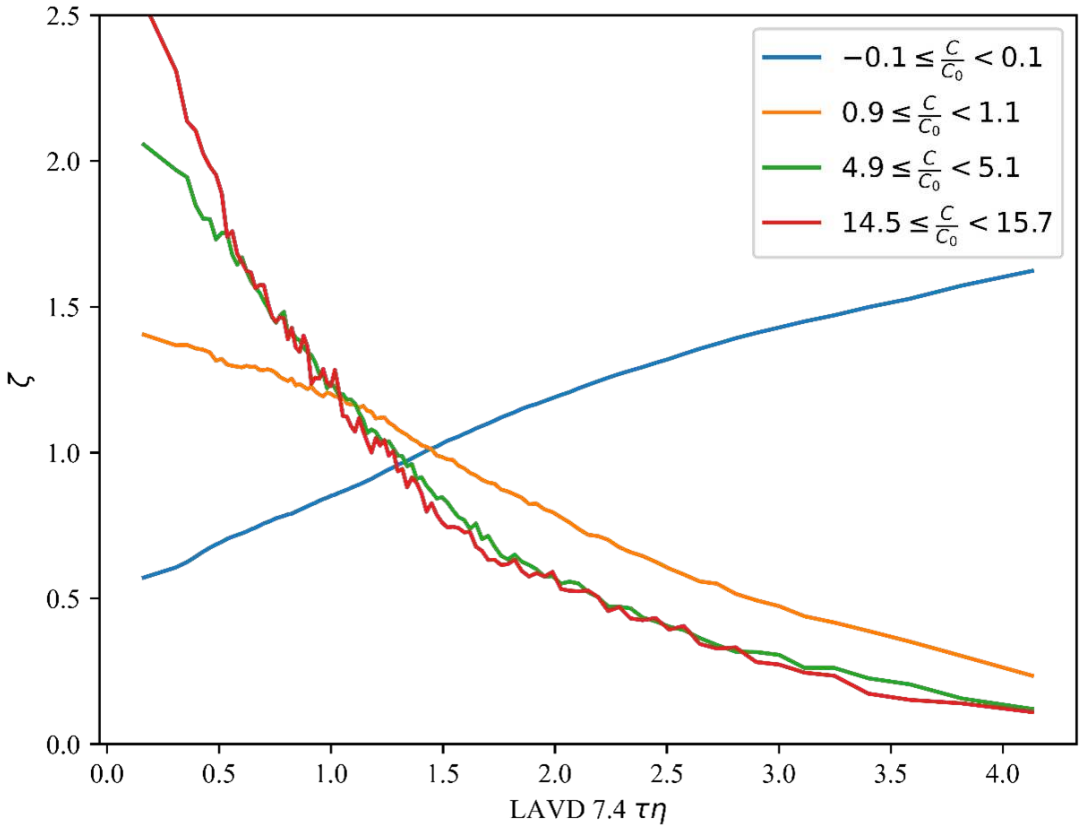


Figure 5.22: Ratio ζ of the probability density functions (PDFs) for four selected particle concentrations: $C/C_0 \approx 0.0$ (voids), $C/C_0 \approx 1.0$ (mean concentration), $C/C_0 \approx 5.0$ (clusters), and $C/C_0 \approx 15.0$ (intense clusters), plotted against the LAVD over a time-window of $7.4\tau\eta$.

the time window used for its calculation compared to the Finite-Time Lyapunov Exponent (FTLE) field, which showed more significant variations.

Overall, the association between the LAVD field and particle concentration with a time window of 7.4 Kolmogorov timescales is slightly weaker than that observed with the longer time window of 15.1 Kolmogorov timescales. However, the consistent results across different time windows highlight the robustness of LAVD as a measure for analysing the rotational coherence of turbulence and its influence on the spatial distribution of particles.

The distribution of void volumes in turbulent flows follows a power-law behaviour, as characterized by Yoshimoto and Goto [176], with a probability density function (PDF) proportional to $V_V^{-1.8}$. The range of void volumes observed spans from approximately $10^3\eta^3$ to $\mathcal{L}^3$, where $\mathcal{L}$ represents the integral length scale of the turbulence. Notably, when considering the volume-weighted PDF of void volumes, it becomes evident that a few very large voids dominate the overall void volume, emphasizing the significance of these large-scale structures in the flow.

Figures 5.19 and 5.21 illustrate that void volumes typically exceed the size

of individual eddies. This observation aligns with the idea that the structures between eddies may either be stable enough to form particle clusters or, alternatively, the influence of multiple eddies might combine to create a single large void. This raises interesting questions about the stability and coherence of these voids, particularly in relation to the surrounding turbulent structures.

Inertial particle clusters, as demonstrated by Baker et al. [6], tend to form tube-like structures that are predominantly one-dimensional, rather than taking the shape of ribbons, sheets, or spheres. The PDF for the coherent cluster volume follows a power-law distribution proportional to $V_C^{-2.0}$, further highlighting the prevalence of these elongated, tube-like formations. Figures 5.20 and 5.22 show that these structures correlate well with regions that we would expect to be associated with the boundaries between eddies. However, these are not the instantaneous boundaries identified by measures like the Q-criterion, but rather the Lagrangian-defined boundaries that account for the convection of eddies over time.

Given the presence of large-scale voids that can span across integral length scales and the extremely long tube-like particle clusters observed, it is worth questioning whether the Kolmogorov timescale is the most appropriate scale for defining the Stokes number. Although the tube-like clusters may have a thickness of the order of the Kolmogorov scale, it is not clear what determines the corresponding lengths. While the Kolmogorov timescale is often used to scale the Stokes number, this assumption may need to be revisited as the Reynolds number increases. As the range between the smallest and largest eddies expands, the most appropriate timescale for the Stokes number may shift towards the average timescale of coherent eddy structures, where most of the turbulent energy is contained.

This remains an open question, but it suggests that as turbulence becomes more intense and the scale separation increases, the traditional scaling with the Kolmogorov timescale may no longer be sufficient. Instead, a new scaling approach that accounts for the size and timescale of the dominant coherent structures in the flow might be necessary to accurately capture the dynamics of particle clustering and void formation in high-Reynolds-number turbulence.

5.5 Conclusions

The conclusions drawn from this study underscore the complex and multifaceted interactions between inertial particles and turbulent structures that characterise their turbulent flow environment. Through a detailed investigation of Lagrangian Coherent Structures (LCS) and their role in the preferential concentration of inertial particles, this work has provided new insights into the mechanisms that govern

particle clustering and void formation in turbulence.

The analysis reveals that the Q-Criterion, Enstrophy, and the Lagrangian-averaged vorticity deviation (LAVD) each play critical roles in influencing the spatial distribution of inertial particles. Among these, the Q-Criterion and Enstrophy have demonstrated a strong correlation with particle concentration, particularly in regions characterised by negative Q/Q_σ and low Enstrophy, where particle clusters tend to form. The study further highlights the importance of time delays in the response of particle concentrations to turbulent structures, with findings suggesting that a time delay of approximately one Kolmogorov timescale optimally correlates with particle clustering. This time-dependent behaviour underscores the non-instantaneous nature of particle responses to the surrounding fluid dynamics, emphasizing the necessity of considering past fluid states when analysing particle distributions.

The exploration of Lagrangian Coherent Structures, particularly through the use of the Finite-Time Lyapunov Exponent (FTLE) and LAVD, offers a deeper understanding of the dynamic processes that shape particle concentration distributions. While the FTLE field provided some correlation with particle clustering, its predictive power was limited compared to the LAVD, which emerged as the most robust indicator of particle spatial distribution. The LAVD field effectively captured the rotational coherence of turbulence, delineating the boundaries of coherent eddies where particle clusters are most likely to form. These findings suggest that the rotational dynamics of turbulence, as captured by the LAVD, play a pivotal role in organizing particle clusters and voids, with regions of low LAVD being particularly conducive to the formation and persistence of these clusters.

However, the study also reveals the inherent complexity of the interaction between inertial particles and turbulent flows. The results indicate that while certain fluid properties, such as the Q-Criterion and LAVD, are strong predictors of particle clustering, other factors, including the time-dependent nature of these interactions, contribute to the spatial heterogeneity observed in particle distributions. This complexity is further highlighted by the observation that even within well-defined Lagrangian Coherent Structures, particle clusters and voids can exhibit varying degrees of stability and coherence, depending on the underlying fluid dynamics.

The particle clusters observed in this study predominantly exhibited tube-like structures, whereas the voids were characterised by large, volumetric regions significantly exceeding the characteristic flow scales. These distinct structural differences indicate that the clustering mechanisms involve more than just local turbulence intensity or Enstrophy; rather, the clusters seem to align with elongated, tube-like regions between vortical structures, while voids form in areas

where the coherent rotational flow allows for larger spatial scales to develop. The persistence of these structures also suggests that Kolmogorov scaling may only partially describe the dynamics of particle clustering, particularly at higher turbulence intensities. While Kolmogorov scaling provides a reliable framework for understanding smaller-scale structures, it struggles to capture the length of tube-like clusters or the vast spatial dimensions of the voids. As turbulence intensity increases, and as the separation of scales becomes more pronounced, the relevant timescales for inertial particle behaviour may shift. In these cases, the most appropriate timescale for the Stokes number may no longer align with the Kolmogorov timescale but rather with the average timescale of coherent eddy structures, where most of the turbulent energy is concentrated. This highlights a potential scaling regime transition that should be considered when interpreting particle dynamics in stronger turbulent flows, especially at high Reynolds numbers.

Future work should focus on extending this analysis to more complex flow conditions, including higher Reynolds numbers and different particle Stokes numbers, to explore the generality of the observed patterns across different turbulent regimes. Further work should also focus on the criteria for when eddies either act singularly when forming a void or if a group of eddies all form one large void. Additionally, the integration of more advanced Lagrangian tracking techniques could offer deeper insights into the time-dependent behaviour of particle clustering and void formation. This could also include looking at multiple fluid properties at once to correlate with the particle concentration rather than just a single property. Finally, investigating the role of other coherent structures, such as those identified through different LCS criteria or by exploring non-hyperbolic structures, could further refine our understanding of the mechanisms driving preferential concentration in turbulent flows.

This final chapter wraps up the thesis by linking back to the broader implications of the studies, particularly in real-world applications like atmospheric science and environmental monitoring. The understanding of particle clustering gained from LCS and turbulence analysis can directly inform improved models for aerosol dispersion, reinforcing the relevance of the findings in the initial chapter.

Chapter 6

Conclusions

6.1 Summary

This thesis presents an integrated analysis of aerosol dispersion, particle preferential concentration, and turbulent flow interactions, offering significant insights into how particles behave in complex flow environments. The research is founded on a combination of experimental studies, numerical simulations, and advanced spectral analyses, each tailored to reveal key mechanisms that govern particle clustering, dispersion, and interaction with turbulence.

The first part (Chapter 2) of the research introduced a computational and experimental framework for predicting aerosol concentrations in enclosed spaces, focusing on the influence of particle size, room layout, and ventilation characteristics. A critical finding of this study is that the conventional metric of air changes per hour (ACH), widely used for assessing room safety in terms of aerosol contamination and disease transmission, is insufficient. ACH does not account for aerosol recycling or sedimentation, both of which play significant roles in particle behaviour. Larger particles, in particular, tend to settle over time, significantly altering the distribution and concentration of aerosols in the room. This work demonstrates that aerosol particles can accumulate in specific regions within a room, leading to localized concentrations many times higher than the average. Consequently, any evaluation of room safety should be complemented by a detailed analysis of air filtration and particle size-dependent sedimentation, particularly for applications involving public health.

The second study (Chapter 3) delved into the preferential concentration of particles in isotropic turbulence, focusing on how different methods—Eulerian and Lagrangian—model the interactions between particles and turbulent eddies. The Eulerian approach, especially when enhanced by second-order velocity moments, demonstrated a clear advantage in accurately predicting particle behaviour

at higher Stokes numbers. This inclusion of kinetic energy contributions proved vital for capturing complex particle-turbulence interactions, particularly the phenomenon of crossing trajectories, which is a hallmark of preferential concentration in turbulence. At higher grid resolutions, the Eulerian method incorporating second-order velocity fluctuations reduced artificial diffusion effects, significantly improving the fidelity of particle concentration spectra. In contrast, the Lagrangian method, though unaffected by artificial diffusion, exhibited sensitivity to Poisson statistics and struggled to uniformly define particle velocity fields across different regions of the flow unless many millions of particles are used. However, both methods converged at low wavenumbers, indicating consistency in capturing large-scale turbulent interactions.

The third study (Chapter 4) extended the investigation of particle clustering by introducing the combined effects of the Stokes, Reynolds, and Froude numbers, which influence particle behaviour across a range of turbulent scales. Notably, the study confirmed that particles with Stokes numbers near unity experience the strongest clustering due to their optimal interaction with turbulent eddies. For smaller Stokes numbers, particles tended to cluster around smaller eddies, while for larger Stokes numbers, particles became more dispersed, indicating a weakening of preferential concentration due to increased inertia. The study also revealed that the Reynolds number plays a critical role in particle clustering, with higher turbulence intensities promoting a broader range of void sizes and more complex particle distributions. The influence of gravity, encapsulated in the Froude number, further modulated clustering patterns, particularly at intermediate and high Stokes numbers, where gravity amplified clustering at both large and small scales, reflecting its impact on anisotropy in particle distributions.

The final study (Chapter 5) explored the role of Lagrangian Coherent Structures (LCS) in shaping particle clustering and void formation in turbulence. It found that metrics such as the Q-Criterion, Enstrophy, and Lagrangian-averaged vorticity deviation (LAVD) are critical in predicting the spatial distribution of inertial particles. Particularly, the LAVD emerged as the most robust indicator of particle clustering, revealing that regions with strong rotational coherence are most conducive to the formation of particle clusters. Additionally, the study identified a time delay, approximately one Kolmogorov timescale, in the response of particle concentrations to surrounding fluid dynamics, which highlights the need to account for the past states of the fluid when predicting current particle distributions. The tube-like structures of particle clusters and large volumetric voids observed in this study suggest a scaling regime that goes beyond classical Kolmogorov scaling, particularly at high turbulence intensities.

Taken together, these studies provide a comprehensive understanding of how

inertial particles interact with turbulent flows and offer valuable predictive tools for applications ranging from aerosol transmission in confined spaces to environmental and industrial fluid dynamics. The insights derived from this research hold practical importance in areas such as atmospheric sciences, environmental engineering, and pollution control, where accurate modelling of particle behaviour in turbulent flows is essential.

6.2 Future Work

While this thesis has advanced our understanding of aerosol dispersion and particle clustering in turbulent flows, several avenues for future research can extend the applicability and accuracy of these findings. One key area that warrants further exploration is the role of third-order velocity moments in Eulerian models of particle dispersion. The current study primarily focused on second-order velocity moments, which have proven effective in capturing preferential concentration dynamics at intermediate Stokes numbers. However, the inclusion of third-order moments could provide a deeper understanding of energy transfer mechanisms and how they influence particle clustering at higher Stokes numbers. Since third-order moments decay more rapidly than second-order moments, their impact is likely more pronounced for larger particles and higher turbulence intensities, making this an important extension for future studies.

Another critical area for future work is the application of the methods developed in this thesis to non-regular grid systems and more complex flow geometries, such as anisotropic and wall-bounded turbulence. The Roe-flux scheme, which was applied to equidistant velocity grids, would need to be adapted for non-regular grids to maintain accuracy in these more complex environments. Given that real-world flow systems are rarely isotropic or confined to regular grids, extending the current computational framework to such conditions would greatly enhance its practical utility. In particular, the application of these models to real-world environments, such as urban air pollution or industrial aerosol dispersion, could offer valuable insights into the behaviour of particles in more realistic settings.

A third area of interest involves studying particle clustering at higher Reynolds and Froude numbers. The current research has provided substantial evidence of the influence of these dimensionless groups on particle behaviour, but the exact mechanisms driving this interaction, particularly at higher turbulence intensities, are not yet fully understood. Investigating how extreme turbulence affects particle clustering could lead to more accurate models for highly turbulent systems, such as those encountered in atmospheric flows or industrial mixing processes. Moreover, the role of gravity in modulating particle clustering across different turbulence

regimes remains an open question. By systematically varying the Froude number in future studies, researchers could better understand how gravitational forces alter particle distributions in both small and large eddies.

Additionally, the study of Lagrangian Coherent Structures (LCS) could be expanded to incorporate more advanced Lagrangian tracking techniques and the simultaneous analysis of multiple fluid properties. This would allow for a more comprehensive understanding of how different coherent structures influence particle clustering and void formation in turbulent flows. Investigating other forms of coherent structures, such as non-hyperbolic structures or those identified through different LCS criteria, could provide further insights into the mechanisms driving preferential concentration. This approach would also help clarify how various fluid properties, when combined, correlate with particle clustering, offering a more nuanced perspective on turbulence-particle interactions.

Finally, future research should investigate scaling regime transitions in highly turbulent flows. The findings from this thesis suggest that traditional Kolmogorov scaling may not fully capture the behaviour of inertial particles at higher turbulence intensities and larger length scales. As turbulence intensity increases, the separation of scales becomes more pronounced, and the most appropriate timescale for the Stokes number may shift from the Kolmogorov timescale to the timescale associated with coherent eddy structures. This shift could represent a transition to a new scaling regime that better describes the dynamics of particle clustering in high-Reynolds-number flows. By developing new scaling laws or modifying existing ones, future studies could significantly enhance our ability to model particle-laden turbulent flows across a wider range of conditions.

In summary, by addressing these areas of future work, researchers can build on the findings presented in this thesis to further improve our understanding and predictive capabilities regarding aerosol dispersion, particle clustering, and turbulent flow interactions. These advancements will have far-reaching implications for fields such as environmental science, industrial fluid dynamics, and public health, where accurate modelling of particles in turbulent systems is essential.

Bibliography

[1] Aliseda, A. and Lasheras, J. [2011], 'Preferential concentration and rise velocity reduction of bubbles immersed in a homogeneous and isotropic turbulent flow', *Physics of Fluids* **23**(9).

[2] Allen, M. D. and Raabe, O. G. [1985], 'Slip correction measurements of spherical solid aerosol particles in an improved millikan apparatus', *Aerosol Science and Technology* **4**(3), 269–286.

[3] Ariki, T., Yoshida, K., Matsuda, K. and Yoshimatsu, K. [2018], 'Scale-similar clustering of heavy particles in the inertial range of turbulence', *Physical Review E* **97**(3), 033109.

[4] Ayala, O., Rosa, B. and Wang, L.-P. [2008], 'Effects of turbulence on the geometric collision rate of sedimenting droplets. part 2. theory and parameterization', *New Journal of Physics* **10**(7), 075016.

[5] Ayala, O., Rosa, B., Wang, L.-P. and Grabowski, W. W. [2008], 'Effects of turbulence on the geometric collision rate of sedimenting droplets. part 1. results from direct numerical simulation', *New Journal of Physics* **10**(7), 075015.

[6] Baker, L., Frankel, A., Mani, A. and Coletti, F. [2017], 'Coherent clusters of inertial particles in homogeneous turbulence', *Journal of Fluid Mechanics* **833**, 364–398.

[7] Baker, L. J. and Coletti, F. [2021], 'Particle–fluid–wall interaction of inertial spherical particles in a turbulent boundary layer', *Journal of Fluid Mechanics* **908**, A39.

[8] Balachandar, S. and Eaton, J. K. [2010], 'Turbulent dispersed multiphase flow', *Annual Review of Fluid Mechanics* **42**(1), 111–133.

[9] Balachandar, S. and Maxey, M. [1989], 'Methods for evaluating fluid velocities in spectral simulations of turbulence', *Journal of Computational Physics* **83**(1), 96–125.

[10] Bassenne, M., Moin, P. and Urzay, J. [2018], 'Wavelet multiresolution analysis of particle-laden turbulence', *Physical Review Fluids* **3**(8), 084304.

[11] Batchelor, G. K. [2000], *An introduction to fluid dynamics*, Cambridge University Press.

[12] Bearden, J. [1939], 'A precision determination of the viscosity of air', *Physical Review* **56**(10), 1023.

[13] Bec, J. [2003], 'Fractal clustering of inertial particles in random flows', *Physics of Fluids* **15**(11), L81–L84.

[14] Bec, J., Biferale, L., Cencini, M., Lanotte, A., Musacchio, S. and Toschi, F. [2007], 'Heavy particle concentration in turbulence at dissipative and inertial scales', *Physical Review Letters* **98**(8), 084502.

[15] Bec, J., Biferale, L., Lanotte, A., Scagliarini, A. and Toschi, F. [2010], 'Turbulent pair dispersion of inertial particles', *Journal of Fluid Mechanics* **645**, 497–528.

[16] Bec, J., Cencini, M., Hillerbrand, R. and Turitsyn, K. [2008], 'Stochastic suspensions of heavy particles', *Physica D: Nonlinear Phenomena* **237**(14-17), 2037–2050.

[17] Bec, J., Gustavsson, K. and Mehlig, B. [2024], 'Statistical models for the dynamics of heavy particles in turbulence', *Annual Review of Fluid Mechanics* **56**(1), 189–213.

[18] Bec, J., Homann, H. and Ray, S. S. [2014], 'Gravity-driven enhancement of heavy particle clustering in turbulent flow', *Physical Review Letters* **112**(18), 184501.

[19] Bergougnoux, L., Bouchet, G., Lopez, D. and Guazzelli, E. [2014], 'The motion of solid spherical particles falling in a cellular flow field at low stokes number', *Physics of Fluids* **26**(9).

[20] Bosse, T., Kleiser, L. and Meiburg, E. [2006], 'Small particles in homogeneous turbulence: settling velocity enhancement by two-way coupling', *Physics of Fluids* **18**(2).

[21] Bradshaw, P. [2013], *An introduction to turbulence and its measurement: thermodynamics and fluid mechanics series*, Elsevier.

[22] Bragg, A. D. and Collins, L. R. [2014], 'New insights from comparing statistical theories for inertial particles in turbulence: I. spatial distribution of particles', *New Journal of Physics* **16**(5), 055013.

[23] Bragg, A. D., Ireland, P. J. and Collins, L. R. [2015], 'Mechanisms for the clustering of inertial particles in the inertial range of isotropic turbulence', *Physical Review E* **92**(2), 023029.

[24] Brennen, C. E. [2005], *Fundamentals of Multiphase Flow*, Cambridge Ltd.

[25] Brethouwer, G. [2005], 'The effect of rotation on rapidly sheared homogeneous turbulence and passive scalar transport. linear theory and direct numerical simulation', *Journal of Fluid Mechanics* **542**, 305–342.

[26] Canuto, C. [2007], *Spectral Methods: Evolution to Complex Geometries and Applications to Fluid Dynamics*, Springer-Verlag.

[27] Canuto, C., Hussaini, M. Y., Quarteroni, A. and Zang, T. A. [2006], *Spectral methods*, Vol. 285, Springer.

[28] Capecelatro, J. and Desjardins, O. [2013], 'An euler–lagrange strategy for simulating particle-laden flows', *Journal of Computational Physics* **238**, 1–31.

[29] Capecelatro, J., Desjardins, O. and Fox, R. O. [2015], 'On fluid–particle dynamics in fully developed cluster-induced turbulence', *Journal of Fluid Mechanics* **780**, 578–635.

[30] Chen, L., Goto, S. and Vassilicos, J. [2006], 'Turbulent clustering of stagnation points and inertial particles', *Journal of Fluid Mechanics* **553**, 143–154.

[31] Chun, J., Koch, D. L., Rani, S. L., Ahluwalia, A. and Collins, L. R. [2005], 'Clustering of aerosol particles in isotropic turbulence', *Journal of Fluid Mechanics* **536**, 219–251.

[32] Coleman, S. and Vassilicos, J. [2009], 'A unified sweep-stick mechanism to explain particle clustering in two-and three-dimensional homogeneous, isotropic turbulence', *Physics of Fluids* **21**(11).

[33] Cox, S. M. and Matthews, P. C. [2002], 'Exponential time differencing for stiff systems', *Journal of Computational Physics* **176**(2), 430–455.

[34] Crowe, C. T., Schwarzkopf, J. D., Sommerfeld, M. and Tsuji, Y. [2011], *Multiphase Flows with Droplets and Particles*, CRC Press.

[35] Cunningham, E. [1910], 'On the velocity of steady fall of spherical particles through fluid medium', *Proceedings of the Royal Society of London. Series A, Containing Papers of a Mathematical and Physical Character* **83**(563), 357–365.

[36] Daitche, A. and Tél, T. [2011], 'Memory effects are relevant for chaotic advection of inertial particles', *Physical Review Letters* **107**(24), 244501.

[37] Davidson, P. [2015], *Turbulence: an introduction for scientists and engineers*, Oxford University Press.

[38] Dbouk, T. and Drikakis, D. [2020*a*], 'On coughing and airborne droplet transmission to humans', *Physics of Fluids* **32**(5).

[39] Dbouk, T. and Drikakis, D. [2020*b*], 'Weather impact on airborne coronavirus survival', *Physics of Fluids* **32**(9).

[40] de Oliveira, P. M., Mesquita, L. C., Gkantonas, S., Giusti, A. and Mastorakos, E. [2021], 'Evolution of spray and aerosol from respiratory releases: theoretical estimates for insight on viral transmission', *Proceedings of the Royal Society A* **477**(2245), 20200584.

[41] Downing, G. H. and Hardalupas, Y. [2024], 'Spectral characteristics of particle preferential concentration in turbulence computed by eulerian and lagrangian methods', *International Journal of Multiphase Flow* **174**, 104788.

[42] Downing, G. H., Hardalupas, Y., Archer, J., Symons, H. E., Baloglu, U. B., Schien, D., Bzdek, B. R. and Reid, J. P. [2022], 'Computational and experimental study of aerosol dispersion in a ventilated room', *Aerosol Science and Technology* **57**(1), 50–62.

[43] Durbin, P. [2011], *Statistical Theory and Modeling for Turbulent Flows*, Wiley Sons Ltd.

[44] Durham, W. M., Climent, E., Barry, M., De Lillo, F., Boffetta, G., Cencini, M. and Stocker, R. [2013], 'Turbulence drives microscale patches of motile phytoplankton', *Nature Communications* **4**(1), 2148.

[45] Eaton, J. K. [2009], 'Two-way coupled turbulence simulations of gas-particle flows using point-particle tracking', *International Journal of Multiphase Flow* **35**(9), 792–800.

[46] Eaton, J. K. and Fessler, J. [1994], 'Preferential concentration of particles by turbulence', *International Journal of Multiphase Flow* **20**, 169–209.

[47] Elghobashi, S. [1994], 'On predicting particle-laden turbulent flows', *Applied Scientific Research* **52**, 309–329.

[48] Elghobashi, S. and Truesdell, G. [1992], 'Direct simulation of particle dispersion in a decaying isotropic turbulence', *Journal of Fluid Mechanics* **242**, 655–700.

[49] Ferry, J. and Balachandar, S. [2002], 'Equilibrium expansion for the eulerian velocity of small particles', *Powder Technology* **125**(2-3), 131–139.

[50] Ferziger, J. H., Perić, M. and Street, R. L. [2019], *Computational methods for fluid dynamics*, springer.

[51] Fevrier, P., Simonin, O. and Squires, K. D. [2005], 'Partitioning of particle velocities in gas–solid turbulent flows into a continuous field and a spatially uncorrelated random distribution: theoretical formalism and numerical study', *Journal of Fluid Mechanics* **533**, 1–46.

[52] Frankel, A., Pouransari, H., Coletti, F. and Mani, A. [2016], 'Settling of heated particles in homogeneous turbulence', *Journal of Fluid Mechanics* **792**, 869–893.

[53] Friendlander, S. [2000], *Smoke, dust and haze: Fundamentals of aerosol dynamics*, Oxford University Press.

[54] Frisch, U. [1995], *Turbulence: the legacy of AN Kolmogorov*, Cambridge university press.

[55] Gelbard, F. and Seinfeld, J. H. [1979], 'The general dynamic equation for aerosols. theory and application to aerosol formation and growth', *Journal of Colloid and Interface Science* **68**(2), 363–382.

[56] Godunov, S. K. and Bohachevsky, I. [1959], 'Finite difference method for numerical computation of discontinuous solutions of the equations of fluid dynamics', *Matematičeskij Sbornik* **47**(3), 271–306.

[57] González-Torres, M., Pérez-Lombard, L., Coronel, J. F., Maestre, I. R. and Yan, D. [2022], 'A review on buildings energy information: Trends, end-uses, fuels and drivers', *Energy Reports* **8**, 626–637.

[58] Good, G., Gerashchenko, S. and Warhaft, Z. [2012], 'Intermittency and inertial particle entrainment at a turbulent interface: the effect of the large-scale eddies', *Journal of Fluid Mechanics* **694**, 371–398.

[59] Good, G., Ireland, P., Bewley, G., Bodenschatz, E., Collins, L. and Warhaft, Z. [2014], 'Settling regimes of inertial particles in isotropic turbulence', *Journal of Fluid Mechanics* **759**, R3.

[60] GÖTHE, C.-J., BJURSTRÖM, R. and Ancker, K. [1988], 'A simple method of estimating air recirculation in ventilation systems', *American Industrial Hygiene Association Journal* **49**(2), 66–69.

[61] Gualtieri, P., Picano, F. and Casciola, C. M. [2009], 'Anisotropic clustering of inertial particles in homogeneous shear flow', *Journal of Fluid Mechanics* **629**, 25–39.

[62] Gualtieri, P., Picano, F., Sardina, G. and Casciola, C. M. [2015], 'Exact regularized point particle method for multiphase flows in the two-way coupling regime', *Journal of Fluid Mechanics* **773**, 520–561.

[63] Gupta, J. K., Lin, C.-H. and Chen, Q. [2011], 'Transport of expiratory droplets in an aircraft cabin', *Indoor Air* **21**(1), 3–11.

[64] Gustavsson, K. and Mehlig, B. [2016], 'Statistical models for spatial patterns of heavy particles in turbulence', *Advances in Physics* **65**(1), 1–57.

[65] Gustavsson, K., Vajedi, S. and Mehlig, B. [2014], 'Clustering of particles falling in a turbulent flow', *Physical Review Letters* **112**(21), 214501.

[66] Haller, G. [2015], 'Lagrangian coherent structures', *Annual Review of Fluid Mechanics* **47**(1), 137–162.

[67] Haller, G. and Yuan, G. [2000], 'Lagrangian coherent structures and mixing in two-dimensional turbulence', *Physica D: Nonlinear Phenomena* **147**(3-4), 352–370.

[68] Hassaini, R. and Coletti, F. [2022], 'Scale-to-scale turbulence modification by small settling particles', *Journal of Fluid Mechanics* **949**, A30.

[69] Haugen, N. E., Brandenburg, A., Sandin, C. and Mattsson, L. [2022], 'Spectral characterisation of inertial particle clustering in turbulence', *Journal of Fluid Mechanics* **934**, A37.

[70] Haugen, N. E. L., Krüger, J., Mitra, D. and Løvås, T. [2018], 'The effect of turbulence on mass transfer rates of small inertial particles with surface reactions', *Journal of Fluid Mechanics* **836**, 932–951.

[71] Haynes, W. M. [2016], *CRC handbook of chemistry and physics*, CRC press.

[72] Hearst, R. J. and Lavoie, P. [2014], 'Decay of turbulence generated by a square-fractal-element grid', *Journal of Fluid Mechanics* **741**, 567–584.

[73] Hedworth, H. A., Karam, M., McConnell, J., Sutherland, J. C. and Saad, T. [2021], 'Mitigation strategies for airborne disease transmission in orchestras using computational fluid dynamics', *Science Advances* **7**(26), eabg4511.

[74] Hill, R. J. [1978], 'Models of the scalar spectrum for turbulent advection', *Journal of Fluid Mechanics* **88**(3), 541–562.

[75] Hinds, W. C. and Zhu, Y. [2022], *Aerosol technology: properties, behavior, and measurement of airborne particles*, John Wiley & Sons.

[76] Horwitz, J. and Mani, A. [2016], 'Accurate calculation of stokes drag for point–particle tracking in two-way coupled flows', *Journal of Computational Physics* **318**, 85–109.

[77] Huck, P. D., Bateson, C., Volk, R., Cartellier, A., Bourgoin, M. and Aliseda, A. [2018], 'The role of collective effects on settling velocity enhancement for inertial particles in turbulence', *Journal of Fluid Mechanics* **846**, 1059–1075.

[78] Hunt, J. C., Wray, A. A. and Moin, P. [1988], Eddies, streams, and convergence zones in turbulent flows, *in* 'Studying turbulence using numerical simulation databases, 2. Proceedings of the 1988 summer program'.

[79] Hwang, W. and Eaton, J. K. [2006], 'Homogeneous and isotropic turbulence modulation by small heavy () particles', *Journal of Fluid Mechanics* **564**, 361–393.

[80] Ireland, P. J., Bragg, A. D. and Collins, L. R. [2016*a*], 'The effect of reynolds number on inertial particle dynamics in isotropic turbulence. part 1. simulations without gravitational effects', *Journal of Fluid Mechanics* **796**, 617–658.

[81] Ireland, P. J., Bragg, A. D. and Collins, L. R. [2016*b*], 'The effect of reynolds number on inertial particle dynamics in isotropic turbulence. part 2. simulations with gravitational effects', *Journal of Fluid Mechanics* **796**, 659–711.

[82] Ireland, P. J. and Desjardins, O. [2017], 'Improving particle drag predictions in euler–lagrange simulations with two-way coupling', *Journal of Computational Physics* **338**, 405–430.

[83] Ireland, P. J., Vaithianathan, T., Sukheswalla, P. S., Ray, B. and Collins, L. R. [2013], 'Highly parallel particle-laden flow solver for turbulence research', *Computers & Fluids* **76**, 170–177.

[84] Israelachvili, J. N. [2011], *Intermolecular and surface forces*, Academic Press.

[85] Jiang, Y., Zhao, B., Li, X., Yang, X., Zhang, Z. and Zhang, Y. [2009], Investigating a safe ventilation rate for the prevention of indoor sars transmission: An attempt based on a simulation approach, *in* 'Building Simulation', Vol. 2, Springer, pp. 281–289.

[86] Jin, G., He, G.-W. and Wang, L.-P. [2010], 'Large-eddy simulation of turbulent collision of heavy particles in isotropic turbulence', *Physics of Fluids* **22**(5).

[87] Kasbaoui, M. H., Koch, D. L. and Desjardins, O. [2019], 'Clustering in euler–euler and euler–lagrange simulations of unbounded homogeneous particle-laden shear', *Journal of Fluid Mechanics* **859**, 174–203.

[88] Kaufmann, A., Moreau, M., Simonin, O. and Helie, J. [2008], 'Comparison between lagrangian and mesoscopic eulerian modelling approaches for inertial particles suspended in decaying isotropic turbulence', *Journal of Computational Physics* **227**(13), 6448–6472.

[89] Kim, I., Elghobashi, S. and Sirignano, W. A. [1998], 'On the equation for spherical-particle motion: effect of reynolds and acceleration numbers', *Journal of Fluid Mechanics* **367**, 221–253.

[90] Kong, B., Feng, H., Capecelatro, J., Patel, R., Desjardins, O. and Fox, R. O. [2017], 'Euler–euler anisotropic gaussian mesoscale simulation of homogeneous cluster-induced gas–particle turbulence', *AIChE Journal* **63**(7), 2630–2643.

[91] Kulmala, M., Vehkamäki, H., Petäjä, T., Dal Maso, M., Lauri, A., Kerminen, V.-M., Birmili, W. and McMurry, P. [2004], 'Formation and growth rates of ultrafine atmospheric particles: a review of observations', *Journal of Aerosol Science* **35**(2), 143–176.

[92] Launder, B. and Spalding, D. [1983], 'Paper 8—the numerical computation of turbulent flows', *Numerical Prediction of Flow, Heat Transfer, Turbulence and Combustion* pp. 96–116.

[93] LeVeque, R. J. [2007], *Finite difference methods for ordinary and partial differential equations: steady-state and time-dependent problems*, SIAM.

[94] Li, C., Lim, K., Berk, T., Abraham, A., Heisel, M., Guala, M., Coletti, F. and Hong, J. [2021], 'Settling and clustering of snow particles in atmospheric turbulence', *Journal of Fluid Mechanics* **912**, A49.

[95] Lian, H., Chang, X. and Hardalupas, Y. [2019], 'Time resolved measurements of droplet preferential concentration in homogeneous isotropic turbulence without mean flow', *Physics of Fluids* **31**(2).

[96] Lian, H., Soulopoulos, N. and Hardalupas, Y. [2017], 'Evaluation of the topological characteristics of the turbulent flow in a 'box of turbulence'through 2d time-resolved particle image velocimetry', *Experiments in Fluids* **58**, 1–17.

[97] Ling, Y., Parmar, M. and Balachandar, S. [2013], 'A scaling analysis of added-mass and history forces and their coupling in dispersed multiphase flows', *International Journal of Multiphase Flow* **57**, 102–114.

[98] Liu, X.-D., Osher, S. and Chan, T. [1994], 'Weighted essentially non-oscillatory schemes', *Journal of Computational Physics* **115**(1), 200–212.

[99] Liu, Y., Shen, L., Zamansky, R. and Coletti, F. [2020], 'Life and death of inertial particle clusters in turbulence', *Journal of Fluid Mechanics* **902**, R1.

[100] Lundgren, T. S. [2003], 'Linearly forced isotropic turbulence', *Center for Turbulence Research Annual Research Briefs 2003* .

[101] M. Kuerten, J. [2016], 'Point-particle dns and les of particle-laden turbulent flow-a state-of-the-art review', *Flow, Turbulence and Combustion* **97**, 689–713.

[102] Marchioli, C., Picciotto, M. and Soldati, A. [2007], 'Influence of gravity and lift on particle velocity statistics and transfer rates in turbulent vertical channel flow', *International Journal of Multiphase Flow* **33**(3), 227–251.

[103] Mathai, V. [2021], 'The air we breathe in a car', *Physics Today* **74**(6), 66–67.

[104] Matsuda, K., Onishi, R., Hirahara, M., Kurose, R., Takahashi, K. and Komori, S. [2014], 'Influence of microscale turbulent droplet clustering on radar cloud observations', *Journal of the Atmospheric Sciences* **71**(10), 3569–3582.

[105] Matsuda, K., Onishi, R. and Takahashi, K. [2017], 'Influence of gravitational settling on turbulent droplet clustering and radar reflectivity factor', *Flow, Turbulence and Combustion* **98**, 327–340.

[106] Matsuda, K., Schneider, K. and Yoshimatsu, K. [2021], 'Scale-dependent statistics of inertial particle distribution in high reynolds number turbulence', *Physical Review Fluids* **6**(6), 064304.

[107] Maxey, M. R. [1987], 'The gravitational settling of aerosol particles in homogeneous turbulence and random flow fields', *Journal of Fluid Mechanics* **174**, 441–465.

[108] Maxey, M. R. and Riley, J. J. [1983], 'Equation of motion for a small rigid sphere in a nonuniform flow', *The Physics of Fluids* **26**(4), 883–889.

[109] Mehrabadi, M., Horwitz, J., Subramaniam, S. and Mani, A. [2018], 'A direct comparison of particle-resolved and point-particle methods in decaying turbulence', *Journal of Fluid Mechanics* **850**, 336–369.

[110] Meneveau, C. and Katz, J. [2000], 'Scale-invariance and turbulence models for large-eddy simulation', *Annual Review of Fluid Mechanics* **32**(1), 1–32.

[111] Milton, D. K., Fabian, M. P., Cowling, B. J., Grantham, M. L. and McDevitt, J. J. [2013], 'Influenza virus aerosols in human exhaled breath: particle size, culturability, and effect of surgical masks', *PLoS Pathogens* **9**(3), e1003205.

[112] Miyawaki, O., Saito, A., Matsuo, T. and Nakamura, K. [1997], 'Activity and activity coefficient of water in aqueous solutions and their relationships with solution structure parameters', *Bioscience, Biotechnology, and Biochemistry* **61**(3), 466–469.

[113] Moin, P. and Mahesh, K. [1998], 'Direct numerical simulation: a tool in turbulence research', *Annual Review of Fluid Mechanics* **30**(1), 539–578.

[114] Monchaux, R., Bourgoin, M. and Cartellier, A. [2010], 'Preferential concentration of heavy particles: a voronoï analysis', *Physics of Fluids* **22**(10).

[115] Monchaux, R., Bourgoin, M. and Cartellier, A. [2012], 'Analyzing preferential concentration and clustering of inertial particles in turbulence', *International Journal of Multiphase Flow* **40**, 1–18.

[116] Monin, A. S. and Yaglom, A. M. [2013], *Statistical fluid mechanics, volume II: mechanics of turbulence*, Vol. 2, Courier Corporation.

[117] Morawska, L., Allen, J., Bahnfleth, W., Bluyssen, P. M., Boerstra, A., Buonanno, G., Cao, J., Dancer, S. J., Floto, A., Franchimon, F. et al. [2021], 'A paradigm shift to combat indoor respiratory infection', *Science* **372**(6543), 689–691.

[118] Nemes, A., Dasari, T., Hong, J., Guala, M. and Coletti, F. [2017], 'Snowflakes in the atmospheric surface layer: observation of particle–turbulence dynamics', *Journal of Fluid Mechanics* **814**, 592–613.

[119] Oka, S. and Goto, S. [2021], 'Generalized sweep-stick mechanism of inertial-particle clustering in turbulence', *Physical Review Fluids* **6**(4), 044605.

[120] Olivieri, S., Picano, F., Sardina, G., Iudicone, D. and Brandt, L. [2014], 'The effect of the basset history force on particle clustering in homogeneous and isotropic turbulence', *Physics of Fluids* **26**(4).

[121] Onishi, R., Baba, Y. and Takahashi, K. [2011], 'Large-scale forcing with less communication in finite-difference simulations of stationary isotropic turbulence', *Journal of Computational Physics* **230**(10), 4088–4099.

[122] Onishi, R., Takahashi, K. and Komori, S. [2009], 'Influence of gravity on collisions of monodispersed droplets in homogeneous isotropic turbulence', *Physics of Fluids* **21**(12).

[123] Oujia, T., Jain, S., Matsuda, K., Schneider, K., West, J. and Maeda, K. [2022], Neural networks for synthesizing preferential concentration of particles in isotropic turbulence, *in* 'Proceedings of the Summer Program', pp. 153–162.

[124] Oujia, T., Matsuda, K. and Schneider, K. [2020], 'Divergence and convergence of inertial particles in high-reynolds-number turbulence', *Journal of Fluid Mechanics* **905**, A14.

[125] Patterson, G. and Orszag, S. A. [1971], 'Spectral calculations of isotropic turbulence: Efficient removal of aliasing interactions', *Physics of Fluids* **14**(11), 2538.

[126] Pendar, M.-R. and Páscoa, J. C. [2020], 'Numerical modeling of the distribution of virus carrying saliva droplets during sneeze and cough', *Physics of Fluids* **32**(8).

[127] Petersen, A. J., Baker, L. and Coletti, F. [2019], 'Experimental study of inertial particles clustering and settling in homogeneous turbulence', *Journal of Fluid Mechanics* **864**, 925–970.

[128] Poelma, C. and Ooms, G. [2006], 'Particle-turbulence interaction in a homogeneous, isotropic turbulent suspension', *Appl. Mech. Rev.* **59**, 78–90.

[129] Poelma, C., Westerweel, J. and Ooms, G. [2007], 'Particle–fluid interactions in grid-generated turbulence', *Journal of Fluid Mechanics* **589**, 315–351.

[130] Pope, S. B. [2000], *Turbulent Flows*, Cambridge University Press.

[131] Poussou, S. B., Mazumdar, S., Plesniak, M. W., Sojka, P. E. and Chen, Q. [2010], 'Flow and contaminant transport in an airliner cabin induced by a moving body: Model experiments and cfd predictions', *Atmospheric Environment* **44**(24), 2830–2839.

[132] Prasath, S. G., Vasan, V. and Govindarajan, R. [2019], 'Accurate solution method for the maxey–riley equation, and the effects of basset history', *Journal of Fluid Mechanics* **868**, 428–460.

[133] Prather, K. A., Marr, L. C., Schooley, R. T., McDiarmid, M. A., Wilson, M. E. and Milton, D. K. [2020], 'Airborne transmission of sars-cov-2', *Science* **370**(6514), 303–304.

[134] Pruppacher, H. R. and Klett, J. D. [2012], *Microphysics of clouds and precipitation: Reprinted 1980*, Springer Science & Business Media.

[135] Qian, H., Li, Y., Nielsen, P. V. and Huang, X. [2009], 'Spatial distribution of infection risk of sars transmission in a hospital ward', *Building and Environment* **44**(8), 1651–1658.

[136] Reade, W. C. and Collins, L. R. [2000], 'Effect of preferential concentration on turbulent collision rates', *Physics of Fluids* **12**(10), 2530–2540.

[137] Reveillon, J. and Demoulin, F.-X. [2007], 'Effects of the preferential segregation of droplets on evaporation and turbulent mixing', *Journal of Fluid Mechanics* **583**, 273–302.

[138] Roberts, P. J. and Webster, D. R. [2002], 'Turbulent diffusion', *Environmental Fluid Mechanics-Theories and Application* pp. 7–47.

[139] Roe, P. L. [1985], 'Some contributions to the modelling of discontinuous flows', *Large-Scale Computations in Fluid Mechanics* pp. 163–193.

[140] Roe, P. L. [1986], 'Characteristic-based schemes for the euler equations', *Annual Review of Fluid Mechanics* **18**(1), 337–365.

[141] Rogallo, R. S. [1981], *Numerical experiments in homogeneous turbulence*, Vol. 81315, National Aeronautics and Space Administration.

[142] Rosales, C. and Meneveau, C. [2005], 'Linear forcing in numerical simulations of isotropic turbulence: Physical space implementations and convergence properties', *Physics of Fluids* **17**(9).

[143] Ruiz, J., Macías, D. and Peters, F. [2004], 'Turbulence increases the average settling velocity of phytoplankton cells', *Proceedings of the National Academy of Sciences* **101**(51), 17720–17724.

[144] Sagaut, P. [2005], *Large eddy simulation for incompressible flows: an introduction*, Springer Science & Business Media.

[145] Sahu, S., Hardalupas, Y. and Taylor, A. [2018], 'Interaction of droplet dispersion and evaporation in a polydispersed spray', *Journal of Fluid Mechanics* **846**, 37–81.

[146] Saito, I. and Gotoh, T. [2018], 'Turbulence and cloud droplets in cumulus clouds', *New Journal of Physics* **20**(2), 023001.

[147] Saw, E.-W., Bewley, G. P., Bodenschatz, E., Sankar Ray, S. and Bec, J. [2014], 'Extreme fluctuations of the relative velocities between droplets in turbulent airflow', *Physics of Fluids* **26**(11).

[148] Saw, E. W., Shaw, R. A., Ayyalasomayajula, S., Chuang, P. Y. and Gylfason, A. [2008], 'Inertial clustering of particles in high-reynolds-number turbulence', *Physical Review Letters* **100**(21), 214501.

[149] Schiller, V. L. [1933], 'Uber die grundlegenden berechnungen bei der schwerkraftaufbereitung', *Z. Vereines Deutscher Inge.* **77**, 318–321.

[150] Shaw, R. A. [2003], 'Particle-turbulence interactions in atmospheric clouds', *Annual Review of Fluid Mechanics* **35**(1), 183–227.

[151] Sklar, M. [1959], Fonctions de répartition à n dimensions et leurs marges, *in* 'Annales de l'ISUP', Vol. 8, pp. 229–231.

[152] Sommerstein, R., Fux, C. A., Vuichard-Gysin, D., Abbas, M., Marschall, J., Balmelli, C., Troillet, N., Harbarth, S., Schlegel, M., Widmer, A. et al. [2020], 'Risk of sars-cov-2 transmission by aerosols, the rational use of masks, and protection of healthcare workers from covid-19', *Antimicrobial Resistance & Infection Control* **9**, 1–8.

[153] Squires, K. D. and Eaton, J. K. [1991*a*], 'Measurements of particle dispersion obtained from direct numerical simulations of isotropic turbulence', *Journal of Fluid Mechanics* **226**, 1–35.

[154] Squires, K. D. and Eaton, J. K. [1991*b*], 'Preferential concentration of particles by turbulence', *Physics of Fluids A: Fluid Dynamics* **3**(5), 1169–1178.

[155] Sreenivasan, K. R. [1991], 'On local isotropy of passive scalars in turbulent shear flows', *Proceedings of the Royal Society of London. Series A: Mathematical and Physical Sciences* **434**(1890), 165–182.

[156] Sukheswalla, P., Vaithianathan, T. and Collins, L. R. [2013], 'Simulation of homogeneous turbulent shear flows at higher reynolds numbers: numerical challenges and a remedy', *Journal of Turbulence* **14**(5), 60–97.

[157] Sumbekova, S., Cartellier, A., Aliseda, A. and Bourgoin, M. [2017], 'Preferential concentration of inertial sub-kolmogorov particles: the roles of mass loading of particles, stokes numbers, and reynolds numbers', *Physical Review Fluids* **2**(2), 024302.

[158] Sundaram, S. and Collins, L. R. [1997], 'Collision statistics in an isotropic particle-laden turbulent suspension. part 1. direct numerical simulations', *Journal of Fluid Mechanics* **335**, 75–109.

[159] Tennekes, H. and Lumley, J. L. [1972], *A first course in turbulence*, MIT press.

[160] Tom, J. and Bragg, A. D. [2019], 'Multiscale preferential sweeping of particles settling in turbulence', *Journal of Fluid Mechanics* **871**, 244–270.

[161] Toschi, F. and Bodenschatz, E. [2009], 'Lagrangian properties of particles in turbulence', *Annual Review of Fluid Mechanics* **41**(1), 375–404.

[162] Tropea, C., Yarin, A. L., Foss, J. F. et al. [2007], *Springer handbook of experimental fluid mechanics*, Vol. 1, Springer.

[163] Vaillancourt, P. A. and Yau, M. [2000], 'Review of particle-turbulence interactions and consequences for cloud physics', *Bulletin of the American Meteorological Society* **81**(2), 285–298.

[164] Van Hinsberg, M., Boonkkamp, J. t. T., Toschi, F. and Clercx, H. [2013], 'Optimal interpolation schemes for particle tracking in turbulence', *Physical Review E—Statistical, Nonlinear, and Soft Matter Physics* **87**(4), 043307.

[165] Vejerano, E. P. and Marr, L. C. [2018], 'Physico-chemical characteristics of evaporating respiratory fluid droplets', *Journal of The Royal Society Interface* **15**(139), 20170939.

[166] Venkatram, A. and Weil, J. [2021], 'Modeling turbulent transport of aerosols inside rooms using eddy diffusivity', *Indoor Air* **31**(6), 1886–1895.

[167] Vié, A., Doisneau, F. and Massot, M. [2015], 'On the anisotropic gaussian velocity closure for inertial-particle laden flows', *Communications in Computational Physics* **17**(1), 1–46.

[168] Vincent, A. and Meneguzzi, M. [1991], 'The spatial structure and statistical properties of homogeneous turbulence', *Journal of Fluid Mechanics* **225**, 1–20.

[169] Wang, L.-P. and Maxey, M. R. [1993], 'Settling velocity and concentration distribution of heavy particles in homogeneous isotropic turbulence', *Journal of Fluid Mechanics* **256**, 27–68.

[170] Wargocki, P. [2013], 'The effects of ventilation in homes on health', *International Journal of Ventilation* **12**(2), 101–118.

[171] Weller, H. G., Tabor, G., Jasak, H. and Fureby, C. [1998], 'A tensorial approach to computational continuum mechanics using object-oriented techniques', *Computers in Physics* **12**(6), 620–631.

[172] Wells, W. F. and Stone, W. [1934], 'On air-borne infection. study iii. viability of droplet nuclei infection.', *American Journal of Hygiene* **20**, 619–627.

[173] Wilkins, M. L. [1980], 'Use of artificial viscosity in multidimensional fluid dynamic calculations', *Journal of Computational Physics* **36**(3), 281–303.

[174] Woittiez, E. J., Jonker, H. J. and Portela, L. M. [2009], 'On the combined effects of turbulence and gravity on droplet collisions in clouds: a numerical study', *Journal of the Atmospheric Sciences* **66**(7), 1926–1943.

[175] Yhee, J. Y., Im, J. and Nho, R. S. [2016], 'Advanced therapeutic strategies for chronic lung disease using nanoparticle-based drug delivery', *Journal of Clinical Medicine* **5**(9), 82.

[176] Yoshimoto, H. and Goto, S. [2007], 'Self-similar clustering of inertial particles in homogeneous turbulence', *Journal of Fluid Mechanics* **577**, 275–286.

[177] Zaichik, L. I. and Alipchenkov, V. M. [2009], 'Statistical models for predicting pair dispersion and particle clustering in isotropic turbulence and their applications', *New Journal of Physics* **11**(10), 103018.

[178] Zamansky, R., Coletti, F., Massot, M. and Mani, A. [2016], 'Turbulent thermal convection driven by heated inertial particles', *Journal of Fluid Mechanics* **809**, 390–437.

[179] Zhu, S., Srebric, J., Spengler, J. D. and Demokritou, P. [2012], 'An advanced numerical model for the assessment of airborne transmission of influenza in bus microenvironments', *Building and Environment* **47**, 67–75.

Appendix A

Roe Decomposition

First, we define the following:

$$v_a = \frac{p_a}{n}, \tag{A.1}$$

$$H_{ab} = \frac{3E_{ab}}{n} - v_a v_b, \tag{A.2}$$

$$C_a = \sqrt{\frac{2E_{aa}}{n} - v_a v_a}, \tag{A.3}$$

$$r_{ab} = \frac{\frac{2E_{ab}}{n} - v_a v_b}{C_a C_b}, \tag{A.4}$$

where v_a is the average particle velocity in direction a, p_a is the particle momentum in direction a, n is the particle number density, E_{ab} is the 'directional' kinetic energy in directions a & b and H_{ab} is a useful intermediate quantity.

Now we define the following:

$$R^m = \sqrt{\frac{n^R}{n^L}}, \tag{A.5}$$

$$n^m = R^m n^L, \tag{A.6}$$

$$v_a^m = \frac{R^m v_a^R + v_a^L}{1 + R^m}, \tag{A.7}$$

$$H_{ab}^m = \frac{R^m H_{ab}^R + H_{ab}^L}{1 + R^m}, \tag{A.8}$$

where superscript L means the left-hand side of a cell boundary and superscript R is the right-hand side of the cell boundary and superscript m represent the roe-average of the left- and right-hand sides on the cell boundary. From these intermediate quantities it is possible to define the roe average vector of conserved properties U^m and the matrix $\mathbf{A}$:

$$\boldsymbol{U}^m = \begin{pmatrix} n^m & p_x^m & p_y^m & p_z^m & E_{xx}^m & E_{xy}^m & E_{yy}^m & E_{xz}^m & E_{zz}^m & E_{yz}^m \end{pmatrix}^\top, \tag{A.9}$$

$$\mathbf{A} = \left.\frac{\partial \boldsymbol{F}}{\partial \boldsymbol{U}}\right|_{\boldsymbol{U}^m}, \tag{A.10}$$

this definition for matrix $\mathbf{A}$ satisfies all the conditions of Equations 3.19, 3.20 & 3.21. The matrix $\mathbf{A}$ is diagonalisable and has the following form:

$$\mathbf{P}_{1-8} = \begin{pmatrix} 0 & 2 & 0 & 0 & 0 & 0 & 0 & 0 \\ 0 & 2v_x & 0 & 0 & 0 & 0 & 0 & 0 \\ 0 & 2v_y & 0 & 0 & 0 & -2 & 0 & 2 \\ 0 & 2v_z & 0 & 0 & -2 & 0 & 2 & 0 \\ 0 & v_x^2 & 0 & 0 & 0 & 0 & 0 & 0 \\ 0 & v_x v_y & 0 & 0 & 0 & C_x - v_x & 0 & C_x + v_x \\ 1 & 0 & 0 & 0 & 0 & 2r_{xy}C_y - v_y & 0 & 2r_{xy}C_y + v_y \\ 0 & v_x v_z & 0 & 0 & C_x - v_x & 0 & C_x + v_x & 0 \\ 0 & 0 & 1 & 0 & 2r_{xz}C_z - v_z & 0 & 2r_{xz}C_z + v_z & 0 \\ 0 & 0 & 0 & 1 & r_{xy}C_y - v_y & r_{xz}C_z - v_z & r_{xy}C_y + v_y & r_{xz}C_z + v_z \end{pmatrix} \tag{A.11}$$

$$\mathbf{P}_{9-10} = \begin{pmatrix} 2 & 2 \\ -2\sqrt{3}C_x + 2v_x & 2\sqrt{3}C_x + 2v_x \\ -2\sqrt{3}r_{xy}C_y + 2v_y & 2\sqrt{3}r_{xy}C_y + 2v_y \\ -2\sqrt{3}r_{xz}C_z + 2v_z & 2\sqrt{3}r_{xz}C_z + 2v_z \\ \left(\sqrt{3}C_x - v_x\right)^2 & \left(\sqrt{3}C_x + v_x\right)^2 \\ \left(\sqrt{3}C_x - v_x\right)\left(\sqrt{3}r_{xy}C_y - v_y\right) & \left(\sqrt{3}C_x + v_x\right)\left(\sqrt{3}r_{xy}C_y + v_y\right) \\ \left(\sqrt{3}r_{xy}C_y - v_y\right)^2 + C_y^2\left(1 - r_{xy}^2\right) & \left(\sqrt{3}r_{xy}C_y + v_y\right)^2 + C_y^2\left(1 - r_{xy}^2\right) \\ \left(\sqrt{3}C_x - v_x\right)\left(\sqrt{3}r_{xz}C_z - v_z\right) & \left(\sqrt{3}C_x + v_x\right)\left(\sqrt{3}r_{xz}C_z + v_z\right) \\ \left(\sqrt{3}r_{xy}C_z - v_z\right)^2 + C_z^2\left(1 - r_{xz}^2\right) & \left(\sqrt{3}r_{xz}C_z + v_z\right)^2 + C_z^2\left(1 - r_{xz}^2\right) \\ \left(\sqrt{3}r_{xy}C_y - v_y\right)\left(\sqrt{3}r_{xz}C_z - v_z\right) & \left(\sqrt{3}r_{xy}C_y + v_y\right)\left(\sqrt{3}r_{xz}C_z + v_z\right) \\ +C_yC_z\left(r_{yz} - r_{xy}r_{xz}\right) & +C_yC_z\left(r_{yz} - r_{xy}r_{xz}\right) \end{pmatrix} \tag{A.12}$$

$$\mathbf{P} = \begin{pmatrix} \mathbf{P}_{1-8} & \mathbf{P}_{9-10} \end{pmatrix} \tag{A.13}$$

$$\mathbf{\Lambda} = \operatorname{diag}\begin{pmatrix} v_x & v_x & v_x & v_x & v_x - C_x & v_x - C_x, \\ & & v_x + C_x & v_x + C_x & v_x - \sqrt{3}C_x & v_x + \sqrt{3}C_x \end{pmatrix} \tag{A.14}$$